



THÈSE DE DOCTORAT
DE L'UNIVERSITÉ PSL

Préparée à École Normale Supérieure

**Engineering Multi-Photon Dissipation In Superconducting
Circuits For Quantum Error Correction**

Soutenue par

Raphaël Lescanne

Le 20 février 2020

École doctorale n°564

Physique en Île de France

Spécialité

Physique Quantique

Composition du jury :

David DiVINCENZO Professeur, Forschungszentrum Jülich	<i>Rapporteur</i>
Philippe GRANGIER Professeur, Institut d'Optique	<i>Président du Jury</i>
Tristan MEUNIER Directeur de recherche, Institut Néel	<i>Rapporteur</i>
Takis KONTOS Directeur de recherche, ENS	<i>Directeur de thèse</i>
Zaki LEGHTAS Chargé de recherche, Mines ParisTech	<i>Directeur de thèse</i>
Benjamin HUARD Professeur, ENS de Lyon	<i>Membre invité</i>

À mes grands-parents

Abstract

Quantum systems can occupy peculiar states, such as superposition or entangled states. These states are intrinsically fragile and eventually get wiped out by inevitable interactions with the environment. Protecting quantum states against decoherence is a fundamental problem in physics and is pivotal for the future of quantum computing. In this thesis, we discuss experiments on superconducting circuits that investigate a new kind of qubit: the Schrödinger cat qubit. It belongs to the class of bosonic codes that store quantum information in the infinite dimensional Hilbert space of a microwave resonator.

By carefully tailoring the dissipation of the resonator, we are able to stabilize the two basis states of the cat-qubit without affecting their superposition. In terms of errors, this translates into a reduced bit-flip rate while keeping a native phase-flip rate. This approach challenges the intuition that a qubit must be isolated from its environment. Instead, the dissipation acts as a feedback loop which continuously and autonomously corrects against errors. This enabling dissipation is known as two-photon dissipation and was engineered by the general method of parametric pumping. In our case, it is used to selectively intensify a two-to-one photon exchange interaction between the cat-qubit resonator and a dissipative resonator.

To demonstrate error correction with cat-qubits, experimental efforts have been made during this thesis to cross the demanding threshold where the correction is faster than the occurrence of all errors, including those induced by the correcting mechanism itself. This has led us to question the current limitations of parametric pumping to better design our superconducting circuits. Mastering the dissipation engineering toolbox also brought us to other applications such as itinerant microwave photon detection for which an experimental proof of principle was realised during this thesis.

Key words

Superconducting circuits, Quantum Error Correction, Dissipation engineering, Josephson junctions.

Résumé

Les états quantiques peuvent occuper des états particuliers tels que les états de superposition ou intriqués. Ces états sont fragiles et finissent toujours par être détruits par d'inévitables interactions avec l'environnement. La protection d'états quantiques contre la décohérence est un problème fondamental en physique mais aussi un point crucial pour l'avenir de l'informatique quantique. Dans cette thèse, nous discutons d'expériences conduites sur des circuits supraconducteurs qui cherchent à mettre en évidence un nouveau qubit : le qubit de chat de Schrödinger. Ce qubit appartient à la classe des codes bosoniques qui encodent l'information quantique dans l'espace de Hilbert de dimension infinie d'un résonateur microonde.

En modelant avec soin la dissipation de ce résonateur, nous parvenons à stabiliser les états de base du qubit de chat sans affecter leurs superpositions. En terme d'erreurs, cela se traduit en un taux de bit-flip réduit sans augmenter le taux de phase-flip initial. Cette approche vient défier l'intuition selon laquelle un qubit doit être isolé de son environnement. Au lieu de cela, cette dissipation bien choisie agit comme une boucle de rétroaction qui corrige les erreurs de manière continue et autonome. Cette dissipation décisive est connue sous le nom de dissipation à deux photons et est générée grâce à la méthode du pompage paramétrique. Dans notre cas, il est utilisé pour intensifier sélectivement une interaction d'échange de photons deux-pour-un entre le résonateur du qubit de chat et un autre résonateur dissipatif.

Pour démontrer la correction d'erreur avec les qubits de chats, des efforts expérimentaux ont été fournis pendant cette thèse pour franchir le seuil au delà duquel la correction est plus rapide que l'apparition de nouvelles erreurs, notamment celles induites par le mécanisme de correction lui-même. Ceci nous a conduit à questionner les limites actuelles du pompage paramétrique afin de mieux concevoir nos circuits supraconducteurs. Maitriser ces dissipations exotiques nous a aussi amené à d'autres applications telles que la détection de photon microondes itinérants pour laquelle une preuve de principe expérimentale a été réalisée au cours de cette thèse.

Mots clés

Circuits supraconducteurs, Correction d'erreur quantique, Ingénierie de dissipation, Jonction Josephson.

Remerciements

Mes premiers mots seront pour remercier les membres du jury pour leur relecture attentive du manuscrit ainsi que pour leur attention et leurs questions lors de la soutenance.

Au cours de cette thèse, j'ai eu la chance d'être encadré par Zaki Leghtas et Takis Kontos. Merci Zaki pour ta patience, ta rigueur et ton enthousiasme. Ces qualités qui font de toi un grand chercheur, ont permis de compenser mon pessimisme latent ainsi que ma vision parfois trop intuitive de la physique. Ces presque quatre années de thèse auront été un véritable régal scientifique et humain. Je ne pouvais espérer être aussi bien encadré que je ne l'ai été, et cela, sans même compter le renfort apporté par Takis. Merci Takis, tu auras été tout du long de la thèse source de précieux conseils : une expérience accumulée grâce à ton "grand âge" comme tu t'amuses souvent à nous le rappeler. Nous amuser, tu sais bien le faire, en témoignent tes innombrables imitations faites sur l'heure du déjeuner. Au delà de mes deux directeurs de thèse, j'aimerais remercier mes autres encadrants. Benjamin Huard est la personne qui m'a fait confiance pour entrer dans le monde des circuits supraconducteurs. Je lui suis reconnaissant d'avoir fait ce choix et j'ai eu grand plaisir à continuer à collaborer avec lui malgré son départ à Lyon avec le reste de son équipe. Une des expériences de ma thèse a été conduite sous la supervision supplémentaire de Samuel Deléglise et Emmanuel Flurin. Cette collaboration qui n'était pas prévue au début de ma thèse fut véritablement passionnante, Samuel nous partageant tout ce qu'il connaissait des photons et Emmanuel complétant les connaissances expérimentales de Zaki. J'espère continuer longtemps à travailler avec vous tous !

Rien de tout cela n'aurait été possible sans toute l'effervescence scientifique dans laquelle j'ai évolué. Pour cela, je me dois de remercier toute l'équipe HQC bien sûr pour leur accueil et leur collaboration expérimentale. En particulier, Matthieu Dartiailh sans qui contrôler les expériences aurait été un cauchemar et pour sa façon bien à lui de nous enseigner Python, Marius Villiers pour tout le travail méticuleux qu'il a effectué sur le cryostat, Clarke Smith pour ses connaissances pointilleuses en circuits supraconducteurs, Camille Berdou pour sa relève consciencieuse, Ulysse Réglade et Anthony Gandon pour leurs contributions aux outils du groupe, Matthieu Desjardins pour son soutien et ses conseils en création de start-up, Lauriane Contamin avec qui j'aurais aimé plus travailler et qui était force motrice de l'esprit du groupe et enfin Tino Cubaynes pour son expertise en fabrication. Je tiens également à remercier toute l'équipe Quantic partagée entre Inria, les Mines et l'ENS Paris, un puit sans fond d'idées et de savoir avec qui nous partageons nos séminaires. Notamment, Mazyar Mirrahimi le cerveau au coeur de nos expériences, Pierre Rouchon qui a le don de savoir parler aux mathématiciens et aux physiciens, Alain Sarlette pour toutes les solutions qu'il nous a façonné, Lucas Verney

pour sa collaboration sur nos premiers papiers, Jérémie Guillaud pour son expertise en qubits de chat et Philippe Campagne-Ibarcq, même s'il n'est arrivé que plus tard, pour le regard nouveau qu'il m'a apporté sur nos problématiques. Vient le tour de nos plus proches parents, le groupe Q-Élec maintenant à l'ENS de Lyon. En particulier, Sébastien Jézouin pour sa rigueur scientifique et son savoir-faire expérimental, Danijela Markovic pour avoir été l'âme du groupe quand j'y étais encore, Nathanaël Cottet pour m'avoir recommandé auprès de Benjamin, Quentin Ficheux pour sa faculté à transformer pessimisme en travail acharné, Théau Peronnin pour son intuition scientifique et pour m'avoir embarqué dans l'aventure entrepreneuriale qu'est Alice&Bob, et Jeremy et Antoine avec qui j'aurai passé un séjour mémorable aux Houches. Il y a aussi l'équipe Flux Quantum du Collège de France en particulier Çağlar Girit pour son expertise en jonction Josephson et Jean-Loup Smirr pour son aide et sa maintenance en salle blanche, et l'équipe d'optomécanique du LKB avec notamment Thibault Capelle et Edouard Ivanov avec qui nous avons étendu nos horizons quantiques. Je remercie également mes parrain et tuteur de thèse Gwendal Fève et Benoit Douçot pour avoir accepté de faire partie de mon comité de thèse. J'ai également passé beaucoup de temps en salle blanche à l'ENS, à l'ESPCI et au collège de France et je remercie en particulier Michaël Rosticher pour les discussions aussi bien en salle blanche qu'en dehors, José Palomo pour son feeling légendaire avec les appareils de la salle blanche et Bruno Bresson pour m'avoir donné accès au MEB de l'ESPCI. Je remercie Christine Chambon de l'Observatoire de Paris et Pierre-François Orfila du groupe Quantronics d'avoir fait nos pulvérisation de niobium. À la fin de ma thèse, je me suis intéressé à l'équivalent mécanique de mon expérience de thèse, je remercie Alexis Bres et Eric Guineveu de m'avoir donné accès à la plateforme expérimentale de Montrouge pour mener à bien cette expérience.

Y a-t-il besoin de rappeler qu'un laboratoire n'est pas seulement un gros ensemble de chercheurs ? Voici les ingrédients clefs nécessaires à son bon fonctionnement, merci à eux. Tout d'abord, vous devrez faire préparer les lieux grâce à une équipe "travaux" incroyablement efficace et serviable, merci à Didier, Catherine, Célia et Théo. Ensuite, il vous faudra (entre autres) commander une bonne quantité de matériel scientifique grâce à une équipe administrative rigoureuse, merci en particulier à Anne, Olga, Christine et Laura. Ce matériel devra être personnalisé, tout d'abord en faisant appel au bureau d'étude pour la conception, merci à Pascal et Anaëlle et ensuite à l'atelier mécanique pour la réalisation, merci pour les innombrables pièces que nous vous avons commandé. Le service électronique sera là pour vos besoins en PCB ou en alimentations stabilisées, merci à Anne et Philippe. Vous aurez besoin d'ordinateurs et d'un réseau fiables, merci au service informatique et en particulier à Yann. Accessoirement, si vous souhaitez que votre cryostat refroidisse, il vous faudra un service cryogénie bienveillant, merci à Olivier

et Florent. Finalement, pour gérer tout ce monde, une équipe de direction est précieuse, merci à Jean-Marc Berroir, Jean-Michel Isac, Jean-François Allemand et Jérôme Tignon.

Les années qui ont précédé cette thèse ont forgé en moi une vocation de physicien. Il y a sans doute beaucoup d'intérêt personnel à la base mais celui-ci n'aurait pas crû sans un enseignement de qualité. J'aimerais prendre le temps ici de remercier ces professeurs qui m'ont appris et toujours poussé à faire mieux pour finalement me conduire jusqu'ici.

On ne peut réussir une thèse sans être entouré et soutenu au quotidien. D'abord, j'aimerais remercier les colocataires avec lesquels j'aurai partagé ces années, Jaime, Rémi et Salomé, Boris, Olivier et Anouk et bien sûr Alice, la seule à m'avoir supporté (et presque nourri) tout du long. Il y a aussi tous les amis du groupe - j'ose presque dire de la famille - d'Arêches pour ces vacances à la montagne ou ailleurs. La musique tient aussi une place importante dans ma vie, je remercie ici toutes les musiciennes et musiciens avec lesquels j'ai joué et me suis ainsi évadé du monde réel. Merci également à toutes celles et ceux avec qui j'ai parcouru les terrasses et les quais parisiens et en la compagnie desquels j'aurai passé de très bons moments. Merci enfin aux quelques amis avec lesquels j'aurai échangé scientifiquement, notamment Bertrand et Antoine ; on comprendra que les atomes et les atomes artificiels sont des sujets proches, on sera plus surpris des similitudes entre les dynamiques planétaires et les circuits supraconducteurs.

Un dernier mot enfin pour remercier les membres de ma famille qui m'ont chacun à leur manière permis d'arriver jusqu'ici. En particulier, j'aimerais remercier mon oncle et ma tante, François et Laurence de m'avoir hébergé une année entière à une période critique pour mes études. Mes grands-parents auront toujours été pour moi synonymes de fierté car ce sont eux qui ont amené ma famille dans le monde des études supérieures. Mes deux petites soeurs, Camille et Élisabeth que je vois trop peu et qui pourtant m'apportent beaucoup. Et enfin, mes parents, Isabelle et Dominique, à qui je dois tout.

Contents

	Page
Acronyms	1
1 Introduction	2
1.1 Quantum information	4
1.2 Quantum error correction	5
1.2.1 Classical error correction	5
1.2.2 Bit-flip Correction	7
1.3 Classical computer memories	8
1.3.1 Dynamic RAM	9
1.3.2 Static RAM	10
1.3.3 Conclusions	11
1.4 Bistable systems in classical mechanics	11
1.4.1 Driven oscillator	12
1.4.2 Parametric oscillator	13
1.5 Superconducting circuits	14
1.6 Outline	16
2 Hamiltonian and dissipation engineering with superconducting circuits	17
2.1 Circuit quantization	18
2.1.1 Circuit description	20
2.1.2 Equations of motion	20
2.1.3 Quantization	21
2.1.4 AC Biases	23
2.2 Engineering dynamics	24
2.2.1 Hamiltonian engineering	24
2.2.2 Dissipation engineering	25
3 Parametric pumping with a transmon	29
3.1 The Transmon qubit	30
3.1.1 Low energy behaviour	30
3.1.2 Full description	33
3.2 Quantum dynamics of a driven transmon	35
3.2.1 Description of the experiment	35
3.2.2 Observing the transmon escape into unconfined states	38
3.2.3 Effect of pump-induced quasiparticles	41

3.3	Additional Material	43
3.3.1	Sample fabrication	43
3.3.2	Photon number calibration	43
3.3.3	Multi-photon qubit drive	45
3.3.4	Charge noise	46
3.3.5	Numerical simulation	47
3.3.6	Quasiparticle generation	49
4	Exponential bit-flip suppression in a cat-qubit	51
4.1	Protecting quantum information in a resonator	52
4.1.1	General considerations	53
4.1.2	The bosonic codes	57
4.2	Exponential bit-flip suppression in a cat-qubit	61
4.2.1	The dissipative cat-qubits	63
4.2.2	Engineering two-photon coupling to a bath	64
4.2.3	Coherence time measurements	67
4.3	Additional Material	69
4.3.1	Full device and wiring	69
4.3.2	Hamiltonian derivation	70
4.3.3	Circuit parameters	73
4.3.4	Semi-classical analysis	74
4.3.5	Bit-flip time simulation	79
4.3.6	Tuning the cat-qubit	81
5	Itinerant microwave photon detection	83
5.1	Dissipation engineering for photo-detection	84
5.1.1	Engineering the Qubit-Cavity dissipator	85
5.1.2	Efficiency	87
5.1.3	Dark Counts	87
5.1.4	Detector Reset	89
5.1.5	QNDness	90
5.2	Additional Material	92
5.2.1	Circuit parameters	92
5.2.2	Purcell Filter	92
5.2.3	System Hamiltonian derivation	94
5.2.4	Adiabatic elimination of the waste mode	96
5.2.5	Qubit dynamics and detection efficiency	98
5.2.6	Reset protocol	101
5.2.7	Spectroscopic characterization of the detector	101
5.2.8	Tomography of the itinerant transmitted photon	102
	Conclusion and perspectives	106
A	Circuit quantization	108
A.1	LC-oscillator	108

A.2	General Circuit quantization	113
B	Native couplings in superconducting circuits	124
B.1	Capacitively coupled resonators	124
B.2	Mutual inductances in superconducting loops	127
B.3	Inductively coupled resonators	128
C	Useful Formulae	131
C.1	Miscellaneous	131
C.2	Standard changes of frame	133
D	Classical mechanical analogy to the stabilisation of cat-qubits	135
E	Fabrication Recipes	138
E.1	Wafer preparation	138
E.2	Circuit patterning	139
E.3	Junction fabrication	140
	 Bibliography	 143

Acronyms

AC	Alternative Current
ATS	Asymmetrically Threaded SQUID
BL	Bit Line
CPB	Cooper Pair Box
CPW	CoPlanar Waveguide
dc	dark count
DC	Direct Current
EOM	Equation Of Motion
GKP	Gottesman Kitaev Preskill
IPA	IsoPropyl Alcohol
JJ	Josephson Junction
JPC	Josephson Parametric Converter
JRM	Josephson Ring Modulator
MMA	Methyl Methacrylate
MIBK	Methyl-Iso-Butyl Ketone
NMOS	N-type Metal-Oxide-Semiconductor
NL	Non-Linear
PCB	Printed Circuit Board
PMMA	Poly Methyl MethAcrylate
PMOS	P-type Metal-Oxide-Semiconductor
QEC	Quantum Error Correction
QED	Quantum ElectroDynamics
QI	Quantum Information
QND	Quantum Non Demolition
QP	Quasiparticles
RAM	Random Access Memory
RF	Radio Frequency
RIE	Reactive Ion Etching
RWA	Rotating Wave Approximation
SEM	Scanning Electron Microscope
SQUID	Superconducting QUantum Interference Device
STM	Scanning tunneling microscope
TEM	Transverse electromagnetic
TLS	Two-Level System
VNA	Vectorial network analyser
WL	Word Line

Chapter 1

Introduction

1.1	Quantum information	4
1.2	Quantum error correction	5
1.2.1	Classical error correction	5
1.2.2	Bit-flip Correction	7
1.3	Classical computer memories	8
1.3.1	Dynamic RAM	9
1.3.2	Static RAM	10
1.3.3	Conclusions	11
1.4	Bistable systems in classical mechanics	11
1.4.1	Driven oscillator	12
1.4.2	Parametric oscillator	13
1.5	Superconducting circuits	14
1.6	Outline	16

There is a reason why a dissertation is called a "mémoire" in French (memory). Indeed memories tend to fade away and people rely on writing them down to recall them later. This has not always been the case as oral transmission has long been the principal way for societies to preserve knowledge, ideas and culture through time. This form of memory is not precisely reliable, though it is impressively resilient as traditions, precepts, folk-tales stood the test of time: even if they got distorted along the way, the core information is still present. This strength probably comes from the fact that, as long as the social bond survives, the traditions are shared by many people and hence they are resilient to the oversight of a single person. Often, poetry or songs were used as a form of narration. For instance, in medieval Europe, troubadours were singing epic poems in verse about chivalry, courtly love or heroic deeds of ancient kings. Versification and melody are different ways of imposing a structure and symmetries to the speech limiting the possible mistakes of the narrator.

Nowadays, the principles used to store and convey information are not so different. Even if a book or a hard drive is an accurate way of storing information, having a single copy is not completely safe since it may burn or fail. Books and hard-drives copied and stored in different locations are much more reliable but eventually what they contain may be forever lost since they assume a specific language is known to be decoded. Also, when having a conversation over the phone, the single bits of data that are transmitted may be disrupted along the way. To detect potential errors upon arrival, one sends the message in chunks of eight bits. The seven first convey the information e.g. 0100110 and the last bit called the parity bit is adjusted so that the total number of ones is even, in this case 1. Upon arrival, if a single bit got modified, the sequence is discarded since its total parity is not even any more. Of course, an error that leads to two modified bits cannot be detected with this scheme. These are naive examples of the broad topic of error correction that was pioneered by Richard Hamming and Claude Shannon in the late 40s.

In the following, we will see that the same kind of ideas hold for storing and protecting information in a quantum memory despite specific constraints set by quantum mechanics. After a brief introduction on quantum information, we will describe the basic principles used to protect quantum bits. In classical computers, memories are very reliable but depend on many different schemes. We will make a brief overview to try to get insight for new ways of storing quantum information. We end up with simple ingredients for which our experimental platform, superconducting circuits, is well suited.

The goal of this dissertation is to reliably store the results of three years of experimental work and I hope it reaches the reader without errors.

1.1 Quantum information

At the lowest level, classical signals e.g. written words, voice, measurements can be digitized and represented by bits that take the values 0 or 1. These bits can be viewed as abstract units but, to store and process information, bits need to have a physical existence. In modern day computer science, bits are encoded in various ways: as magnetic domains orientations in hard drive disks, as small light pulses that travel inside optical fibers or as voltages at the nodes of well designed electrical circuits. While the first two forms are used to store and transmit data respectively, the last one is used for storing information that is being processed at the heart of the computer.

Each of these storage media can be conceptually scaled down to the quantum level. They become a single spin, a single photon, a single electron that have discrete states. This led the quantum physicists of the early 80s to wonder if computation could be performed using these states that obey the rules of quantum mechanics, in particular two of those that define a quantum bit. Even if the experiments that would allow for the manipulation of these single quantum entities were far out of reach at the time [1], these seminal ideas grew rapid interest, leading to the field of quantum computing. Not only classical computation is doable with a register of two-level quantum system but also it enables algorithms that are not possible in the classical world [2] leading up to the exponential speed-up of certain tasks [3].

These novel algorithms leverage the possibility for the qubit register to be in large superposition and entangled states during computation. Indeed, while a classical bit is limited to two values, a quantum bit can be in a superposition of its two basis states, $|0\rangle$ and $|1\rangle$ also refereed to as the computational basis. The general state of a qubit is better represented on a sphere fig. 1.1 by the vector $\alpha|0\rangle + \beta|1\rangle$ where α and β are complex numbers satisfying $|\alpha|^2 + |\beta|^2 = 1$. While the qubit state is intrinsically a continuous object, the qubit only communicates a classical bit of information upon measurement and $|\alpha|^2$ and $|\beta|^2$ represent the probability of finding the qubit in state $|0\rangle$ and $|1\rangle$ respectively when measuring along the vertical axis. After the measurement, the qubit is left either in $|0\rangle$ or $|1\rangle$ so that fully characterizing the qubit state requires preparing it many times and accumulating statistics along various measurement axes. A n -qubit register can be in the superposition of 2^n states and fully determining its state becomes an exponentially hard problem with n . Hence, to be useful, the usual flow of a quantum algorithm is to start with a register in a classical-like state, then take advantage of the full state space via entangling gates and finally use a subtle interference process to give the result as the superposition of a few, ideally one, states of the register that is measured in the computational basis.

However, even at the single qubit level, we realise that due to ever-existing noise in physical implementations, the qubit state randomly drifts from its expected position during the algorithm. The entangling and the interference process are extremely sensitive to those drifts which eventually lead to errors of the quantum algorithm. This is in stark contrast with a classical bit, the discrete values of which come from the thresholding of a continuous quantity and hence are more robust to noise. For a bit encoded as a voltage 0 or 1 V, the noise can induce deviations up to 0.5 V before the value of the bit flips, leading to an error. Quantum computation would be hopeless if it were not for the final measurement. Indeed, this measurement can be viewed as a thresholding process that discretizes the deviations that occurred until then. The key statement of quantum error correction is that if one can correct for randomly occurring \mathbf{X} , \mathbf{Y} and \mathbf{Z} operations then one can correct for any perturbation.

Being able to focus on a discrete set of errors despite the continuous nature of quantum information is fundamental. In the next section, we will see that quantum error correction provides strategies to fight against these errors and keep quantum computing within the realm of possibility.

1.2 Quantum error correction

In this section and in all this thesis, we will be focussing on how to protect a single bit of quantum information. The three discrete errors that a qubit suffer from are the \mathbf{X} operation which consists of a π -rotation around the x -axis or bit-flip, the \mathbf{Z} operation which is a π -rotation around the z -axis or phase-flip and the \mathbf{Y} operation which is a combination of the two. The bit-flip is an error that also occurs in a classical bit. Below, we explain how bit-flips may be corrected in classical memories and use that as a starting point to understand the first proposal for quantum error correction by Shor [4].

1.2.1 Classical error correction

Error correction relies on encoding the information redundantly to make it more robust to errors. A distinction needs to be drawn between the *logical* bit that is the information and the *physical* bits that are the physical support. Hereafter, we describe a simple repetition code that allows for sending a single logical bit more accurately by encoding it into several physical bits.

Suppose that Alice wants to transmit one bit of information to Bob, say a 1 for example. She sends her favourite physical bit in state 1 but there is a small error probability p that

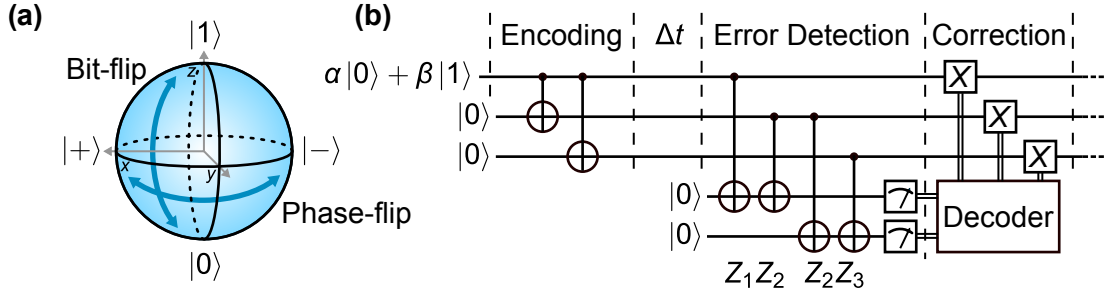


FIGURE 1.1: **Qubit and Bit-flip error correction** (a) The state of a qubit is well described as a point on the Bloch sphere. Bit-flips are unwanted switching between states $|0\rangle$ and $|1\rangle$, phase-flips between $|+\rangle$ and $|-\rangle$. (b) A 3-qubit repetition code. First the quantum information is redundantly encoded into a 3-qubit entangled state. To check if an error happened during the storing time Δt , one measures Z_1Z_2 and Z_2Z_3 through 2 ancillary qubits. The result of the measurement is interpreted by a classical decoder (tab. 1.2) that corrects the qubit that had most likely flipped.

Alice	encoding	receiving	probability	decoding	total probability
1	111	111	$(1-p)^3$	1	$1 - 3p^2 + 2p^3$
		110/101/011	$3p(1-p)^2$	1	
		100/010/001	$3p^2(1-p)$	0	$3p^2 - 2p^3$
		000	p^3	0	

TABLE 1.1: **A 3-bit repetition code.** Alice wants to send a bit 1 to Bob. She encodes it using a repetition code into 111. This bit string may suffer no, one or more errors with given probabilities. Upon receiving the altered bit string, Bob decodes it by performing a majority vote and determines what was the most likely bit that Alice sent. If no or one error happened, the information is retrieved, otherwise a logical bit-flip occurs

Bob receives a 0 instead due to some noise in the communication channel. Therefore, the success probability of this transmission is $1 - p$. To increase this probability, Alice sends three bits to Bob, 111, that altogether encode the logical information 1. Each travelling bit has the same probability as earlier to undergo an error but, provided Bob uses the right decoder, the overall success probability is $1 - 3p^2 + 2p^3$ (see tab. 1.1). This success probability is increased provided p is below a given threshold, $1/2$ in this case.

The error probability of this protocol goes from p to $3p^2$ at leading order. The form of this probability illustrates a fundamental point of error correction:

- the factor 3 illustrates that we start by making things worse, indeed errors are now three times more likely to happen.
- but this is balanced by insensitivity to single errors as shown by the square and things get better when the error probability is low enough.

Sending the information five times, lowers the error probability down to $O(p^3)$, seven times to $O(p^4)$, etc. Hence, provided the noise is below a threshold, it is possible to reach an arbitrary reliability by transmitting a sufficient amount of noisy bits, i.e. increasing the redundancy. However, this is true within some assumptions on the type of errors that

may happen. For example, let us imagine there is an eavesdropper on the line during the communication. This eavesdropper is present with a small probability p_e but, if present, flips every bit that travels. In this case, whatever the level of redundancy Alice chooses, Bob gets the wrong information and the success probability of the protocol can never be better than $1 - p_e$ due to this source of highly correlated errors. This example emphasizes that a given protocol is only suited for correcting a given set of errors.

Storing information can be done in a similar way. A physical bit has an error rate κ such that for a small time Δt there is a small probability $p = \kappa \Delta t \ll 1$ that the bit flips. Using the repetition protocol, by stroboscopically detecting and correcting for errors for each time interval Δt , one decreases the error probability to $3p^2$ and hence the error rate of the logical bit is reduced to $3\kappa^2 \Delta t$. Here, it is best to measure fast as the error rate decreases with Δt . Including errors in the detection and correction parts leads to an optimal finite measurement rate.

Directly transposing this repetition protocol into the quantum world is problematic for two reasons. First, one wants to be able store not only states $|0\rangle$ and $|1\rangle$ but also unknown superpositions of the two. Yet, copying the state of an unknown quantum system is not possible in quantum mechanics as shown by the no-cloning theorem. Second, to determine which error occurred, one cannot directly measure the quantum system since it would destroy the superposition information that it carries. Fortunately, it is possible to circumvent these issues and below we derive part of the original proposal by Shor [4].

1.2.2 Bit-flip Correction

Say one wants to store the state $\alpha|0\rangle + \beta|1\rangle$ with α and β unknown. Copying this state is forbidden by quantum mechanics. Instead, an entangled state of three qubits is built using the encoding circuit of fig. 1.1b and writes $\alpha|000\rangle + \beta|111\rangle$. As with classical error correction, this entangled state is susceptible to more errors but is insensitive to single errors provided detecting and correcting these errors are possible.

In the quantum case, error detection is done indirectly by measuring joint observables. Indeed, if one probes a qubit by asking: "Are you in 0 or 1?" this will destroy quantum information. Instead, one must ask the subtle question "Are you in the same state as your neighbour?". It is crucial that certain bits of information are accessed while keeping unknown others. This translates into measuring the operators $Z_1 Z_2$ and $Z_2 Z_3$. To do so, one introduces two ancillary qubits as shown in fig. 1.1b which are then measured tab. 1.2. Assuming only one error occurred, we get different outcomes for each altered state so that appropriate feedback corrects the error. As in the classical case, to correct against more than one bit-flip, the redundancy simply needs to get bigger.

state	encoding	altered	measurements
$\alpha 0\rangle + \beta 1\rangle$	$\alpha 000\rangle + \beta 111\rangle$	$\alpha 000\rangle + \beta 111\rangle$	00
		$\alpha 001\rangle + \beta 110\rangle$	01
		$\alpha 010\rangle + \beta 101\rangle$	11
		$\alpha 100\rangle + \beta 011\rangle$	10

TABLE 1.2: **3-qubit repetition code for bit-flip protection.** The state is redundantly encoded in 3 entangled qubit. For a small amount of time, the state is subject to bit-flip and here we only present the cases with 1 or less error. Detecting the error consist in measuring the joint operators $Z_1 Z_2$ and $Z_2 Z_3$. For example, measuring 01 tells us that qubit 1 and 2 are in the same state but that qubit 2 and 3 are not. Assuming that at most one error occurred, one deduces that qubit 3 has flipped. Of course, if more than one error occurred the correction mechanism flips the wrong qubit leading to a so-called logical error.

A qubit is also susceptible to another error channel, the phase-flip Z . This second error channel can be corrected by increasing the redundancy of the code. The most straightforward way is to encode each one of the three qubits of the bit-flip protocol into three qubits leading to the 9-qubit repetition code proposed by Shor [4]. Interestingly, this encoding is also robust to a bit-flip plus a phase-flip occurring, the Y error and hence is able to fully protect the logical qubit against single physical errors. Since then, there have been many proposals [5] to improve this scheme and experimentally implement quantum error correction. One of the most promising approaches is the surface code [6] which has many appealing properties. In this code, data qubits and ancillary qubits are physically arranged into two interlocked square lattices, which makes it compatible with a 2D architecture. Also, once the unit-cell of this lattice reaches below-threshold error rates (achievable with state-of-art superconducting circuits [7]), it may be replicated many times to increase the error protection. However, this encoding requires tremendous resources of the order of thousands of physical qubits per logical qubit [8] which is far beyond the capabilities of current experiments [9].

In the following, we try to rethink how one can protect a quantum system without relying on physical redundancy and hence to making it manageable for experimental implementation.

1.3 Classical computer memories

Among many features, classical computers perform well thanks to a fast and reliable memory. Each memory is composed of many unit cells. Below, we describe the working principle of two of those, the dynamic RAM and the static RAM cells. These are only

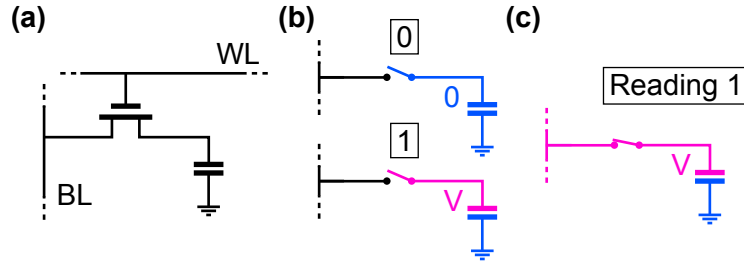


FIGURE 1.2: **Dynamic RAM working principle** **a.** A DRAM unit cell consists of a transistor and a capacitor. The line WL sends the readout signal and the line BL collects the information. **b.** WL serves as the gate for the transistor. When a voltage is applied, the transistor acts as a short circuit, and in the absence of voltage, the transistor is an open. In the later case, the capacitor is isolated from the rest of the circuit and the bit state 0 and 1 are mapped to the discharged and charged state of the capacitor respectively. **c.** When line WL is biased, the capacitor releases its charge (or not) into line BL. The resulting signal is measured to deduce the state of the cell.

two examples among many types of architectures but gives a glimpse of how data about to be processed¹ is stored in a classical computer.

1.3.1 Dynamic RAM

Dynamic RAM is based on a capacitor (see fig. 1.2). A charged capacitor represents a 1, a discharged one a 0. To write on the capacitor, the isolating transistor is turned on and voltage bias is applied to charge the capacitor. To reset, the same operation is performed with a zero voltage. To read the information, the isolating transistor is closed again so that the stored charges can flow in line BL. If the resulting voltage is over a given threshold, one assumes the capacitor was storing a 1, below the threshold, a 0.

Over time, due to the finite resistance in parallel of the capacitor and across the transistor, the charge of the capacitor leaks out leading to bit-flip errors. To prevent this, the memory cell is periodically read out (hence the name "dynamic"). If the capacitor is found to be charged, it is set back to its original level with a bias voltage.

The major advantage of this architecture is that it requires a limited amount of hardware: one capacitor and one transistor for one bit of data. The storage density in dynamic RAMs is high. In return, this memory cell needs constant control and feedback which makes it harder to operate and slower to access.

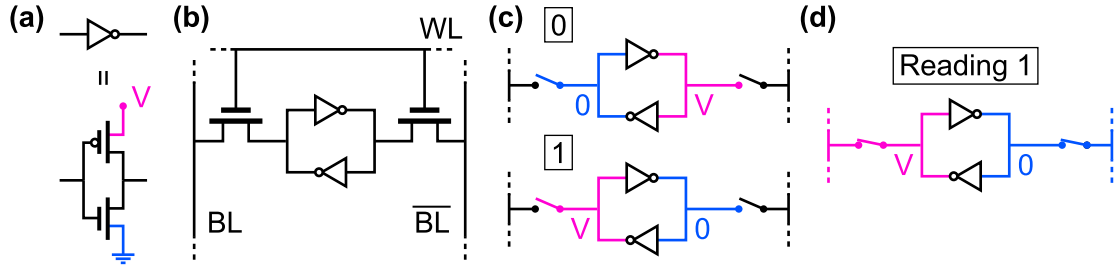


FIGURE 1.3: **Static RAM working principle** (a) Inverter symbol (top) and actual circuit diagram (bottom). An inverter is constituted of one PMOS and one NMOS transistor (open dot symbol and normal symbol respectively). These two transistors let the current pass for opposite gate conditions. (b) A SRAM unit cell consists of a inverter loop connected to the outside world via two transistors. The line WL sends the readout signal and the lines BL and \overline{BL} collect the normal and opposite information respectively. (c) When there is no voltage in line WL, the inverter loop is isolated from the rest of the circuit. The bit state 0 and 1 are mapped to the two stable states of the inverter loop: grounded on the left, biased on the right and conversely. (d) When line WL is biased, the isolating transistors close and the lines BL and \overline{BL} get biased according the loop state. Note that contrary to the DRAM readout, the resulting signal can be integrated for ever since the inverter loop is powered. Also, the isolating transistors are bigger than the inverter one to be able to write on the inverter loop by forcing the bias of BL and \overline{BL} .

1.3.2 Static RAM

Static RAM is based on a type flip-flop circuit, the inverter loop (see fig. 1.3). When isolated, this loop stores a 0 when there is a positive voltage on the right and the left is grounded and conversely. To read the data, the isolating transistors are switched on, the voltage propagates in line BL or \overline{BL} and the resulting signal is amplified. To write 1 in the memory while 0 was stored, first line BL is biased and line \overline{BL} is grounded. When, the isolating transistors turn on, there is a value conflict on each side of the loop and, provided that the isolating transistors are bigger than the inverters transistors, the memory cell switches state.

This kind of memory cell is more complex and has a lower storing density than the previous one but has several advantages. It does not require constant monitoring of the memory state to prevent losing information (hence the name "static"), so it is easier to control and faster to access. Also, as long as the power is supplied (via the voltage source V) for the inverters to work and cooling is provided (via a bath at temperature T) to keep the temperature low enough, once the state is set, it remains for a time exponentially long in $eV/k_B T$ (where e is the charge of the electron and k_b is the Boltzmann constant).

¹We do not detail how data is stored in mass storage devices, because these data is further from the actual processing.

1.3.3 Conclusions

The first scheme we presented, the dynamic RAM, fights against dissipation by control and feedback. Reading the system out to protect it, is not allowed for a quantum system since it destroys any superposition. Still, we saw in sec. 1.2 that there are ways around this. One can encode the information redundantly and only read joint quantities out. In this sense, dynamic RAM is similar to the standard strategy for quantum error correction except that the constraints set by quantum mechanics increases the complexity of the control and feedback.

On the other hand, the static RAM never needs to measure the state of the inverter loop to maintain it. Actually, the power supply, which is always on to fight against the losses in the circuit, is agnostic about the information it contains. This feature makes this kind of architecture very appealing for quantum error correction. At the heart of the static RAM is a flip-flop circuit which is a bistable system. Stable means that if the system is perturbed it relaxes back to its original state that we call a steady-state. A bistable system has two such states and can flip from one to the other only if the perturbation is big enough. Such a perturbation is used for writing on the memory cell for instance. To illustrate, imagine that a sudden disturbance sets the left bias to some voltage, while bit 0 is being stored. As long as this disturbance is smaller than V , the system relaxes back to 0. Otherwise the state relaxes to 1 leading to bit-flip error and hence, the quality of this memory cell is directly related to the ratio between the voltage noise level and the voltage bias. The disturbance dissipates due to the finite resistance of the wires composing the circuit associated with a cold bath that absorbs the resulting heat. In this example and more generally, dissipation has profound consequences on the stability of a system.

In the following we try to find a more simple bistable system which is able to protect information against bit-flips, in the same spirit flip-flop circuits store bits of information.

1.4 Bistable systems in classical mechanics

It is easy to build bistable systems in the classical world. One can think of a power switch for which the on and off positions are stable. However, transposing such a device into the quantum world is challenging. Indeed, each individual atom that it is made of, adds additional degrees of freedom that are potential decoherence path. The ideal bistable candidate is a dynamical system with only 1 degrees of freedom, the couple of conjugate variables: position and momentum. This brings us to the 1D-oscillator for which the “steady-states” are periodic orbits or limit cycles in phase-space. Below, we

quickly explain how to make an oscillator bistable. We refer the reader to [Appendix D](#) for a concrete example.

From the consideration of the previous section, several ingredients should be present:

- losses, they are a necessary condition for the system to be stable
- a power supply, otherwise the losses bring us into a trivial state.

In the case of our oscillator, the power supply consists of a time-dependant drive and there are inherent losses that are modelled via a regular damping term. We will see that losses can also be engineered to provide bistability.

1.4.1 Driven oscillator

Driven-damped harmonic oscillator We work with normalized position and momentum coordinates, x and p respectively or equivalently the mass of the oscillator is set to 1. We renormalize time so that the natural frequency of the oscillator is 1. Under these conditions, the equations of motion of a damped harmonic oscillator driven at resonance writes

$$\dot{x} = p, \quad \dot{p} = -x - Q^{-1}p + \epsilon \cos(t)$$

where Q is the quality factor of the oscillator and ϵ the driving strength. As we expect for a driven-damped harmonic oscillator, it has a single limit cycle as shown in [fig. 1.4](#).

Poincaré map By defining a new variable θ , the system becomes autonomous

$$\dot{x} = p, \quad \dot{p} = -x - Q^{-1}p + \epsilon \cos(\theta), \quad \dot{\theta} = 1,$$

and since the equations are periodic in θ , this new variable is conveniently defined modulo 2π . A trajectory, i.e. a solution of these equations for a given initial condition, is a curve in the 3D phase-space (x, p, θ) . To study the dynamics of the system and in particular the existence of stable periodic orbits, it is advantageous to consider only the intersections between the trajectories and a section of phase-space. Here, we choose the section $\theta = 0$. On this section, we can define the Poincaré map that is the application defined from the section to itself that maps a point of intersection to the following one in time. An important property is that fixed points of a Poincaré map are periodic orbits of the full dynamics.

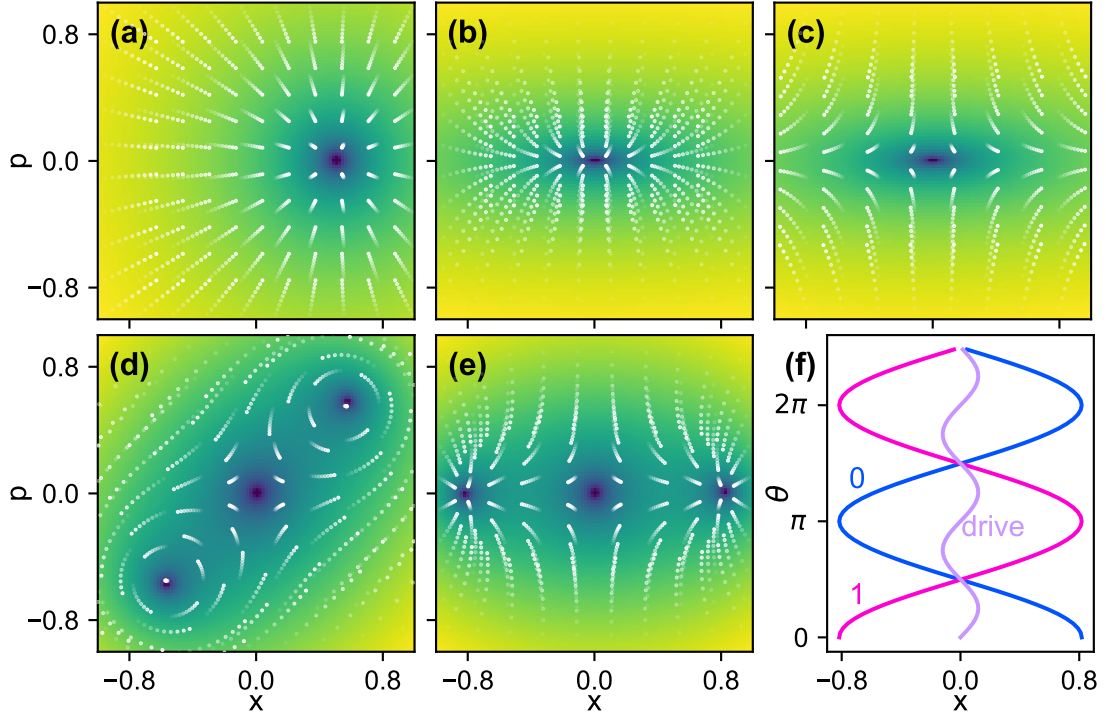


FIGURE 1.4: **Dynamics of various oscillators.** In each panel, the white dots represent intersections between typical trajectories and the Poincaré section $\theta = 0$, the transparency of the dots decreasing with time. The colormap represents the function $\|P(m) - m\|$ (blue is 0) where m is the point $(x, p, \theta = 0)$ and P is the Poincaré map. The zeros of this function define the periodic orbits of the dynamics. (a) Driven harmonic oscillator. There exists a single fixed point. (b,c) Parametric oscillator. When the parametric drive is not strong enough with respect to dissipation, there is a single fixed point at the origin (b), when it is too strong the system diverges (c). (d) Non-linear parametric oscillator. There are three fixed points, two of which being stabilized by the natural damping of the oscillator. The so-called Kerr-cat qubit [10] is based on this system. (e) Parametric oscillator with non-linear dissipation. Same as before except now, the two fixed points are stable regardless of the natural damping of the system. Our approach, the dissipative cat-qubit [11] is based on these dynamics. (f) Time-evolution for the position of the two periodic orbits of (e). The parametric drive amplitude is plotted alongside to emphasize that it is agnostic to the oscillator state for symmetry reasons.

1.4.2 Parametric oscillator

A parametric oscillator is an oscillator for which the drive modulates a parameter of the system. For a mass-spring system, the modulated parameter may be the mass or the spring constant. A pendulum whose anchoring is driven up and down is a good example of such oscillator. This type of oscillators are known to act as amplifiers when the drive frequency is at twice the oscillator frequency [12]. We investigate this particular regime.

Linear parametric oscillator When the spring constant is modulated at twice the oscillator frequency, the equations of motion write

$$\dot{x} = p, \quad \dot{p} = -(1 + \epsilon \cos(2\theta)) x - Q^{-1}p, \quad \dot{\theta} = 1$$

where ϵ is now the strength of the parametric drive. Regarding the periodic orbits, this system is linear and periodic and hence the Floquet theorem applies. As shown in fig. 1.4b,c, either the solution exponentially converges to zero or diverges towards $x = \pm\infty$ ¹ depending on the relative strength of the dissipation Q^{-1} and the parametric drive ϵ . Hence, there is at most one fixed point.

Non-linear parametric oscillator The diverging case is not physical. At some point, non-linearities arise preventing the system to go to $\pm\infty$. If the system neither goes to infinity nor stays at zero, we expect it settles somewhere in between for a carefully chosen non linearity leading to two periodic orbits (one for $x > 0$, one for $x < 0$).

Having the frequency changing with the oscillations amplitude is a possible non-linearity. This way, the parametric drive gets detuned from the resonance condition as the amplitude increases

$$\dot{x} = p, \quad \dot{p} = -(1 + \omega_{\text{nl}}x^2 + \epsilon \cos(2\theta))x - Q^{-1}p, \quad \dot{\theta} = 1.$$

The system dynamics are represented in fig. 1.4d and lead to two stable limit cycles. However their stability is only guaranteed by the presence of the losses $Q^{-1}p$. This is detrimental: making progress on the quality factor of the oscillator affects the stability of these orbits.

Another possibility is to have the losses scale with the amplitude of the oscillations

$$\dot{x} = p, \quad \dot{p} = -(1 + \epsilon \cos(2\theta))x - Q^{-1}p - \kappa_{\text{nl}}p^3, \quad \dot{\theta} = 1. \quad (1.1)$$

The system dynamics are represented in fig. 1.4e and lead to two stable limit cycles. This stability is provided by the non-linear dissipation and hence the two limit cycles remain attracting even when $Q \rightarrow \infty$. The doubled frequency of the drive is crucial here fig. 1.4f, this allows for the energy source to be agnostic of the state of the oscillator like in the SRAM memory. We will see in chapter 4 that crucially, although this mechanism is dissipative, it is not detrimental for storing quantum information.

1.5 Superconducting circuits

Let us dive more into the details of how to physically implement quantum bits. For a physical quantum system to be a good candidate, it must satisfy several criteria [13]. As

¹If this system is used as an amplifier, the converging case is the amplifying regime and the diverging case is the self-oscillating regime.

we mentioned in the beginning, there are natural candidates that natively have discrete quantum states that can be addressed to form a qubit. Examples of such physical entities are electronic or nuclear spins [14], neutral atoms [15], trapped ions [16], photons [17], or even non-abelian particles [18]. Outstanding experimental progress has been made in the past few decades, realizing the thought experiments of the founders of quantum mechanics [1] and increasing the likelihood of building a quantum computer someday.

In this thesis, we work on superconducting circuits [19, 20] that are not microscopic entities but rather consist of pieces of superconducting material arranged together into electrical circuits that contain a macroscopic number of atoms. Retrospectively, it is not straightforward that these circuits have quantized energy levels [21] that are addressable specifically to be used as qubits. In a normal metal, each atom contributes electrons to the Fermi sea and a single excitation consists of an electron-hole pair formed on both sides of the Fermi surface, a so-called quasiparticle. At finite temperature, there is a macroscopic number of such quasiparticles because any tiny external perturbation can generate them: they are not good qubits. In superconductors things work differently [22]. At low temperature, a superconductor experiences a phase transition during which electrons pair together to form Cooper pairs. These pairs have a finite binding energy, equal to the superconducting energy gap (typically 43 GHz in aluminium), such that quasiparticles require a finite perturbation to be generated. Hence, collective motions of the sea of Cooper pairs are able to flow with no dissipation despite the small defects of the system, leading to the so-called supercurrent. The superconductor can be shaped into distributed capacitances and inductances so that this supercurrent oscillates with very small dissipation. Also, as collective excitations, these modes have large coupling capabilities. During the past two decades great progress has been made in the field to increase the coherence of these modes by improving circuit design, fabrication, shielding and control techniques.

However, these superconducting circuits would be linear and hence useless for quantum information if it were not for existence of the Josephson junction. In this thesis we work with Josephson tunnel junctions that are composed of a thin insulating barrier separating two superconductors that allow Cooper pairs to tunnel through. On a macroscopic scale it can be viewed as a non-linear inductor that brings non-trivial dynamics to the circuits without inducing dissipation. In particular, the electromagnetic modes that have some current flowing through the junction inherit its non-linearity. Thus, single transitions can be addressed, so that the circuit behaves as an artificial atom or, more simply, as a qubit. superconducting circuits have a great flexibility in design which lead to a flock of different qubits, finding ingenious ways to increase the coherence times from tens of nanoseconds to almost milliseconds [19]. This non-linearity is also leveraged in many

applications such as amplifying signals [23], detecting photons [24–28] or coupling to other quantum devices [29–31].

Superconducting circuits consist of plates and wires that are in the micrometer range (hundreds of nanometers for Josephson junctions) and are easy to fabricate using the standard lithography techniques of the semiconductor industry. Also, in order to lie below the superconducting gap, the electromagnetic modes of superconducting circuits are typically in the GHz range. This makes them practical to operate with the commercially available microwave components used in radars and telecommunications. To perform experiments in the single excitation regime, these modes should be in a cold environment so that thermal photons do not randomly excite them. For the black body radiation to be small in the GHz range, the temperature should be much less than 200 mK (for a mode at 4 GHz). Superconducting circuits are usually clamped at the base plate of a commercially available dilution cryostat at 20 mK.

Superconducting circuits seem to have the good ingredients to implement the ideas of the previous section: low inherent losses and strong non-linearity.

1.6 Outline

The main goal of this thesis is to realise a non-linear dissipation of the form (1.1) in a superconducting resonator and to experimentally verify that it is compatible with the protection of quantum information encoded on the basis of Schrödinger cat states [11]. Superconducting circuits are an ideal platform to experiment with quantum dynamics thanks to the powerful tools that are Hamiltonian and dissipation engineering. These methods will be presented in chapter 2. We have already had a glimpse that parametric pumping is at the heart of the dynamics. However, previous experiments [32, 33] failed to demonstrate the gain in qubit lifetime this paradigm has to offer due to limitations that are proper to their circuit design. In chapter 3, we investigate these limitations [34, 35] to design circuits more suitable for parametric pumping. In chapter 4, we explain in detail the cat-qubits paradigm and demonstrate the exponential suppression of bit-flips [36]. Mastering the dissipation engineering toolbox also brought us to other applications such as an itinerant microwave photon detector [37] that is presented in chapter 5.

Chapter 2

Hamiltonian and dissipation engineering with superconducting circuits

2.1	Circuit quantization	18
2.1.1	Circuit description	20
2.1.2	Equations of motion	20
2.1.3	Quantization	21
2.1.4	AC Biases	23
2.2	Engineering dynamics	24
2.2.1	Hamiltonian engineering	24
2.2.2	Dissipation engineering	25

A superconducting circuit is a solid-state platform used to perform quantum optics experiments in the microwave domain:

- Microwave light can be sent on and retrieved from the circuit via transmission lines or waveguides.
- Superconductivity endows the circuit with high quality electromagnetic modes with frequencies ω_i that host microwave photons for a time which is long compared to $1/\omega_i$.
- The Josephson junction provides lossless non-linear couplings between those modes.

All the platforms that are mentioned in the introduction, start with god-given quantum systems. However, with well chosen voltage biases, laser beams, magnetic field, neighbouring materials, experimentalists modify their properties and engineer peculiar dynamics. Superconducting circuits are no exception. There are two steps of engineering. The first one is to design and fabricate a circuit, that comprises capacitors, inductors, Josephson junctions with a well chosen topology. The second one is to bias this circuit using DC sources (voltage, current, and magnetic field) and microwave drives usually referred to as pumps in this case¹.

As depicted in fig. 2.1, the goal is to design specific quantum dynamics between the electromagnetic modes of a superconducting circuit. To do so, we start by working on an abstract circuit representation that would realize the dynamics before settling a lithography pattern or a 3D architecture that approximately behaves as the ideal circuit model. There is no unique path to go from quantum dynamics to circuits, hence one usually works the other way around in a process called circuit quantization.

There is a large literature on circuit quantization [20, 38–44]. In the following, we borrow from this heritage to put together our recipe for quantizing biased circuits. The goal is to make it as systematic and simple as possible to be able to implement it in software, in the same spirit as [45] but with different requirements.

First, we describe the procedure we use to quantize a DC- and AC-biased superconducting circuit and then we show how one is able to engineer specific Hamiltonian or dissipative dynamics from there.

2.1 Circuit quantization

The spirit of this quantization procedure is to keep the circuit analysis classical and use it to deduce the quantum parameters. Hereafter, we present the major steps and results.

¹We distinguish the drives that are used to resonantly inject photons in the circuit modes and the pumps that are usually not resonant with any mode and used to bias the dynamics.

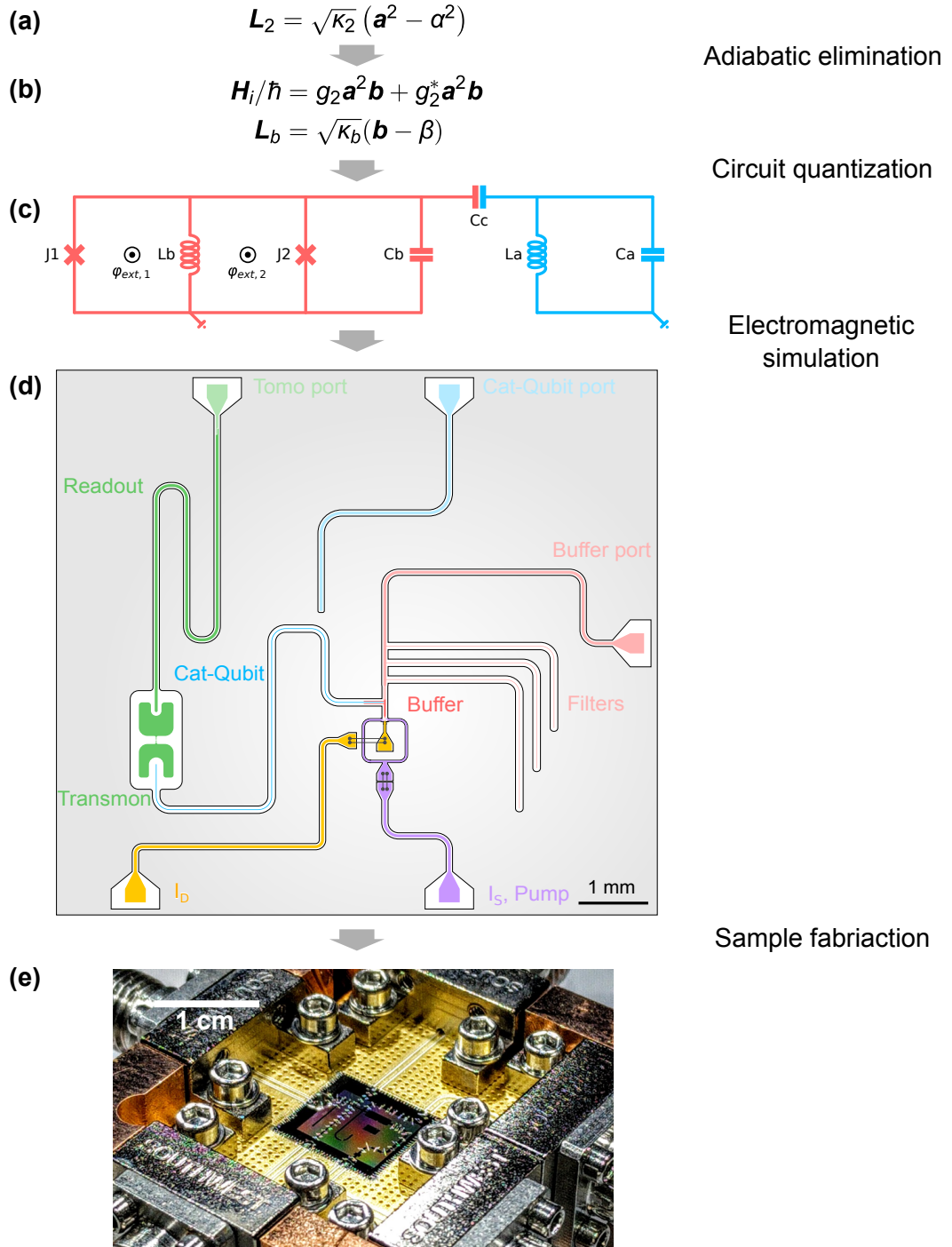


FIGURE 2.1: Workflow of a superconducting circuit experiment. (a) One wants to study a peculiar quantum dynamics e.g. two-photon driven dissipation of an electromagnetic mode \mathbf{a} that is detailed in chapter 4. (b) In fact, this is the effective dynamics of a two-mode system. It is deduced from the global dynamics by adiabatic elimination as explained in sec. 2.2.2. (c) The next step is to find a biased superconducting circuit that behaves as such. Given a circuit, we describe in this chapter how to find its Hamiltonian and loss operators. (d) A true 2D superconducting circuit is designed and electromagnetically simulated to closely match the circuit diagram properties. (e) Eventually the circuit is fabricated (see appendix E) and connectorized to be measured at the 20 mK base plate of a dilution cryostat.

Quantity	Capacitor	Resistor	Inductor	Josephson junction
Current/ φ_0	$C\ddot{\varphi}$	$\frac{1}{R}\dot{\varphi}$	$\frac{1}{L}\varphi$	$\frac{1}{L_J}\sin(\varphi)$
Energy/ φ_0^2	$\frac{C}{2}\dot{\varphi}^2$	n/a	$\frac{1}{2L}\varphi^2$	$-\frac{1}{L_J}\cos(\varphi)$

TABLE 2.1: **Current and energy for each dipole type.** The reduced flux quantum is defined as $\varphi_0 = \Phi_0/2\pi = \hbar/2e$. The inductance of a Josephson junction is referred to as $L_J = \varphi_0/I_0 = \varphi_0^2/E_J$ where I_0 is the critical current of the junction and E_J its Josephson energy.

The derivation is done in more detail in appendix [A](#).

2.1.1 Circuit description

A simple superconducting circuit diagram is composed of capacitors, inductors, and Josephson junctions. Input and output transmission lines are modelled by $50\,\Omega$ resistors [\[46\]](#) for it is the regular characteristic impedance of the cables we use.

Without loss of generality the biases are modelled by current sources that inject DC or AC current at one node of the circuit and retrieve it at another one (not necessarily ground). This also enables to model the voltage biases through the Thévenin-Norton equivalence for non ideal sources, and the magnetic field biases if the relevant coils and the mutual inductances are included in the circuit (see sec. [B.2](#)).

At any point in time, the circuit is fully described by the voltage and current across each dipole $V(t)$ and $I(t)$ respectively. The underlying variable is the flux threading each dipole defined as $\dot{\Phi}(t) = V(t)$ [\[39\]](#). This is one of the two canonical variables used to describe the state of the circuit, the other one being the charge defined as $\dot{Q}(t) = I(t)$. As we deal with circuits that are superconducting, one defines the phase variable

$$\varphi(t) = 2\pi \frac{\Phi(t)}{\Phi_0}, \quad (2.1)$$

where $\Phi_0 = h/2e = 2\pi\varphi_0$ is the superconducting flux quantum. In tab. [2.1](#), we summarize the current flowing through each dipole type in terms of the phase variable.

2.1.2 Equations of motion

The goal is to find the equations of motion of the classical electrical circuit that contain all the information we need to quantize the system. To do so, we use the Kirchhoff's laws.

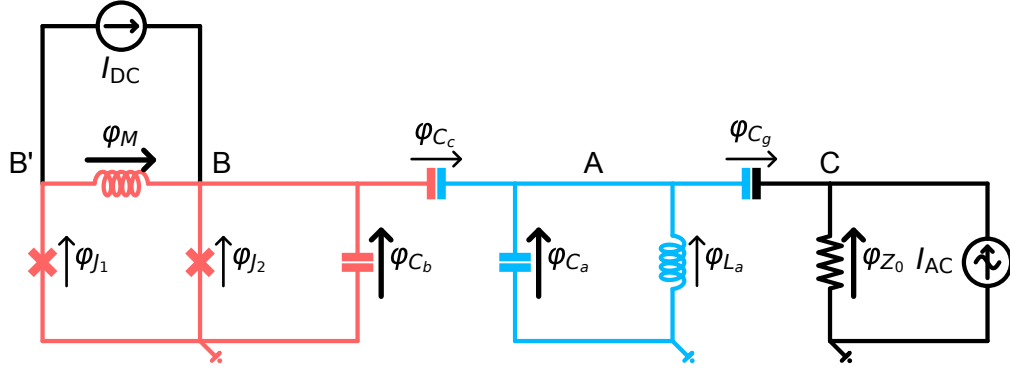


FIGURE 2.2: **Typical superconducting circuit.** This circuit consist of a tunable transmon (red) capacitively coupled to a resonator (blue). The transmon acquires its tunability from the two junctions in parallel that form a SQUID which can be biased by the DC current source via the mutual inductance M (see sec. B.2). The resonator is capacitively coupled to a transmission line, modelled by the resistor, through which one sends RF drives as represented by the AC current source. The state of the circuit is represented by the vector $\varphi(t)$ that contains all φ_{dipole} . Yet, with the constraints set by the Kirchhoff's voltage law, only a subset γ (bold arrows) are necessary to fully describe the circuit. The circuit has five nodes, A , B , B' , C and ground. The vector $\mathbf{I}(\gamma)$ has 5 components one for each node. The DC bias current vector \mathbf{I}_{DC} is non-zero for node B and B' , \mathbf{I}_{AC} for C and ground.

Let us write the state of the circuit as a vector φ that contains the phase differences across each dipole of the circuit. The voltage Kirchhoff's law establishes relations between the elements of $\dot{\varphi}$. For a subset of dipoles $\{\varphi_j\}$ that are arranged in a loop, this relation writes $\sum_j \dot{\varphi}_j = 0$. As we decided to replace direct magnetic fields biases by bias currents in mutual inductances, the previous relation can be integrated simply as $\sum_j \varphi_j = 0$. When taking into account the constraints set by every loop of the circuit, the number of variables required to fully describe the circuit decreases, we denote this reduced state vector γ .

The Kirchhoff's current law is straightforward to apply. The current going through each dipole is determined using tab. 2.1 and, from the circuit topology, one deduces the current going away from each node that we denote by the vector $\mathbf{I}(\gamma)$. If we denote by \mathbf{I}_{DC} and \mathbf{I}_{AC} the bias current going towards each node, then, using the Kirchhoff's current law, the equations of motion write

$$\mathbf{I}(\gamma(t)) = \mathbf{I}_{\text{DC}} + \mathbf{I}_{\text{AC}}(t). \quad (2.2)$$

2.1.3 Quantization

The goal here is to find the time evolution of the quantum system, represented by its density matrix ρ , which is governed by the Lindblad master equation

$$\frac{d}{dt}\rho = -\frac{i}{\hbar}[\mathbf{H}, \rho] + \sum_i \mathcal{D}[\mathbf{L}_i]\rho \quad (2.3)$$

where the Hamiltonian \mathbf{H} and the Lindblad operators $\{\mathbf{L}_i\}$ are operators to be determined and \mathcal{D} is the dissipation super-operator (C.3).

The first step is to find an equilibrium point of the DC biased circuit. The electromagnetic modes of the system eventually consist of deviations around this point. An equilibrium point γ_{eq} is defined as $\mathbf{I}(\gamma_{\text{eq}}) = \mathbf{I}_{\text{DC}}$. To be a stable equilibrium point, the solution should also minimize the potential energy (sum of the inductances and junctions energies) that is computed using tab. 2.1. When there exist several stable equilibrium points, the one with lowest energy is usually chosen. Still, the system may be trapped in a local minima for a long time, depending on the energy barrier that separates it from the global one.

To find the electromagnetic modes, small deviations $\delta\gamma(t) = \gamma(t) - \gamma_{\text{eq}}$ around this minimum are analysed. Equation (2.2) (with no drives so far) is linearised into

$$\mathbf{I}(\gamma_{\text{eq}} + \delta\gamma(t)) = \mathbf{I}_{\text{DC}} = \mathbf{I}(\gamma_{\text{eq}}) + \mathbf{I}_{\text{eq}}(\delta\gamma(t)) + o(\delta\gamma(t)) \Rightarrow \mathbf{I}_{\text{eq}}(\delta\gamma(t)) = 0 \quad (2.4)$$

where the final equation can be viewed as the equation of motion of an equivalent equilibrium circuit where Josephson junctions are replaced with inductors with inductances $L_J / \cos(\varphi_{\text{eq}})$ ¹. Indeed, the current flowing through a Josephson junction writes

$$\frac{1}{L_J} \sin(\varphi_{\text{eq}} + \delta\gamma) = \frac{1}{L_J} \sin(\varphi_{\text{eq}}) + \frac{\cos(\varphi_{\text{eq}})}{L_J} \delta\gamma + o(\delta\gamma) \quad (2.5)$$

the first term being the persistent current that flows through the junction at equilibrium and the second one is the linear deviation. The newly defined equation of motion (2.4) is linear and hence suitable for frequency analysis. By replacing $\delta\gamma(t)$ with $\delta\gamma[\Omega]e^{-i\Omega t}$, it rewrites as

$$\mathbf{M}(\Omega)\delta\gamma[\Omega] = 0. \quad (2.6)$$

where $\mathbf{M}(\Omega)$ is a matrix. This system has non-trivial solutions when $\det(\mathbf{M}(\Omega)) = 0$ and these solutions are precisely the eigenmodes of the circuit. This eigenvalue problem gives a set of complex eigenfrequencies $\{\Omega_i\} = \{\omega_i - i\kappa_i/2\}$ from which we deduce the mode frequencies $\{\omega_i\}$ and their loss rates $\{\kappa_i\}$. Provided $\kappa_i \ll \omega_i$, the time evolution of the system is indeed of the Lindblad form (2.3), and we can already write the

¹Recall there is the full set of variables φ and the set of independent ones γ . In this expression, φ_{eq} represents the phase difference across the junction at equilibrium which may be directly in γ_{eq} or simply expressed as a linear combination of elements of γ_{eq} .

Hamiltonian and loss operators that lead to the linear dynamics

$$\begin{aligned} \mathbf{H} &= \hbar \sum_i \omega_i \mathbf{a}_i^\dagger \mathbf{a}_i \\ \mathbf{L}_i &= \sqrt{\kappa_i} \mathbf{a}_i \end{aligned} \tag{2.7}$$

where \mathbf{a}_i and \mathbf{a}_i^\dagger are the annihilation and creation operators of mode i respectively. Here, we assumed that the environment is cold enough so that no significant thermal excitations impinge on the system.

From the elements of $\ker(\mathbf{M}(\Omega_i))$, one deduces the eigenvectors $\{\boldsymbol{\lambda}_i\}$ that describe how each eigenmode participates into the circuit elements. This vector is normalized [47] so that the magnetic energy associated to the quantum vacuum fluctuations is $\hbar\Omega_i/4$ (sec. A.1.1). If one writes $\boldsymbol{\lambda}_i \equiv [\dots, \phi_{i,j}, \dots]$, the non-linear quantum dynamics of the circuit are governed by (sec. A.2)

$$\begin{aligned} \mathbf{H} &= \hbar \sum_i \omega_i \mathbf{a}_i^\dagger \mathbf{a}_i + \sum_j E_{J,j} \left(\sin(\varphi_{\text{eq},j}) \sin_3(\boldsymbol{\phi}_j) - \cos(\varphi_{\text{eq},j}) \cos_4(\boldsymbol{\phi}_j) \right) \\ \text{with } \boldsymbol{\phi}_j &= \sum_i \phi_{i,j} (\mathbf{a}_i + \mathbf{a}_i^\dagger) \\ \mathbf{L}_i &= \sqrt{\kappa_i} \mathbf{a}_i \end{aligned} \tag{2.8}$$

where the second sum runs over the junctions, $E_{J,j}$ and $\varphi_{\text{eq},j}$ are respectively the Josephson energy and phase difference at equilibrium of junction j , $\sin_3(\phi)$ and $\cos_4(\phi)$ are defined as $\sin(\phi) - \phi$ and $\cos(\phi) - 1 + \phi^2/2$.

2.1.4 AC Biases

As we mentioned, off-resonant AC current drives are used to further bias the circuit dynamics. To account for them, one should find the limit cycle of the classical equations of motion (2.2) and write the solution as $\gamma_{\text{sol}}(t) = \gamma_{\text{eq}} + \gamma_{\text{AC}}(t)$ from which one deduces $\varphi_{\text{AC}}(t)$. This oscillating solution is then plugged¹ into the Hamiltonian (2.8) as

$$\begin{aligned} \mathbf{H} &= \hbar \sum_i \omega_i \mathbf{a}_i^\dagger \mathbf{a}_i + \sum_j E_{J,j} \left(\sin(\varphi_{\text{eq},j}) \sin_3(\boldsymbol{\phi}_j) - \cos(\varphi_{\text{eq},j}) \cos_4(\boldsymbol{\phi}_j) \right) \\ \text{with } \boldsymbol{\phi}_j &= \varphi_{\text{AC},j}(t) + \sum_i \phi_{i,j} (\mathbf{a}_i + \mathbf{a}_i^\dagger) \\ \mathbf{L}_i &= \sqrt{\kappa_i} \mathbf{a}_i. \end{aligned} \tag{2.9}$$

¹The drives displace the mode of the system. Here, we are implicitly redefining the annihilation and creation operators by moving into the displaced frame so that the new modes are in vacuum (see sec. 5.2.3 or sec. B.1).

Solving for the full non-linear equations of motion proves to be computationally involved. Usually, we restrict the amplitude of the drive so that the non-linearity is negligible and $\gamma_{AC}(t)$ is simply the solution of

$$\mathbf{I}_{eq}(\gamma_{AC}(t)) = \mathbf{I}_{AC}(t) \quad (2.10)$$

where we recall that \mathbf{I}_{eq} is associated with the linearised circuit. This linear treatment ensures that the frequency components of the drives are the same as the one of the solution $\gamma_{AC}(t)$.

Now that we have the general quantum dynamics of our circuits, we analyse it more in detail to see how specific coupling terms can be isolated.

2.2 Engineering dynamics

With the technique of parametric pumping, that is the topic of chapter 3, one can tailor specific coupling terms of the form

$$\mathbf{H}_c = \left(\hbar g \prod_i \mathbf{a}_i^{\dagger k_i} \mathbf{a}_i^{\ell_i} \right) + \text{h.c.} . \quad (2.11)$$

where g is the coupling strength and k_i and ℓ_i are sets of integers. Hereafter, we detail how these couplings emerge from the general Hamiltonian (2.9).

Beyond Hamiltonian engineering, one can further engineer the system dynamics and tailor loss operators of the form

$$\mathbf{L} = \sqrt{\kappa} \prod_i f_i(\mathbf{a}_i, \mathbf{a}_i^\dagger) . \quad (2.12)$$

where κ is the loss rate and f_i are analytical functions. This process is called dissipation engineering [48] and is used in various applications such as mode cooling [49], state [50, 51] or manifold [32, 33] stabilisation and to engineer non-reciprocal dynamics [52–55]. This technique is at the heart of chapters 4 and 5.

2.2.1 Hamiltonian engineering

In the expansion of the non-linear terms in (2.9), every combination of annihilation and creation operators of the form (2.11) is present. In the regime of weakly anharmonic circuits where $\|\phi_j\| \ll 1$, the low order ones, $\sum_i k_i + \ell_i$ small, are dominant.

These coupling terms fall into two categories. When $\forall i, k_i = \ell_i$, the term is called non-rotating, resonant or energy preserving, indeed it has as many creation as annihilation operators. Examples of such terms are Kerr terms $\mathbf{a}_i^{\dagger 2} \mathbf{a}_i^2$ that shift the mode frequency for each added excitation or cross-Kerr terms $\mathbf{a}_i^{\dagger} \mathbf{a}_i \mathbf{a}_j^{\dagger} \mathbf{a}_j$ that shift the frequency of mode i when j gets excited and conversely. However, the desired coupling Hamiltonian \mathbf{H}_c is not resonant in general and rotates at frequency $\omega_c \equiv \sum_i (k_i - \ell_i) \omega_i$ that is of the order of the mode frequency. This means that when performing the rotating wave approximation (RWA) on the full Hamiltonian, this term has no effect on average on the dynamics. Indeed, it rotates much faster (GHz) than the typical evolution timescale of the state of the system (MHz).

Still, this term can be made resonant by leveraging the AC biases. From now on, let us assume there is a single pump at frequency ω_p acting on the system such that $\varphi_{AC,j}(t) = \varphi_{j,0} \cos(\omega_p t)$. Depending on the parity of $\sum_i k_i + \ell_i$, a term of the form

$$\tilde{\mathbf{H}}_c \propto \varphi_{j,0} e^{i\omega_p t} \prod_i \mathbf{a}_i^{\dagger k_i} \mathbf{a}_i^{\ell_i} + \text{h.c.} \quad (2.13)$$

arises either from the expansion of the \sin_3 terms if even, or from the \cos_4 terms if odd. Then, if ω_p is tuned to the specific frequency matching condition $\omega_p + \sum_i (k_i - \ell_i) \omega_i = 0$, $\tilde{\mathbf{H}}_c$ becomes resonant and the system experiences the desired dynamics. In fact, the pump provides the lacking energy to make the coupling Hamiltonian resonant. Moreover, the coupling strength scales with the pump amplitude¹ since $\varphi_{j,0}$ appears as a prefactor of \mathbf{H}_c .

This parametric pumping scheme is used to make various terms resonant. For instance, by pumping a non-linear system at twice its natural frequency, one can turn on terms of the form $\mathbf{a}^2 + \mathbf{a}^{\dagger 2}$ to make an amplifier. By pumping at the frequency difference between two modes, a conversion Hamiltonian emerges $\mathbf{a} \mathbf{b}^{\dagger} + \mathbf{a}^{\dagger} \mathbf{b}$. In chapter 4, we will see that by pumping a system with two modes at frequency $\omega_p = 2\omega_a - \omega_b$, one can turn on a 2-to-1 photon exchange Hamiltonian of the form $\mathbf{a}^2 \mathbf{b}^{\dagger} + \mathbf{a}^{\dagger 2} \mathbf{b}$.

2.2.2 Dissipation engineering

The goal of dissipation engineering is to tailor a specific loss operator for the system of the form (2.12) that we call $\sqrt{\kappa} \mathbf{A}$ for short. However, only trivial loss operators $\mathbf{L}_i = \sqrt{\kappa_i} \mathbf{a}_i$ occur naturally. The key idea is to have an additional mode, dubbed the buffer, to leverage both the non-linear couplings seen in the previous section and the

¹This is true for $\varphi_{j,0} \ll 1$. When it increases, the scaling becomes Bessel-like due to the averaging of the sin or cos function with an oscillating argument.

natural loss operators. More precisely, if the system+buffer dynamics are governed by

$$\begin{aligned} \mathbf{H}/\hbar &= g\mathbf{A}\mathbf{b}^\dagger + g^*\mathbf{A}^\dagger\mathbf{b} \\ \mathbf{L}_b &= \sqrt{\kappa_b}\mathbf{b}. \end{aligned} \quad (2.14)$$

then, in the limit where $\kappa_b \gg |g|$, the effective dynamics of the system only is given by

$$\mathbf{L}_{\text{eff}} = \sqrt{\kappa_{\text{eff}}}\mathbf{A} \quad \text{with} \quad \kappa_{\text{eff}} = \frac{4|g|^2}{\kappa_b} \quad (2.15)$$

The physical intuition behind this statement is that, in the limit where the buffer interacts with the bath much faster than the non-linear coupling rate, from the point of view of the system, the buffer acquires the same properties as a bath¹. Hence, a non-linear coupling to a bath is realised, resulting in a Lindblad operator of the form (2.15).

In the following, we provide a simple derivation [32] to understand the effective dynamics. This is a process known as adiabatic elimination, more technical analyses can be found in [56, 57].

Adiabatic elimination The system+buffer state is denoted by the density matrix ρ and evolves according to the following master equation

$$\frac{d}{dt}\rho = -\frac{i}{\hbar}[\mathbf{H}, \rho] + \kappa_b \mathcal{D}[\mathbf{b}] \quad (2.16)$$

$$\frac{1}{\kappa_b} \frac{d}{dt}\rho = -\frac{i}{\kappa_b}[g\mathbf{A}\mathbf{b}^\dagger + g^*\mathbf{A}^\dagger\mathbf{b}, \rho] + \left(\mathbf{b}\rho\mathbf{b}^\dagger - \frac{1}{2}\mathbf{b}^\dagger\mathbf{b}\rho - \frac{1}{2}\rho\mathbf{b}^\dagger\mathbf{b} \right). \quad (2.17)$$

We solve this time-evolution using the following ansatz with δ of order $|g|/\kappa_b$

$$\begin{aligned} \rho &= \rho_{00} \otimes |0\rangle\langle 0| \\ &+ \delta \left(\rho_{10} \otimes |1\rangle\langle 0| + \rho_{01} \otimes |0\rangle\langle 1| \right) \\ &+ \delta^2 \left(\rho_{11} \otimes |1\rangle\langle 1| + \rho_{20} \otimes |2\rangle\langle 0| + \rho_{02} \otimes |0\rangle\langle 2| \right) + O(\delta^3), \end{aligned} \quad (2.18)$$

where $\rho_{mn} = \langle m|\rho|n\rangle$ is the reduced density matrix acting on the system only, $|m\rangle$ and $|n\rangle$ being Fock states of the buffer and the operator $|n\rangle\langle m|$ acts on the buffer only. The goal here is to derive the dynamics of $\rho_{\text{sys}} = \text{Tr}_b(\rho) = \rho_{00} + \delta^2\rho_{11}$ up to second order in δ , where Tr_b denotes the partial trace over the buffer degrees of freedom. This expansion is justified because the large loss rate κ_b guarantees the low occupancy of the buffer.

¹Essentially that it is Markovian.

Let us determine the time-evolution of ρ_{00} and ρ_{11} by projecting eq. (2.17).

$$\langle 0 | \dots | 0 \rangle \rightarrow \frac{1}{\kappa_b} \frac{d}{dt} \rho_{00} = -i\delta^2 (\bar{\mathbf{A}}^\dagger \rho_{10} - \rho_{01} \bar{\mathbf{A}}) + \delta^2 \rho_{11} + O(\delta^3) \quad (2.19)$$

$$\langle 1 | \dots | 1 \rangle \rightarrow \frac{1}{\kappa_b} \frac{d}{dt} \rho_{11} = i(\rho_{10} \bar{\mathbf{A}}^\dagger - \bar{\mathbf{A}} \rho_{01}) - \rho_{11} + O(\delta) \quad (2.20)$$

where $\bar{\mathbf{A}} = \frac{g}{\delta \kappa_b} \mathbf{A}$ so that $\|\bar{\mathbf{A}}\|$ is of order 1. We also compute the evolution of the off-diagonal terms that appeared

$$\langle 0 | \dots | 1 \rangle \rightarrow \frac{1}{\kappa_b} \frac{d}{dt} \rho_{01} = i\rho_{00} \bar{\mathbf{A}}^\dagger - \frac{1}{2} \rho_{01} + O(\delta) \quad (2.21)$$

$$\langle 1 | \dots | 0 \rangle \rightarrow \frac{1}{\kappa_b} \frac{d}{dt} \rho_{10} = i\bar{\mathbf{A}} \rho_{00} - \frac{1}{2} \rho_{10} + O(\delta). \quad (2.22)$$

Considering eq. (2.21), we see that the derivative of ρ_{01} is composed of a term proportional to ρ_{00} that can be viewed as an external drive, and a term proportional to ρ_{01} , that can be viewed as a damping term. Since the variation of ρ_{00} is slow (of order δ^2 see eq. (2.19)) in comparison to the damping term (of order δ^0), we can make the adiabatic approximation: we consider that ρ_{01} is continuously in its steady state. The same reasoning applies to ρ_{10} and ρ_{11} , we thus set to 0 the derivatives of the left hand sides of (2.20), (2.21) and (2.22). This leads to

$$\rho_{01} = 2i\rho_{00} \bar{\mathbf{A}}^\dagger, \quad \rho_{10} = -2i\rho_{00} \bar{\mathbf{A}}^\dagger \quad (2.23)$$

$$\rho_{11} = i(\rho_{10} \bar{\mathbf{A}}^\dagger - \bar{\mathbf{A}} \rho_{01}) = 4\bar{\mathbf{A}} \rho_{00} \bar{\mathbf{A}}^\dagger. \quad (2.24)$$

Plugging these relations into (2.19), we have

$$\frac{d}{dt} \rho_{00} = 4\kappa_b \delta^2 (\bar{\mathbf{A}} \rho_{00} \bar{\mathbf{A}}^\dagger - \frac{1}{2} \bar{\mathbf{A}}^\dagger \bar{\mathbf{A}} \rho_{00} - \frac{1}{2} \rho_{00} \bar{\mathbf{A}}^\dagger \bar{\mathbf{A}}) \quad (2.25)$$

$$= \frac{4|g|^2}{\kappa_b} (\mathbf{A} \rho_{00} \mathbf{A}^\dagger - \frac{1}{2} \mathbf{A}^\dagger \mathbf{A} \rho_{00} - \frac{1}{2} \rho_{00} \mathbf{A}^\dagger \mathbf{A}) \quad (2.26)$$

$$= \frac{4|g|^2}{\kappa_b} \mathcal{D}[\mathbf{A}] \rho_{00}. \quad (2.27)$$

The adiabatic approximation also guarantees that the dynamics of ρ_{sys} is identical to the one of ρ_{00} at this order in δ and hence we recover that the dynamics of the system are governed by the Lindblad operator (2.15).

Conclusion

In this chapter, we described the methods of circuit quantization and Hamiltonian and dissipation engineering that are the key tools required to design a quantum optics experiment in superconducting circuits. However, Hamiltonian engineering is a subtle art. Indeed, to reach large coupling strengths or to engineer high order terms, all the approximations we mentioned are pushed to their limits. In particular, beyond the linear response of the circuit to the pump, the number of frequency components increases making it hard to keep track of all the coupling terms that are turned on. Also, the non-rotating terms that are always present may affect the dynamics at higher pump amplitudes. Exploring part of these limitations is the topic of the next chapter.

Chapter 3

Parametric pumping with a transmon

3.1	The Transmon qubit	30
3.1.1	Low energy behaviour	30
3.1.2	Full description	33
3.2	Quantum dynamics of a driven transmon	35
3.2.1	Description of the experiment	35
3.2.2	Observing the transmon escape into unconfined states	38
3.2.3	Effect of pump-induced quasiparticles	41
3.3	Additional Material	43
3.3.1	Sample fabrication	43
3.3.2	Photon number calibration	43
3.3.3	Multi-photon qubit drive	45
3.3.4	Charge noise	46
3.3.5	Numerical simulation	47
3.3.6	Quasiparticle generation	49

As we described in chapter 2, by applying well chosen microwave drives, or pumps, on a superconducting circuit, one can virtually engineer any coupling Hamiltonian. This technique is called parametric pumping. A multitude of tasks rely on this capability, such as amplifying signals [58–60], generating non-classical light [61, 62], stabilizing single quantum states [50, 51] or manifolds [32, 33], releasing and catching propagating modes [25, 63, 64], and simulating quantum systems [65]. The desired Hamiltonian is only the leading term of a plethora that arises from the expansion of the junction Hamiltonian. In the low pump power regime, the system behaves in a stable manner and the strength of the engineered Hamiltonian increases with the pump power (2.13). However, as the pump power is increased to seek stronger couplings, this non-linear out-of-equilibrium open quantum system can display complex dynamics [66] leading to the degradation of coherence times [32, 67] and instabilities [34].

In this chapter, we report the experiment we performed to better understand the origin of these limitations and to guide us towards improved circuit designs for parametric pumping. In particular, we investigate a circuit based on a transmon qubit. This type of architecture is omnipresent [32, 33, 68] when a four-wave mixing Hamiltonian is required. In particular, the non-linear dissipation we want to engineer arises from this type of mixing as we will see in the next chapter. First, we present the transmon and its specificities regarding the derivation of the previous chapter and grasp the underlying complications for parametric pumping. Then, we check our physical intuition on a particular circuit with experimental data and numerical simulation.

3.1 The Transmon qubit

In the low energy regime, the transmon is well described by the derivation of the previous chapter. Here our goal is to investigate the high power behaviour. Hence, we perform the exact derivation for the transmon qubit that can be found in the original paper by Koch et al. [69]. For completeness, we briefly remind the main results.

3.1.1 Low energy behaviour

Let us first derive the low energy Hamiltonian of the transmon following chapter 2.

Single transmon The transmon consists of a Josephson junction shunted by large capacitor (as shown in fig. 3.1 if one ignore the biasing part). Following the quantization procedure of the previous chapter we find the Hamiltonian of the transmon in terms of

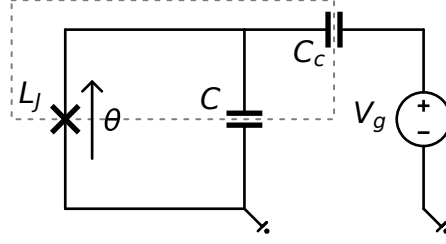


FIGURE 3.1: **Circuit diagram of a voltage biased Cooper pair box.** A Cooper box consists of a superconducting island (dashed box) connected to ground by a Josephson junction. It can be voltage biased to modify the gate charge N_g . In the limit where $E_J \gg E_C$, the charge offset does not perturb the low energy eigenstates and the treatment of chapter 2 holds.

the annihilation and creation operators $\mathbf{q}, \mathbf{q}^\dagger$

$$\mathbf{H} = \hbar\omega_q \mathbf{q}^\dagger \mathbf{q} - E_J \cos_4 \left(\phi_q (\mathbf{q} + \mathbf{q}^\dagger) \right) \quad (3.1)$$

where $\omega_q = 1/\sqrt{L_J C}$, $E_J = \varphi_0^2/L_J$ and $\varphi_0^2 \phi_q^2 = \hbar\sqrt{L_J/C}/2$. These quantities may be written in terms of the charging energy $E_C = e^2/2C$ and the Josephson energy E_J as follows $\hbar\omega_q = \sqrt{8E_J E_C}$, $\phi_q^2 = \sqrt{2E_C/E_J}$. Developing the cosine-4 at the next order, we find the first transitions energies

$$\begin{aligned} \hbar\omega_{01} &= \langle 1 | \mathbf{H} | 1 \rangle - \langle 0 | \mathbf{H} | 0 \rangle = \hbar\omega_q - E_C \\ \hbar\omega_{12} &= \langle 2 | \mathbf{H} | 2 \rangle - \langle 1 | \mathbf{H} | 1 \rangle = \hbar\omega_q - 2E_C \end{aligned} \quad (3.2)$$

from which we can deduce the anharmonicity/Kerr non-linearity of the transmon defined as $K = \omega_{12} - \omega_{01} = -E_C/\hbar$. This anharmonicity allows for the independent control of the two lower states that define a qubit with Hamiltonian $\mathbf{H} = \hbar\omega_{01}\sigma_z/2$.

Transmon coupled to resonators Quite similarly the Hamiltonian of a transmon capacitively coupled to several resonators reads

$$\mathbf{H} = \sum_i \hbar\omega_i \mathbf{a}_i^\dagger \mathbf{a}_i - E_J \cos_4 \left(\sum_i \phi_i (\mathbf{a}_i + \mathbf{a}_i^\dagger) \right) \quad (3.3)$$

where $\{\omega_i\}$ are the eigenfrequencies of the linear system and $\{\phi_i\}$ are linked to the participation of each mode into the junction [47]. The mode that participates the most in the junction is the transmon mode. Developing the cosine-4 term at first order one

gets [42]

$$\begin{aligned}
\mathbf{H} &= \sum_i \mathbf{H}_{i,\text{single}} + \sum_{i>j} \mathbf{H}_{ij,\text{coupling}} + \text{rotating terms} + O(\phi^6) \\
\mathbf{H}_{i,\text{single}}/\hbar &= (\omega_i + K_i) \mathbf{a}_i^\dagger \mathbf{a}_i + \frac{K_i}{2} \mathbf{a}_i^{\dagger 2} \mathbf{a}_i^2 \\
\mathbf{H}_{ij,\text{coupling}}/\hbar &= -\chi_{ij} \mathbf{a}_i^\dagger \mathbf{a}_i \mathbf{a}_j^\dagger \mathbf{a}_j
\end{aligned} \tag{3.4}$$

where $\hbar K_i = -E_J \phi_i^4/2$, $\hbar \chi_{ij} = -E_J \phi_i^2 \phi_j^2$ and the rotating terms are averaged out by moving to the interaction picture. The coefficients K_i are the Kerr non-linearities or anharmonicity of each mode, adding one excitation in the mode shifts its frequency by K_i . The dispersive coupling χ_{ij} corresponds to the shift in frequency of mode i when one excitation is present in mode j and conversely. Note the following relation $\chi_{ij} = -2\sqrt{K_i K_j}$.

Driven system When adding an off-resonant drive at frequency ω_d , the linear response of the system leads to the following Hamiltonian

$$\mathbf{H}^{\text{driven}} = \sum_i \hbar \omega_i \mathbf{a}_i^\dagger \mathbf{a}_i - E_J \cos_4 \left(\sum_i \phi_i (\mathbf{a}_i + \mathbf{a}_i^\dagger) + \varphi_d(t) \right) \tag{3.5}$$

where $\varphi_d(t) = \varphi_{d0} \cos(\omega_d t)$ is the oscillating phase induced by the drive across the junction. Developing the cosine-4 term at first order and only keeping the time-independent terms, the non-driven Hamiltonian (3.4) gets modified as follows

$$\mathbf{H}_{i,\text{single}}^{\text{driven}}/\hbar = \mathbf{H}_{i,\text{single}}/\hbar - \frac{E_J \phi_i^2 \varphi_{d0}^2}{4} \mathbf{a}_i^\dagger \mathbf{a}_i \tag{3.6}$$

When only one mode, m , is significantly populated, we write $\varphi_d(t) = 2\phi_m \alpha_m \cos(\omega_d t)$ where α_m is the amplitude of the coherent state living in mode m . This leads to

$$\mathbf{H}_{i,\text{single}}^{\text{driven}}/\hbar - \mathbf{H}_{i,\text{single}} = \begin{cases} 2\alpha_m^2 K_i \mathbf{a}_i^\dagger \mathbf{a}_i & \text{if } i = m \\ \alpha_m^2 \chi_{im} \mathbf{a}_i^\dagger \mathbf{a}_i & \text{if } i \neq m \end{cases} . \tag{3.7}$$

Hence, one effect of this non-resonant drive is to shift the modes frequencies. This effect is always present and does not depend on the drive frequency. Here, we did not track the other terms of the Hamiltonian that may become resonant/energy preserving when ω_d hits peculiar frequencies (see sec. 2.2.1) but they exist and are the reason the system is driven.

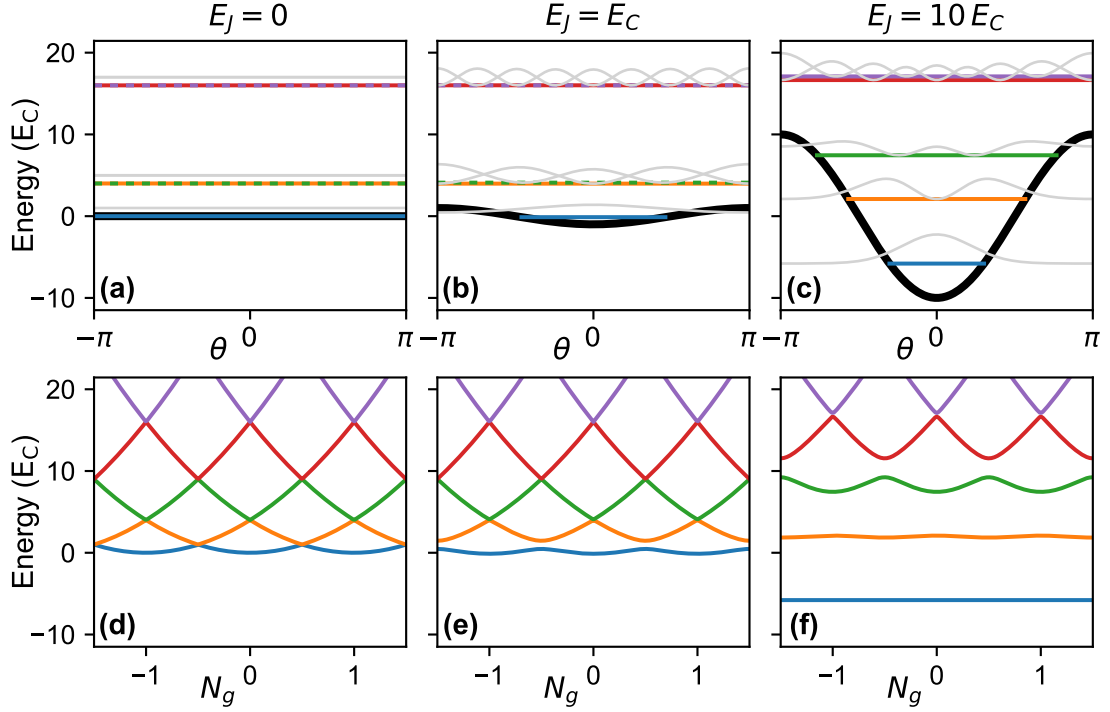


FIGURE 3.2: **From the Cooper pair box to the transmon** The following spectrum were derived by numerical diagonalization of Hamiltonian (3.9) in the charge basis. (a,b,c) Energy levels (colours) of a Cooper pair box in units of E_C with increasing E_J . The cosine potential originating from the Josephson junction is plotted in black and the probability density of the eigenstates are plotted in grey. When E_J increases, the low energy states get confined by the cosine potential and resemble oscillator states. The high energy states are not sensitive to the potential and remain charge-like. (d,e,f) Energy levels dispersion in units of E_C with respect to the offset charge N_g . At $E_J = 0$ the integer charge states are the eigenstate of the system and have a parabolic dispersion as a function of N_g . When E_J increases and that we enter the transmon regime, the low energy states become insensitive to N_g .

3.1.2 Full description

The potential energy of the transmon is a cosine function. In the former derivation, we expanded the cosine potential up to order 4 to get the low-energy behaviour of the transmon. One could expand it further to improved the description but a better approach is to modify the quantization procedure to take into account the periodic nature of the potential.

From the Cooper pair box to the Transmon The transmon is actually a direct descendant of the Cooper pair box [70]. A Cooper pair box is simply a superconducting island (delimited by the dashed lines in dashed lines in fig. 3.1) connected to ground via a Josephson junction which allows Cooper pairs to tunnel. It is conveniently described in the charge basis. The Hamiltonian of the superconducting island without the junction

writes

$$\mathbf{H} = 4E_C(\mathbf{N} - N_g)^2, \quad (3.8)$$

where $\mathbf{N} = \sum_N N |N\rangle\langle N|$ is the number operator for the Cooper pairs transferred across the junction and $E_C = e^2/2C_\Sigma$ is the energy required to add a single electron¹ to the superconducting island also known as the charging energy. The capacitance $C_\Sigma = C_g + C_j$ is the total capacitance of the island to ground. The eigenstates of this Hamiltonian are the charge states $|N\rangle$, $N \in \mathbb{Z}$ and the offset charge number $N_g = C_g V_g / 2e$ describes how the voltage source changes the energy of these charge states fig. 3.2d. Since the charge is perfectly determined, the conjugate variable i.e. the phase is maximally uncertain. Note that since N is integer, as the conjugate variable, the phase is defined on the compact $[-\pi, \pi]$ [20].

Adding the junction, enables Cooper pairs to tunnel in and out of the island. This translates into the Hamiltonian as

$$\mathbf{H} = 4E_C(\mathbf{N} - N_g)^2 - \frac{E_J}{2} \sum_N |N\rangle\langle N+1| + |N+1\rangle\langle N|, \quad (3.9)$$

where the second term is the transfer operator for Cooper pairs across the junction and E_J is the transfer rate. This transfer operator induces a coupling between the charge states which modifies the eigenspectrum as a function of N_g see fig. 3.2e,f. When the anti-crossing $\sim E_J$ would become much larger than the level spacing $\sim E_C$, we enter in the transmon regime fig. 3.2f. The first eigenenergies do not depend on the offset charge any more which makes the transmon a good qubit. Now, the Cooper pair number is not a good quantum number to describe the eigenstates so we switch to the phase representation.

Phase representation In the phase representation, the superconducting island Hamiltonian looks like the kinetic energy of a free phase-particle. The eigenstates are the plane waves in θ see fig. 3.2a, $|e^{iN\theta}\rangle$ and N is the momentum. Connecting the island to ground via a junction adds a periodic potential energy term in the Hamiltonian. When the height of this potential $2E_J$ is large enough compared to $\sim E_C$, the new low energy eigenstates are those of a trapped phase-particle which have a well defined phase fig. 3.2c.

A direct mechanical analogy for the transmon is the rotor fig. 3.3b. Without a gravitational potential, the rotor can freely rotate around its axis, the angular momentum being the direct analogue of N . When adding gravity, the low energy states are states

¹Hence the factor 4, since the operator \mathbf{N} accounts for pairs of electrons

oscillating around $\theta = 0$ and have a confined support in θ fig. 3.2c. Hence, in this regime, it is justified to treat the system as a weakly anharmonic oscillator as we did in the previous section. On the contrary, high energy states still resemble charge states, in other words, a rotor spinning really fast around its axis is not perturbed by gravity fig. 3.3b.

3.2 Quantum dynamics of a driven transmon ¹

As we explained previously, the transmon has an infinite number of energy levels that fall in two categories. First, those with energies smaller than the Josephson energy and that are confined by the Josephson potential. Second, those which lie above the cosine potential which we refer to as unconfined states. Due to their high energies, unconfined states have always been considered irrelevant for circuit dynamics and disregarded [71–76].

In this section, we show that unconfined states play a central role in the dynamics of strongly driven Josephson circuits. This time-periodic system has periodic orbits known as Floquet states. In the dissipative steady state regime, the system converges to a statistical mixture of Floquet states. For weak pump powers, the steady state remains pure and occupies low energy confined states. Above a critical pump power, the steady state suddenly jumps to a statistical mixture of many Floquet states, with a significant population on unconfined states. The dramatic change in the steady state when the pump power is slightly increased above the threshold is a signature of structural instability [34].

3.2.1 Description of the experiment

Our device consists of a single transmon in a 3D copper cavity [77] coupled to a transmission line. The system is well modeled by the circuit depicted in fig. 3.3a, whose Hamiltonian is given by [69]

$$\begin{aligned} \mathbf{H}(t) = & 4E_C \mathbf{N}^2 - E_J \cos(\boldsymbol{\theta}) + \hbar\omega_a \mathbf{a}^\dagger \mathbf{a} + \hbar g \mathbf{N} (\mathbf{a} + \mathbf{a}^\dagger) \\ & + \hbar \mathcal{A}_p(t) (\mathbf{a} + \mathbf{a}^\dagger), \end{aligned} \quad (3.10)$$

where \mathbf{N} is the Cooper pair number operator and $\boldsymbol{\theta}$ is the phase operator [20]. The operator $\cos(\boldsymbol{\theta})$ is the transfer operator for Cooper pairs across the junction while \mathbf{a}^\dagger

¹The following was published as “Escape of a Driven Quantum Josephson Circuit into Unconfined States”, Raphaël Lescanne, Lucas Verney, Quentin Fichoux, Michel H. Devoret, Benjamin Huard, Mazhar Mirrahimi and Zaki Leghtas, Phys. Rev. Applied 11, 014030 (2019) [35].

and \mathbf{a} are the creation and annihilation operators for the resonator mode. The Josephson and charging energies are denoted E_J and E_C , respectively. The angular frequency of the resonator in the absence of the JJ (E_J taken to be 0) is denoted ω_a and is known as the bare resonator frequency and g is the coupling rate between the transmon and the resonator. Note that this definition of g differs from the one usually used in the Jaynes-Cummings Hamiltonian [78]. The pump couples capacitively to the circuit, and is accounted for by the second line in (3.10), where $\mathcal{A}_p(t) = A_p \cos(\omega_p t)$, A_p and ω_p being the pump amplitude and angular frequency.

Our physical picture of the dynamics of a pumped transmon in a cavity is the following. When the pump power is sufficiently large, the transmon is excited above its bounded potential well (fig. 3.3c,d). This is reminiscent to an electron escaping from the bound states of the atomic Coulomb potential and leaving the atom ionized. The transmon can occupy highly excited states which resemble charge states, or equivalently, plane waves in the phase representation. A classical analogy would be a strongly driven rotor which rotates indefinitely, making turns around its anchoring point (fig. 3.3b). When occupying such a state, the transmon behaves like a free particle which is almost not affected by the cosine potential. Thus the Josephson energy can be set to zero in Eq. (3.10). The Hamiltonian is now that of a superconducting island capacitively coupled to a resonator, with no Josephson junction. The island-resonator coupling term commutes with the Hamiltonian of the island, which consists of the charging energy only. The coupling is now longitudinal and therefore the cavity frequency is fixed to the bare frequency ω_a , independently of the island state.

The dynamics governed by Hamiltonian (3.10) is difficult to numerically simulate in the regime of large pump amplitudes for two reasons. First, the simulated Hilbert space needs to be large. Indeed, the number of transmon states needs to be much larger than the number of states in the well. For our experimental parameters we find that about 45 states are necessary. Moreover, the resonator is also driven to large photon number states. Second, the pump amplitude is so large that we reach regimes where $A_p \gg \omega_a$. It is therefore excluded to use the rotating wave approximation in its usual form. These two difficulties are surmounted by the theory introduced in [34]. Using an adequate change of frame in which the resonator is close to the vacuum, we can decrease the number of computed states to 10 for the resonator, hence reducing the dimensionality of the Hilbert space (sec. 3.3.5). Since $\mathbf{H}(t)$ is $2\pi\omega_p^{-1}$ -periodic, Floquet-Markov theory [79, 80] is well suited [81, 82] to find the system steady state, as shown in fig. 3.3c. This theory assumes weak coupling to the bath, but can treat pumps of arbitrary amplitude and frequency. For small pump powers, the transmon remains close to its ground state, and after the power is increased beyond a critical value, it is driven into highly excited states, above its cosine potential (orange dashed line in fig. 3.3c).

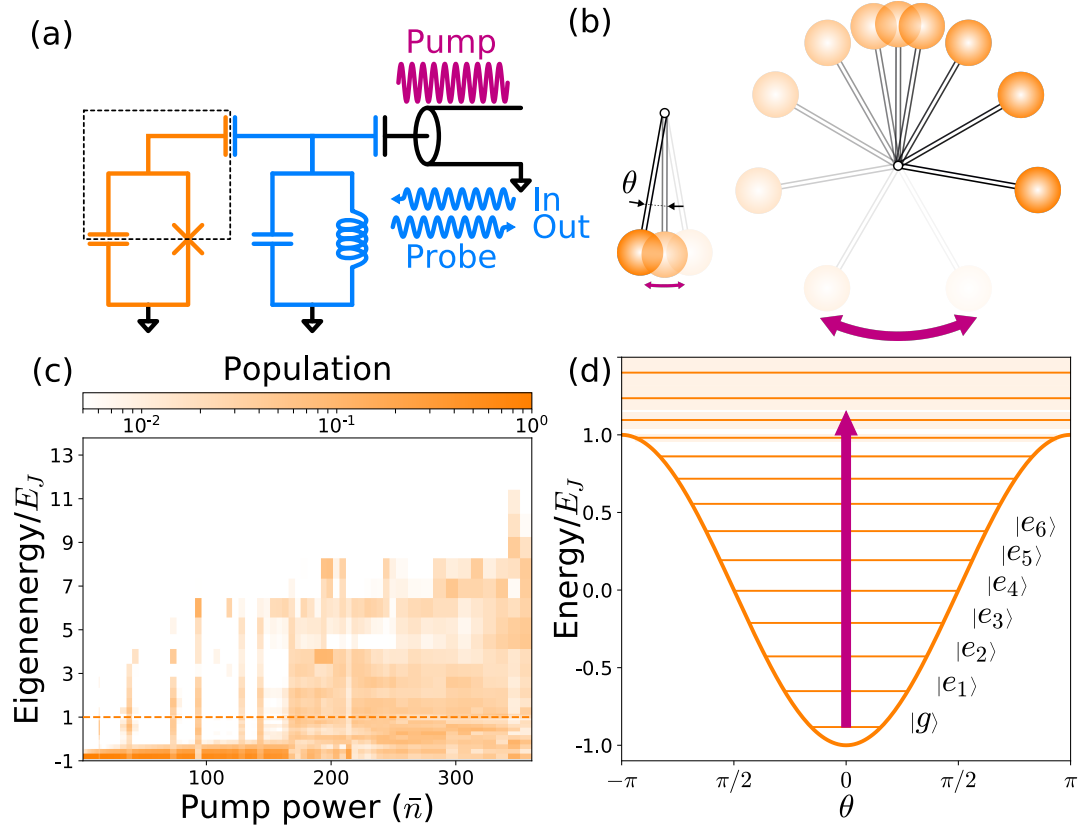


FIGURE 3.3: Principle of the experiment demonstrating the effect of a strong pump on a Josephson circuit. (a) A superconducting island (within the dashed lines) is coupled to ground through a Josephson junction (JJ), which is shunted by a capacitor, forming a transmon mode (orange). It is capacitively coupled to an LC resonator (blue) which represents the lowest mode of a 3D waveguide cavity. The system is pumped and probed through a transmission line (black). (b) Classical picture: The transmon is represented by a rotor [69], where the deviation angle from equilibrium, denoted θ , is the phase difference across the JJ. The gravitational potential energy represents the Josephson energy. For small pump powers (left), the rotor acquires a small kinetic energy and oscillates around its equilibrium. For large pump powers (right), it acquires sufficient energy to escape from its trapping potential well, and rotates indefinitely. (c) Numerical simulation of the population (colour) of the energy levels of the transmon (y-axis) as a function of the number of photons \bar{n} (sec. 3.3.2) in the resonator due to the pump (x-axis). For small \bar{n} , the transmon is close to its ground state, except for small population bursts (see text). Above a critical \bar{n} (here about 170 photons), the transmon jumps into highly excited states above its cosine potential (orange dashed line). (d) Quantum picture: cosine potential and energy levels (orange lines) for charge offset $N_g = 0$. Light orange areas represent the band of levels appearing when varying N_g [70] (see fig. 3.2). Large pump powers (big arrow) induce transitions from the ground state $|g\rangle$ with a phase localized around $\theta = 0$, into highly excited states with a delocalized phase.

The parameters of Hamiltonian (3.10) are deduced from measurements involving a low number of excitations in the system. In this regime, it is well approximated by the Hamiltonian of two non-linearly coupled effective modes, one transmon qubit-like and one resonator-like, respectively denoted by subscripts q and r (3.4):

$$\begin{aligned} \mathbf{H}_{\text{low}}(t)/\hbar = & \bar{\omega}_q \mathbf{a}_q^\dagger \mathbf{a}_q - \frac{\alpha_q}{2} \left(\mathbf{a}_q^\dagger \right)^2 \mathbf{a}_q^2 - \chi_{qr} \mathbf{a}_q^\dagger \mathbf{a}_q \mathbf{a}_r^\dagger \mathbf{a}_r \\ & + \bar{\omega}_r \mathbf{a}_r^\dagger \mathbf{a}_r - \frac{\alpha_r}{2} \left(\mathbf{a}_r^\dagger \right)^2 \mathbf{a}_r^2 \\ & + \mathcal{A}_{p,r}(t) \left(\mathbf{a}_r + \mathbf{a}_r^\dagger \right), \end{aligned} \quad (3.11)$$

where $\bar{\omega}_{q,r}$ are the modes angular frequencies, $\alpha_{q,r}$ their Kerr non-linearities, and χ_{qr} their dispersive coupling. In this basis, the pump is represented by the term in $\mathcal{A}_{p,r}(t) = A_{p,r} \cos(\omega_p t)$, with a renormalized amplitude $A_{p,r}$, where we neglect the linear coupling of the pump to mode q .

We measure $\bar{\omega}_q/2\pi = 5.353$ GHz, $\bar{\omega}_r/2\pi = 7.761$ GHz, $\alpha_q/2\pi = 173$ MHz and $\chi_{qr}/2\pi = 5$ MHz. In order to compute E_J , E_C , g and ω_a , we write Hamiltonian (3.10) in matrix form in the charge basis for the transmon and the Fock basis for the resonator. We calculate the energy differences of the lowest energy levels, and fit the measured values with: $E_C/h = 166$ MHz, $E_J/h = 23.3$ GHz, $g/2\pi = 179$ MHz and $\omega_a/2\pi = 7.739$ GHz. From these parameters, we deduce $\alpha_r/2\pi = 43$ kHz.

3.2.2 Observing the transmon escape into unconfined states

We experimentally observe the transmon jump into highly excited states by performing the spectroscopy of the resonator while the pump is applied (fig. 3.4). For small pump powers, the system is well described by the low energy Hamiltonian (3.11). The pump populates the resonator with photons at the pump frequency with an average number $\bar{n}_r = \left| \frac{A_{p,r}/2}{i(\omega_r - \omega_p) + \kappa_r/2} \right|^2$, and shifts the resonance to $\omega_r(\bar{n}_r) = \bar{\omega}_r - 2\alpha_r \bar{n}_r$ [32, Supplement section 2.1]. We calibrate the photon number \bar{n}_r (sec. 3.3.2) and, using the anharmonicity α_r deduced from the model (3.11), we plot $\omega_r(\bar{n}_r)$ (solid line in fig. 3.4b). The data points match this prediction in the regime of small photon numbers, over a wide range of pump frequencies. This linear dependence is disrupted by abrupt frequency jumps, as seen for a pump power of about $30P_{1ph}$ in fig. 3.4a. This behavior suggests that the system frequencies, at this specific power, have shifted into resonance with a process which excites the transmon. This resembles the population bursts observed for example at 90 photons in the simulation of fig. 3.3c, before the population jumps at around 170 photons.

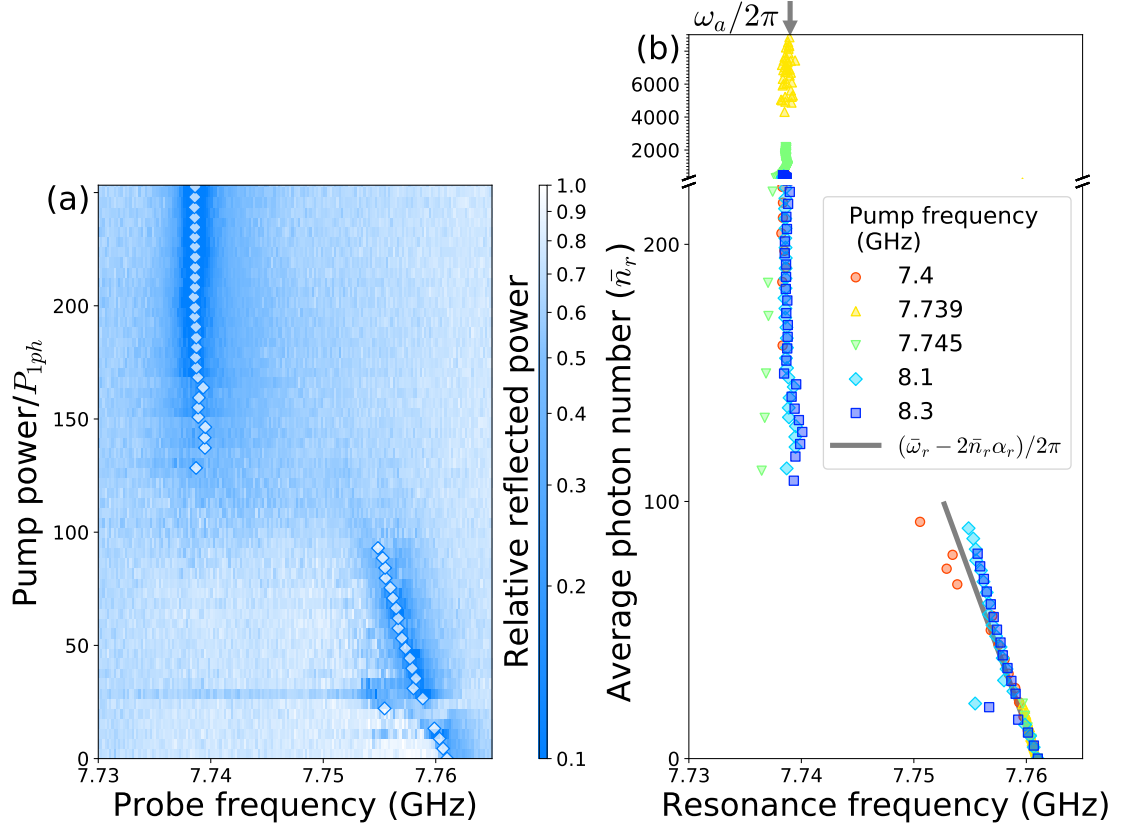


FIGURE 3.4: Effect of the pump on the cavity resonance frequency. (a) Relative reflected power of a weak probe as a function of probe frequency (x-axis), and pump power (y-axis) in units of P_{1ph} , the power needed to populate the cavity with one photon in average. The pump frequency is fixed at 8.1 GHz, about 300 MHz above the cavity frequency. The reduced reflected power is due to internal losses when the probe is resonant with the cavity. We indicate the fitted cavity resonance $\omega_r/2\pi$ with white diamonds. As the pump power increases, two regimes are distinguishable. For small powers, ω_r shifts linearly with the pump power. Above a critical power, the cavity resonance jumps to a new frequency $\omega_a/2\pi = 7.739$ GHz which is independent of pump power. (b) Fitted cavity resonance as a function of pump power for various pump frequencies. Pump powers are converted into a mean number of photons \bar{n}_r (sec. 3.3.2). The y-axis of (a) and (b) slightly differ because \bar{n}_r takes into account the resonator frequency shift. The general behavior is the same for all pump frequencies. The low power linear dependence is well reproduced by the AC Stark shift [32] for an independently measured Kerr α_r (solid gray line).

Above a critical \bar{n}_r (of about 100 photons for the most detuned pump frequencies), the resonance jumps to a new frequency close to $\omega_a/2\pi$ (arrow in fig. 3.4b), which is independent of the pump frequency and power. This is the resonator frequency expected when the transmon is highly excited so that the JJ behaves as an “open”. Such a jump of the resonance has been used for qubit readout [66] and modeled in previous works with a strong drive which plays the role of the pump and the probe, applied close to resonance with the resonator. Those models involve two-level [72] and multi-level [73] approximations for the transmon. Such approximations are incompatible with our following measurements. In recent work [81, 82], numerical simulations suggest that the resonator frequency jump is accompanied by an increase in the transmon population.

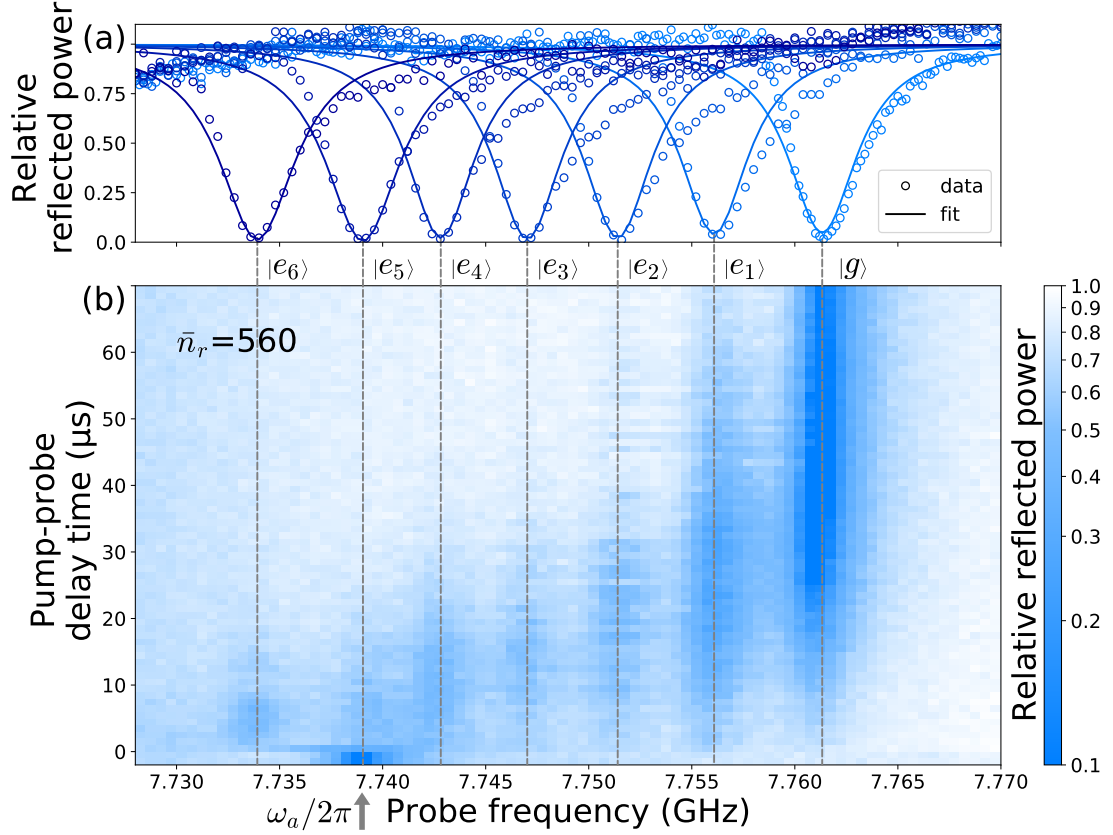


FIGURE 3.5: Probing the transmon decay out of highly excited states populated by a strong off-resonant pump. (a) Cavity spectroscopy after the transmon is prepared in various eigenstates. Each transmon state $|e_k\rangle$ ($k=1$ to 6) is prepared using a k -photon π -pulse (fig. 3.8) and higher states could not be prepared due to charge noise (sec. 3.3.4). (b) Time resolved measurement: first, a pump is applied for $50 \mu\text{s}$ at 8.1 GHz populating the cavity with a sufficiently large photon number to induce a jump in ω_r , here $\bar{n}_r = 560$. After a time-delay t , a weak probe is applied for $2 \mu\text{s}$. We plot the relative reflected power of the probe as a function of probe frequency (x-axis), and time-delay t (y-axis). For $t < 0$, as in fig. 3.4, the cavity is probed while the pump is on, and the resonance frequency is $\omega_a/2\pi$, confirming that the system has jumped. At $t > 0$, the photons in the cavity rapidly decay at a rate $\kappa_r = 1/(55 \text{ ns})$, and the cavity can now be used, as in fig. 3.5a, to read the transmon state. The transmon is found in a highly excited state, and after $t = 60 \mu\text{s}$, it has fully decayed into its ground state which is compatible with $T_1 = 14 \mu\text{s}$.

In the next paragraphs, we experimentally measure a sudden population increase which corresponds to the jump of the transmon state out of its potential well into unconfined states. In order to model this effect, it is crucial to consider all levels confined in the cosine potential and a number of levels above which depends on the pump power.

For states well confined inside the cosine potential, the transmon state is encoded in the resonance frequency of the resonator. As seen from Hamiltonian (3.11), each additional excitation in the transmon pulls the resonator frequency to $\omega_r(n_q) = \bar{\omega}_r - n_q \chi_{qr}$ (fig. 3.5a). However, for states above the cosine potential, the resonator adopts a frequency ω_a which is now independent of the particular transmon state.

The highly excited nature of the transmon can be confirmed by turning off the pump,

and waiting for the transmon to decay to lower lying states which can be resolved by probing the resonator frequency. In this experiment, the highest of these states was the sixth excited state $|e_6\rangle$. As expected, after the pump is turned off ($t = 0$ in fig. 3.5b), we observe a population decay of the transmon compatible with a highly excited state at $t \leq 0$.

3.2.3 Effect of pump-induced quasiparticles

Strongly pumping a superconducting circuit generates non-equilibrium quasiparticles [83, 84], which poses the question: what is the influence of quasiparticles on this dynamics? We detect whether quasiparticles have been generated by the pump pulse by measuring the transmon T_1 after a time delay large enough to ensure that all modes have decayed back to their ground states. We find that for the pump frequency and power used for the experiment of fig. 3.5b, the T_1 is unaffected (fig. 3.10). This indicates that the pump can expel the transmon out of its potential well, without generating a measurable amount of quasiparticles, and therefore the simulation of fig. 3.3c, which does not include quasiparticles, is relevant.

In order to observe a measurable decrease in T_1 , we need to insert a much larger number of photons in the resonator. We enter this regime by applying a pump at frequency ω_a , so that the pump is resonant with the resonator at large powers. As shown in fig. 3.6b, the T_1 drops at high pump powers indicating that we have successfully generated quasiparticles. Furthermore, we find that the transmon T_1 recovers its nominal value after a few milliseconds, a typical timescale for quasiparticle recombination [83, 84]. In fig. 3.6a, we probe the transmon dynamics as in fig. 3.5b, in the presence of pump-induced quasiparticles. The increased quasiparticle density does not qualitatively modify the transmon dynamics, but only increases the decay rate back to its ground state.

Conclusion

Transmons are good mixing elements for parametric pumping in the low pump regime for they are easy to implement and have good coherence properties. However, when reaching higher pump powers for stronger couplings, transmon based circuits may experience complex out-of-equilibrium dynamics that have deleterious effects. In our experiment, we measured the dynamics of a transmon in a cavity in the presence of a strong off-resonant pump and identified one prejudicial mechanism where the transmon escapes its potential well. The transmon then behaves like a free particle which no longer induces any non-linearity on the cavity. This escape, which is due to the boundedness

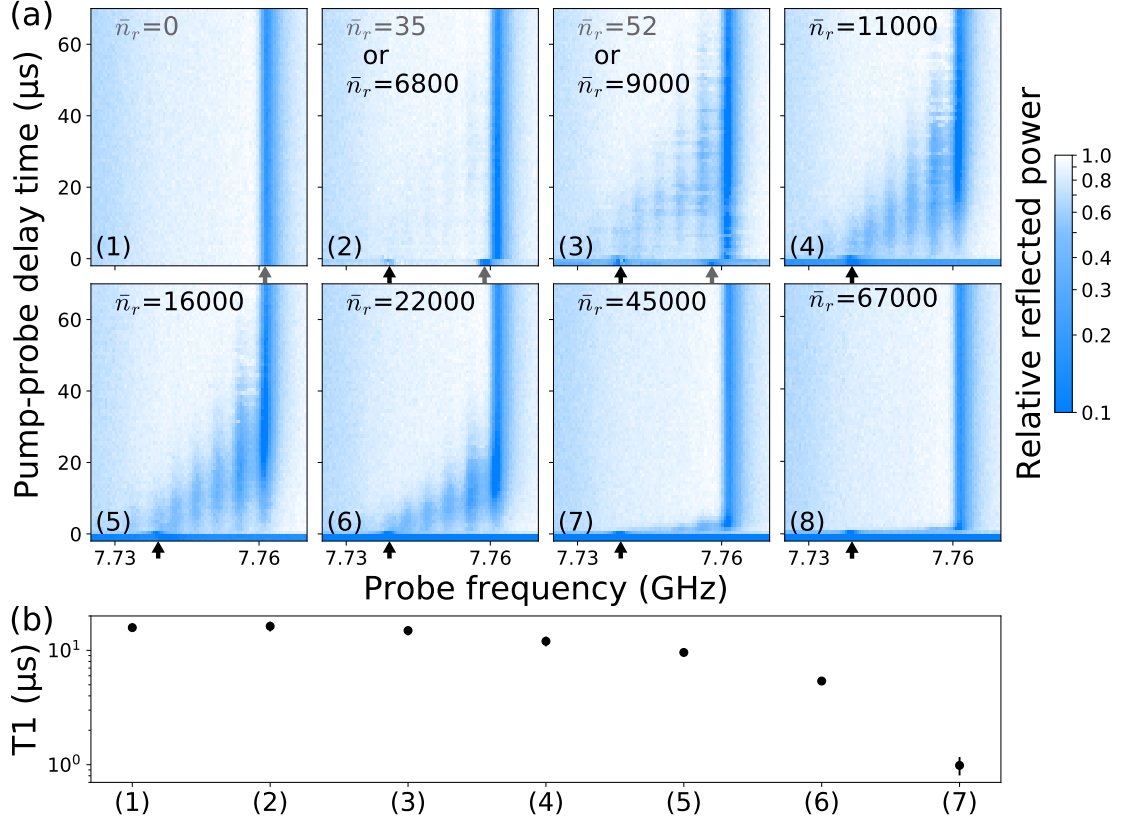


FIGURE 3.6: Transmon relaxation following a pump pulse of increasing power. (a) Same experiment as in fig. 3.5b with increasing pump power (a1 to a8). The pump frequency is fixed at $f_p = \omega_a/2\pi = 7.739$ GHz in order to populate the cavity with a large number of photons. Each pump power is converted into the mean number of photons \bar{n}_r in the cavity. The conversion factor depends on the observed cavity frequency at $t \leq 0$, indicated by the arrows (sec. 3.3.2). (a1) The pump power is too low to induce a shift or a jump in the cavity frequency. (a2-a3) At intermediate pump powers, the system is in a statistical mixture of two configurations, as indicated by the two arrows at $t < 0$. First, a weakly shifted resonance due to the AC Stark shift with a small cavity population. Second, a resonance at ω_a coinciding with the pump frequency and hence a large cavity population. (a4-a5) At higher pump powers, the cavity frequency always jumps to ω_a and the transmon decays as in fig. 3.5b. (a6-a8) At even higher pump powers, the transmon decay rate increases significantly. (b) Transmon T_1 (y-axis) measured 50 μs after a pump is applied. The pump duration and powers (x-axis) correspond to the ones used for the experiments shown in (a). We observe a decrease in T_1 as the pump power increases, which is consistent with an increasing quasi-particle density induced by the pump [83, 84], and explains the significantly higher decay rates in (a6-a8). For pump power (3), T_1 is marginally reduced, while the system dynamics is highly affected (a3). The T_1 corresponding to (a8) was too small to be accurately measured.

of the cosine potential, could be prevented by adding an unbounded parabolic potential, provided by an inductive shunt. One could then further increase the non-linear couplings by increasing the pump power, without driving the transmon into free particle states and losing the resource of non-linearity. This points towards inductively shunted JJs [85] as better suited than standard transmons for pump-induced non-linear couplings [34]. In particular, this work led us to the design of a new dipole to induce non-linear damping in a resonator. This dipole is presented in the next chapter.

3.3 Additional Material

3.3.1 Sample fabrication

The sample measured in this work is the same one as in [86]. The transmon is made of a single aluminum Josephson junction and is embedded in a copper cavity of $26.5 \times 26.5 \times 9.5 \text{ mm}^3$ thermalized on the base plate of a dilution fridge at about 10 mK. More details can be found in [86, Sections 1.A and 1.B].

3.3.2 Photon number calibration

In this section, we explain how we convert a pump power in mW, to an average number of photons at the pump frequency inside the cavity. We exploit the AC Stark shift and measurement induced-dephasing [87], where a drive on the resonator inserts photons which detune and dephase the qubit. We use a 2-level approximation of the low energy Hamiltonian from Eq. (3.11):

$$\bar{H}_{\text{low}}^{(2)}/\hbar = \omega_q \frac{\sigma_z}{2} + \omega_r \mathbf{a}_r^\dagger \mathbf{a}_r - \chi_{qr} |e\rangle \langle e| \mathbf{a}_r^\dagger \mathbf{a}_r + A_{p,r} \cos(\omega_p t) (\mathbf{a}_r + \mathbf{a}_r^\dagger) \quad (3.12)$$

where $\sigma_z = |e\rangle \langle e| - |g\rangle \langle g|$, and $|g\rangle, |e\rangle$ are the transmon's ground and first excited states. Moving into a frame rotating at the pump frequency ω_p for the resonator, and the qubit frequency ω_q for the qubit, and performing the rotating wave approximation (RWA), we get

$$\bar{H}_{\text{low}}^{(2)}/\hbar = \Delta \mathbf{a}_r^\dagger \mathbf{a}_r - \chi_{qr} |e\rangle \langle e| \mathbf{a}_r^\dagger \mathbf{a}_r + A_{p,r} \mathbf{a}_r / 2 + A_{p,r} \mathbf{a}_r^\dagger / 2, \quad (3.13)$$

where $\Delta = \omega_r - \omega_p$.

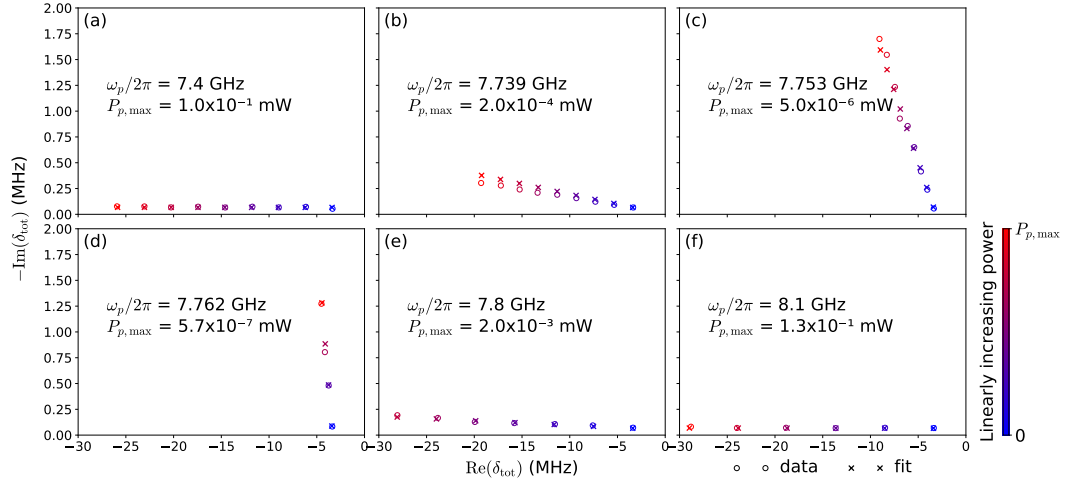


FIGURE 3.7: Calibration to convert the pump power (mW) into an average number of photons \bar{n}_r , using the AC Stark shift and measurement-induced dephasing [87]. By performing a Ramsey experiment in the presence of a pump at frequency ω_p and power P_p , we measure the detuning between the drive and the qubit $\delta_q(\omega_p, P_p)$, and the qubit dephasing rate $\gamma_\phi(\omega_p, P_p)$. We introduce $\delta_{tot} = \delta_q - i\gamma_\phi$. For each plot (a) to (f), the pump frequency is fixed, and γ_{tot} is plotted in the complex plane (hollow circles), for increasing P_p (blue is 0 mW, red is $P_{p,max}$). For each pump frequency, the data points are fitted with Eq. (3.17), where δ_m is given in Eq. (3.16), and the constant C is the only fitting parameter. All other parameters: $\Delta, \kappa_r, \chi_{qr}, P_p, \delta_0$ are measured independently. (a),(f) Large detuning between the pump and the cavity. The pump mostly induces a detuning on the qubit, without inducing any dephasing. (d) The pump is resonant with the cavity, and mostly induces dephasing on the qubit. (b), (c), (e) Intermediate regimes where the pump both dephases and detunes the qubit.

Depending on the qubit state $|g\rangle$ [resp: $|e\rangle$], the resonator reaches a steady state which is a coherent state of amplitude α_g [resp: α_e], where

$$\alpha_g = \frac{-iA_{p,r}/2}{i\Delta + \kappa_r/2} \quad \text{and} \quad \alpha_e = \frac{-iA_{p,r}/2}{i(\Delta - \chi_{qr}) + \kappa_r/2}. \quad (3.14)$$

The measurement induced complex detuning is [87]

$$\delta_m = -\chi_{qr}\alpha_e\alpha_g^* = -\chi_{qr} \frac{A_{p,r}^2/4}{(i(\Delta - \chi_{qr}) + \kappa_r/2)(-i\Delta + \kappa_r/2)}, \quad (3.15)$$

$\text{Re}(\delta_m)$ being the AC Stark frequency shift, and $-\text{Im}(\delta_m)$ being the measurement induced dephasing rate. The quantity $A_{p,r}^2$ is proportional to the output power of our instrument P_p , and hence we write it in the following form: $A_{p,r}^2 = \kappa_r^2 C P_p$, where C is the proportionality constant we aim to calibrate and is expressed in a number of photons per mW. Since our microwave input lines do not have a perfectly flat transmission over a GHz range, C can be dependent on ω_p . We get

$$\delta_m(\omega_p, P_p) = -C \frac{\kappa_r^2 \chi_{qr} P_p / 4}{(i(\Delta - \chi_{qr}) + \kappa_r/2)(-i\Delta + \kappa_r/2)}. \quad (3.16)$$

For each pump frequency ω_p , we vary the pump power P_p between 0 and $P_{p,max}$, and perform a T_2 Ramsey experiment. The Ramsey fringes oscillation frequency and exponential decay provide a complex frequency shift δ_{tot} , such that $\text{Re}(\delta_{tot})$ is the oscillation frequency, and $-\text{Im}(\delta_{tot})$ is the dephasing rate. We have

$$\delta_{tot}(\omega_p, P_p) = \delta_0 + \delta_m(\omega_p, P_p) , \quad (3.17)$$

where δ_0 is due to the chosen drive-qubit detuning and to the qubit dephasing rate in the absence of the pump. Thus, we measure δ_{tot} , and the only unknown is the constant C , which we fit at each pump frequency. In fig. 3.7, we plot for each pump frequency, δ_{tot} (open circles), and the fitted values (crosses), where C is the only fitting parameter. Once we know C , the average photon number is given by

$$\bar{n}_r(\omega_p, P_p) = \left| \frac{-iA_{p,r}/2}{i(\omega_r - \omega_p) + \kappa_r/2} \right|^2 = CP_p \frac{\kappa_r^2/4}{(\omega_r - \omega_p)^2 + \kappa_r^2/4} , \quad (3.18)$$

where ω_r is the measured resonance frequency which itself depends on ω_p and P_p . We use Eq. (3.18) to calculate all the given values of \bar{n}_r , and for the y-axis of fig. 3.4b.

3.3.3 Multi-photon qubit drive

In the main paper, we show that at large pump powers, when the resonator frequency jumps, the transmon is in a highly excited state. We observe the decay of the transmon to its ground state (fig. 3.5b), and verify that the measured resonances coincide with the resonator frequency when the transmon is prepared in excited state $|e_k\rangle$ (fig. 3.5a). In order to drive the transmon from its ground state into state $|e_k\rangle$, we apply a strong pulse at frequency ω_{0k}/k where

$$\omega_{0k} = \frac{E_k - E_0}{\hbar} . \quad (3.19)$$

E_k is the eigenenergy of eigenstate $|e_k\rangle$, and E_0 is the eigenenergy of the ground state $|g\rangle$. This induces a k -photon transition between $|g\rangle$ and $|e_k\rangle$, as schematically represented in fig. 3.8b. This k -photon transition is then used to perform all standard qubit experiments, such as Rabi oscillations between $|g\rangle$ and $|e_k\rangle$, T_2 Ramsey and T_1 measurements. We verify that this is indeed a k -photon transition by performing a Ramsey measurement: two $\pi/2$ rotations with a drive at frequency ω_d slightly detuned from ω_{0k}/k , separated by a varying time, and followed by the measurement of σ_z . We obtain the oscillation frequency of the Ramsey fringes by taking the Fourier transform of the measurement (fig. 3.8). If we detune the drive frequency by δ : $\omega_d = \omega_{0k}/k - \delta$, then $k\omega_d$ is detuned from the resonance ω_{0k} by $k\delta$. We perform a first Ramsey experiment

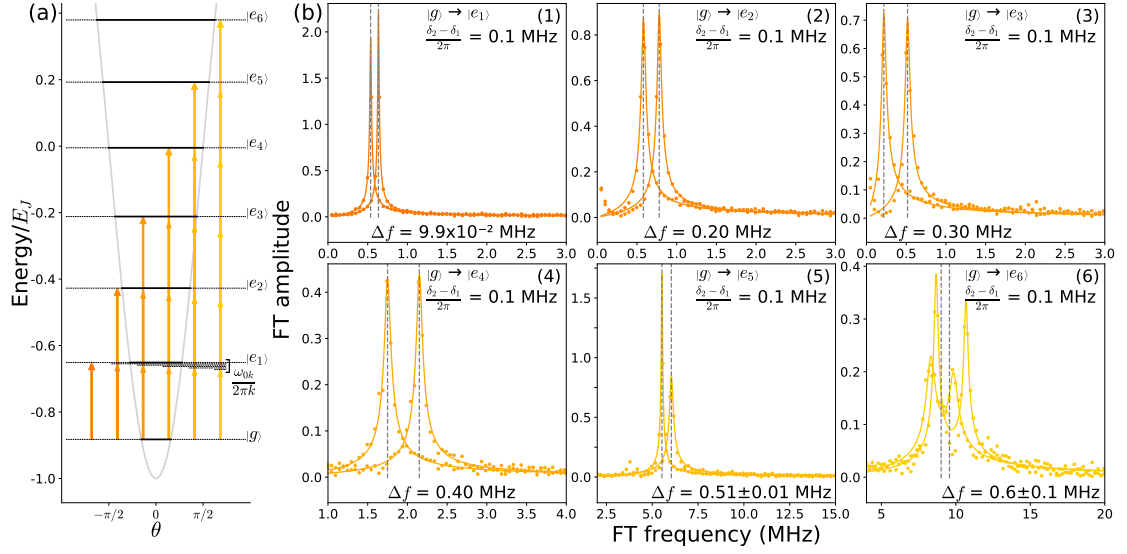


FIGURE 3.8: Characterization of k -photon transitions. (a) Bottom of the cosine potential well of the transmon (grey line) in units of E_J (y-axis), as a function of the phase across the junction (x-axis). The ground state $|g\rangle$ and the first six excited states $|e_{k=1\dots 6}\rangle$ are represented (black horizontal lines). Each excited state $|e_k\rangle$ is prepared with a k -photon transition (arrows) with a drive at $\omega_d = \omega_{0k}/k$ (see text). (b1)-(b6) Fourier transform (FT) of a Ramsey signal (dots) for two different drive detunings δ_1 and $\delta_2 = \delta_1 + 2\pi \times 0.1$ MHz. The data is fitted (line) by the Fourier transform of an exponentially decaying cosine function (a sum of two cosines is needed for (b6)), which provides the detuning between the k -photon drive with effective frequency $k\omega_d$ and the transition frequency ω_{0k} . We verify that the difference between these detunings Δ_f scales as $k(\delta_2 - \delta_1)/2\pi$, as expected for a k -photon transition. Unlike (b1)-(b5), in (b6) we observe two peaks for each curve. This shows that the Ramsey signal has two frequency components, which is a consequence of quasi-particles tunneling across the junction (see text and fig.3.9).

with a drive detuned by δ_1 , which serves as a reference. A second Ramsey experiment is performed with a detuning $\delta_2 = \delta_1 + 2\pi \times 0.1$ MHz. By subtracting the frequencies of the Ramsey fringes, denoted Δ_f , we get $\Delta_f = k(\delta_2 - \delta_1)/2\pi$, as shown in fig. 3.8b1-b6.

3.3.4 Charge noise

Observing fig. 3.8b, we see that the Ramsey signal is not composed of a single frequency. This is reminiscent of charge noise, where a single quasiparticle is tunneling across the junction in and out of the superconducting island, thus changing its charge parity. This parity change corresponds to changes between N_g and $N_g \pm 1/2$, which occur on the millisecond timescale [88]. Our Ramsey measurements take 16 seconds, hence our data shows the average of these charge offset configurations. Note that despite the fact that we are deep in the transmon regime: $E_J/E_C = 140$, the higher energy levels disperse with charge offset.

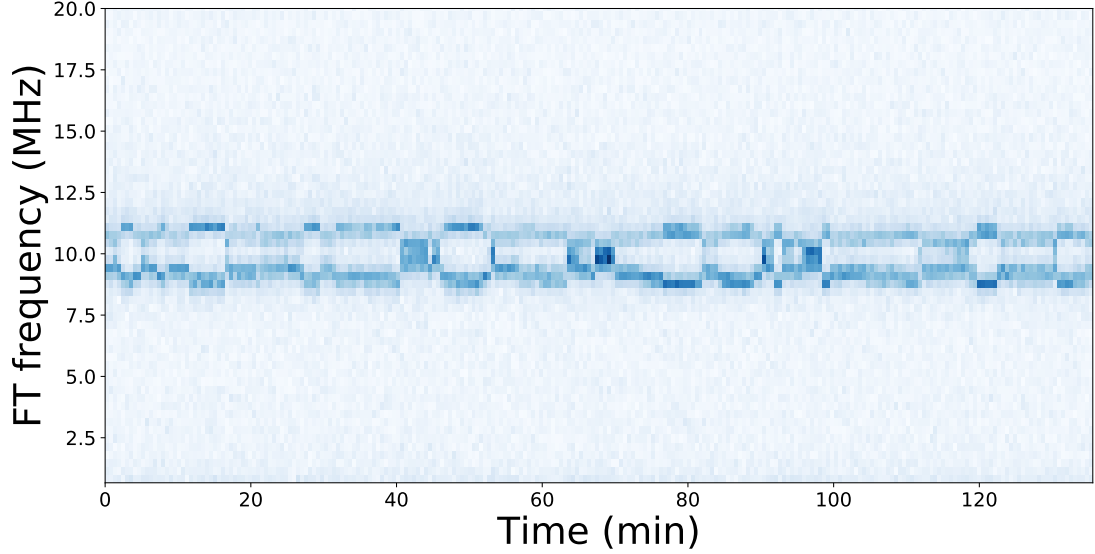


FIGURE 3.9: Fourier transform (FT) of the Ramsey signal of the $|g\rangle$ to $|e_6\rangle$ transition, measured repeatedly every 32 seconds over a period of about 2 hours. Due to quasiparticle tunneling, two frequencies appear in each Ramsey signal. These frequencies drift over a timescale of several minutes due to background charge motion [88].

We confirm this effect by plotting the Fourier transform of the Ramsey signal for the $|g\rangle$ to $|e_6\rangle$ transition vs. time (fig. 3.9). We see the slow symmetric drift of the two frequencies, due to the background charge motion [88].

The following energy level ($|e_7\rangle$ and above) fluctuate much more than $|e_6\rangle$ with charge offsets, and this is why we could not prepare the transmon in states above $|e_6\rangle$.

3.3.5 Numerical simulation

In this section, we describe the numerical simulation of fig. 3.3c. The details of this simulation can be found in [34], and for completeness, we explain the main principles here. We denote $\rho(t)$ the density operator of the transmon-resonator system. This system's dynamics are driven by the time dependent Hamiltonian $\mathbf{H}(t)$ of Eq. (3.10), and by a coupling to a bath through an operator \mathbf{X} . Typically, $\mathbf{X} = \mathbf{a} + \mathbf{a}^\dagger$, and the bath is a transmission line. For simplicity, we neglect the direct coupling of the transmon to the bath, but this can easily be included in the theory by changing \mathbf{X} . We recall that $\mathbf{H}(t)$ is periodic with period $T_p = 2\pi/\omega_p$, where ω_p is the pump frequency. The goal is to find $\rho(t)$ in the infinite time limit.

After a sufficiently long time, $\rho(t)$ reaches a limit-cycle: a T_p -periodic trajectory denoted $\bar{\rho}(t)$. We find this limit-cycle using Floquet-Markov theory [79]. This theory assumes a weak coupling to the bath, but can treat pumps of arbitrary amplitudes and frequencies.

Change of frame The first step is to write the Hamiltonian in a frame where the resonator is close to the vacuum state. We do this by solving the quantum Langevin equations when $E_J = 0$. We denote $\mathbf{a}_0, \mathbf{N}_0, \boldsymbol{\theta}_0$ the solutions of the Langevin equations associated to Hamiltonian (3.10) with $E_J = 0$. We find, using (C.10)

$$\begin{aligned}\frac{d}{dt}\mathbf{a}_0 &= \frac{1}{i\hbar}[\mathbf{a}_0, \mathbf{H}] = -i\omega_0\mathbf{a}_0 - ig\mathbf{N}_0 - i\mathcal{A}_p(t) \\ \frac{d}{dt}\mathbf{N}_0 &= \frac{1}{i\hbar}[\mathbf{N}_0, \mathbf{H}] = 0 \\ \frac{d}{dt}\boldsymbol{\theta}_0 &= \frac{1}{i\hbar}[\boldsymbol{\theta}_0, \mathbf{H}] = 8E_C/\hbar\mathbf{N}_0 + g(\mathbf{a}_0 + \mathbf{a}_0^\dagger),\end{aligned}\tag{3.20}$$

where $\mathcal{A}_p(t) = A_p \cos(\omega_p t)$, and $A_p \geq 0$. These equations are linear, and are therefore easy to solve. We introduce the expectation values: $\langle \mathbf{a}_0 | \mathbf{a}_0 \rangle = a_0$, $\langle \mathbf{N}_0 | \mathbf{N}_0 \rangle = N_0$, $\langle \boldsymbol{\theta}_0 | \boldsymbol{\theta}_0 \rangle = \theta_0$. Using some approximations [34], we find

$$\begin{aligned}a_0(t) &= \frac{A_p/2}{(\omega_p - \omega_a)} e^{-i\omega_p t} \\ N_0(t) &= 0 \\ \theta_0(t) &= g \frac{A_p}{\omega_p(\omega_p - \omega_a)} \sin(\omega_p t).\end{aligned}\tag{3.21}$$

We define

$$\bar{n} = \left| \frac{A_p/2}{\omega_p - \omega_a} \right|^2.\tag{3.22}$$

For simplicity we assume $\omega_p > \omega_a$. If $\omega_p < \omega_a$ then one needs to multiply the following solutions by -1 . We get

$$\begin{aligned}a_0(t) &= \sqrt{\bar{n}} e^{-i\omega_p t} \\ N_0(t) &= 0 \\ \theta_0(t) &= 2 \frac{g}{\omega_p} \sqrt{\bar{n}} \sin(\omega_p t).\end{aligned}\tag{3.23}$$

Comparing Eq. (3.22), and Eq. (3.18), we see that the expressions of \bar{n} and \bar{n}_r are very similar, and differ only by the presence of subscripts r , and the term in κ_r in Eq. (3.18). In the limit of large detunings: $|\omega_r - \omega_p| \gg \kappa_r$, and hence the term in κ_r can be neglected. The pump amplitude $A_{p,r}$ slightly differs from A_p due to the transmon-resonator mode hybridization. For our experimental parameters, $A_{p,r}$ and A_p differ by less than 1%. The measured resonator frequency ω_r roughly varies between $\bar{\omega}_r$ and ω_a , spanning about 20 MHz. For the simulation of fig. 3.3b, we consider a pump at frequency $\omega_p/2\pi = 8.1$ GHz, which is detuned from the resonator by about 340 MHz. This detuning is much larger than the frequency variation of ω_r . Hence \bar{n} and \bar{n}_r differ

by less than 15%.

We now move to a frame around the solutions given in Eq. (3.23), introducing $\tilde{\theta} = \theta - \theta_0$, $\tilde{N} = N - N_0$ and $\tilde{a} = a - a_0$. This frame is chosen such that the deviation of the resonator from the vacuum is small, and hence we can use a low truncation for the resonator mode. This change of frame leads to the following Hamiltonian [34]

$$\tilde{H} = 4E_C \tilde{N}^2 - E_J \cos(\tilde{\theta} + \theta_0(t)) \quad (3.24)$$

$$\begin{aligned} & + \hbar\omega_a \tilde{a}^\dagger \tilde{a} + \hbar g \tilde{N} (\tilde{a} + \tilde{a}^\dagger) \\ & = 4E_C \tilde{N}^2 - E_J \left(\cos(\tilde{\theta}) \cos(\theta_0(t)) - \sin(\tilde{\theta}) \sin(\theta_0(t)) \right) \\ & + \hbar\omega_a \tilde{a}^\dagger \tilde{a} + \hbar g \tilde{N} (\tilde{a} + \tilde{a}^\dagger) \end{aligned} \quad (3.25)$$

We write \tilde{H} as a matrix in the basis spanned by $|T_k\rangle \otimes |F_l\rangle$, where $|T_k\rangle$ are eigenstates of the transmon Hamiltonian $4E_C \tilde{N}^2 - E_J \cos(\tilde{\theta})$, and $|F_l\rangle$ are Fock states: eigenstates of the resonator Hamiltonian $\hbar\omega_a \tilde{a}^\dagger \tilde{a}$. We truncate this basis to $M = 450$ states, with 45 states for the transmon and 10 states for the resonator.

Floquet analysis Using functions provided by the Quantum Toolbox in Python (Qutip), we compute the Floquet states of $\tilde{H}(t)$, which we denote $|\psi_\alpha(t)\rangle$ for $\alpha = 1, \dots, M$. We can then calculate the dissipation operator \mathbf{X} matrix elements in the Floquet basis $|\psi_\alpha\rangle$ [79, p. 245].

With these matrix elements, we can now calculate the master equation followed by the density matrix [79, p. 251] and compute its steady state in the Floquet basis: $\bar{\rho}(t) = \sum_\alpha \rho_{\alpha\alpha} |\psi_\alpha(t)\rangle \langle \psi_\alpha(t)|$. We recall that $\bar{\rho}(t)$ is T_p -periodic and we define $\bar{\rho}_0 = \bar{\rho}(0)$. We can express $\bar{\rho}_0$ in the basis $\{|T_k\rangle \otimes |F_l\rangle\}_{k,l}$, and calculate the partial trace with respect to the cavity $\bar{\rho}_{0q} = \text{Tr}_{\text{cav}}(\bar{\rho}_0) = \sum_l \langle F_l | \bar{\rho}_0 | F_l \rangle$. The diagonal of $\bar{\rho}_{0q}$: $\text{diag}(\bar{\rho}_{0q})$ is the list of the transmon eigenstate populations. Note that at times $t_m = 0 + mT_p$, $\theta_0(t_m) = 0$, hence the unitary which transforms states between the displaced frame back to the original one is the identity for the transmon degree of freedom. In fig. 3.3c, we plot $\text{diag}(\bar{\rho}_{0q})$ as a function of \bar{n} , where \bar{n} given in Eq. (3.22).

3.3.6 Quasiparticle generation

In section 3.2.3, we discuss whether the strong pump we apply on the system generates quasiparticles. If the pump significantly increases the quasiparticle density, the transmon T_1 will decrease [83, 84]. In fig. 3.10a, we reproduce the experiment of fig. 3.5b for various pump powers, which correspond to various numbers of photons \bar{n}_r . For small \bar{n}_r , the transmon is not excited, while for large \bar{n}_r , the transmon is driven to highly excited

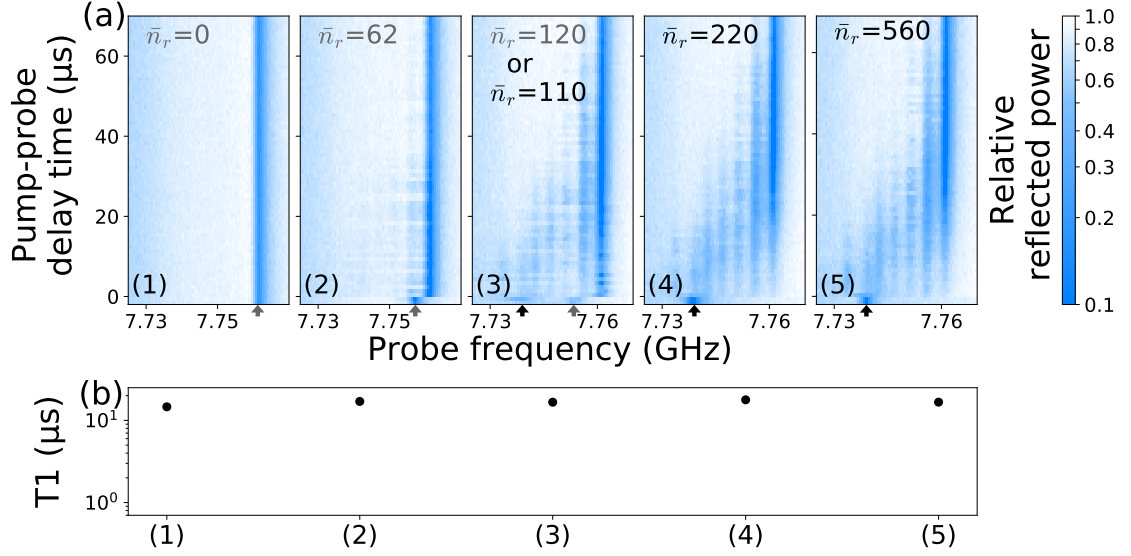


FIGURE 3.10: Transmon relaxation following a pump pulse of increasing power. (a) Same experiment as in fig. 3.5b for increasing pump power from a1 to a5, a5 corresponding to the maximum power the microwave source could deliver. (a1-a2) The pump induces an AC Stark shift proportional to \bar{n}_r at $t < 0$ but does not significantly excite the transmon. (a3) At intermediate pump powers, the system is in a statistical mixture of two configurations, as indicated by the two dips at $t < 0$. One corresponds to the AC Stark shifted cavity, the other to the bare cavity frequency ω indicating that the transmon gets highly excited. (a4-a5) At higher pump powers, the cavity frequency always jumps to ω and the transmon decays as in fig. 3.5b. (b) Transmon T_1 (y-axis) measured 50 μs after a pump is applied. The pump duration and powers (x-axis) correspond to the ones used for the experiments shown in (a). T_1 does not decrease as the pump power increases which indicates that the pump does not generate a measurable increase in the quasiparticle density [83, 84].

states. Additionally, after each pump pulse, we measure the transmon T_1 after a time delay chosen so that all modes have decayed back to their ground state. We find no decrease in T_1 (fig. 3.10b) which means that the pump can expel the transmon out of its potential well without producing a measurable amount of quasiparticles.

Chapter 4

Exponential bit-flip suppression in a cat-qubit

4.1	Protecting quantum information in a resonator	52
4.1.1	General considerations	53
4.1.2	The bosonic codes	57
4.2	Exponential bit-flip suppression in a cat-qubit	61
4.2.1	The dissipative cat-qubits	63
4.2.2	Engineering two-photon coupling to a bath	64
4.2.3	Coherence time measurements	67
4.3	Additional Material	69
4.3.1	Full device and wiring	69
4.3.2	Hamiltonian derivation	70
4.3.3	Circuit parameters	73
4.3.4	Semi-classical analysis	74
4.3.5	Bit-flip time simulation	79
4.3.6	Tuning the cat-qubit	81

Schrödinger cat states are quantum superpositions of two classical-like states. These states have been vastly studied theoretically [89] and experimentally [1, 90] to understand the nature of decoherence. Decoherence is a quantum dynamics during which the system gets entangled with the environment that progressively erases the information on the phase of a quantum superposition. In the language of quantum information processing, if the two classical states are labelled $|0\rangle$ and $|1\rangle$, decoherence is associated with phase-flips. On the contrary, bit-flips bear a clear classical analogue: the random switch between two classical states. For example, a coherent state $|\alpha\rangle$ that is a classical-like state of a resonator is subject to shifts of its amplitude or phase. Hence, bit-flips should be suppressed by stabilizing the two classical states $|0\rangle$ and $|1\rangle$. As we mentioned in introduction, stabilisation is fundamentally related to dissipation, yet, luckily, dissipation is not necessarily synonym of decoherence. In particular, early works [91–93] realised that it is possible to stabilise two coherent states of a resonator with opposite phases $|\alpha\rangle$ and $|\alpha\rangle$ without affecting the quantum superposition of the two by engineering the dissipation of the resonator. This process, known as two-photon driven dissipation, was later used to propose a qubit encoded in a resonator that is robust against bit-flips, the so-called cat-qubit paradigm [11]. In fact, more generally, quantum error correction is about finding ingenious ways to dissipate the entropy of the quantum register that rises due to the interactions with the environment in the same manner as a classical computer requires cooling to maintain a sufficiently low noise level to operate without errors [94]. The appealing feature of the cat-qubit paradigm is that part of this dissipation, the one that is used to protect against bit-flips, is autonomous which means that it requires neither measurement nor feedback from the operator which simplifies drastically the experimental endeavour.

This chapter is about an experimental realisation of this two-photon dissipation that was compatible with the observation of the bit-flip rate decrease and that did not affect significantly the phase-flip rate. We start by taking a second look at the cat-qubit paradigm from the point of view of quantum error correction. Then, we present the experiment and the results.

4.1 Protecting quantum information in a resonator

The goal of this section is to illustrate how error correction is able to fight against errors in general to better understand the strategy of the cat-qubit encoding. To do so, we first start by briefly reviewing the theoretical framework that is convenient to describe errors in quantum mechanics and understand what are the conditions for an error to be correctable. The Shor code is used to illustrate these principles before moving on to the

bosonic codes. These codes [11, 95, 96] ingeniously use the infinite dimensional Hilbert space of a resonator to encode quantum information.

4.1.1 General considerations

Quantum error correction works by encoding QI into two states $|0\rangle_L$ and $|1\rangle_L$ that are called logical i.e. that are robust against a set of errors. They are robust in the sense that for the most likely errors, there exists a syndrome that identifies which error occurred and a recovery operation that undoes the error. A convenient way to characterize errors is to use the Kraus representation with which the Knill-Laflamme condition [97, 98], a central criteria of quantum error correction codes, is stated.

Kraus representation In the Kraus representation, the general evolution of a quantum system is given by [1, 99]

$$\rho(t + \Delta t) = \sum_i \mathbf{K}_i \rho(t) \mathbf{K}_i^\dagger \quad (4.1)$$

where the Kraus operators \mathbf{K}_i have to satisfy $\sum_i \mathbf{K}_i^\dagger \mathbf{K}_i = \mathbf{I}$ for the evolution to preserve the trace. For a n -dimension Hilbert space, there are at most n^2 different Kraus operators. In the following, what we call errors are precisely these Kraus operators ¹. The probability for a given error i to happen is simply $\text{Tr}(\mathbf{K}_i \rho \mathbf{K}_i^\dagger)$ or $\langle \psi | \mathbf{K}_i^\dagger \mathbf{K}_i | \psi \rangle$ if the system starts in a pure state.

For example, the Kraus operators of a two-level system, subject to bit-flips only, are

$$\begin{aligned} \mathbf{K}_0 &= \sqrt{1 - p_x} \mathbf{I} \\ \mathbf{K}_x &= \sqrt{p_x} \mathbf{X} \end{aligned} \quad (4.2)$$

where p_x is the probability for a bit-flip to happen during the time interval Δt associated with a bit-flip rate $\kappa_x = p_x / \Delta t$. The time interval is chosen so that $\kappa_x \Delta t \ll 1$. The Kraus operators set for a register constituted of 3 of these qubits is given in table tab. 4.1 assuming no correlated errors arise. Looking at this table, after a time Δt there is a small probability $p_x^2(1 - p_x)$ that two consecutive errors occurred. However, this should not be confused with correlated errors even though they result in the same form of Kraus operator. The difference lies in the prefactor scaling with Δt . Let us say that 2-bit-flip errors happen with a rate κ_{xx} . In the uncorrelated case, the 2-error probability is given by $(\kappa_x \Delta t)^2$ at leading order. In the correlated case, it goes as $\kappa_{xx} \Delta t$ at leading

¹Usually, there is one Kraus operator which is close to identity. Calling it an error is a debatable question but quite often this Kraus operator still distort the logical states.

Prefactors	$\sqrt{1-p_x}^3$	$\sqrt{p_x}(1-p_x)$	$p_x\sqrt{1-p_x}$	$\sqrt{p_x}^3$
Operators	<i>III</i>	<i>IIX</i>	<i>IXX</i>	
		<i>IXI</i>	<i>XIX</i>	<i>XXX</i>
		<i>XII</i>	<i>XXI</i>	

TABLE 4.1: **Kraus operators set of a 3-qubit register subject to bit-flips only.** The prefactors are given assuming no-correlated errors arise so that the probability of several bit-flips occurring decreases rapidly. The correctable errors are coloured in green, the uncorrectable ones in red.

order. Hence, measuring faster improves drastically uncorrelated errors in comparison with correlated ones.

Knill-Laflamme condition Let us define \mathcal{E} , the set of Kraus operators that governs the evolution of a quantum system for a time Δt . A subset \mathcal{E}_c of these operators is correctable provided the two basis states $|0\rangle_L$ and $|1\rangle_L$ satisfy

$$\forall \{\sigma, \sigma'\} \in \{0, 1\}^2, \{\mathbf{K}_i, \mathbf{K}_j\} \in \mathcal{E}_c^2, \quad {}_L\langle \sigma' | \mathbf{K}_j^\dagger \mathbf{K}_i | \sigma \rangle_L = \alpha_{ij} \delta_{\sigma\sigma'} \quad (4.3)$$

with α an Hermitian and positive semidefinite matrix. In short, this condition summarizes that:

- the errors should send $|0\rangle_L$ and $|1\rangle_L$ to orthogonal subspaces as represented by the zeros of $\delta_{\sigma\sigma'}$. This is required for the errors to be distinguishable and the recovery operation possible.
- the errors probability¹ should be independent of the logical state, that is α independent of σ, σ' . This is for ensuring the environment does not get information about the protected state and project it. Indeed, let us say an error is more likely to happen when the system is in $|1\rangle_L$ than in $|0\rangle_L$. If this error occurs, beforehand the state was more probably in $|1\rangle_L$ which gives information about the current state of the system [99].

Below, we focus on how to satisfy the first condition but we keep in mind the rest should also apply for a valid encoding.

Local errors A quantum system undergoes errors described by Kraus operators. An adequate choice for a basis spanning the system Hilbert space is one where these operators act *locally*: they map one basis state to a few of its neighbours. For example, the natural basis for a 3-qubit register is $\{|000\rangle, |001\rangle, \dots, |111\rangle\}$ (fig. 4.1a) that we also call direct space. Indeed, in this space, a bit-flip acting on a single qubit is a unit translation

¹Strictly speaking the off-diagonal elements do not represent probabilities. Still, the Kraus operators are defined up to a unitary transformation which can be chosen to make α diagonal.

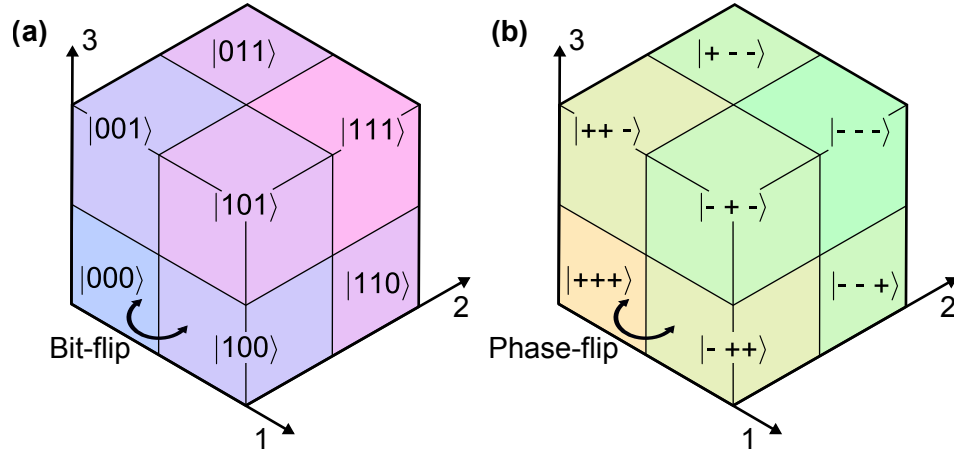


FIGURE 4.1: **Encoding space of the 3-qubit repetition code** (a) The state space of a 3-qubit register is represented in 3D. Each dimension represents the Hilbert space of a qubit (the labels indicating which qubit) so that each cube is a possible state. A bit-flip on one qubit acts as a unit translation along one of the axis, and hence is a local operator. States $|000\rangle$ and $|111\rangle$ are far apart (the colour gradient represents the increasing distance from $|000\rangle$), therefore they are a robust encoding against bit-flips. (b) The reciprocal space is represented. A phase-flip on one qubit acts as a unit translation along one of the axis, and hence is a local operation. States $|000\rangle$ and $|111\rangle$ are completely delocalized over this space. States $|000\rangle + |111\rangle$ and $|000\rangle - |111\rangle$ have disjoint supports but are interlocked so that a single phase-flip connects them. Hence, this encoding is not robust against phase-flips.

and hence is dubbed a local error. The register is also subject to single qubit phase-flips that are local in the reciprocal space spanned by $\{|+++ \rangle, |++- \rangle, \dots, |-- - \rangle\}$ (fig. 4.1b) since they are unit translations in this space. Quite interestingly, on a native system most error channels seem to be either local in direct space or in reciprocal space. In the next paragraph, we will comment on this assumption but before, we figure out good encoding practice within this assumption.

Let us consider the 3-qubit register that is only subject to bit-flips and find a good encoding. In the appropriate space i.e. the 3-dimensional cube in fig. 4.1a in which bit-flips are local errors, the logical states are chosen to have *disjoint* support and to be *far apart*. They consist of the two opposite corners of the cube

$$|0\rangle_L = |000\rangle \quad \text{and} \quad |1\rangle_L = |111\rangle. \quad (4.4)$$

This way, it takes multiple local errors to go from one to the other and we have a chance to correct before too many happen. By increasing the number of qubits, the distance between the logical states $|00\dots 0\rangle$ and $|11\dots 1\rangle$ is made bigger, and the code even more robust.

By definition, as superposition states, $|+\rangle_L$ and $|-\rangle_L$ have the same support in direct space. In reciprocal space, they have disjoint support

$$|+\rangle_L = \frac{|000\rangle + |111\rangle}{\sqrt{2}} = \frac{1}{2} \left(|+++ \rangle + |+- - \rangle + |-+ - \rangle + |--+ \rangle \right) \quad (4.5)$$

$$|-\rangle_L = \frac{|000\rangle - |111\rangle}{\sqrt{2}} = \frac{1}{2} \left(|++- \rangle + |+ - + \rangle + |-+ + \rangle + |-- - \rangle \right) \quad (4.6)$$

but they are not far apart as they differ by a single phase-flip. Hence, this code is no longer robust if we add phase-flips to the error model. The question is: how to make $|0\rangle_L$ and $|1\rangle_L$ distant in direct space and $|+\rangle_L$ and $|-\rangle_L$ distant in reciprocal space?

The idea is to concatenate two codes, one local in direct space, the other local in reciprocal space as follows. Let us start with a good logical basis in reciprocal space that is $|+\rangle_L = |+++ \rangle$ and $|-\rangle_L = |-- - \rangle$ for they are far apart, see fig. 4.1b. As we saw earlier, the resulting states $|0\rangle_L$ and $|1\rangle_L$ are close in the direct space fig. 4.1a unless each qubit that they consist of are replaced by the logical ones that we defined in (4.4) for these are distant in direct space. Eventually, using 9 qubits, the states

$$|+\rangle_L = \frac{|000\rangle + |111\rangle}{\sqrt{2}} \otimes \frac{|000\rangle + |111\rangle}{\sqrt{2}} \otimes \frac{|000\rangle + |111\rangle}{\sqrt{2}} \quad (4.7)$$

$$|-\rangle_L = \frac{|000\rangle - |111\rangle}{\sqrt{2}} \otimes \frac{|000\rangle - |111\rangle}{\sqrt{2}} \otimes \frac{|000\rangle - |111\rangle}{\sqrt{2}} \quad (4.8)$$

are distant in reciprocal space $\{|+\rangle, |-\rangle\}^{\otimes 9}$ and the resulting $|0\rangle_L$ and $|1\rangle_L$ are distant in direct space $\{|0\rangle, |1\rangle\}^{\otimes 9}$. This encoding is precisely the one proposed by Shor [4] up to a change of notation for the logical states. By increasing the number of qubits used for encoding, it can be made robust against a given number of bit-flips and phase-flips. The key idea is that quantum error correction protects quantum information from local errors by dispatching it in distant locations of space.

Non-Local errors There are three main sources of non-local errors that we order by criticality.

Consecutive local errors In our 3-qubit register, even when uncorrelated bit-flips are the only errors channels, 2-bit-flip and 3-bit-flip errors arise in the set of Kraus operator that describes the evolution after a time interval Δt , see tab. 4.1. These errors are less local since they bring the system in a further location in direct space and eventually, they lead to a logical error. However, there exists two solutions to mitigate them. First, by increasing the space size, some consecutive errors can become local enough to be correctable. Second, by measuring more frequently, their probability decreases fast. This leads to the notion of approximate quantum error correction [100].

Correction induced non local errors Performing quantum error correction consist in measuring non-local operators in order not to disrupt quantum information (that is encoded non-locally) and only get information on the local errors that are induced by the environment [101]. In the 3-qubit code against bit-flips, these operators were $Z_1 Z_2$ and $Z_2 Z_3$. One can either come up with elaborate schemes to directly measure these observables or add ancillary quantum systems on which these observables are mapped via specific interactions. In any case, it is not straightforward to make sure that measuring these non-local observables do not induce non-local errors. In other words, if one has access to non-local observables, so may the environment. Hence, the assumption that the environment only impinges local error may break down. In our example, a phase-flip acting on the ancillary qubit that measures $Z_1 Z_2$ leads to a phase-flip on qubits 1 and 2. This leads to the notion of fault-tolerance [102].

Direct non local errors The environment may also directly non-locally disrupt the qubit register. For example, a high energy particle impinging on the substrate of the chip may affect many qubits at a time. However, QEC assumes these errors happen rarely and depending on the noise model of these non-local errors, QEC may still be possible [94]. Correlated noise may also arise from unforeseen phenomena [103] to which delocalized quantum information would be sensitive. Probing these phenomena would be a beautiful application of quantum information science.

4.1.2 The bosonic codes

Superconducting resonators are good candidates to store quantum information. Natively, up to a good approximation, they have a single error channel, photon loss with very small rate especially in 3D-architectures [104]. These linear oscillators can store information but detecting and correcting for errors necessitates to couple them to non-linear elements. External noise on these elements eventually affects the resonator frequency leading to an additional error channel, dephasing [105, 106].

The resonator state lives in a infinite dimensional Hilbert space that is used to redundantly encode information. Since the resonator excitations are bosons, these codes are named bosonic codes. In the standard approach for QEC, redundancy is achieved by increasing the number of physical systems. However, each new system comes with its own decoherence channels and eventually increases the number of possible errors. With bosonic codes, redundancy is increased without adding decoherence channels and at the mere cost of increasing the rates of the existing ones.

Two simple pairs of conjugate variables can be used to describe the Hilbert space of a resonator:

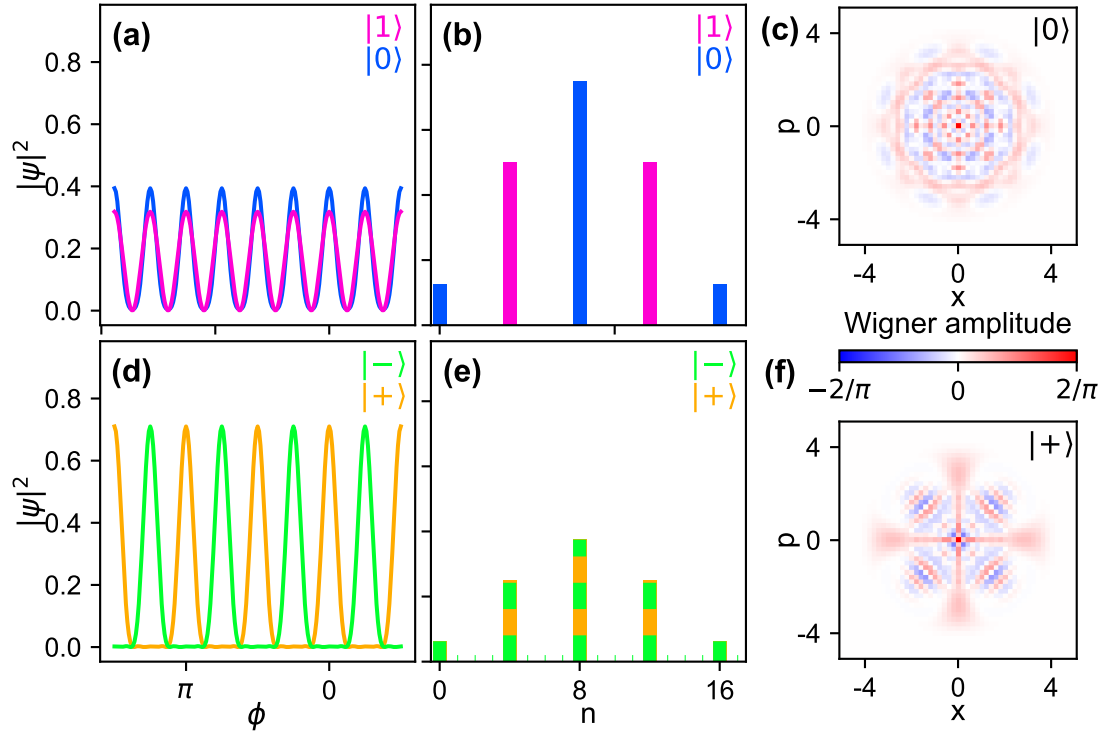


FIGURE 4.2: **Binomial code for $N=S=3$.** The basis states have an average photon number $\bar{n}=8$. **(a,b,d,e)** The probability densities of the states $|0\rangle$, $|1\rangle$, $|+\rangle$ and $|-\rangle$ are represented in the $|\phi\rangle$ - and $|n\rangle$ -spaces. **(a,b)** The states $|0\rangle$ and $|1\rangle$ are designed to have distant supports in $|n\rangle$ -space to protect against photon losses that are local in this space and would lead to bit-flips. **(d,e)** Since the support of states $|+\rangle$ and $|-\rangle$ are almost disjoint in $|\phi\rangle$ -space, small dephasing events can be approximately corrected hence mitigating phase-flips. **(c,f)** Wigner representation [1] of the $|0\rangle$ and $|+\rangle$ states. Wigner representation is a more familiar way of visualising the state of a resonator.

- the Fock space, $\{|n\rangle, n \in \mathbb{N}\}$ that is spanned by the eigenstates of the photon number operator and its reciprocal space $\{|\phi\rangle, \phi \in [0, 2\pi]\}$ that is spanned by the phase operator eigenvectors.
- the position space, $\{|x\rangle, x \in \mathbb{R}\}$ that is spanned by the eigenstates of the position operator and its reciprocal space $\{|p\rangle, p \in \mathbb{R}\}$ that is spanned by the eigenstates of the momentum operator.

These four spaces are referred to as $|n\rangle$ -, $|\phi\rangle$ -, $|x\rangle$ - and $|p\rangle$ -space respectively.

Hereafter, we present the strategies of the different bosonic codes and focus on the binomial codes [96], the GKP code [95, 107] and the cat-code [11, 108]. We do not go into detail, as the advantages and drawbacks of each encoding are analysed in depth in each article, but merely provide an illustration of their non-locality regarding the error model.

Binomial codes The main error channel of a resonator is photon loss with operator \mathbf{a} that is local in Fock space since it maps Fock state $|n+1\rangle$ to $|n\rangle$. Hence, one adequate

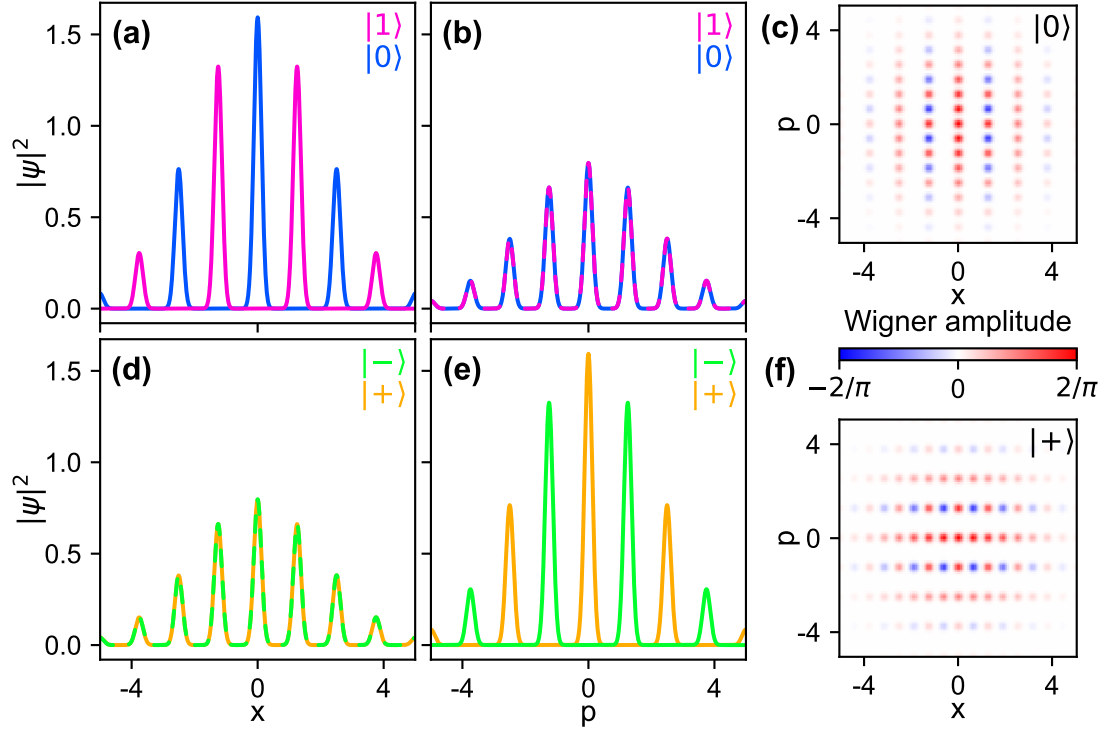


FIGURE 4.3: **Symmetric approximate GKP code for $\sigma=0.17$.** The basis states have an average photon number $\bar{n}=8$. **(a,b,d,e)** The probability densities of the basis states $|0\rangle$, $|1\rangle$, $|+\rangle$ and $|-\rangle$ are represented in the $|x\rangle$ - and $|p\rangle$ -spaces. **(a,b)** The states $|0\rangle$ and $|1\rangle$ are designed to have disjoint supports in $|x\rangle$ -space to protect against small translations that would lead to bit-flips. **(d,e)** The states $|+\rangle$ and $|-\rangle$ are designed to have disjoint supports in $|p\rangle$ -space to protect against small translations that would lead to phase-flips. **(c,f)** Wigner representation of the $|0\rangle$ and $|+\rangle$ states. This representation emphasizes the grid nature of the GKP states.

choice to encode information non-locally while satisfying the Knill-Laflamme condition is [96]

$$|0/1\rangle = \frac{1}{\sqrt{2^N}} \sum_{\substack{p \text{ even/odd} \\ p \in [0, N+1]}} \sqrt{\binom{N+1}{p}} |p(S+1)\rangle \quad (4.9)$$

expressed in the Fock basis, where S and N are two positive integer parameters. Indeed, as illustrated in fig. 4.2b the basis states have distant supports in the $|n\rangle$ -basis. The distance being $S+1$, the robustness to photon loss (or gain) increases with S . The dephasing error channel acts as a diffusion in $|\phi\rangle$ -space. In this space, states $|+\rangle$ and $|-\rangle$ almost have disjoint supports (see fig. 4.2d) so that small dephasing events¹ can be approximately corrected. This approximation improves with the second parameter N .

¹Note that what we call a dephasing event is a small translation of distance θ in $|\phi\rangle$ -space with operator $\exp(i\theta\mathbf{n})$ and is well approximated by the standard dephasing operator \mathbf{n} for small angles.

Approximate GKP code Instead of photon loss and dephasing, the errors occurring on a resonator may be modelled as a diffusion of the state in the position and momentum spaces. The resulting displacements are local provided the time step between two corrections is small enough. Note that, by carefully expanding the photon loss and dephasing operators, the two error models can be mapped to one another [95, 107]. In the proposal by Gottesman, Kitaev and Preskill, the relevant symmetric encoding regarding this error model is [95]

$$|0/1\rangle = \sqrt{2\sigma} \sum_{\substack{s \text{ even/odd} \\ s \in \mathbb{Z}}} e^{-\frac{\pi}{2}(\sigma s)^2} \mathbf{T}(\sqrt{\pi}s) |\psi_0\rangle \quad (4.10)$$

$$|\psi_0\rangle = \frac{1}{(\pi\sigma^2)^{1/4}} \int_{-\infty}^{\infty} dx e^{-\frac{1}{2}\left(\frac{x}{\sigma}\right)^2} |x\rangle \quad (4.11)$$

where σ is a real parameter, \mathbf{T} is the translation operator along x , $|\psi_0\rangle$ is the state corresponding to a single peak. These states are plotted in fig. 4.3. By construction, they are distant in $|x\rangle$ -space and their superpositions are in $|p\rangle$ -space. Hence, this encoding is relevant for the assumed error model and the protection can be increased by reducing σ and decreasing the waiting time between two measurements.

Cat-code There exist several types of cat states encodings [11]. Here, we focus on the so-called two-legged cats that are superpositions of the coherent states $|\alpha\rangle$ and $|\alpha\rangle$. Contrary to the previous codes that aim at delocalizing information in both direct space and in reciprocal space, the strategy of the cat encoding is to relax one constraint by only delocalizing in one space. The resulting qubit is only protected against one of the two error channels but consequently the acquired protection is more efficient in terms of required photon number. The cat encoding is represented in the $|n\rangle$ - and $|\phi\rangle$ -space in fig. 4.4 and in the $|x\rangle$ - and $|p\rangle$ -space in fig. 4.5. As we will see later, we expect an exponential decrease of the bit-flip rate in $|\alpha|^2$ while only linearly increasing the phase-flip rate.

This strategy is only valid because the remaining phase-flips are correctable in a way that do not generate bit-flips [108]. Indeed, by redundantly encoding information in several cat-qubits, one can correct against phase-flips with a 1D repetition code as described earlier (fig. 4.1). This scheme requires CNOT gates that, in general, convert a phase-flip occurring during the gate into a bit-flip. However, with the cat encoding, the 2D-phase space of the resonator can be accessed to perform the CNOT gate while preserving the protection against bit-flips [108].

We did not discuss the recovery operations of these encodings which were realized experimentally in [109] for the smallest binomial code and in [110, 111] for the GKP code. The

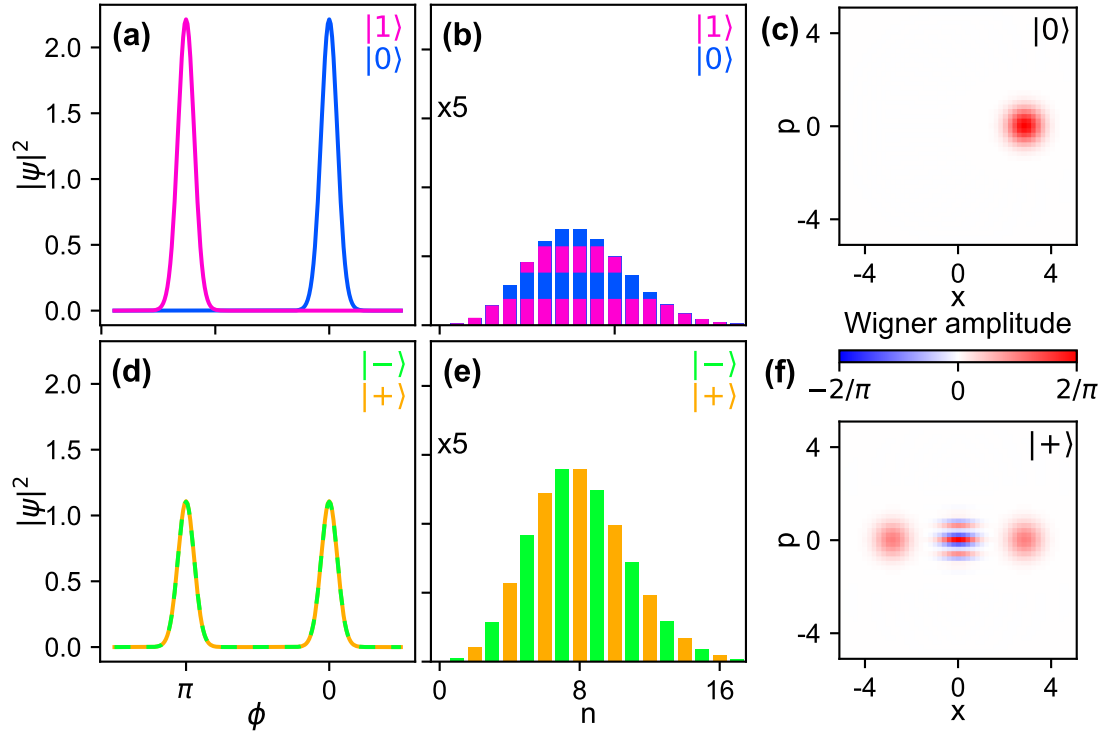


FIGURE 4.4: **Two-legged cat code for $\alpha = \sqrt{8}$.** The basis states have an average photon number $\bar{n}=8$. **(a,b,d,e)** The probability densities of the basis states $|0\rangle$, $|1\rangle$, $|+\rangle$ and $|-\rangle$ are represented in the $|\phi\rangle$ - and $|n\rangle$ -spaces. **(a,b)** The states $|0\rangle$ and $|1\rangle$ are designed to have distant supports in $|\phi\rangle$ -space to protect against dephasing events that would lead to bit-flips. **(d,e)** However, the states $|+\rangle$ and $|-\rangle$ are directly mapped to one another with the loss of a photon and hence the qubit is not protected against phase-flips. **(c,f)** Wigner representation of the $|0\rangle$ and $|+\rangle$ states.

final advantage of the cat-qubit is that there exists a simple recovery operation that is autonomous i.e. that do not require active measurement and feedback. This is to be detailed in the following section.

Aside from bosonic codes, there are many other ways to protect quantum information using more than a two-level system, such as the so-called $0-\pi$ [112–114] or $\cos(2\varphi)$ [115, 116] qubits.

4.2 Exponential bit-flip suppression in a cat-qubit ¹

Recent superconducting circuit experiments [32, 33] have demonstrated that a resonator endowed with two-photon dissipation develops a manifold of steady states spanned by two states $|0\rangle_\alpha$ and $|1\rangle_\alpha$, lying in two distinct locations of the resonator two-dimensional (2D) phase space. As we saw earlier, the combination of dissipation and non-locality

¹The following was published as “Exponential suppression of bit-flips in a qubit encoded in an oscillator”, Raphaël Lescanne, Marius Villiers, Théau Peronnin, Alain Sarlette, Matthieu Delbecq, Benjamin Huard, Takis Kontos, Mazyar Mirrahimi, Zaki Leghtas, Nature Physics (2020) [36].

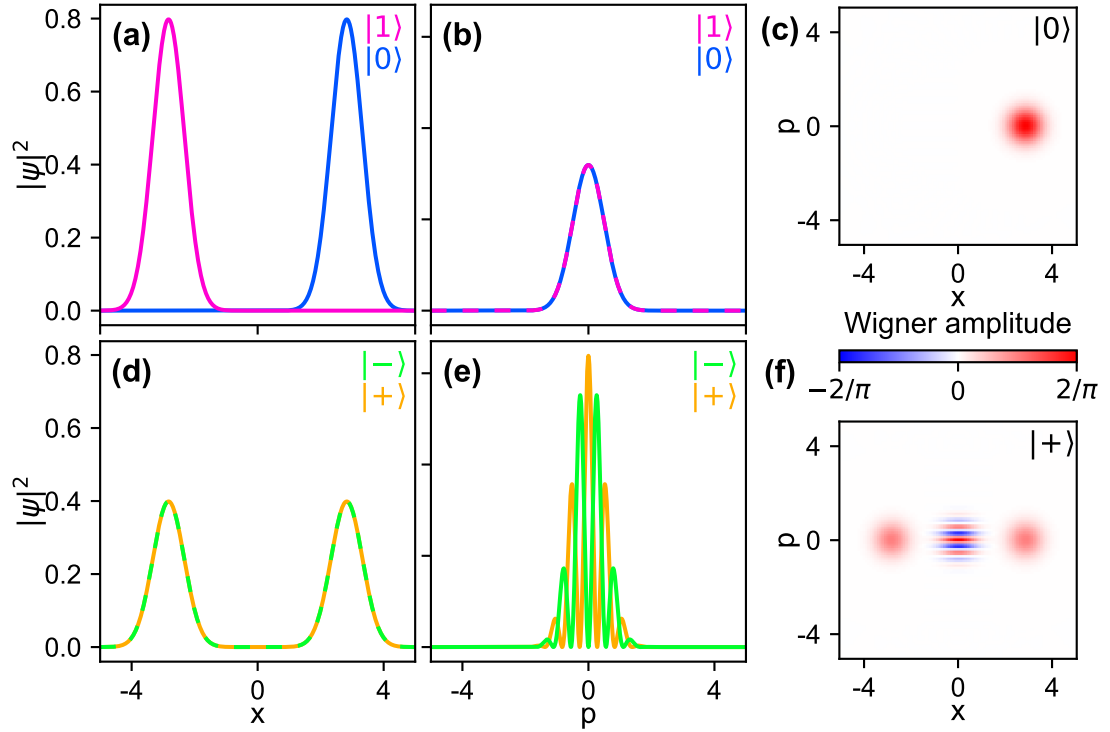


FIGURE 4.5: **Two-legged cat code for $\alpha = \sqrt{8}$.** The basis states have an average photon number $\bar{n}=8$. **(a,b,d,e)** The probability densities of the basis states $|0\rangle/|+\rangle/|-\rangle$ are represented in the $|x\rangle$ - and $|p\rangle$ -spaces. **(a,b)** The states $|0\rangle$ and $|1\rangle$ are designed to have distant supports in $|x\rangle$ -space to protect against translations along x that would lead to bit-flips. **(d,e)** However, the states $|+\rangle$ and $|-\rangle$ are close to one another in $|p\rangle$ -space and hence noise on the p quadrature leads to phase-flips. This sensitivity is used to perform Z -rotations on the cat-qubit [33]. **(c,f)** Wigner representation of the $|0\rangle$ and $|+\rangle$ states.

should prevent random swaps between $|0\rangle_\alpha$ and $|1\rangle_\alpha$ (bit-flips). However, the circuit architectures mediating the two-photon dissipation impinged errors on the resonator. These experiments fell short of crossing the demanding threshold where the correction is faster than the occurrence of all errors, including those induced by the correcting mechanism itself.

In our experiment, we measure an exponential decrease of the bit-flip rate as we increase the separation between states $|0\rangle_\alpha$ and $|1\rangle_\alpha$, while only linearly increasing the phase-flip rate (errors that scramble the phase of a superposition of $|0\rangle_\alpha$ and $|1\rangle_\alpha$). The bit-flip time reaches 1 ms, a 300-fold improvement over the energy decay time of the resonator. This was made possible by inventing a circuit which mediates a pristine non-linear coupling between the resonator and its environment, thus circumventing the problems of previous implementations [32, 33]. Our qubit combines two unique features: only phase-flips remain to be actively corrected [108], and its 2D phase space can be accessed to perform gates [11, 108, 117, 118], making it an ideal building block for scalable fault-tolerant quantum computation with a significant reduction in hardware overhead [108].

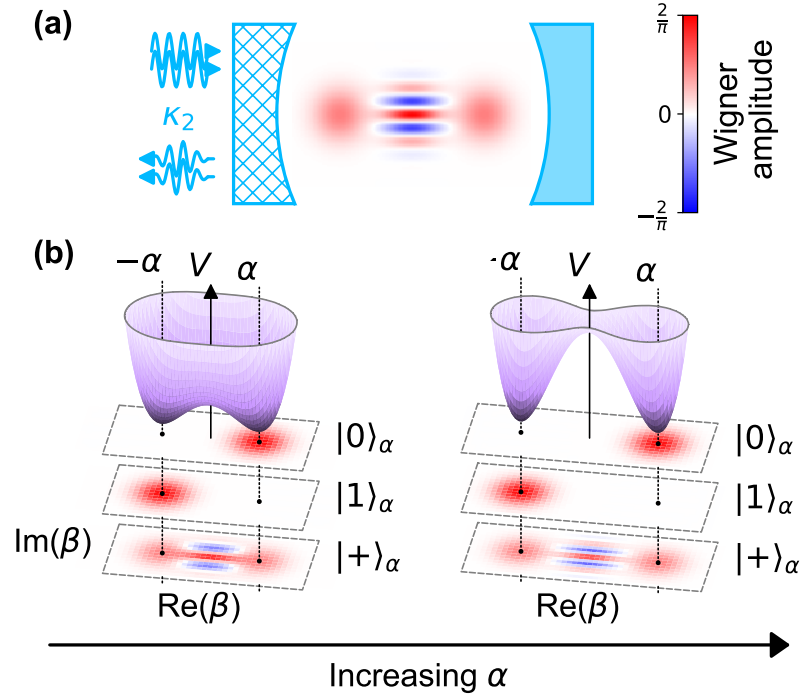


FIGURE 4.6: **The cat-qubit** (a) Quantum information is encoded in a resonator (blue mirrors) coupled to its environment through a special apparatus (hatched mirror) where pairs of photons are exchanged at rate κ_2 (double arrows). (b) This dynamics is illustrated by a pseudo-potential V (purple) defined over the resonator quadrature phase space (β plane). The cat-qubit states $|0\rangle_\alpha$ and $|1\rangle_\alpha$ lie in the minima of V and are separated in phase space as shown by their Wigner representations (stacked color plots). Bit-flip errors, which randomly swap $|0\rangle_\alpha$ and $|1\rangle_\alpha$, are exponentially suppressed by increasing this separation. Crucially, this pseudo-potential does not alter quantum superpositions of $|0\rangle_\alpha$ and $|1\rangle_\alpha$ such as the Schrödinger cat state $|+\rangle_\alpha$.

4.2.1 The dissipative cat-qubits

We follow the paradigm of cat-qubits [11, 119] where information is encoded in quantum superpositions of resonator states (see Fig. 4.6):

$$\begin{aligned} |0\rangle_\alpha &= \frac{1}{\sqrt{2}} (|+\rangle_\alpha + |-\rangle_\alpha) = |+\alpha\rangle + \mathcal{O}(e^{-2|\alpha|^2}) \\ |1\rangle_\alpha &= \frac{1}{\sqrt{2}} (|+\rangle_\alpha - |-\rangle_\alpha) = |-\alpha\rangle + \mathcal{O}(e^{-2|\alpha|^2}) \end{aligned}$$

where $|\pm\rangle_\alpha = \mathcal{N}_\pm (|\alpha\rangle \pm |-\alpha\rangle)$, $|\alpha\rangle$ is a coherent state with complex amplitude α , and $\mathcal{N}_\pm = 1/\sqrt{2(1 \pm e^{-2|\alpha|^2})}$. All these states contain an average number of photons $|\alpha|^2$. A significant source of errors in a resonator is energy decay which collapses all states ($|0\rangle_\alpha$ and $|1\rangle_\alpha$ included) towards the vacuum, thus erasing any encoded information. This decay is compensated by two-photon dissipation: a mechanism where the resonator exchanges only pairs of photons with its environment (Fig. 4.6a) [32]. This dynamics is

modelled by the following loss operator

$$\mathbf{L}_2 = \sqrt{\kappa_2} (\mathbf{a}^2 - \alpha^2), \quad (4.12)$$

where \mathbf{a} is the annihilation operator of the resonator, κ_2 is the rate at which pairs of photons are exchanged with the environment and the term in α^2 results from a drive which inserts pairs of photons [120]. The cat-qubit states $|0\rangle_\alpha$, $|1\rangle_\alpha$ and all their superpositions are steady states of this dynamics. A convenient tool to visualize the semi-classical dynamics of (4.12) is the pseudo-potential V defined over the complex plane as $-\nabla V(\beta) = \frac{d\beta}{dt}$, where β is the expectation value of \mathbf{a} at time t in a semi-classical approximation 4.3.4. Stable steady states are local minima of V (see Fig. 4.6b) and correspond to $\beta = \pm\alpha$. An error process can disrupt the stability of these states and induce transitions between them. By analogy with a particle in a double well potential, tunneling (or bit-flips) from one well to another is exponentially suppressed in the separation between the two wells (here defined as $|\alpha|^2$), as long as the error process fulfills two criteria: it has to be local and sufficiently weak. An error process is local if it transforms a state into neighboring states in phase space [95]. As an example, dominant errors such as photon loss, gain and dephasing are local. Moreover, the effective error rate κ_{err} must be weaker than the confining rate $\kappa_{\text{conf}} = 2|\alpha|^2\kappa_2$ (4.31) inherited from the confining potential V , in order for the cat-qubit states to remain localized near the potential minima. The outstanding challenge to observe an exponential increase in the bit-flip time is therefore to engineer $\kappa_{\text{conf}} > \kappa_{\text{err}}$ for all dominant local error processes.

4.2.2 Engineering two-photon coupling to a bath

Two-photon exchange between a resonator and its environment does not occur spontaneously. Instead, it is synthesized by engineering an interaction that exchanges pairs of photons of the cat-qubit resonator with one photon of an intentionally lossy mode referred to as the buffer [32] that is eventually adiabatically eliminated as detailed in section 2.2.2. The interaction Hamiltonian takes the form

$$\mathbf{H}_i/\hbar = g_2 \mathbf{a}^{\dagger 2} \mathbf{b} + g_2^* \mathbf{a}^2 \mathbf{b}^\dagger, \quad (4.13)$$

where \mathbf{b} is the annihilation operator of the buffer and g_2 is the interaction strength. Adding a resonant drive on the buffer, we recover (4.12) with $\kappa_2 \approx 4|g_2|^2/\kappa_b$ and $\alpha^2 = -\epsilon_b/g_2^*$, where ϵ_b is the drive amplitude and κ_b is the buffer energy decay rate, engineered to be larger than g_2 [32, 121]. Conveniently, the separation $|\alpha|^2$ between the cat-qubit states is readily tunable *in situ* since it is proportional to the buffer drive amplitude.

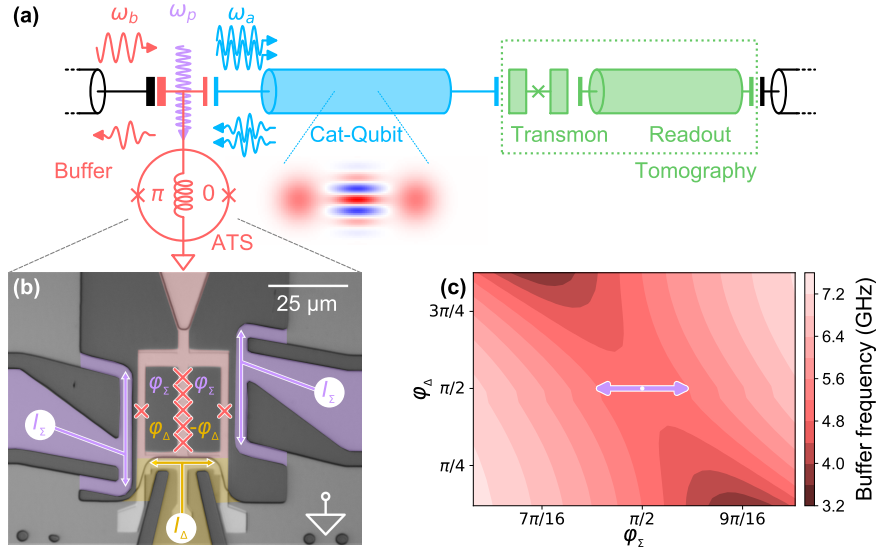


FIGURE 4.7: Circuit diagram and implementation (a) The cat-qubit resonator (blue) is coupled on one end to a transmon qubit and a readout resonator (green) to measure its Wigner function, and on the other end to the buffer (red), a lumped element resonator connected to ground through a non-linear element coined the Asymmetrically Threaded SQUID (ATS). The ATS consists of a SQUID shunted by an inductance, forming two loops. Pumping the ATS at frequency $\omega_p = 2\omega_a - \omega_b$ (purple arrow), where $\omega_{a,b}$ are the cat-qubit and buffer frequencies, mediates the exchange of two photons of the cat-qubit (blue arrows) with one photon of the buffer (red arrows) (b) False color optical image of the ATS. The shunt inductance is made of an array of 5 Josephson junctions (marked by large red crosses). The left and right flux lines (purple) are connected to the same input through an on-chip hybrid (not represented). They carry the radio-frequency pump and the DC current I_Σ , which thread both loops with flux φ_Σ . The bottom flux line (yellow) carries current I_Δ and threads each loop with flux $\pm\varphi_\Delta$. Combining these two controls, we bias the ATS at the $\pi/0$ asymmetric DC working point. (c) Measured buffer frequency (color) as a function of φ_Σ (x-axis) and φ_Δ (y-axis), around the working point $\varphi_\Sigma, \varphi_\Delta = \pi/2, \pi/2$ (white dot). As expected, for $\varphi_\Sigma = \pi/2$ (open SQUID), the buffer frequency does not depend on φ_Δ . We operate the ATS by modulating the flux along the orthogonal direction φ_Σ (purple arrow). From this measurement, we extract all the ATS parameters tab. 4.3.

We implement our cat-qubit in a circuit quantum electrodynamics architecture described in Fig 4.7a operated at 10 mK. It consists of a sputtered niobium film on a silicon substrate patterned into coplanar waveguide resonators. The cat-qubit mode resonates at $\omega_a/2\pi = 8.0381$ GHz, has a single photon lifetime $T_1 = 3.0$ μ s and is probed through a transmon qubit coupled to a readout resonator followed by a parametric amplifier [122]. At the flux operating point, the buffer mode resonates at $\omega_b/2\pi = 4.8336$ GHz and is coupled to its transmission line at a rate $\kappa_b/2\pi = 13$ MHz.

It is a technical challenge to engineer the interaction (4.13) without inducing spurious effects which are detrimental for the protection of quantum information. Examples of such effects are induced relaxation [67, 75], escape to unconfined states [35] and quasiparticle generation [83]. To mitigate these effects, the interaction (4.13) is induced by a novel non-linear dipole: the Asymmetrically Threaded SQUID (ATS, Fig 4.7b). The

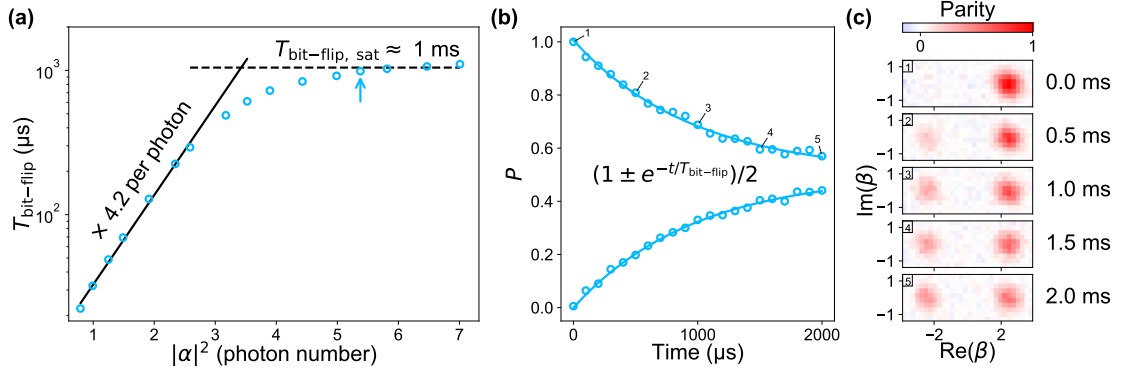


FIGURE 4.8: **Exponential increase of the bit-flip time with the cat size.** (a) The bit-flip time (y-axis) is measured (open circles) as a function of the cat size defined as $|\alpha|^2$ (x-axis). Up to $|\alpha|^2 \approx 3.5$, $T_{\text{bit-flip}}$ undergoes an exponential increase to $\approx 0.8 \text{ ms}$, rising by a factor of 4.2 per added photon (solid line). The bit-flip time then saturates (dashed line is a guide for the eye) for $|\alpha|^2 \geq 5$ at 1 ms , a factor of 300 larger than the cat-qubit resonator lifetime T_1 in the absence of the pump and drive. Each circle is obtained from measurements such as in (b) for the circle indicated by the blue arrow. (b) The cat-qubit is initialized in $|0\rangle_\alpha$, for a cat size $|\alpha|^2 = 5.4$. After applying the pump and drive for a variable duration (x-axis), the population P (y-axis) of $|0\rangle_\alpha$ (top curve) and $|1\rangle_\alpha$ (bottom curve) is measured. The data (open circles) are fitted to decaying exponential functions (solid lines) from which we extract the bit-flip time. (c) Each panel displays the measured Wigner function of the cat-qubit after a pump and drive duration indicated on the right of each plot. Labels 1-5 mark the correspondence with (b). The cat-qubit is initialized in $|0\rangle_\alpha$ (top panel) and over a millisecond timescale, the population escapes towards $|1\rangle_\alpha$ (lower panels). The two-photon dissipation ensures that the cat-qubit resonator state remains entirely in the steady state manifold spanned by $|0\rangle_\alpha$ and $|1\rangle_\alpha$.

ATS consists of a symmetric SQUID (Superconducting Quantum Interference Device) shunted in its center by a large inductance, thus forming two loops. Here the inductance is built from an array of Josephson junctions. The ATS mediates an interaction of the form $U_I = -2E_J \cos(\varphi_\Sigma) \cos(\varphi + \varphi_\Delta)$, where E_J is the Josephson energy of the SQUID junctions, φ is the phase across the dipole, and $2\varphi_{\Sigma, \Delta}$ are the sum and differences of flux threading the two loops fig. 4.12. We bias the ATS at $\varphi_\Sigma = \varphi_\Delta = \pi/2$, or equivalently, we thread the left and right loops with flux π and 0 , respectively. In addition, we drive the sum port with a radio-frequency flux pump $\epsilon(t)$. At this bias point $U_I = -2E_J \sin(\epsilon(t)) \sin(\varphi)$. The ATS is coupled to the buffer and cat-qubit, so that φ is a linear combination of $\mathbf{a}, \mathbf{a}^\dagger, \mathbf{b}, \mathbf{b}^\dagger$, and $\sin(\varphi)$ contains only odd powers of these operators. The desired interaction (4.13) is present in the expansion of $\sin(\varphi)$, and is resonantly selected by a flux pump frequency $\omega_p = 2\omega_a - \omega_b$ [123]. In contrast with previous strategies [32, 33], the ATS mediates a pristine two-photon coupling, since (4.13) is the only leading order non-rotating term, the presence of the inductive shunt prevents instabilities [34], and the device operates at a first order flux insensitive point (Fig 4.7c). These features are key in order not to introduce inherent error processes that cannot be corrected by two-photon dissipation.

4.2.3 Coherence time measurements

The root advantage of the cat-qubit is that its computational states $|0\rangle_\alpha$ and $|1\rangle_\alpha$ can be made arbitrarily long-lived simply by increasing the cat size $|\alpha|^2$, provided that $\kappa_{\text{conf}} > \kappa_{\text{err}}$. In this experiment, the dominant error is due to energy decay so that $\kappa_{\text{err}}/2\pi = (2\pi T_1)^{-1} = 53$ kHz tab. 4.2, and $\kappa_{\text{conf}} = 2|\alpha|^2\kappa_2$ with a measured $\kappa_2/2\pi = 40$ kHz (from which we infer $g_2/2\pi = 360$ kHz). Hence, we enter the regime $\kappa_{\text{conf}} > \kappa_{\text{err}}$ as soon as $|\alpha|^2 > 0.6$. We have measured that for each added photon in the cat-qubit state, the bit-flip time is multiplied by 4.2. This exponential scaling persists up to $|\alpha|^2 \approx 3.5$, and the bit-flip time saturates for $|\alpha|^2 \geq 5$ at 1 ms, a 300-fold improvement over the resonator intrinsic lifetime (see Fig. 4.8). We expect a saturation when the corrected bit flip rate reaches the rate of residual errors which are not correctable, such as non-local errors. In the present experiment, we attribute this saturation (sec. 4.3.5) to the coupling with the transmon employed for the resonator tomography fig. 4.10, which has a thermal occupation of 1%, a lifetime $T_{1,q} = 5$ μs and is dispersively coupled to the cat-qubit resonator with a rate $\chi/2\pi = 720$ kHz. Over a timescale in the millisecond range, the transmon acquires a thermal excitation that shifts the cat-qubit resonator frequency by χ . This triggers a rotation of the resonator states which overcomes the confining potential since in this experiment $\chi \gg \kappa_{\text{conf}}/2$, see sec. 4.3.4 (note that tomography protocols compatible with smaller values of χ have been recently demonstrated [68, 111]). During an average time $T_{1,q}$, the resonator states acquire an angle of order $\chi T_{1,q} \gg 2\pi$. When the transmon excitation decays, the rotation stops and the two-photon dissipation brings the resonator state back into the cat-qubit computational basis. By virtue of the dissipative nature of the protection mechanism, this process, which is an example of a non-Markovian error, may result in a bit-flip but does not cause any leakage.

Schrödinger cat states like $|\pm\rangle_\alpha$ living in a resonator with a lifetime T_1 , lose their coherence at a rate $2|\alpha|^2/T_1$ [124]. In the cat-qubit paradigm, this translates into a phase-flip rate which increases linearly with the cat size $|\alpha|^2$. In addition, our cat-qubit undergoes a flux pump, a drive and non-linear interactions, which could further increase the phase-flip rate. We measure the phase-flip rate for increasing $|\alpha|^2$ and confirm a linear scaling (Fig. 4.9a). Moving towards three dimensional cavities and engineering ever-improving non-linear interactions should decrease the phase-flip rate below a threshold where a line repetition code can actively correct remaining errors [108].

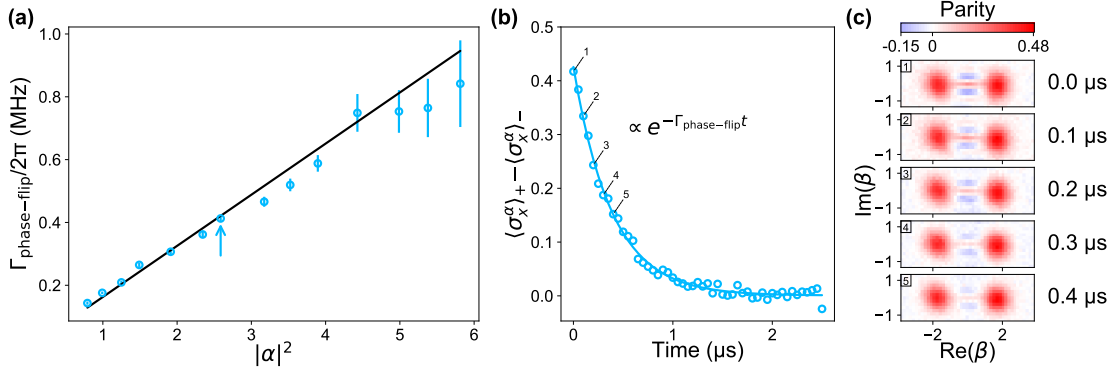


FIGURE 4.9: **Linear increase of the phase-flip rate with the cat size.** (a) The phase-flip rate (y-axis) is measured as a function of the cat size $|\alpha|^2$. The data (open circles) follow a linear trend (solid line) as expected for the decay rate of a Schrödinger cat coherence $\Gamma_{\text{phase-flip}} = 2|\alpha|^2/T_{1,\text{eff}}$. We measure $T_{1,\text{eff}} = 2.0 \mu\text{s}$, comparable to the intrinsic resonator lifetime of $3.0 \mu\text{s}$. Each circle is obtained from measurements such as in (b) for the circle indicated by the blue arrow. (b) The cat-qubit is prepared in the initial states $|\pm\rangle_\alpha$, for a cat size $|\alpha|^2 = 2.6$. After applying the pump and drive for a variable duration (x-axis), $\langle \sigma_x^\alpha | \sigma_x^\alpha \rangle_\pm$ is measured for each initial state and the difference is represented on the y-axis. The X Pauli operator of the cat-qubit σ_x^α corresponds to the photon number parity. The data (open circles) are fitted to a decaying exponential (solid line) from which we extract the phase-flip rate. (c) Each panel displays the measured Wigner function of the cat-qubit after a pump and drive duration indicated on the right of each plot. Labels 1-5 mark the correspondence with (b). The cat-qubit is initialized in the $|+\rangle_\alpha$ state and the positive and negative fringes demonstrate the quantum nature of this initial state (top panel). The fringe contrast is reduced by single photon loss which mixes $|+\rangle_\alpha$ with $|-\rangle_\alpha$.

Conclusion

In conclusion, we have observed the exponential decrease of the bit-flip rate between our cat-qubit states $|0\rangle_\alpha$ and $|1\rangle_\alpha$, as a function of their separation in phase space, while only linearly increasing their phase-flip rate. Such an exponential scaling is necessary to bridge the gap between the modest performance of quantum hardware and the exquisite performance needed for quantum computation [8]. This was made possible by inventing a Josephson circuit which mediates a pristine non-linear coupling between our cat-qubit mode and its environment. Further improving the lifetime of the cavity to the state of the art of a millisecond [105] and a cat size of $|\alpha|^2 \approx 5$ (resp: 10) should lead to a bit-flip time of ≈ 1 second (resp: 0.5 hour), and a phase-flip time of $\approx 100 \mu\text{s}$ (resp: $50 \mu\text{s}$). With such a long bit-flip time, the entire effort of active QEC will be focused on correcting the only significant error: phase-flips. In addition, conditional rotations in the 2D phase space of our cat-qubit form a universal set of gates, thus bypassing the need for magic states. These features indicate a significant reduction in hardware overhead for QEC [108].

4.3 Additional Material

4.3.1 Full device and wiring

The circuit consists of a sputtered niobium film with a thickness of 120 nm deposited on a 280 μm -thick wafer of intrinsic silicon. The main circuit is etched after an optical lithography step. Then the Josephson junctions are made of evaporated aluminum through a PMMA/MAA resist mask written in a distinct e-beam lithography step. A single Dolan bridge is used to make the small junctions of the ATS and of the transmon, and a series of 3 Dolan bridges delimit the 5-junction array which serves as the ATS inductor.

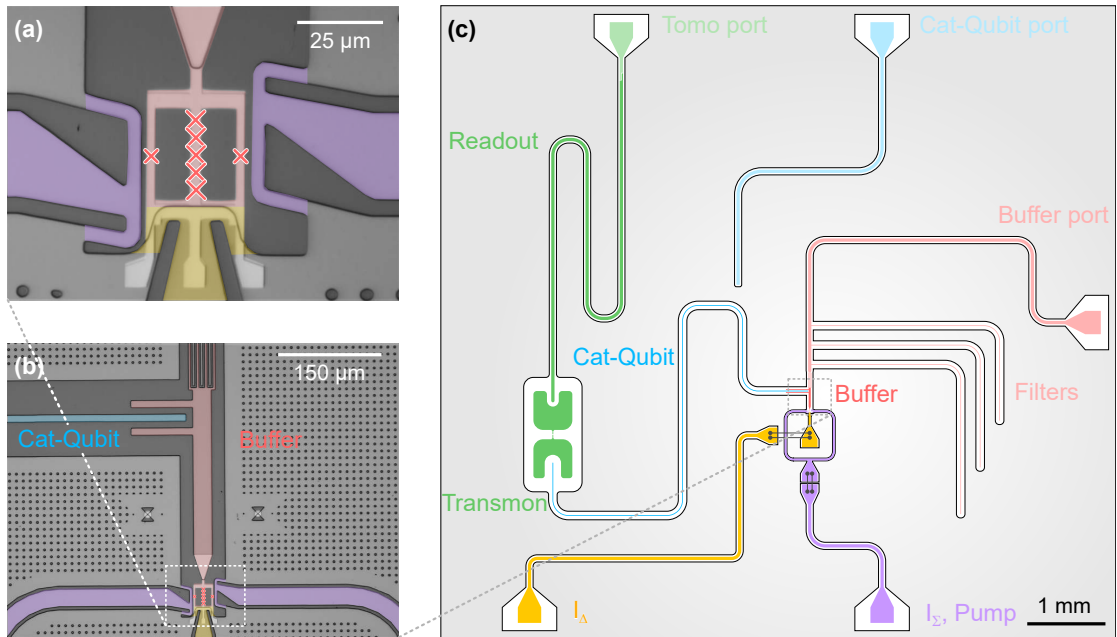


FIGURE 4.10: Full device layout. (a) False color optical image of the ATS. Note, that the 5 junction symbols are separated for clarity, the actual junctions are much closer and centered in the middle of the arm. (b) Zoom-out, false color optical image of the buffer. The buffer (red) is well coupled to its transmission line via an interdigitated capacitor (top). It is also capacitively coupled to the cat-qubit resonator (blue). This is actually a picture of a twin sample where this coupling was smaller. In panel (c), the real size of the coupling capacitor is shown. (c) Full device layout. The cat-qubit resonator is coupled on its other side to a transmon qubit, itself coupled to a readout resonator which together enable to perform the cat-qubit tomography. After the interdigitated capacitor, the buffer input is filtered via three $\lambda/4$ -stub filters. These filters are band-stops at the cat-qubit resonator frequency to mitigate its direct coupling to the input line of the buffer (b). The on-chip hybrid along the pump path (purple), equally splits the pump tone to RF-flux bias the ATS with the right symmetry. The black lines linking two dots are a schematic representation of the crucial wirebonds of the device. The wirebonds linking the pump input to the on-chip hybrid were implemented to reduce the area of the loop delimited by the center conductor and the ground plane, leading to a reduced sensitivity to flux noise.

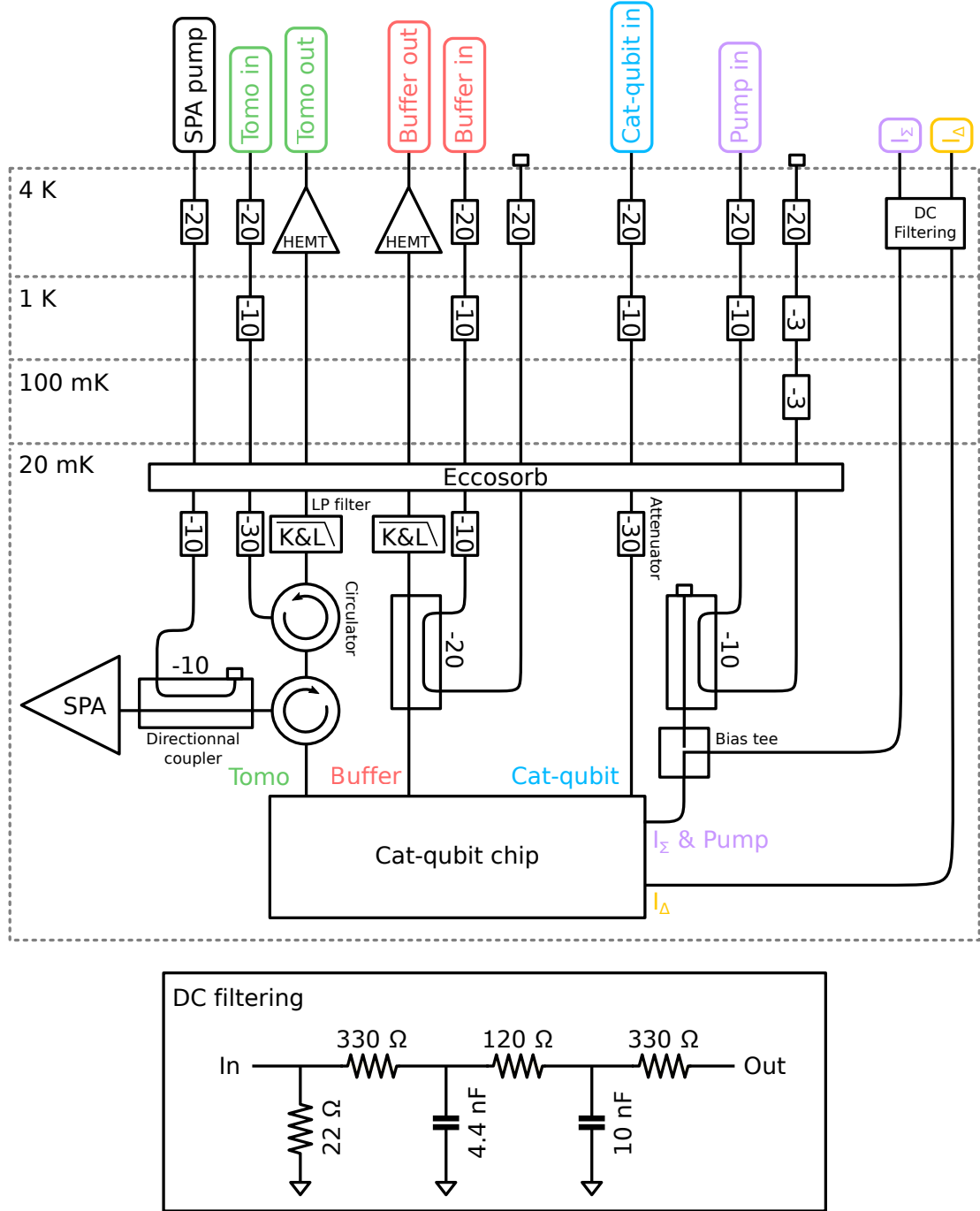


FIGURE 4.11: **RF and DC wiring of the dilution refrigerator.** Note that the pump and drive tones are attenuated at the base plate via directional couplers so that the attenuated power is dissipated at higher fridge stages, far from the sample. The I_z DC current and the RF pump signal are combined at 20 mK with a bias-tee. We have used a homemade “Snail Parametric Amplifier” (SPA) [122].

4.3.2 Hamiltonian derivation

The potential energy of the ATS dipole element To understand the interaction Hamiltonian (4.12), let’s first derive the potential energy of the ATS element alone. Its

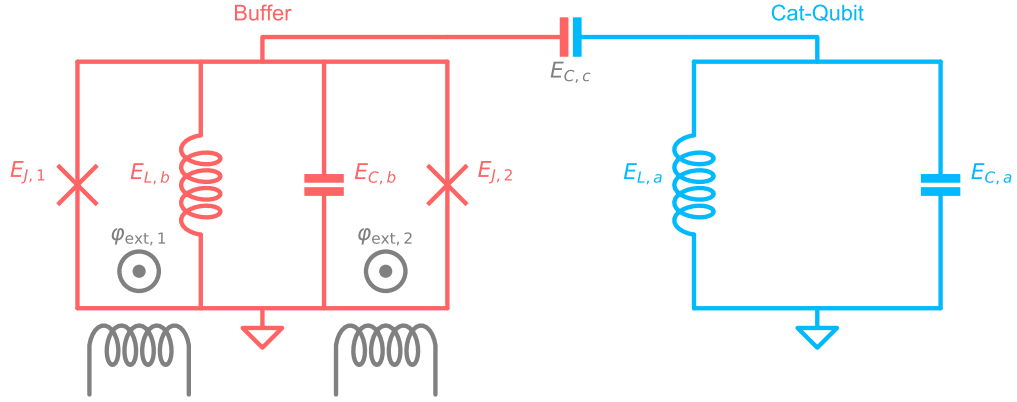


FIGURE 4.12: Equivalent circuit diagram. The cat-qubit (blue), a linear resonator, is capacitively coupled to the buffer (red). One recovers the circuit of Fig. 4.7 by replacing the buffer inductance with a 5-junction array and by setting $\varphi_{\Sigma} = (\varphi_{\text{ext},1} + \varphi_{\text{ext},2})/2$ and $\varphi_{\Delta} = (\varphi_{\text{ext},1} - \varphi_{\text{ext},2})/2$. Not shown here: the buffer is capacitively coupled to a transmission line, the cat-qubit resonator is coupled to a transmon qubit

equivalent circuit is represented in red in Fig. 4.12 and the phase across its inductor φ is the only degree of freedom (here we assume that the coupling capacitor to the cat-qubit mode is replaced by an open circuit). The potential energy of the ATS reads

$$U(\varphi) = \frac{1}{2}E_{L,b}\varphi^2 - E_{J,1}\cos(\varphi + \varphi_{\text{ext},1}) - E_{J,2}\cos(\varphi - \varphi_{\text{ext},2}). \quad (4.14)$$

Due to fabrication imperfections, the ATS junctions are not symmetric. We write $E_{J,1} = E_J + \Delta E_J$ and $E_{J,2} = E_J - \Delta E_J$ and we factorize U

$$U(\varphi) = \frac{1}{2}E_{L,b}\varphi^2 - 2E_J\cos(\varphi_{\Sigma})\cos(\varphi + \varphi_{\Delta}) + 2\Delta E_J\sin(\varphi_{\Sigma})\sin(\varphi + \varphi_{\Delta}), \quad (4.15)$$

where $\varphi_{\Sigma} = (\varphi_{\text{ext},1} + \varphi_{\text{ext},2})/2$ and $\varphi_{\Delta} = (\varphi_{\text{ext},1} - \varphi_{\text{ext},2})/2$. The antisymmetric flux bias of the ATS is $\varphi_{\Sigma} = \varphi_{\Delta} = \pi/2$ (this is a saddle point of the buffer frequency map). On top of this DC bias, we add the RF flux bias on φ_{Σ} so that

$$\varphi_{\Sigma} = \pi/2 + \epsilon(t), \text{ with } \epsilon(t) = \epsilon_0 \cos(\omega_p t) \quad (4.16)$$

$$\varphi_{\Delta} = \pi/2. \quad (4.17)$$

The time-dependent potential at first order in $\epsilon(t)$ then reads

$$U(\varphi) = \frac{1}{2}E_{L,b}\varphi^2 - 2E_J\epsilon(t)\sin(\varphi) + 2\Delta E_J\cos(\varphi). \quad (4.18)$$

This potential is unbounded which prevents the system from escaping towards higher energy states in the presence of the pump [34, 35]. In practice, with the 5-junction array

replacing the inductance, the confining part of the potential is replaced by $5E_{J,L} \cos(\varphi/5)$ where $E_{J,L} = 5E_{L,b}$ is the Josephson energy of each individual junction of the array. This potential is no longer unbounded, however the bound is high enough ($5E_{J,L} \gg 2E_J\epsilon_0$) for our pump power regime.

In the ideal case ($\Delta E_J = 0$), this potential only produces odd powers of φ from the sine non-linearity. A small asymmetry of the junctions produces small even powers of φ , leading to parasitic Kerr non-linearities. Typically $|\Delta E_J/E_J| \approx 10\%$. In the following we assume $\Delta E_J = 0$ for simplicity.

The coupled buffer and cat-qubit resonators We now consider the buffer and cat-qubit modes, and their coupling through the ATS dipole element. The full Hamiltonian reads

$$\mathbf{H} = \hbar\omega_{a,0}\mathbf{a}^\dagger\mathbf{a} + \hbar\omega_{b,0}\mathbf{b}^\dagger\mathbf{b} - 2E_J\epsilon(t) \sin(\varphi_b + \varphi_a) \quad (4.19)$$

$$\text{with } \varphi_a = \varphi_a(\mathbf{a} + \mathbf{a}^\dagger), \varphi_b = \varphi_b(\mathbf{b} + \mathbf{b}^\dagger) \quad (4.20)$$

where \mathbf{a}/\mathbf{b} are the annihilation operators of the cat-qubit and buffer modes, $\omega_{a/b,0}$ their resonant frequencies, and $\varphi_{a/b}$ their zero point phase fluctuations across the ATS dipole. Due to the circuit geometry, we expect $\varphi_b \gg \varphi_a$. When expanding the sine up to third order in $\varphi = \varphi_b + \varphi_a$ we get

$$\begin{aligned} \mathbf{H} = & \hbar\omega_{a,0}\mathbf{a}^\dagger\mathbf{a} + \hbar\omega_{b,0}\mathbf{b}^\dagger\mathbf{b} - 2E_J\epsilon(t)\varphi_b(\mathbf{b} + \mathbf{b}^\dagger) - 2E_J\epsilon(t)\varphi_a(\mathbf{a} + \mathbf{a}^\dagger) \\ & + \frac{1}{3}E_J\epsilon(t)(\varphi_b + \varphi_a)^3 \end{aligned} \quad (4.21)$$

The first two terms of the expansion are drives at frequency ω_p on the buffer and cat-qubit respectively. They can be absorbed in the frame displaced by $\xi_a(t) = \xi_a e^{-i\omega_p t}$ and $\xi_b(t) = \xi_b e^{-i\omega_p t}$ for \mathbf{a} and \mathbf{b} respectively, where

$$\xi_{a/b} \xrightarrow{t \gg 1/\kappa_{a/b}} \frac{iE_J\epsilon_0\varphi_{a/b}}{\kappa_{a/b}/2 + i(\omega_{a/b,0} - \omega_p)} \quad (4.22)$$

In this displaced frame, the Hamiltonian writes

$$\begin{aligned} \mathbf{H}_{\text{disp}} = & \hbar\omega_{a,0}\mathbf{a}^\dagger\mathbf{a} + \hbar\omega_{b,0}\mathbf{b}^\dagger\mathbf{b} \\ & + \frac{1}{3}E_J\epsilon(t) \left(\varphi_b(\mathbf{b} + \mathbf{b}^\dagger) + \xi_b e^{-i\omega_p t} + \xi_b^* e^{i\omega_p t} + \varphi_a(\mathbf{a} + \mathbf{a}^\dagger) + \xi_a e^{-i\omega_p t} + \xi_a^* e^{i\omega_p t} \right)^3 \end{aligned} \quad (4.23)$$

In practice, the buffer mode is driven with an additional microwave drive at frequency ω_d , not included here for simplicity. We place ourselves in the frame rotating at $(\omega_p + \omega_d)/2$ and ω_d for \mathbf{a} and \mathbf{b} respectively. In this frame, the Hamiltonian reads

$$\begin{aligned} \mathbf{H}_{\text{rot}} = & \hbar \left(\omega_{a,0} - \frac{\omega_p + \omega_d}{2} \right) \mathbf{a}^\dagger \mathbf{a} + \hbar (\omega_{b,0} - \omega_d) \mathbf{b}^\dagger \mathbf{b} \\ & + \frac{1}{3} E_J \epsilon(t) \left(\varphi_b (\mathbf{b} e^{-i\omega_d t} + \mathbf{b}^\dagger e^{i\omega_d t} + \xi_b e^{-i\omega_p t} + \xi_b^* e^{i\omega_p t}) \right. \\ & \left. + \varphi_a (\mathbf{a} e^{-i\frac{\omega_p + \omega_d}{2} t} + \mathbf{a}^\dagger e^{i\frac{\omega_p + \omega_d}{2} t} + \xi_a e^{-i\omega_p t} + \xi_a^* e^{i\omega_p t}) \right)^3 \end{aligned} \quad (4.24)$$

Performing the rotating wave approximation (RWA), we get

$$\mathbf{H}_{\text{RWA}}/\hbar = \left(\omega_a - \frac{\omega_p + \omega_d}{2} \right) \mathbf{a}^\dagger \mathbf{a} + (\omega_b - \omega_d) \mathbf{b}^\dagger \mathbf{b} + g_2^* \mathbf{a}^2 \mathbf{b}^\dagger + g_2 \mathbf{a}^{\dagger 2} \mathbf{b}, \quad (4.25)$$

where the modes frequencies are AC-Stark shifted to $\omega_{a/b} = \omega_{a/b,0} - \Delta_{a/b}$ and

$$\hbar \Delta_{a/b} = \frac{1}{3} E_J \varphi_{a/b}^2 (\text{Re}(\xi_b) \varphi_b + \text{Re}(\xi_a) \varphi_a) \quad (4.26)$$

with $\hbar g_2 = E_J \epsilon_0 \varphi_a^2 \varphi_b / 2$. When we verify the frequency matching condition

$$\omega_d = \omega_b, \quad \omega_p = 2\omega_a - \omega_b,$$

we recover (4.13)

$$\mathbf{H}_2/\hbar = g_2^* \mathbf{a}^2 \mathbf{b}^\dagger + g_2 \mathbf{a}^{\dagger 2} \mathbf{b}. \quad (4.27)$$

4.3.3 Circuit parameters

Most of the circuit parameters can be readily deduced from standard circuit-QED measurements and are gathered in Table 4.2. Here we explain the methodology we used to deduce the 6 dipole parameters of Fig. 4.12 (see Table 4.3) and the mapping of (I_Σ, I_Δ) to $(\varphi_\Sigma, \varphi_\Delta)$. Independently of this mapping, the ATS saddle point is unambiguously found. At this flux point, $E_J \cos(\varphi_\Sigma) = 0$, and we directly measure ω_{a_0} and $\omega_{b,0}$. The energies E_J and $E_{L,b}$ are computed from the Ambegaokar-Baratoff and the room temperature measurements of neighbouring test junction resistances. The general linear transformation mapping (I_Σ, I_Δ) to $(\varphi_\Sigma, \varphi_\Delta)$ is found by fitting the measured buffer frequency as a function of (I_Σ, I_Δ) (see Fig. 4.13c,d). The impedance Z_a of the cat-qubit resonator is estimated from the aspect ratio of the coplanar waveguide geometry. The energy $E_{C,c}$ is adjusted to match the measured anti-crossing of the buffer and cat-qubit mode when I_Σ is varied (see Fig. 4.13b).

Cat-qubit mode		Buffer		Pump	
$\omega_a/2\pi$	8.03805 GHz	$\omega_b/2\pi$	4.8336 GHz	$\omega_p/2\pi$	11.2425 GHz
$\omega_{a,0}/2\pi$	8.0389 GHz	$\omega_{b,0}/2\pi$	4.886 GHz		
T_1	3 μ s	$\kappa_b/2\pi$	13 MHz		
$\kappa_a/2\pi$	53 kHz	$\chi_{bb}/2\pi$	-32 MHz		
$\chi_{aa}/2\pi$	-7 kHz	$\chi_{ba}/2\pi$	0.79 MHz		
Transmon		Readout			
$\omega_q/2\pi$	4.4156 GHz	$\omega_r/2\pi$	6.4598 GHz		
$T_{1,q}$	5 μ s	$\kappa_r/2\pi$	1.47 MHz		
$T_{2,q}$	8 μ s				
$\chi_{qq}/2\pi$	180 MHz				
$\chi_{qa}/2\pi$	720 kHz				
π/χ_{qa}	0.69 μ s				

TABLE 4.2: Measured system parameters at the ATS working point. The pump shifts the cat-qubit resonator and buffer frequencies. The frequencies in the absence of the pump are noted $\omega_{a/b,0}$ and those in its presence are denoted $\omega_{a/b}$. The Kerr couplings χ_{mn} enter the full Hamiltonian in the form $-\chi_{mn}m^\dagger mn^\dagger n$ when $m \neq n$ and $-\frac{\chi_{mm}}{2}m^{\dagger 2}m^2$, where m, n denote the mode indices.

Circuit parameters		Dipole parameters	
$\omega_{a,0}/2\pi$	8.0389 GHz	$E_{L,a}/h$	96.6 GHz
Z_a	90 Ω	$E_{C,a}/h$	92.7 MHz
$\omega_{b,0}/2\pi$	4.886 GHz	$E_{C,b}/h$	73.5 MHz
$E_{C,c}/h$	720 MHz	$E_{C,c}/h$	720 MHz
$E_{L,b}/h$	45 GHz	$E_{L,b}/h$	45 GHz
E_J/h	90 GHz	E_J/h	90 GHz

TABLE 4.3: Measured and estimated circuit parameters (left), and their corresponding dipole energies (right).

4.3.4 Semi-classical analysis

Two-photon dynamics Under two-photon dissipation, the cat-qubit resonator state ρ undergoes the following dynamics

$$\frac{d}{dt}\rho = \kappa_2 D[\mathbf{a}^2 - \alpha^2]\rho, \quad (4.28)$$

where the Lindblad operator D is defined for any operator \mathbf{O} as $D[\mathbf{O}]\rho = \mathbf{O}\rho\mathbf{O}^\dagger - \frac{1}{2}\rho\mathbf{O}^\dagger\mathbf{O} - \frac{1}{2}\mathbf{O}^\dagger\mathbf{O}\rho$. Any combination of the states $|0, 1\rangle_\alpha$ is a steady state of this dynamics. Moreover, these steady states are global attractors. To gain insight, we restrict this dynamics to the set of coherent states $\rho(t) = |\beta(t)\rangle\langle\beta(t)|$, and introduce the pseudo-potential V defined over the resonator phase space as $-\nabla V(\beta) = \frac{d\beta}{dt}$. This pseudo-potential depicts in which direction of the phase space a coherent state $|\beta\rangle$ evolves.

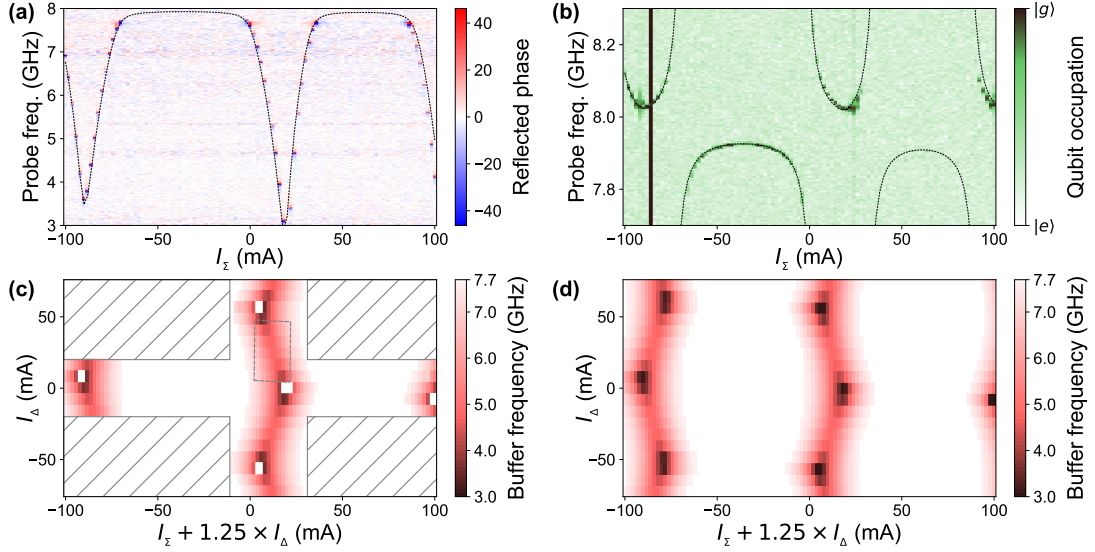


FIGURE 4.13: Flux dependence. (a) Buffer spectroscopy. Phase of the reflected probe signal (color map) on the buffer port as a function of I_z (x-axis) and probe frequency (y-axis). The buffer frequency follows an arch-like pattern typical of squid-based devices. The probe frequency range is limited to 3-8 GHz due to the 4-8 GHz circulator on the output line. The black dashed line represents the expected buffer/cat-qubit frequency for the best fitting parameter set. The slight aperiodicity may be explained by small asymmetries in the loop areas of the ATS. (b) Cat-qubit resonator two-tone spectroscopy. A continuous probe is applied on the cat-qubit resonator at various frequencies (y-axis) and a second tone attempts to π -pulse the qubit on resonance. When the probe populates the cat-qubit, the qubit shifts in frequency due to the cross-Kerr coupling, and is insensitive to the π -pulse. The resulting qubit state is plotted in color and we repeat the experiment for various values of I_z (x-axis). The black dashed line represents the expected buffer/cat-qubit frequency for the best fitting parameter set. The black vertical line corresponds to a flux bias where the buffer is exactly at the qubit frequency resulting in a strong decrease in the qubit lifetime. (c) For each value of I_z (x-axis) and I_Δ (y-axis), we extract the buffer frequency from a spectroscopy measurement (panel a) and report it in color (white is when the resonance frequency is beyond the measurement range). Contrary to what they were designed for, the two flux lines do not perfectly apply symmetric (I_z) and antisymmetric (I_Δ) bias on the ATS. We compensate for this imbalance while taking the data by shifting the I_z span for each value of I_Δ as indicated on the x-axis label. Data were only taken on the area outside the hatched regions to prevent the heating of the dilution refrigerator beyond a tolerable temperature. The grey dashed-rectangle corresponds to the flux range presented in Fig. 4.7 of the main text. (d) Simulated flux dependence of the buffer mode for the best fitting parameter set.

Hence, the coherent steady states of the dynamics are the minima of V . We find [32]

$$\frac{d\beta}{dt} = -\kappa_2 \beta^* (\beta^2 - \alpha^2). \quad (4.29)$$

In the following we introduce $x = \text{Re}(\beta)$ and $y = \text{Im}(\beta)$ and we consider α real. Separating the real and imaginary part of equation (4.29), we get

$$\begin{aligned} \frac{dx}{dt} &= -\kappa_2 (x^3 + xy^2 - x\alpha^2) \\ \frac{dy}{dt} &= -\kappa_2 (y^3 + yx^2 + y\alpha^2). \end{aligned}$$

The speed of a coherent state $|\beta\rangle$ in phase space is $(\frac{dx}{dt}, \frac{dy}{dt})$ (see Fig. 4.14a, 4.15a). By integrating this speed over space, we get the pseudo-potential

$$V(x, y) = \kappa_2 \left(\frac{1}{4}(x^4 + y^4) + \frac{1}{2}x^2y^2 - \alpha^2(x^2 - y^2) \right) \quad (4.30)$$

depicted in Fig. 4.6b of the main text. It has two minima in $-\alpha$ and α . Analyzing small deviations δx and δy around these minima, we find

$$\begin{aligned} \frac{d}{dt}\delta x &= -\kappa_{\text{conf}}\delta x \\ \frac{d}{dt}\delta y &= -\kappa_{\text{conf}}\delta y, \end{aligned}$$

where the confinement rate κ_{conf} is defined as

$$\kappa_{\text{conf}} = 2\kappa_2\alpha^2 \quad (4.31)$$

This confinement pins down computational states to the minima location and protects the cat-qubit against errors. Next, we analyze the effect of errors on the cat-qubit resonator.

Single photon loss When added, most Hamiltonian or dissipative mechanisms (such as detuning or single photon loss) will perturb the system so that the two-dimensional cat-qubit space is no longer a steady-manifold of the overall dynamics. Instead, only one mixed state is a steady-state of the dynamics. This seems incompatible with encoding a qubit, but, as we will see in the following, this steady-state will be exponentially long to reach for the cat-qubit computational states $|0\rangle_\alpha$ and $|1\rangle_\alpha$ and we will call them meta-stable states. Still, the pseudo-potential description is useful and we use it to understand the main effects of single photon loss and detuning.

Let us derive V in the presence of single photon loss at rate κ_a . The loss operator is $L_1 = \sqrt{\kappa_a}\mathbf{a}$ and the overall dynamics reads

$$\frac{d}{dt}\rho = \kappa_2 D[\mathbf{a}^2 - \alpha^2]\rho + \kappa_a D[\mathbf{a}]\rho. \quad (4.32)$$

Following the same computation as previously, we have

$$\frac{d\beta}{dt} = -\kappa_2\beta^*(\beta^2 - \alpha^2) - \frac{1}{2}\kappa_a\beta$$

so that

$$\begin{aligned}\frac{dx}{dt} &= -\kappa_2 (x^3 + xy^2 - x\alpha^2) - \frac{1}{2}\kappa_a x \\ \frac{dy}{dt} &= -\kappa_2 (y^3 + yx^2 + y\alpha^2) - \frac{1}{2}\kappa_a y.\end{aligned}\quad (4.33)$$

This speed field is represented in Fig. 4.14a for $\kappa_a = \kappa_2$ and $\alpha = 2$. By integrating it over space we get

$$V(x, y) = \kappa_2 \left(\frac{1}{4}(x^4 + y^4) + \frac{1}{2}x^2y^2 - \alpha^2(x^2 - y^2) \right) + \frac{1}{4}\kappa_a (x^2 + y^2). \quad (4.34)$$

Cuts that pass through the two minima are plotted in Fig. 4.14b for various values of κ_a and α .

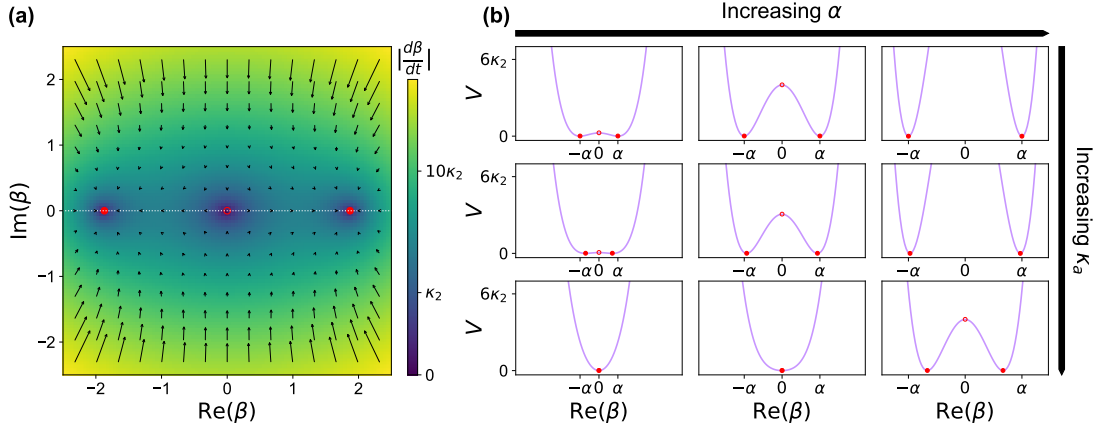


FIGURE 4.14: **Dynamics under single photon loss.** (a) This color map represents the magnitude of the speed field (4.33) over phase space (β plane) for $\kappa_a = \kappa_2$ and $\alpha = 2$. The black arrows represent the speed at various locations. The two stable/ one unstable steady-states are indicated with full/open red circles (the stability is inferred from the direction of the arrows). The white dotted line represents the cut along which we plot the potential. (b) Cuts ($\text{Re}(\beta) = 0$) of the potential (4.34) with $\alpha = (1, 2, 3)$ (left to right) and $\kappa_a = (0, \kappa_2, 10\kappa_2)$ (top to bottom). The top row represents the unperturbed potential and the steady states are $-\alpha$ and α (red circles). As we increase κ_a , the amplitude α_∞ of the meta-stable states (red circles) decreases until reaching 0. However for a given value of κ_a , we can always find a value of α to recover two meta-stable states (bottom row).

The minima are located in $\pm\alpha_\infty$ with

$$\alpha_\infty = \begin{cases} \sqrt{\alpha^2 - \kappa_a/(2\kappa_2)} & \text{if } \alpha^2 \geq \kappa_a/(2\kappa_2) \\ 0 & \text{otherwise} \end{cases} \quad (4.35)$$

In this semi-classical analysis, we find that two meta-stable states form when the error rate κ_a is below the threshold

$$\kappa_a < \kappa_{\text{conf}} = 2|\alpha|^2\kappa_2.$$

Detuning In the main text, we discussed the causes of the bit-flip time saturation and blamed the random frequency shifts induced by the transmon thermal excitations. Let us see how a detuning Δ of the cat-qubit frequency affects the two-photon stabilisation. In this case, we have

$$\frac{d\beta}{dt} = -\kappa_2\beta^*(\beta^2 - \alpha^2) - i\Delta\beta \quad (4.36)$$

so that

$$\begin{aligned} \frac{dx}{dt} &= -\kappa_2(x^3 + xy^2 - x\alpha^2) + \Delta y \\ \frac{dy}{dt} &= -\kappa_2(y^3 + yx^2 + y\alpha^2) - \Delta x. \end{aligned} \quad (4.37)$$

Note that $\text{rot}(\frac{dx}{dt}, \frac{dy}{dt}) = -2\Delta \neq 0$ so we cannot perform the spatial integration to find $V(x, y)$. We can obtain the steady states directly by analyzing the speed field (Fig. 4.15a) but there exists a direction in phase-space parametrized by a real parameter λ such that $y = \lambda x$ and $\frac{dy}{dt} = \lambda \frac{dx}{dt}$ along which the integration is meaningful. Plugging in this relation into (4.37) we get the following condition on λ

$$\lambda^2\Delta + 2\lambda\kappa_2\alpha^2 + \Delta = 0 \quad \Rightarrow \quad \lambda = -\frac{\kappa_{\text{conf}}}{2\Delta} + \sqrt{\left(\frac{\kappa_{\text{conf}}}{2\Delta}\right)^2 - 1} \quad (4.38)$$

with $\kappa_{\text{conf}} = 2\kappa_2\alpha^2$. We have chosen the solution λ which approaches 0 when $\Delta \rightarrow 0$ and which crosses the steady states. Along this cut indexed by β' , we have

$$\frac{d\beta'}{dt} = \left(\sqrt{\left(\frac{\kappa_{\text{conf}}}{2}\right)^2 - \Delta^2} \right) \beta' - \kappa_2\beta'^3 \quad (4.39)$$

leading to

$$V(\beta') = -\frac{1}{2} \left(\sqrt{\left(\frac{\kappa_{\text{conf}}}{2}\right)^2 - \Delta^2} \right) \beta'^2 + \frac{1}{4} \kappa_2 \beta'^4 \quad (4.40)$$

that is plotted in Fig. 4.15b. There are two minima located along the direction β' in

$$|\alpha_\infty| = \begin{cases} \left(\alpha^4 - \left(\frac{\Delta}{\kappa_2}\right)^2 \right)^{\frac{1}{4}} & \text{if } \Delta < \frac{\kappa_{\text{conf}}}{2} \\ 0 & \text{otherwise} \end{cases} \quad (4.41)$$

In this semi-classical analysis, we find that two meta-stable states form provided Δ is below the threshold

$$\Delta < \kappa_{\text{conf}}/2 = |\alpha|^2 \kappa_2. \quad (4.42)$$

In our experiment, $\Delta/2\pi = \chi/2\pi = 720$ kHz which is larger than $\kappa_{\text{conf}}/2/2\pi = 7\kappa_2/2\pi \approx 280$ kHz for the largest $|\alpha|^2 = 7$.

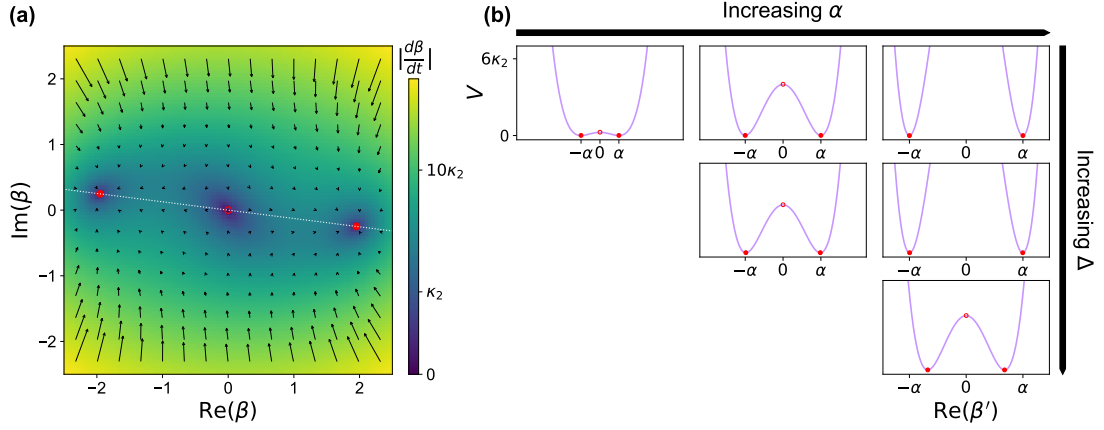


FIGURE 4.15: **Dynamics under detuning.** (a) This color map represents the magnitude of the speed field (4.37) over the phase space (β plane) for $\Delta = \kappa_2$ and $\alpha = 2$. The black arrows represent the speed at various locations. The two stable/ one unstable steady-states are indicated with full/open red circles (the stability is inferred from the knowledge of the direction of the arrows). The white dotted line represents the cut along which we represent the potential. (b) Cuts ($\text{Im}(\beta) = \lambda \text{Re}(\beta)$) of the potential (4.40) with $\alpha = (1, 2, 3)$ (left to right) and $\Delta = (0, \kappa_2, 8\kappa_2)$ (top to bottom). The top row represents the unperturbed potential and the steady states are $-\alpha$ and α (red circles). As we increase Δ , the amplitude $|\alpha_\infty|$ of the meta-stable states (red circles) decreases until reaching 0. However for a given value of Δ , we can always find a value of α to recover two meta-stable states (bottom row).

4.3.5 Bit-flip time simulation

In the previous part, we gained insight on how the main error channels affect the cat-qubit protection. In the following, we perform a full master equation simulation of the system with the measured system parameters. The circuit consists of three relevant modes: the buffer, cat-qubit and transmon qubit. We can write the Hamiltonian and loss operators (in the rotating frame of each mode)

$$\begin{aligned} H_3/\hbar &= \left(g_2^*(a^2 - \alpha^2)b^\dagger + \text{h.c.} \right) - \frac{\chi_{aa}}{2} a^{\dagger 2} a^2 - \chi_{qa} a^\dagger a q^\dagger q \\ L_a &= \sqrt{\kappa_a} a, \quad L_b = \sqrt{\kappa_b} b, \quad L_q = \sqrt{\kappa_q(1 + n_{\text{th}})} q, \quad L_{q^\dagger} = \sqrt{\kappa_q n_{\text{th}}} q^\dagger \end{aligned} \quad (4.43)$$

where we have (from left to right) in the Hamiltonian, the two-to-one photon exchange factored with a drive on the buffer with strength $\epsilon_d = -g_2^* \alpha^2$, the anharmonicity of the cat-qubit, the cross Kerr between the cat-qubit and the transmon. The last loss operator accounts for the thermal occupation of the transmon measured to be $n_{\text{th}} \sim 1\%$ in the presence of the pump and drive. In order to determine the effect of the transmon on the cat-qubit, it is useful to remove the transmon from the simulation. We simulate the

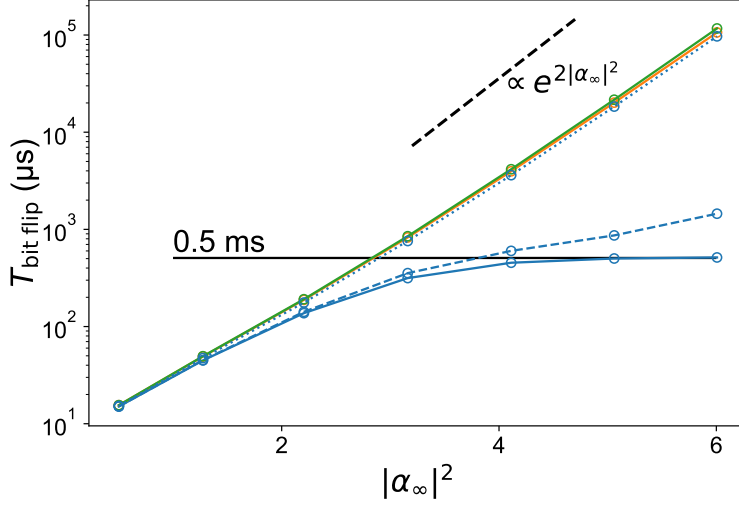


FIGURE 4.16: Simulated bit-flip time as a function of the cat-qubit size $|\alpha_\infty|^2$. We simulate the experiment performed in Fig. 4.8 of the main text given the measured system parameters (Tables 4.2 and 4.3) with a master equation solver (QuTiP) for various values of α^2 . The cat-qubit size is given by $|\alpha_\infty|^2 = |\langle \mathbf{a}^2 | \mathbf{a}^2 \rangle|$ after a time $t \gg \kappa_2^{-1}$. The dynamics we simulate correspond to various levels of abstraction. The green curve corresponds to the simulation of the equivalent dynamics of the cat-qubit resonator alone (4.45). We get an exponential increase of the bit-flip time with a dependence on the cat size close to the expected $\exp(2|\alpha_\infty|^2)$ [125] (dashed black line is a guide for the eye). The orange curve corresponds to the simulation of the dynamics of the buffer and cat-qubit together (4.44). The good agreement between these two curves indicates that the adiabatic elimination of the buffer is valid (indeed $g_2 \ll \kappa_b$). Finally the blue solid curve is the simulation including the transmon with its thermal occupation (4.43). In this case, the bit-flip time saturates at around 0.5 ms which is compatible to the experimentally measured value (1 ms). This saturation follows a prior exponential increase where the bit-flip time is multiplied by 3.7 for each added photon (experimentally 4.2). We also simulated for $\chi_{qa} = \chi_{qa,\text{exp}}/3$ (dashed blue line) and $\chi_{qa,\text{exp}}/10 = 72$ kHz and as expected, the curve follows back the exponential scaling when χ_{qa} is low enough.

dynamics generated by

$$\begin{aligned} \mathbf{H}_2/\hbar &= \left(g_2^* (\mathbf{a}^2 - \alpha^2) \mathbf{b}^\dagger + \text{h.c.} \right) - \frac{\chi_{aa}}{2} \mathbf{a}^{\dagger 2} \mathbf{a}^2 \\ \mathbf{L}_a &= \sqrt{\kappa_a} \mathbf{a}, \quad \mathbf{L}_b = \sqrt{\kappa_b} \mathbf{b} \end{aligned} \quad (4.44)$$

Finally by adiabatically eliminating the buffer [32] we reduce to the following equivalent Hamiltonian and loss operator (provided $g_2 \ll \kappa_b$)

$$\begin{aligned} \mathbf{H}_1/\hbar &= -\frac{\chi_{aa}}{2} \mathbf{a}^{\dagger 2} \mathbf{a}^2 \\ \mathbf{L}_a &= \sqrt{\kappa_a} \mathbf{a}, \quad \mathbf{L}_2 = \sqrt{\kappa_2} (\mathbf{a}^2 - \alpha^2) \end{aligned} \quad (4.45)$$

with $\kappa_2 = 4|g_2|^2/\kappa_b$.

For each of these models, we numerically solve the master equation for the cat-qubit resonator prepared in state $|+\alpha\rangle$ for various α . By fitting the decay of $\langle \mathbf{a} | \mathbf{a} \rangle$ to an exponential decay, we extract $T_{\text{bit-flip}}$ that we reported in Fig. 4.16 (full lines). For the

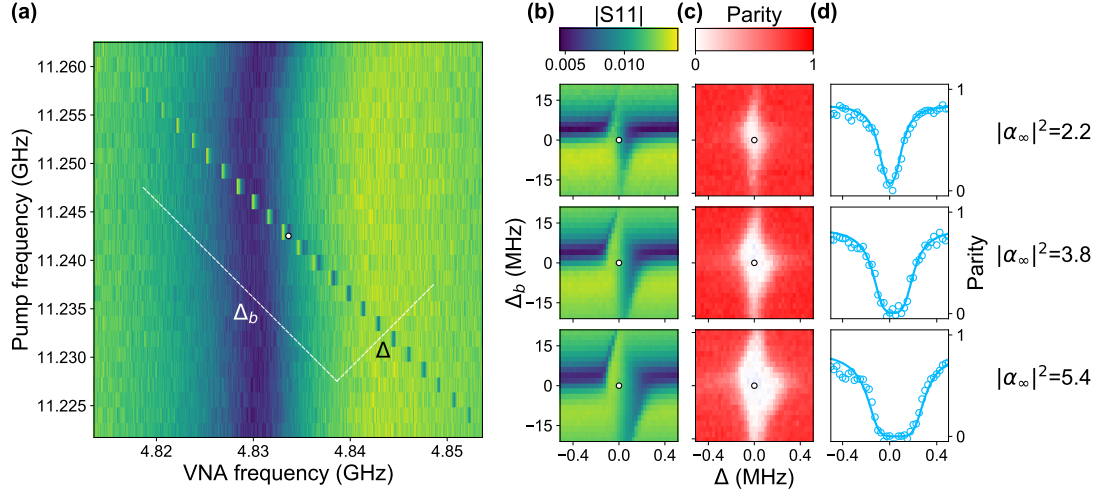


FIGURE 4.17: Tuning the pump and drive frequencies. (a) Reflected relative drive amplitude (VNA measurement) as a function of drive frequency (x-axis) and pump frequency (y-axis). When $\omega_p = 2\omega_a - \omega_d$, a sharp feature indicates that the two-to-one photon exchange is resonant and as expected, it has a slope -1 . To observe this feature, we switch to the basis $\Delta = (\Delta_{\text{pump}} + \Delta_{\text{drive}})/2$, $\Delta_b = (\Delta_{\text{pump}} - \Delta_{\text{drive}})/2$. (b,c) Reflected relative drive amplitude (color) and parity of the cat-qubit resonator (red) as a function of Δ (x-axis) and Δ_b (y-axis) for increasing drive amplitude (top to bottom). The drive amplitude is expressed in units of the cat-size $|\alpha_\infty|^2$ which is calibrated in Fig 4.18. (c) When the two-to-one photon exchange is resonant, the cat-qubit resonator is displaced and the parity drops to 0 if we measure after a time greater than κ_a^{-1} . Later, we perform the cat-qubit resonator tomography and verify that the resonator is in the fully-mixed cat-qubit state. In all these plot, the white circles correspond to the chosen pump and drive frequencies. We verify that whatever the drive amplitude, this point remains centered in the resonant range. We do not need to adapt the frequencies when increasing the cat size. (d) Cut of the previous color plot around $\Delta_b = 0$ representing the parity (open circle) of the cat-qubit steady state as a function of Δ . The relation (4.41) shows that the frequency window over which a non-trivial state is stabilized in the cavity scales as $2\kappa_2|\alpha|^2$. This enables us to determine κ_2 assuming photon loss is the main loss mechanism. We fit (solid line) the measured parity with the expected steady-state parity (QuTiP) were the two fitting parameters are the parity contrast and κ_2 . We find $\kappa_2/2\pi = 40$ kHz.

last two models, we recover the exponential increase of the bit-flip time which scales as $\sim \exp(2\alpha^2)$. The three mode model reproduces the saturation we have in the experiment and associates it with the thermal excitation of the transmon. Indeed one transmon excitation detunes the cat-qubit by χ which exceeds $\kappa_{\text{conf}}/2$ when $\alpha^2 < 29$, well above cat sizes we could achieve experimentally. In future experiment, we plan on reducing χ . By dividing χ by 10, we expect to fully circumvent this saturation (dotted lines in Fig. 4.16).

4.3.6 Tuning the cat-qubit

As explained in the main text, the flux point at which the ATS should operate is a saddle point of the buffer frequency map. It is very simple to find experimentally as we do not need to know the full mapping between I_Σ , I_Δ and φ_Σ , φ_Δ to recognize a saddle

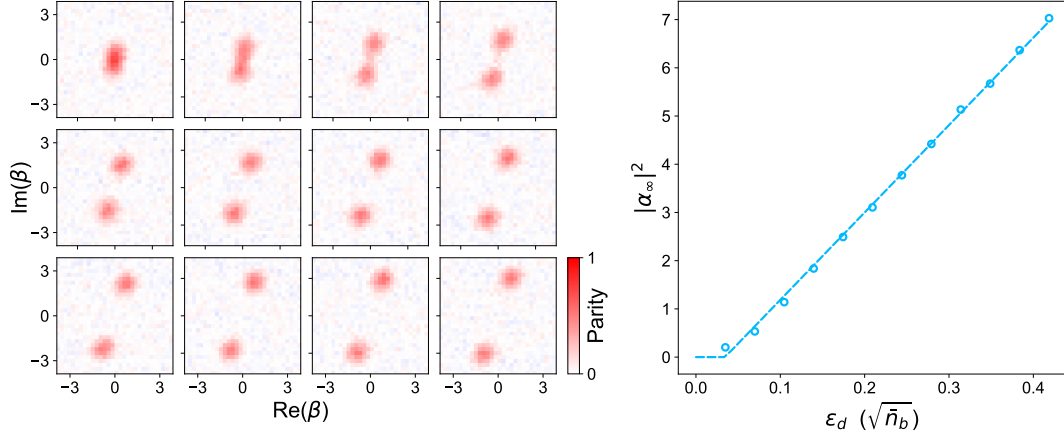


FIGURE 4.18: **Increasing the cat-qubit size.** (a) Measured Wigner distribution of the cat-qubit state as a function of drive amplitude (left to right, top to bottom) after a pump and drive pulse duration of $20 \mu\text{s}$. (b) Fitted cat size $|\alpha_\infty|^2$ (open circles) as a function of the drive amplitude ϵ_d . The drive amplitude is expressed in terms of the square root of the photon number the buffer would contain without the conversion process. For each Wigner distribution of panel (a), we fit a sum of two 2D-Gaussian (coherent states) diametrically opposed which are separated by a distance $2|\alpha_\infty|$. Note that for simplicity, in the main text, we use $|\alpha|^2$ instead of $|\alpha_\infty|^2$. In the presence of single photon loss at rate κ_a , we expect $|\alpha_\infty|^2$ to follow the relation (4.35) (dashed line) a linear trend as a function of ϵ_d shifted by $\kappa_a/(2\kappa_2)$. Fitting this relation to the data enabled us to calibrate the x-axis scaling.

point. There are actually two types of saddle points as one can see on Fig. 4.13, the ones that are tilted to the left and the ones tilted to the right. If the single junctions of the ATS are perfectly symmetric, these points are equivalent. Otherwise, the buffer gets some Kerr and the two-points differ by the sign of this Kerr.

Then, once we know the buffer and cat-qubit frequencies we perform two-tone spectroscopy on the buffer (Fig. 4.17). A weak tone, referred to as the drive, is probing the buffer resonance and the pump is swept in the relevant frequency range (around $2\omega_a - \omega_b$). When the two-to-one exchange occurs between the buffer and the cat-qubit, we observe a sharp feature within the buffer resonance (Fig. 4.17a,b). The width of this feature depends on the weak tone strength and more importantly on the pump power. The pump power is pushed until before this feature becomes ill defined, when other non-linear dynamics start to play a significant role. On the cat-qubit side, within this feature the drive combined with the pump should populate the cat-qubit resonator. We check so by measuring the parity of the cat-qubit resonator and verify that it is indeed displaced. We tune the pump and buffer frequency in the middle of the displacement area (Fig. 4.17c). The width along Δ of this region enables us to determine κ_2 .

We perform the cat-qubit resonator full tomography after a long ($20 \mu\text{s} \gg \kappa_a^{-1}$) pump and drive pulse (Fig. 4.18) and we set the drive power so as to see well separated cat-states. The experiment is now tuned and from there we characterize the cat-qubit performances as shown in the main text.

Chapter 5

Itinerant microwave photon detection

5.1	Dissipation engineering for photo-detection	84
5.1.1	Engineering the Qubit-Cavity dissipator	85
5.1.2	Efficiency	87
5.1.3	Dark Counts	87
5.1.4	Detector Reset	89
5.1.5	QNDness	90
5.2	Additional Material	92
5.2.1	Circuit parameters	92
5.2.2	Purcell Filter	92
5.2.3	System Hamiltonian derivation	94
5.2.4	Adiabatic elimination of the waste mode	96
5.2.5	Qubit dynamics and detection efficiency	98
5.2.6	Reset protocol	101
5.2.7	Spectroscopic characterization of the detector	101
5.2.8	Tomography of the itinerant transmitted photon	102

In the previous chapter, we described the central experiment of this thesis which relied on dissipation engineering to stabilize a quantum manifold. Hereafter, we propose and experimentally realise an itinerant microwave photon detector based on this technique. This idea spontaneously emerged from black board discussions with Emmanuel Flurin, Zaki Leghtas, Samuel Deléglise, and myself. Each one of us was interested in single microwave photon detection for different applications, respectively, sensing a single spin [126, 127] or a carbon nanotube [29] and synthesizing non Gaussian states of motion of a mechanical oscillator [128].

Single photon detection has become standard at optical frequencies [129] and is the enabling technology of various quantum optics experiments: by combining them with Gaussian resources such as optical parametric oscillators or beamsplitters, they have been used to generate non-classical states [130], entanglement between remote stationary qubits [131], long distance quantum cryptography protocols [132] or one-way quantum computing [133]. In this frequency domain, single photon detection relies on irreversible photo-assisted ionization of various natural materials. However, microwave photons have energies 5 orders of magnitude lower than optical photons, and are therefore ineffective at triggering measurable phenomena at macroscopic scales.

On the other hand, great progress has been made in the detection of single excitations of superconducting circuits, the energy of which lies in the microwave range. Hence, the main idea of itinerant microwave photon detection is to leverage this ability by designing superconducting circuits that are sensitive to the arrival of a single microwave photon.

5.1 Itinerant microwave photon detection with dissipation engineering ¹

The detection of individual photons trapped in long-lived microwave cavities has been pioneered by atomic cavity quantum electrodynamics experiments [134, 135], and later on transposed to circuit quantum electrodynamics [25, 136]. In these detection schemes, the trapping of the photon into a long-lived cavity enhances the interaction to the measurement apparatus. Two fundamental difficulties arise in the detection of itinerant photons: the incoming photon only interacts briefly with the detector and occupies an unknown temporal mode out of a continuum. Recently, several strategies have been explored experimentally. In a first approach, a current biased Josephson circuit develops a macroscopic voltage [24] or a photon avalanche [26] upon the absorption of a single

¹The following is in preprint as “An irreversible qubit-photon coupling for the detection of itinerant microwave photons”, Raphaël Lescanne, Samuel Deléglise, Emanuele Albertinale, Ulysse Réglade, Thibault Capelle, Edouard Ivanov, Thibaut Jacqmin, Zaki Leghtas, Emmanuel Flurin (2019) [37].

photon. Another strategy involves an AC-modulated flux qubit that transits into an excited state through a photon induced Raman transition [137]. Finally, in detection schemes based on the Ramsey interferometry of a transmon qubit, the photon imprints a phase on the qubit as it reflects off a cavity [27, 28]. These experiments demonstrate the Quantum Non-Demolition (QND) detection of the itinerant photons

Here, we use dissipation engineering to irreversibly couple a transmission line toward a single two-level system (qubit). A photon propagating in the line is absorbed by the qubit, but the reverse process is inhibited: an excitation in the qubit does not propagate back in the line. Upon arrival of a single photon, the qubit is left in its excited state, leaving ample time for it to be measured with a microwave pulse containing tens to hundreds of photons, which is measurable with readily available amplification techniques [60]. In practice, we demonstrate that implementing this engineered dissipation triggers dark counts at a rate one order of magnitude smaller compared to state-of-the-art experiments [25–28, 137].

5.1.1 Engineering the Qubit-Cavity dissipator

The detector, depicted in Fig. 5.1a is composed of two superconducting microwave resonators, the buffer which hosts the incoming field and the waste, which plays the role of the bath, releases the detected photon. The resonators are coupled through a Josephson junction in a bridge transmon configuration [138], and are strongly coupled to transmission lines at a rate $\kappa_b/2\pi = 1.0$ MHz and $\kappa_w/2\pi = 2.4$ MHz, respectively. A microwave drive, referred to as the pump, is applied to the transmon qubit at frequency

$$\omega_p = \bar{\omega}_q + \omega_w^e - \omega_b^g, \quad (5.1)$$

where $\bar{\omega}_q$ is the qubit frequency shifted by the pump power through the AC-stark effect (5.52), ω_w^e and ω_b^g are the buffer and waste frequencies conditioned on the qubit being in its excited state $|e\rangle$ and its ground state $|g\rangle$, respectively. In the absence of the pump $\omega_q/2\pi = 4.532$ GHz, $\omega_b^g/2\pi = 5.495$ GHz and $\omega_w^e/2\pi = 5.770$ GHz. The pumped system is well described by the effective Hamiltonian (5.14)

$$\mathbf{H}_{\text{eff}}/\hbar = g_3 \mathbf{b} \boldsymbol{\sigma}^\dagger \mathbf{w}^\dagger + g_3^* \mathbf{b}^\dagger \boldsymbol{\sigma} \mathbf{w}, \quad (5.2)$$

where g_3 is the parametrically activated three-wave mixing rate, and verifies $g_3 = -\xi_p \sqrt{\chi_{qb} \chi_{qw}}$. Here, $\chi_{qb}/2\pi = 1.02$ MHz and $\chi_{qw}/2\pi = 2.73$ MHz are the dispersive couplings of the buffer and waste to the qubit, respectively. The pump amplitude ξ_p is expressed in units of square root of photons and is typically smaller than one. The buffer and waste annihilation operators are denoted \mathbf{b} and \mathbf{w} , and $\boldsymbol{\sigma}$ denotes the lowering

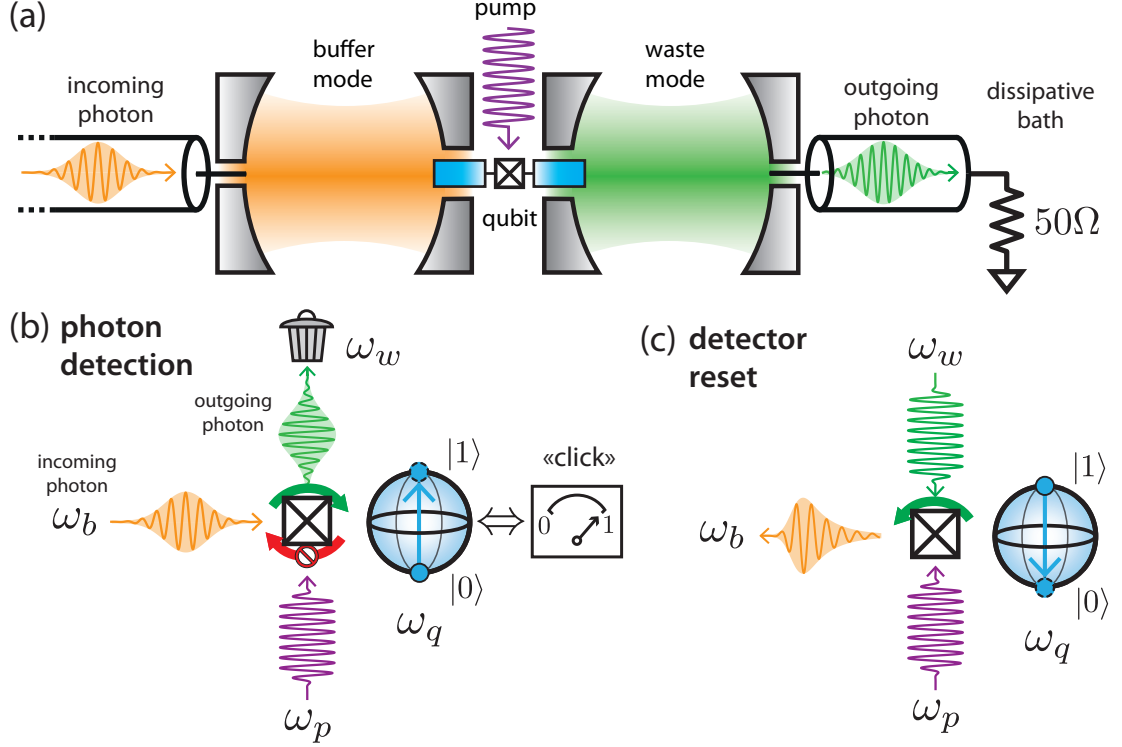


FIGURE 5.1: **Principle of the itinerant photon detector.** (a) The circuit consists of two microwave modes, a buffer (orange) and a waste (green) coupled to a transmon qubit (blue). Each mode is well coupled to its own transmission line so that a photon can enter the device on the left and leave on the right into the dissipative 50Ω environment. A pump (purple) is applied on the Josephson junction to make the three-wave mixing interaction resonant (eq. (5.2)). (b) When a photon enters the buffer, the pump converts it via the Josephson non-linearity (black cross) into one excitation of the qubit and one photon in the waste. The waste excitation is irreversibly radiated away in the transmission line, so that the reverse three-wave process cannot occur. The quantum state of the qubit is measured with a standard dispersive readout via the waste to detect whether or not a photon arrived while the pump was on. (c) When a coherent tone drives the waste, the qubit excitation can combine with waste photons and be released via the Josephson non-linearity in the buffer, enabling a fast reset of the detector.

operator of the qubit. The itinerant photon to be detected, incident on the buffer, is converted into a pair of excitations in the qubit and in the waste by the term $b\sigma^\dagger w^\dagger$. We place ourselves in the regime where $|g_3| \ll \kappa_w$ so that the photon in the waste is immediately dissipated in the natural environment while the qubit excitation is stored. Since the waste remains close to its vacuum state throughout the dynamics, the reverse process ($b^\dagger \sigma w$) is effectively inhibited. The subsequent detection of the qubit in the excited state based on single-shot dispersive readout [139] reveals the transit of the photon during the detection time (see Figure 5.1b).

The irreversible buffer-qubit dynamics, arising from the adiabatic elimination of the waste, is entirely described by a single loss operator (5.26)

$$L = \sqrt{\kappa_{nl}} b \sigma^\dagger, \quad (5.3)$$

where the engineered dissipation rate is $\kappa_{\text{nl}} = 4|g_3|^2/\kappa_w$. This dissipator is unusual for two reasons. First, it is non-local [53], since it involves operators from two different modes. Second, it is non-linear [32], since it involves the product of these operators. These properties are at the heart of the detection process: under the effect of \mathbf{L} , the qubit dissipates towards its excited state conditioned (non-linear) on the buffer (non-local) occupation. As a consequence, the detector is oblivious to the specific mode-shape of the incoming photons (within the detector bandwidth) by evacuating the associated entropy into the unread dissipative channel.

5.1.2 Efficiency

The efficiency η of the detector is defined as the probability of detecting the qubit in its excited state assuming a single incoming photon. For mode-shapes well within the detector bandwidth $(\kappa_{\text{nl}} + \kappa_b)/2\pi = 1.34$ MHz and short compared to the qubit relaxation time, the efficiency is (5.14)

$$\eta = 4 \frac{\kappa_{\text{nl}}\kappa_b}{(\kappa_{\text{nl}} + \kappa_b)^2}. \quad (5.4)$$

The efficiency reaches unity for $\kappa_{\text{nl}} = \kappa_b$, when the non-linear dissipation matches the coupling to the transmission line.

In practice, we satisfy eq. (5.1) by performing a calibration experiment (Fig. 5.2a). The pump power is chosen as the largest that did not induce significant qubit heating, thus maximizing the efficiency to dark-count ratio. The chosen pump power leads to $\kappa_{\text{nl}}/2\pi = 0.370$ MHz which results in an efficiency predicted by eq. (5.4) of 80% (red line of Fig. 5.2c). The detector efficiency is measured by varying the amplitude of a calibrated coherent pulse [35] as shown in Fig. 5.2b. The measurement is repeated for increasing pulse length as shown in Fig. 5.2c. We observe a smooth dependence of the efficiency as a function of the pulse length, that is well reproduced by our model if we take into account the finite detector bandwidth at short pulse duration (green curve of Fig. 5.2c), and the finite qubit lifetime for long pulses (orange curve of Fig. 5.2c), resulting in a maximum detection efficiency of $\eta_{\text{max}} = 58\%$ for a $2 \mu\text{s}$ pulse length.

5.1.3 Dark Counts

A crucial figure of merit of the detector is the dark count rate Γ_{dc} , defined as the number of clicks per unit-time in the absence of incoming photons. By virtue of our dissipation engineering approach, Γ_{dc} is robust against the two main decoherence mechanisms of the qubit: dephasing and energy relaxation. This is in stark contrast with the best

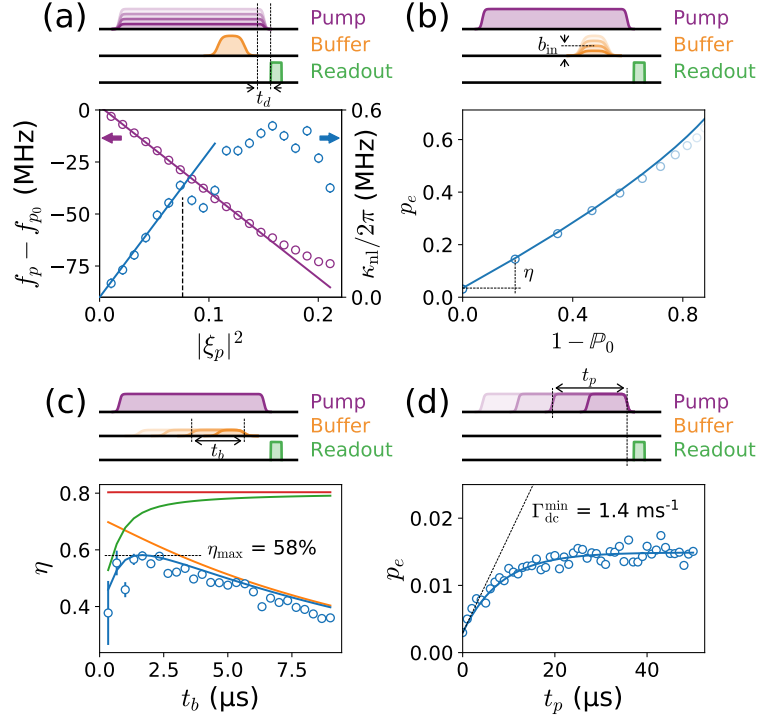


FIGURE 5.2: **Calibration and diagnosis of the detector.** (a-d) A pump tone (purple pulse) of duration t_p powers the device through the qubit port, and an incoming coherent wave-packet (orange pulse) of duration t_b and amplitude b_{in} is applied on the buffer. The qubit excited state population p_e is detected after a delay t_d through the waste (green pulse). (a) We plot the pump frequency f_p which maximizes p_e for various pump powers (x-axis). The first 10 data points (purple open circles) are fitted using a linear regression (purple line), leading to a y-intercept within 0.04% of the expected value $f_{p0} = (\omega_q + \omega_w^e - \omega_b^g)/2\pi$. The slope of this line provides a calibration of the pump power in units of photon number $|\xi_p|^2$ (see eq. 5.13). For each pump power, we plot the induced non-linear dissipation rate κ_{nl} (blue open circles), which is extracted from a full model simulation (see eq. (5.30)), to best match all measured values of p_e for small values of b_{in} and all values of t_b . For pump powers $|\xi_p|^2 < 0.076$, these extracted values follow the expected linear trend (blue line) $\kappa_{nl} = 4|\xi_p|^2 \chi_{qb} \chi_{wq} / \kappa_w$, with a 5% deviation at the value fixed for all subsequent experiments $|\xi_p|^2 = 0.076$ (dashed vertical line). The saturation of κ_{nl} is mainly due to the fact that, as g_3 increases with the pump power, we are leaving the adiabatic elimination regime. (b) Measured p_e (open circles) as a function of $1 - \mathbb{P}_0$, where \mathbb{P}_0 is the probability of the incoming wave-packet being in the vacuum see eq. (5.39). This quantity is varied by increasing b_{in} for a fixed $t_b = 2 \mu s$. The slope at the origin is the detection efficiency η , and the y-intercept is the dark-count. The theory (solid line) is obtained by simulating the full model eq. (5.30). (c) For each t_b (x-axis), η is measured (open circles) as in (b). The theory curves (solid lines) are obtained by simulating the full model eq. (5.30), in four regimes: $T_1, \kappa_b = \infty$ (red), $\kappa_b = \infty$ (orange), $T_1 = \infty$ (green), and the measured T_1, κ_b (blue). Note that the discrepancy between orange and red at small time is due to the finite rising time of the pump pulse $t_d = 500 \text{ ns}$. (d) Measured p_e (open circles) as a function of t_p with $b_{in} = 0$, at a repetition rate of 2 ms. An exponential fit (solid line) rises from $p_e = 0.003$ to $p_e = 0.015$ at a rate $1/T_1$.

performing schemes relying on Ramsey interferometry [27, 28], where the dark count rate scales with the qubit decoherence rate such that $\Gamma_{\text{dc}}^{\text{Ramsey}} \sim 1/(2T_2)$, in other words, the detection outcome is completely blurred after a detection time of order T_2 . In our case, the dominant source of dark count is given by the next limiting process: the qubit thermal excitation. Therefore the dark count rate is given by the qubit thermalization rate $\Gamma_{\text{dc}} \sim n_{\text{q,th}}/T_1$ with $n_{\text{q,th}}$ the qubit thermal occupancy. Fig. 5.2d shows the detection probability p_e as a function of the detection window t_p in the absence of buffer excitation. At short time compared to the qubit relaxation time T_1 , we find $p_e = 0.003 + \Gamma_{\text{dc}} \times t_p$. The first term of 0.003 results from the improper initialization of the qubit in its ground state and detection errors. We find $\Gamma_{\text{dc}} = 1.4 \text{ ms}^{-1}$, limited by pump-induced heating of the qubit bath [34, 35] (see fig. 5.2d and fig. 5.6). We have observed that for the same detection window, when the repetition rate increases from $(2 \text{ ms})^{-1}$ to $(50 \text{ } \mu\text{s})^{-1}$, the dark-count rate increases to 4 ms^{-1} , suggesting that the qubit bath thermalizes over timescales of hundreds of microseconds. In spite of the modest lifetime of our transmon qubit, the dark count rate reported here is one order of magnitude lower than the values reported previously in the literature [25, 27, 28, 137].

5.1.4 Detector Reset

A key requirement for practical photon detectors is a fast and high-fidelity reset, which we achieve using the reverse process $g_3^* b^\dagger \sigma w$ (see Fig. 5.1c). By shining a resonant tone on the waste in the presence of the pump, the qubit relaxes to the ground state with the emission of a photon in the buffer, leading to a fast reset at a rate $\gamma_{\text{reset}} = (370 \text{ ns})^{-1}$ and a ground state preparation fidelity of $F_{|g\rangle}^{\text{reset}} = 99.3\%$ improved to $F_{|g\rangle}^{\text{herald}} = 99.6\%$ with a subsequent heralding readout (Fig. 5.3a). The down time of the detector comprises the reset, heralding and readout pulses, and is as low as $3.5 \text{ } \mu\text{s}$ (Fig. 5.3b). The cyclic operation is demonstrated, by running the detector with a 43% duty cycle in the presence of a coherent tone on the buffer of variable strength (Fig. 5.3c). Moreover, the qubit is at all times either in $|g\rangle$ or $|e\rangle$ (5.31), and therefore a weak and continuous dispersive readout could be added to detect uninterruptedly the incoming photons with a precise timing of the clicks. Fig. 3c and 3d are an example of 1000 samples from such measurement sequences in the absence of the probe tone giving a dark count rate of $2800 \text{ counts.s}^{-1}$ and a total efficiency, including the photons lost during the detector's down-time and T_1 event during the detection, given by $\eta_{\text{cyclic}} = 0.19$.

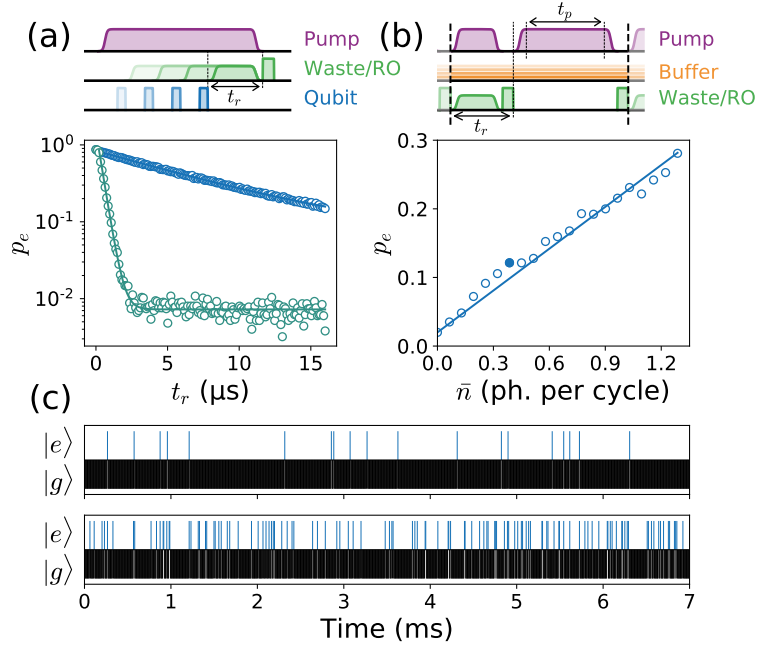


FIGURE 5.3: **Reset protocol and cyclic operation.** (a) The qubit is initialized in its excited state (blue pulse) and the pump is activated. The decay of p_e is measured (open circles) in the presence (green) or absence (blue) of a reset tone of duration t_r applied to the waste mode (green pulse). The exponential fits (solid lines) yield a qubit T_1 reduced from $7.7 \mu\text{s}$ to 370 ns . Note that the residual qubit population is reduced in the presence of the reset tone from 3.5% (see Fig. 5.2) to 0.7%, demonstrating that the reset is in fact cooling the qubit below its effective bath occupation. (b) Cyclic operation of the pulse sequence in between the two vertical dashed lines, in the presence of a continuous input tone of variable amplitude (orange pulse). First, the qubit is reset for $2 \mu\text{s}$ (first green and purple pulses), followed by a heralding measurement to confirm the preparation in the ground state (second green pulse). The detector is then activated during a time $t_p = 3 \mu\text{s}$ by switching on the pump (second purple pulse), and finally, the qubit state is readout (third green pulse). The measured p_e (open circles) is plotted as a function of the photon number in the input pulse integrated over the cycle time $7 \mu\text{s}$. A linear regression (solid line) yields an overall efficiency of 20 % (which accounts for the 43% duty cycle), and a dark count of 2 % per cycle. (c) Real-time trajectories of 1000 successive detection cycles, with $\bar{n} = 0$ (top) and $\bar{n} = 0.38$ (bottom), as marked by the full dot in (b).

5.1.5 QNDness

Finally, the waste which up to now has been considered as a bath, can in fact be monitored to demonstrate that our detector is quantum non-demolition. Indeed, the qubit acts as a witness of the photon passage, the latter is first absorbed in the buffer and released through the waste at another carrier frequency (Fig. 5.1b). By performing the heterodyne detection of the outgoing field, heralded by the click of the detector, we first extract the temporal mode of the photon based on the eigen-mode expansion of the auto-correlation function [140]. Then, we reconstruct the density matrix of the photon by measuring the moments of the signal distribution up to the fourth order [141]. Based on a maximum likelihood reconstruction, we perform the tomography of the outgoing

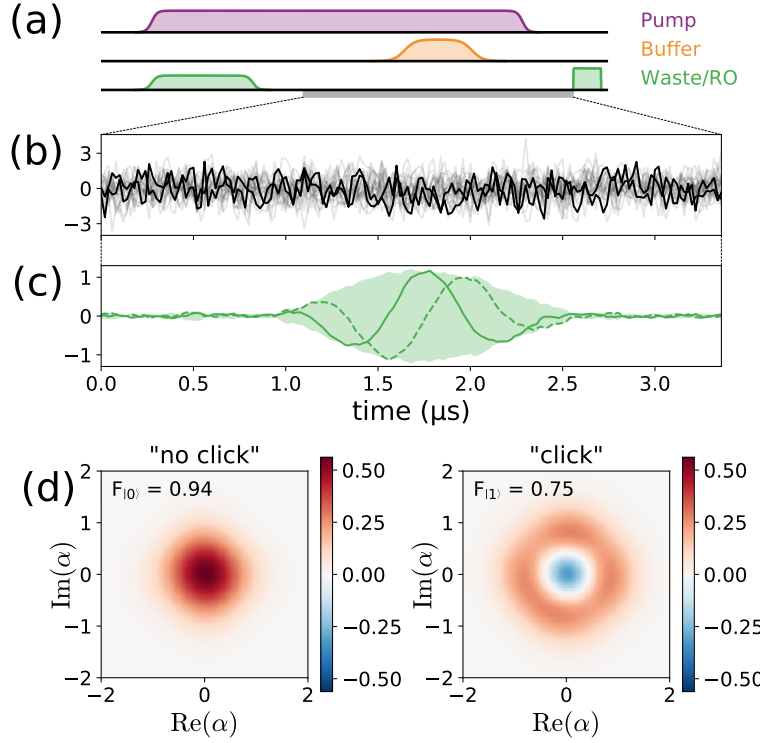


FIGURE 5.4: **Quantum non-demolition characterization by tomography of the quantum state released in the waste line.** (a) The three wave-mixing interaction is activated by a pump tone (purple pulse) during which the detector is first initialized by a reset pulse on the waste port (first green pulse) preceding the injection of a small coherent field (mean occupation $\bar{n} = 0.35$) on the buffer port. The qubit excitation, detected at the end of the sequence by a readout pulse (second green pulse) is correlated with the creation of a single photon by the waste. During the detection process, a near quantum-limited phase-preserving amplifier is used to monitor the field emitted by the waste (grey-shaded rectangle). (b) The signal, demodulated at the frequency $(\omega_w^g + \omega_w^e)/2$, is dominated by quantum and amplifier noise, as exemplified with 20 overlaid single-quadrature time-traces (2 time traces have been coloured in black for readability). (c) The waveform of the emitted wavepacket can be deconvoluted from the uncorrelated detection noise by statistical analysis of the traces [140]. The real, imaginary part, and envelope of the waveform retrieved experimentally are represented in full line, dashed line, and green shaded area respectively. (d) The quantum state of the field in the temporal mode plotted in (c) is reconstructed by analyzing the moments of the measured amplitude distribution [141] (see sec. 5.2.8). The Wigner function of the state conditioned on the detection of the qubit in state $|g\rangle$ (resp. $|e\rangle$) is represented on the left (resp. right).

field (Fig. 5.4) and obtain a single photon fidelity $F_{|1\rangle} = 75\%$ conditioned on a click of the detector and a vacuum fidelity $F_{|0\rangle} = 94\%$ conditioned on the absence of a click.

Conclusion

We have realized a non-linear and non-local dissipator involving a qubit coupled to a resonator. Conditioned on the impact of a photon on the resonator, the qubit irreversibly switches to its excited state which is then detected with a single-shot readout. This photon detector achieves both high efficiency and an unprecedentedly low dark count rate

owing to its robustness against the main decoherence mechanisms of superconducting circuits. Alike Josephson parametric amplifiers, this new class of robust detectors based on dissipation engineering constitute an essential step towards the practical use of photon detectors in the microwave domain. By engineering higher-order dissipators, one can envision more complex detection patterns, such as number-resolving or multi-mode correlation detectors.

5.2 Additional Material

5.2.1 Circuit parameters

The circuit consists of $\lambda/2$ -coplanar waveguide resonators as depicted in Fig.5.5(b). The circuit is made out of sputtered Niobium with a thickness of 120 nm deposited on a 280 μm -thick wafer of intrinsic silicon. The main circuit is etched after an optical lithography step and then the Josephson junction is made of evaporated aluminum through a PMMA/MAA resist mask written in a distinct ebeam lithography step.

Qubit		Waste Mode		Buffer Mode	
$\omega_q/2\pi$	4.532 GHz	$\omega_b^g/2\pi$	5.7725 GHz	$\omega_w^g/2\pi$	5.4952 GHz
T_1	8 – 9 μs	$\kappa_{\text{ext}}/2\pi$	2.38 MHz	$\kappa_{\text{ext}}/2\pi$	0.890 MHz
T_2^*	10 μs	$\kappa_{\text{int}}/2\pi$	< 100 kHz	$\kappa_{\text{int}}/2\pi$	80 kHz
$\chi_{qq}/2\pi$	146 MHz				
$\chi_{qb}/2\pi$	1.02 MHz				
$\chi_{qw}/2\pi$	2.73 MHz				

TABLE 5.1: Measured system parameters. Note that the internal losses of the waste are too small in comparison to the external losses to be accurately measured.

5.2.2 Purcell Filter

In order to strongly couple the waste resonator to the cold 50 Ω environment which provides the dissipative character of the scheme without degrading the qubit relaxation time T_1 , we have employed a Purcell filter in series with the waste resonator as depicted in Fig.5.5(b). As described in ref. [142], another benefit of the Purcell filter is that the readout time of the qubit is reduced hence the readout fidelity is enhanced.

The Purcell filter is a bandpass filter consisting in a $\lambda/2$ resonator coupled in series with the waste resonator at a rate \mathcal{G} and placed on resonance with the latter, $\omega_{\text{Purcell}} = 2\pi \times 5.786$ GHz, and coupled to the transmission line at a rate $\kappa_{\text{Purcell}} = 2\pi \times 36$ MHz. The filter is designed to be in the strong damping regime $\kappa_{\text{Purcell}} \gg \mathcal{G}$ so that the

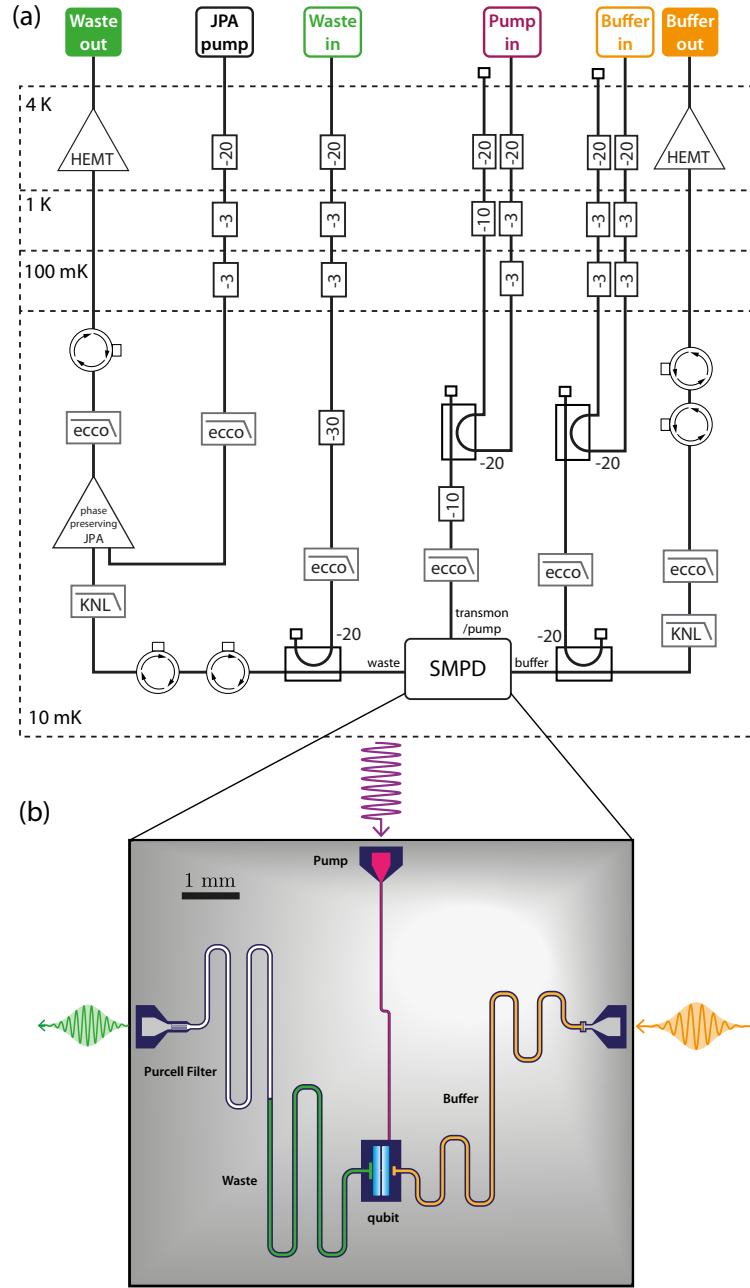


FIGURE 5.5: (a) Schematic of microwave cabling of the dilution refrigerator. (b) Superconducting coplanar-waveguide layout, note that this vector layout is the exact mask used for the circuit fabrication.

expected anti-crossing due to the hybridization of the modes is irrelevant. The effective decay rate of the waste resonator to the transmission line through the filter is then given by

$$\kappa_w = \frac{4\mathcal{G}^2}{\kappa_{\text{Purcell}}} \frac{1}{1 + [2(\omega_{\text{Purcell}} - \omega_w)/\kappa_{\text{Purcell}}]^2} \approx \frac{4\mathcal{G}^2}{\kappa_{\text{Purcell}}} \quad (5.5)$$

Experimentally, we extract an effective decay rate of $\kappa_w = 2\pi \times 2.38$ MHz leading to

a coupling strength $\mathcal{G} = 2\pi \times 5.6$ MHz between the waste and the Purcell filter. The qubit is coupled to the waste resonator at a rate $g = 2\pi \times 41$ MHz. Its residual decay rate through the waste channel in presence of the Purcell filter is given by

$$\begin{aligned}\kappa_q^{(w)} &= \frac{g^2}{(\omega_w - \omega_q)^2} \frac{4\mathcal{G}^2}{\kappa_{\text{Purcell}}} \frac{1}{1 + [2(\omega_{\text{Purcell}} - \omega_q)/\kappa_{\text{Purcell}}]^2} \\ &\approx \frac{g^2\mathcal{G}^2}{(\omega_w - \omega_q)^4} \kappa_{\text{Purcell}} = 2\pi \times 1 \text{ Hz}.\end{aligned}\tag{5.6}$$

Note that for a given decay rate of the waste in the transmission line, the Purcell filter enables the suppression of the qubit relaxation through the waste channel by a factor $\kappa_{\text{Purcell}}^2/(\omega_{\text{Purcell}} - \omega_q)^2 \sim 10^{-3}$.

5.2.3 System Hamiltonian derivation

Our system consists of three electromagnetic modes, referred to as the buffer, the waste, and the qubit, coupled through a Josephson junction. A strong radio-frequency drive, referred to as the pump, is applied to the qubit mode. The Hamiltonian of this system is well described by

$$\begin{aligned}H/\hbar &= \sum_{m=b,w,q} \omega_m \mathbf{m}^\dagger \mathbf{m} - \frac{E_J}{\hbar} \left(\cos(\varphi) + \varphi^2/2 \right) + 2\epsilon_p \cos(\omega_p t) (\mathbf{q} + \mathbf{q}^\dagger) \\ \varphi &= \sum_{m=b,w,q} \varphi_m (\mathbf{m} + \mathbf{m}^\dagger),\end{aligned}\tag{5.7}$$

where the index $m = b, w, q$ refers to the buffer, waste and qubit modes respectively, of angular frequency ω_m , and annihilation operator \mathbf{m} . The Josephson energy is denoted E_J , and φ is the phase across the junction, which can be decomposed as the sum of the phase $\varphi_m(\mathbf{m} + \mathbf{m}^\dagger)$ across each mode, where φ_m is the zero point fluctuation of the phase across mode m . The pump's amplitude and angular frequency are denoted ϵ_p and ω_p respectively.

The strong pump is accounted for by moving into a frame where the qubit mode is displaced by its mean field amplitude $\xi_p e^{-i\omega_p t}$ where $\xi_p \approx -\epsilon_p/(\omega_q - \omega_p)$ [32], provided that the pump is adiabatically switched on and off with respect to the detuning $\omega_q - \omega_p$ (about 300 MHz in our experiment) [68].

Following this frame displacement, we place ourselves in the interaction picture with respect to the Hamiltonian $\sum_{m=b,w,q} (\omega_m - \delta_m) \mathbf{m}^\dagger \mathbf{m}$, where δ_m are arbitrary detunings that will be used to cancel the AC Stark-shifts due to the Kerr effect. The transformed

Hamiltonian reads

$$\mathbf{H}'/\hbar = \sum_{m=b,w,q} \delta_m \mathbf{m}^\dagger \mathbf{m} - \frac{E_J}{\hbar} \left(\cos(\varphi') + \varphi'^2/2 \right), \quad (5.8)$$

$$\varphi' = \sum_{m=b,w,q} \varphi_m \left(\mathbf{m} e^{-i(\omega_m - \delta_m)t} + \mathbf{m}^\dagger e^{i(\omega_m - \delta_m)t} \right) + \varphi_q \left(\xi_p e^{-i\omega_p t} + \xi_p^* e^{i\omega_p t} \right) \quad (5.9)$$

We now take

$$\omega_p = (\omega_q - \delta_q) + (\omega_w - \delta_w) - (\omega_b - \delta_b), \quad (5.10)$$

and expanding the cosine term to 4th order, and keeping only the non-rotating terms leads to

$$\begin{aligned} \mathbf{H}' &\approx \mathbf{H}_{\text{Stark}} + \mathbf{H}_{\text{Kerr}} + \mathbf{H}_{4WM} \\ \mathbf{H}_{\text{Stark}}/\hbar &= \sum_{m=b,w} (\delta_m - \chi_{qm} |\xi_p|^2) \mathbf{m}^\dagger \mathbf{m} + (\delta_q - 2\chi_{qq} |\xi_p|^2) \mathbf{q}^\dagger \mathbf{q} \\ \mathbf{H}_{\text{Kerr}}/\hbar &= \sum_{m=b,w,q} -\frac{\chi_{mm}}{2} \mathbf{m}^{\dagger 2} \mathbf{m}^2 - \chi_{qb} \mathbf{b}^\dagger \mathbf{b} \mathbf{q}^\dagger \mathbf{q} - \chi_{qw} \mathbf{w}^\dagger \mathbf{w} \mathbf{q}^\dagger \mathbf{q} - \chi_{bw} \mathbf{b}^\dagger \mathbf{b} \mathbf{w}^\dagger \mathbf{w} \\ \mathbf{H}_{4WM}/\hbar &= g_3 \mathbf{b} \mathbf{w}^\dagger \mathbf{q}^\dagger + g_3^* \mathbf{b}^\dagger \mathbf{w} \mathbf{q} \end{aligned} \quad (5.11)$$

With the coefficients $\hbar\chi_{mm} = E_J\phi_m^4/2$, $\hbar\chi_{qb} = E_J\phi_q^2\phi_b^2$, $\hbar\chi_{qw} = E_J\phi_q^2\phi_w^2$, $\hbar\chi_{bw} = E_J\phi_b^2\phi_w^2$ and $\hbar g_3 = -E_J\xi_p\phi_q^2\phi_b\phi_w$, which can also be written as

$$g_3 = -\xi_p \sqrt{\chi_{qb}\chi_{qw}}. \quad (5.12)$$

Note that we have neglected terms of the form $\mathbf{m}^\dagger \mathbf{m}$ arising from the normal ordering of the 4th order term, since they simply shift the bare frequencies ω_m by a constant amount. Since the qubit anharmonicity χ_{qq} is much larger than all the dissipation and excitation rates, in the following, we project the qubit mode onto its two lowest energy levels $|g\rangle$ and $|e\rangle$. We thus replace the bosonic operator \mathbf{q} by the two-level lowering operator $\boldsymbol{\sigma} = |g\rangle\langle e|$. Moreover, we choose the mode reference frames such that $\delta_q = 2\chi_{qq}|\xi_p|^2$, $\delta_b = \chi_{qb}|\xi_p|^2$ and $\delta_w = \chi_{qw}|\xi_p|^2 + \Delta$. We have introduced an arbitrary detuning Δ which, as we will see in the next section, can be chosen to cancel the effect of the cross-Kerr between the qubit and the waste χ_{qw} . This leads to $\mathbf{H}_{\text{Stark}}/\hbar = \Delta \mathbf{w}^\dagger \mathbf{w}$. The pump frequency thus needs to be adapted for each value of ξ_p in order to always verify (5.10)

$$\omega_p = \omega_q + \omega_w - \omega_b - \Delta - |\xi_p|^2 (2\chi_{qq} + \chi_{qw} - \chi_{qb}). \quad (5.13)$$

The Hamiltonian now reads:

$$\begin{aligned} H''/\hbar = & g_3 b w^\dagger \sigma^\dagger + g_3^* b^\dagger w \sigma + \Delta w^\dagger w \\ & + \sum_{m=b,w} -\frac{\chi_{mm}}{2} m^{\dagger 2} m^2 - \chi_{qb} b^\dagger b \sigma^\dagger \sigma - \chi_{qw} w^\dagger w \sigma^\dagger \sigma - \chi_{bw} b^\dagger b w^\dagger w \end{aligned} \quad (5.14)$$

5.2.4 Adiabatic elimination of the waste mode

A crucial resource in our system is the intentional dissipation of the waste mode w , which is coupled to a transmission line with a rate κ_w . In addition, the buffer mode is over-coupled (rate κ_w) to the input line which carries the incoming photons. Finally, the qubit mode is designed to be isolated from its environment, but inevitably has a residual uncontrolled dissipation at a rate κ_q , and dephasing κ_ϕ .

$$\frac{d}{dt} \rho = -i[H''/\hbar, \rho] + \kappa_w \mathcal{D}[w] \rho + \kappa_b \mathcal{D}[b] \rho + \kappa_q \mathcal{D}[\sigma] \rho + \frac{\kappa_\phi}{2} \mathcal{D}[\sigma_z] \rho \quad (5.15)$$

where the dissipation superoperator is defined in (C.3). We place ourselves in the regime where $|g_3|, \chi_{qb}, \chi_{bw}, \chi_{bb}, \kappa_b, \kappa_q, \kappa_\phi \sim \delta \kappa_w$, and δ is a small parameter $\delta \ll 1$. In our experiment, $\chi_{qw}/\kappa_w \sim 1$, and we assume $\Delta/\kappa_w \sim 1$. In this regime, the waste mode can be adiabatically eliminated, leading to an effective dynamics for the buffer and qubit modes alone. Following [32], we search for a solution of the full buffer-qubit-waste dynamics of the form

$$\begin{aligned} \rho = & \rho_{00} \otimes |0\rangle \langle 0| \\ & + \delta (\rho_{10} \otimes |1\rangle \langle 0| + \rho_{01} \otimes |0\rangle \langle 1|) \\ & + \delta^2 (\rho_{11} \otimes |1\rangle \langle 1| + \rho_{20} \otimes |2\rangle \langle 0| + \rho_{02} \otimes |0\rangle \langle 2|) + O(\delta^3), \end{aligned} \quad (5.16)$$

where $\rho_{mn} = \langle m | \rho | n \rangle$ is the reduce density matrix acting on the buffer Hilbert space with $|m\rangle, |n\rangle$ being the fock states basis of the waste mode, whereas $|n\rangle \langle m|$ acts on the waste Hilbert space. The goal here is to derive the dynamics of $\rho_{qb} = \text{Tr}_w(\rho) = \rho_{00} + \delta^2 \rho_{11}$ up to second order in δ , where Tr_w denotes the partial trace over the waste degrees of freedom. The low occupancy of the waste mode justifies this expansion. We are interested in the dynamics of the reduced density operator for the qubit-buffer modes ρ_{qb} , which is obtained by taking the partial trace over the waste mode. We rewrite the Hamiltonian of eq. (5.14) in the following form

$$\begin{aligned} H''/\hbar = & g_3 b \sigma^\dagger w^\dagger + g_3^* b^\dagger \sigma w + \left(\Delta - \chi_{qw} \sigma^\dagger \sigma - \chi_{bw} b^\dagger b \right) w^\dagger w + H_{qb}/\hbar \\ H_{qb}/\hbar = & -\frac{\chi_{bb}}{2} b^{\dagger 2} b^2 - \chi_{qb} b^\dagger b \sigma^\dagger \sigma \end{aligned} \quad (5.17)$$

and we define

$$\mathcal{L}_{qb}(\rho_{qb}) = -\frac{i}{\hbar}[\mathbf{H}_{qb}, \rho_{qb}] + \kappa_b \mathcal{D}[\mathbf{b}]\rho_{qb} + \kappa_q \mathcal{D}[\boldsymbol{\sigma}]\rho_{qb} + \frac{\kappa_\phi}{2} \mathcal{D}[\boldsymbol{\sigma}_z]\rho_{qb} \quad (5.18)$$

By projecting eq. (5.15) with $\langle 0| \dots |0\rangle$, $\langle 0| \dots |1\rangle$, and $\langle 1| \dots |1\rangle$ respectively, we get

$$\frac{d}{\kappa_w dt} \rho_{00} = \delta^2 \left(i \rho_{01} \mathbf{A} - i \mathbf{A}^\dagger \rho_{10} + \rho_{11} \right) + \frac{1}{\kappa_w} \mathcal{L}_{qb}(\rho_{00}) + O(\delta^3) \quad (5.19)$$

$$\frac{d}{\kappa_w dt} \rho_{01} = i \rho_{00} \mathbf{A}^\dagger - \rho_{01} \left(\frac{1}{2} - i \boldsymbol{\Delta} \right) + O(\delta) \quad (5.20)$$

$$\frac{d}{\kappa_w dt} \rho_{11} = i \rho_{10} \mathbf{A}^\dagger - i \mathbf{A} \rho_{01} - i[\boldsymbol{\Delta}, \rho_{11}] - \rho_{11} + O(\delta) \quad (5.21)$$

where

$$\mathbf{A} = \frac{g_3}{\kappa_w \delta} \mathbf{b} \boldsymbol{\sigma}^\dagger \quad \text{and} \quad \boldsymbol{\Delta} = \frac{\Delta - \chi_{qw} \boldsymbol{\sigma}^\dagger \boldsymbol{\sigma}}{\kappa_w} \quad (5.22)$$

Note that $\|\mathbf{A}\|$ and $\|\boldsymbol{\Delta}\|$ are of order δ^0 . Considering eq. (5.20), we see that the derivative of ρ_{01} is composed of a term proportional to ρ_{00} that can be viewed as an external drive, and a term proportional to ρ_{01} , that includes a damping term. Since the variation of ρ_{00} is slow ($d\rho_{00}/\kappa_w dt$ of order δ^2 , see eq. (5.19)) in comparison to the damping term (of order δ^0), we can make the adiabatic approximation: we consider that ρ_{01} is continuously in its steady state. The same reasoning applies to ρ_{11} , we thus set to 0 the derivatives of the left hand sides of eqs. 5.20 and 5.21. Moreover, by noting that $\boldsymbol{\Delta} \mathbf{a} = (\Delta - \chi_{qw}) \mathbf{A} / \kappa_w$, we can solve for $\rho_{01}, \rho_{10}, \rho_{11}$ as a function of ρ_{00} . We find

$$\rho_{01} = \frac{1}{1 + 4 \left| \frac{\Delta - \chi_{qw}}{\kappa_w} \right|^2} \left(2i - 4 \frac{(\Delta - \chi_{qw})}{\kappa_w} \right) \rho_{00} \mathbf{A}^\dagger \quad (5.23)$$

$$\rho_{11} = \frac{1}{1 + 4 \left| \frac{\Delta - \chi_{qw}}{\kappa_w} \right|^2} 4 \mathbf{A} \rho_{00} \mathbf{A}^\dagger. \quad (5.24)$$

We denote

$$\kappa_{nl} = \frac{4|g_3|^2/\kappa_w}{1 + 4 \left| \frac{\Delta - \chi_{qw}}{\kappa_w} \right|^2} \quad \text{and} \quad \Delta_{nl} = \frac{4|g_3|^2/\kappa_w}{1 + 4 \left| \frac{\Delta - \chi_{qw}}{\kappa_w} \right|^2} \frac{\chi_{qw} - \Delta}{\kappa_w}. \quad (5.25)$$

Inserting the solutions (5.23), (5.24) into eq. (5.19) we find

$$\frac{d}{dt} \rho_{00} = -i \Delta_{nl} [\mathbf{b}^\dagger \mathbf{b} \boldsymbol{\sigma} \boldsymbol{\sigma}^\dagger, \rho_{00}] + \kappa_{nl} \mathcal{D}[\mathbf{b} \boldsymbol{\sigma}^\dagger] \rho_{00} + \mathcal{L}_{qb}(\rho_{00}) + O(\delta^3). \quad (5.26)$$

The term proportionnal to κ_{nl} is the non-linear damping term at the heart of the Single Microwave Photon Detector. It is maximized for $\Delta = \chi_{qw}$. In this configuration, the pump angular frequency $\omega_p = \omega_q + \omega_w - \omega_b - \chi_{qw}$ is such that $\hbar\omega_p$ exactly matches the energy difference between the initial state $\mathbf{b}^\dagger |0, 0\rangle |0\rangle = |1, 0\rangle |0\rangle$ (ω_b) and final state

$\sigma^\dagger \mathbf{w}^\dagger |0, 0\rangle |0\rangle = |0, 1\rangle |1\rangle (\omega_q + \omega_w - \chi_{qw})$, and $\kappa_{nl} = 4|g_3|^2/\kappa_w$. The term proportional to Δ_{nl} is a “generalized frequency pull” that corresponds to a tunable cross-Kerr effect between the qubit and buffer modes. Note that the $\rho_{qb} = \rho_{00} + \delta^2 \rho_{11}$ follows the same dynamics as eq. (5.26) (since we assumed $d\rho_{11}/\kappa_w dt = 0$).

5.2.5 Qubit dynamics and detection efficiency

Efficiency for single-photon Fock states The detector efficiency is defined as the probability p_e to find the qubit in the excited state, when a Fock state $|1\rangle$ is incident on the buffer cavity. However in this experiment, we calibrate our photon-detector with coherent states. In the following, we provide a simple argument to bridge the gap between this definition of η and the experiment performed with coherent states.

We can formally describe the output of a random source that emits a single-photon with a small probability ϵ with the density matrix

$$\rho = (1 - \epsilon) |0\rangle \langle 0| + \epsilon |1\rangle \langle 1|. \quad (5.27)$$

With such a source, the detector should click with a probability $p_e = \eta\epsilon$. Besides, a coherent state with a small complex amplitude α writes

$$|\psi\rangle \approx (1 - \frac{1}{2}|\alpha|^2)(|0\rangle + \alpha|1\rangle), \quad (5.28)$$

and thus the statistical mixture of coherent states with unknown phase writes

$$\rho \approx (1 - |\alpha|^2) |0\rangle \langle 0| + |\alpha|^2 |1\rangle \langle 1|. \quad (5.29)$$

Therefore, one can identify this statistical mixture with an intermittent single photon source providing that $\epsilon = |\alpha|^2$ is small. The probability of click will then be $p_e = \eta\epsilon = \eta\bar{n}$ in either case.

Efficiency for coherent states In order to describe the effect of coherent states on the detector and to compute η , we now add an input drive of amplitude $\epsilon = \sqrt{\kappa_b} b_{in}$ where b_{in} is the amplitude of the coherent pulse. We start from eq. (5.26), where we neglect $\chi_{bb}, \chi_{qb}, \kappa_q \ll \kappa_{nl}, \kappa_b$, and take $\Delta = \chi_{qw}$

$$\frac{d}{dt} \rho_{qb} = \kappa_{nl} \mathcal{D}[b\sigma^\dagger] \rho_{qb} + \kappa_b \mathcal{D}[b] \rho_{qb} + \epsilon [b - b^\dagger, \rho_{qb}]. \quad (5.30)$$

We would now like to calculate the qubit excited state population p_e as a function of the number of photons in the incoming wave-packet of length T : $\bar{n}_{in} = |b_{in}|^2 \times T$, where

we assume for simplicity that b_{in} is time-independent. We may write the solution of eq. (5.30) in the general form $\rho_{qb} = \rho_{gg} |g\rangle \langle g| + \rho_{ge} |g\rangle \langle e| + \rho_{eg} |e\rangle \langle g| + \rho_{ee} |e\rangle \langle e|$, and we are interested in $p_e = \text{tr}(\rho_{ee})$. We find

$$\frac{d}{dt} \rho_{gg} = -\frac{\kappa_{nl}}{2} (\mathbf{b}^\dagger \mathbf{b} \rho_{gg} + \rho_{gg} \mathbf{b}^\dagger \mathbf{b}) + \kappa_b \mathcal{D}[\mathbf{b}] \rho_{gg} + \epsilon [\mathbf{b} - \mathbf{b}^\dagger, \rho_{gg}] \quad (5.31)$$

$$\frac{d}{dt} \rho_{ee} = \kappa_{nl} \mathbf{b} \rho_{gg} \mathbf{b}^\dagger + \kappa_b \mathcal{D}[\mathbf{b}] \rho_{ee} + \epsilon [\mathbf{b} - \mathbf{b}^\dagger, \rho_{ee}] \quad (5.32)$$

Hence

$$\frac{d}{dt} p_e = \kappa_{nl} \text{tr}(\mathbf{b} \rho_{gg} \mathbf{b}^\dagger), \quad (5.33)$$

and we now need to solve eq. (5.31) for which, remarkably, we find a simple ansatz:

$$\rho_{gg}(t) = \exp\left(-4 \frac{\epsilon^2}{(\kappa_{nl} + \kappa_b)^2} \kappa_{nl} t\right) |\beta\rangle \langle \beta| \quad (5.34)$$

$$\beta = -2\epsilon/(\kappa_{nl} + \kappa_b) \quad (5.35)$$

where $|\beta\rangle$ is a coherent state of amplitude β . Note that $\text{tr}(\mathbf{b} \rho_{gg} \mathbf{b}^\dagger) = \beta^2 \exp\left(-4 \frac{\epsilon^2}{(\kappa_{nl} + \kappa_b)^2} \kappa_{nl} t\right)$, and hence inserting this expression in eq. (5.33), we find

$$\frac{d}{dt} p_e = 4\kappa_{nl} \frac{\epsilon^2}{(\kappa_{nl} + \kappa_b)^2} \exp\left(-4 \frac{\epsilon^2}{(\kappa_{nl} + \kappa_b)^2} \kappa_{nl} t\right). \quad (5.36)$$

Assuming the qubit in its ground state at $t = 0$, we find

$$p_e(T) = 1 - \exp\left(-\eta |b_{in}|^2 T\right), \quad (5.37)$$

where

$$\eta = 4 \frac{\kappa_b \kappa_{nl}}{(\kappa_{nl} + \kappa_b)^2}, \quad (5.38)$$

which can be written as

$$p_e = 1 - \mathbb{P}_0^\eta \underset{\bar{n}_{in} \rightarrow 0}{\sim} \eta \bar{n}_{in}. \quad (5.39)$$

Here $\mathbb{P}_0 = \exp(-\bar{n}_{in})$ is the population of Fock state 0 of the incoming coherent pulse which has a mean photon number $\bar{n}_{in} = |b_{in}|^2 \times T$ and follows a Poisson distribution. We see from eq.(5.4) that $\eta = 1$ when $\kappa_{nl} = \kappa_b$.

Time-dependent pulses This derivation was made for a time independent pulse amplitude ϵ but one arrives to a similar result for $\epsilon(t)$. We start from eq. (5.31) and

eq. (5.32) where ϵ is replaced by a time-dependent pulse $\epsilon(t)$. We assume that $\epsilon(t)$ represents a wavepacket so that $\epsilon(t \rightarrow -\infty) = \epsilon(t \rightarrow \infty) = 0$. We define $\tilde{\rho}_{gg}$ such as

$$\frac{d}{dt}\tilde{\rho}_{gg} = (\kappa_b + \kappa_{nl})\mathcal{D}[\mathbf{b}]\tilde{\rho}_{gg} + \epsilon(t)[\mathbf{b} - \mathbf{b}^\dagger, \tilde{\rho}_{gg}] \quad (5.40)$$

which is the intracavity state of a two-port driven cavity. Importantly, this is a coherent state at all time. We can show that

$$\rho_{gg}(t) = f(t)\tilde{\rho}_{gg}(t) \quad (5.41)$$

is solution of eq. (5.31) with a time dependent pulse where

$$f(t) = \exp\left(-\kappa_{nl} \int_0^t |\beta(t)|^2 dt\right) \quad (5.42)$$

$$|\beta(t)|^2 = \text{tr}(\mathbf{b}\tilde{\rho}_{gg}(t)\mathbf{b}^\dagger) \quad (5.43)$$

and $\beta(t)$ is easy to compute. We have that

$$\frac{d}{dt}p_e = \kappa_{nl} \text{tr}(\mathbf{b}\rho_{gg}\mathbf{b}^\dagger) = \kappa_{nl}f(t)|\beta(t)|^2 \quad (5.44)$$

so we can find the occupation of the qubit after the pulse $p_e(+\infty) \equiv p_e = 1 - f(+\infty)$

$$\begin{aligned} p_e &= 1 - \exp\left(-\kappa_{nl} \int_{-\infty}^{+\infty} |\beta(t)|^2 dt\right) \\ &= 1 - \exp\left(-\kappa_{nl} \frac{1}{2\pi} \int_{-\infty}^{+\infty} |\beta(\omega)|^2 d\omega\right) \\ &= 1 - \exp\left(-\frac{1}{2\pi} \int_{-\infty}^{+\infty} \kappa_b \kappa_{nl} \left| \frac{b_{in}(\omega)}{(\kappa_{nl} + \kappa_b)/2 + i\omega} \right|^2 d\omega\right) \end{aligned} \quad (5.45)$$

where $b_{in}(\omega)$ is the incoming pulse in the frequency domain. We can rewrite this as

$$p_e = 1 - \exp(-\bar{n}_{cav}) = 1 - \mathbb{P}_{0,cav} \quad (5.46)$$

where \bar{n}_{cav} is the overall number of photons that actually reach into the buffer. This is to be compared to

$$\bar{n}_{pulse} = \frac{1}{2\pi} \int_{-\infty}^{+\infty} |b_{in}(\omega)|^2 d\omega \quad (5.47)$$

the number of photons in the incoming pulse. eq. (5.45) shows the filtering of the incoming pulse due to the loss mismatch ($\kappa_b \neq \kappa_{nl}$) of the detector and its finite bandwidth ($\kappa_b + \kappa_{nl}$).

5.2.6 Reset protocol

For the reset procedure, we switch off the drive on the buffer mode, and instead, we add a resonant drive on the waste port (this drive is sent at $\omega_w - \chi_{qw}$ since the qubit is in $|e\rangle$ when we want to reset). This adds to the Hamiltonian of equation (5.17) the following term $\mathbf{H}_{\text{drive}} = \epsilon_w (\mathbf{w} + \mathbf{w}^\dagger)$, which can be absorbed by replacing the operator $\mathbf{b}\sigma^\dagger \rightarrow \mathbf{b}\sigma^\dagger + \epsilon_w/g_3$. Using this modified expression, the rest of the calculation follows. Note that

$$\kappa_{\text{nl}} \mathcal{D}[\mathbf{b}\sigma^\dagger + \frac{\epsilon_w}{g_3}] \rho_{qb} = \kappa_{\text{nl}} \mathcal{D}[\mathbf{b}\sigma^\dagger] \rho_{qb} + \kappa_{\text{nl}} \frac{\epsilon_w}{2g_3} [\mathbf{b}\sigma^\dagger - \mathbf{b}^\dagger \sigma, \rho_{qb}] \quad (5.48)$$

This leads to

$$\frac{d}{dt} \rho_{qb} = \kappa_b \mathcal{D}[\mathbf{b}] \rho_{qb} + \kappa_{\text{nl}} \mathcal{D}[\mathbf{b}\sigma^\dagger] \rho_{qb} + \epsilon_{\text{nl}} [\mathbf{b}\sigma^\dagger - \mathbf{b}^\dagger \sigma, \rho_{qb}] , \quad (5.49)$$

where $\epsilon_{\text{nl}} = \kappa_{\text{nl}} \frac{\epsilon_w}{2g_3}$. Instead of repeating the entire analysis of the previous sections, we will proceed using a useful analogy. We see that eq. (5.49) can be mapped to eq. (5.30) by making the following substitutions $\kappa_b \leftrightarrow \kappa_{\text{nl}}$, $\mathbf{b} \leftrightarrow \mathbf{b}\sigma^\dagger$ and $\epsilon_{\text{nl}} \leftrightarrow \epsilon$. We have shown that the dynamics of eq. (5.30) leads the qubit to dissipate from its ground to its excited state at rate $4 \frac{\epsilon^2}{(\kappa_{\text{nl}} + \kappa_b)^2} \kappa_{\text{nl}}$ (see eq. (5.37)). By analogy, the dynamics of eq. (5.49) leads the qubit to dissipate from its excited state to its ground state at a rate

$$\kappa_{\text{reset}} = 4 \frac{\epsilon_{\text{nl}}^2}{(\kappa_b + \kappa_{\text{nl}})^2} \kappa_b \quad (5.50)$$

$$= 4 \frac{\epsilon_w^2}{(\kappa_b + \kappa_{\text{nl}})^2} \kappa_{\text{nl}} \frac{\kappa_b}{\kappa_w} . \quad (5.51)$$

5.2.7 Spectroscopic characterization of the detector

When inserting the optimal pump frequency predicted by eq. (5.26) ($\Delta = \chi_{qw}$) into the frequency matching condition (5.13), we find

$$\omega_p = \left(\omega_q - 2\chi_{qq}|\xi_p|^2 \right) + (\omega_w - \chi_{qw}(1 + |\xi_p|^2)) - (\omega_b - \chi_{qb}|\xi_p|^2) . \quad (5.52)$$

This equation is equivalent to eq. (5.1) with $\bar{\omega}_q \equiv \omega_q - 2\chi_{qq}|\xi_p|^2$, $\omega_w^e \equiv \omega_w - \chi_{qw}(1 + |\xi_p|^2)$ and $\omega_b^g \equiv \omega_b - \chi_{qb}|\xi_p|^2$. Notice that in the previous section, for clarity, we have neglected the AC-Stark shifts on the buffer and waste since $|\xi_p|^2 \chi_{qb,w} < |g_3|$. To match this condition, we realize a calibration experiment where the pump power and frequency are scanned over the relevant range of parameter space and we measure the probability p_e to find the qubit in the excited state. We first perform a control experiment, where the buffer is left undriven (Figure 5.6a). The experiment is then repeated with a small

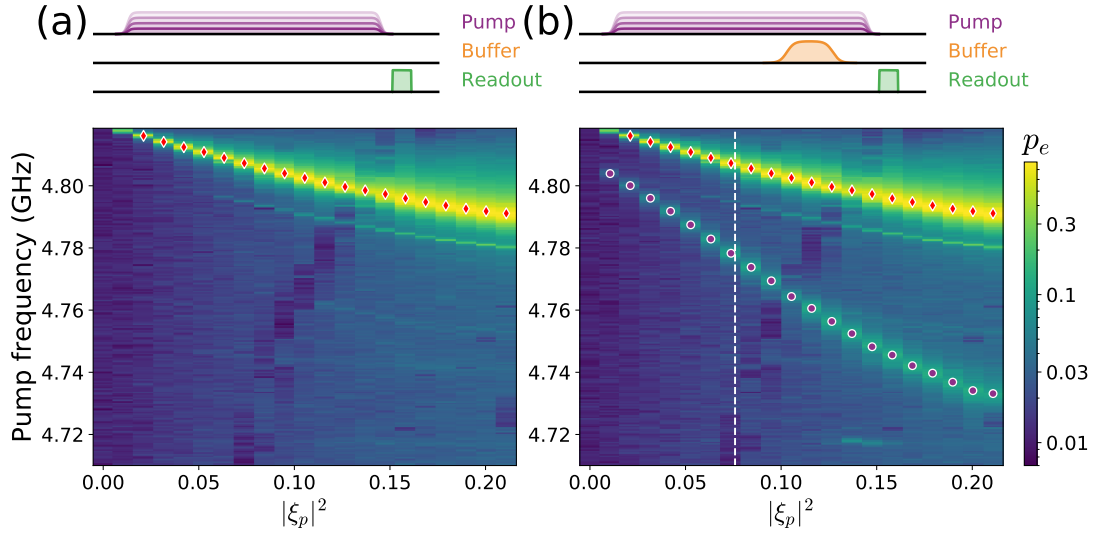


FIGURE 5.6: Complete spectroscopic data: (a-b) The excited state population of the qubit p_e (color-coded) is represented as a function of the pump amplitude (x-axis) and pump-frequency (y-axis). (a) When there is no incoming photon on the buffer port, we find one spectroscopic line (red diamonds) for which the qubit is sent into its excited. This corresponds to a higher order amplification process of the form . We also observe that the background p_e is rising approximately linearly with the pump power at all the frequencies which is consistent with the heating of the qubit bath by the pump. (b) When we add a pulse on the buffer port at frequency ω_b , another line (purple circles) appears. This line corresponds the process $b\sigma^\dagger w^\dagger$ and the white dashed line indicates the chosen pump power which maximize the ratio η/Γ_{dc} . We can also observe a spectroscopic line which goes upward which seems to cool the qubit and thus decreases the efficiency (see dip in κ_{nl} in Fig. 5.1a). This was the main reason for limiting the pump power to the chosen value. Also, past this line, the dark count rate increases too much compared to the gain in the efficiency

coherent drive pulse on the buffer (Figure 5.6b). The line corresponding to the process $b\sigma^\dagger w^\dagger$ is clearly identified since the qubit excitation probability p_e vanishes in the absence of buffer drive. For each pump power, the frequency f_{p0} that maximizes the qubit excitation probability within the relevant line is represented with a red dot on Fig. 5.6, and it is also reported in Fig. 5.1a. The linear dependence of f_{p0} as a function of $|\xi_p|^2$ is used, together with the independently measured value $\chi_{qq} = 146$ MHz, to calibrate $|\xi_p|^2$ in terms of photon number via the relation (5.52). We attribute the spurious line appearing in both control and calibration experiments to the 6th order non-linear process $\xi_p^3 b^\dagger \sigma^\dagger \sigma_{ef}^\dagger$, where σ_{ef} is the lowering operator between the second and first qubit excited states. Indeed, the frequency and slope of the line as a function of pump-power are in good qualitative agreement with the expected value $\omega_{p,spurious} = (\bar{\omega}_q + \bar{\omega}_q^{ef} + \omega_b)/3$.

5.2.8 Tomography of the itinerant transmitted photon

The non-linear process at the heart of the single photon detector converts the incoming photons (centered around the buffer frequency ω_b) into photons emitted into the waste

line at the waste frequency ω_w^e (the frequency of the waste when the qubit is in the excited state). The field propagating in the waste line is amplified by a near quantum-limited phase-preserving amplifier and demodulated at the frequency $(\omega_w^g + \omega_w^e)/2$. Examples of demodulated time traces, with a sampling rate of 50 MS/s are shown in figure 5.7c. Besides providing a strongly damped mode for the converted photons, in our experiment, the waste is used to read-out the qubit state. Consequently, the time traces are split in two consecutive segments (see Fig. 5.7c). The first part of the traces of duration $t_m = 3.4 \mu\text{s}$ contains an excess noise directly attributable to the up-converted photon and are used to reconstruct the quantum state of propagating field. The second part of the traces of duration $t_r = 0.6 \mu\text{s}$, during which the waste cavity is coherently driven by the readout pulse, are used to infer the qubit state.

Determination of the outgoing photon mode shape The complex mode-shape in which single-photons are emitted by the waste corresponds to the input pulse mode-shape which is filtered by the buffer and waste bandwidth as well as the qubit thresholding response, it also undergoes an overall frequency conversion. We employ the method described in Ref. [140] to determine this waveform experimentally from the 88000 traces where the qubit was detected in state $|e\rangle$: we first combine the raw I and Q quadratures from the digitizer to form the complex discrete-time traces

$$z(t_j) = I(t_j) + iQ(t_j). \quad (5.53)$$

We then compute the autocorrelation matrix $\langle z^*(t_j)z(t_k) \rangle$ by averaging the two-time correlators over the full dataset. The autocorrelation matrix is diagonalized to find the basis of uncorrelated temporal modes. While most of the eigenvalues have a comparable weight, corresponding to the vacuum and amplifier noise in the unpopulated temporal modes, the largest eigenvalue is significantly larger (by $\sim 25\%$). The corresponding complex eigenfunction $f(t_j)$ provides thereby the optimal temporal mode, as plotted in Fig. 5.4c and 5.7c and is normalized such that $\sum_j |f(t_j)|^2 = 1$.

Photon reconstruction Now that the temporal-shape of the itinerant mode is identified, we will focus on its quantum state. Following Ref. [141], we infer the quantum state in the mode-shape f by calculating the various moments of the complex amplitude distribution

$$S = \sum_j f^*(t_j)z(t_j). \quad (5.54)$$

The experimental phase-space distribution of S conditioned on measuring the qubit in $|g\rangle$ and $|e\rangle$ is presented in Fig. 5.7d. The measured distributions –that would correspond to the field’s Q-function for a quantum-limited detection– are significantly broadened by the amplifier’s classical-noise. However, a clear excess-noise is visible on the distribution corresponding to $|e\rangle$, that reflects the increased fluctuations in the mode of interest due to the emitted photon. On a formal level, the observable S can be expressed as a function of the amplifier gain G , the annihilation operator \mathbf{a} in mode f , and the annihilation operator \mathbf{H} in an external mode describing the noise added by the amplifier

$$\mathbf{S} = \sqrt{G} (\mathbf{a} + \mathbf{H}^\dagger). \quad (5.55)$$

Under the assumption that the amplifier noise \mathbf{H} is uncorrelated with the signal \mathbf{a} , we get the following expression for the moments of \mathbf{S} [141]

$$\langle (\mathbf{S}^\dagger)^n \mathbf{S}^m \rangle_\rho = G^{(n+m)/2} \sum_{i,j=0}^{n,m} \binom{m}{j} \binom{n}{i} \langle (\mathbf{a}^\dagger)^i \mathbf{a}^j \rangle_\rho \langle \mathbf{H}^{n-i} (\mathbf{H}^\dagger)^{m-j} \rangle. \quad (5.56)$$

Remarkably, the moments $\langle \mathbf{H}^n (\mathbf{H}^\dagger)^m \rangle = G^{-(n+m)/2} \langle (\mathbf{S}^\dagger)^n \mathbf{S}^m \rangle_{|0\rangle\langle 0|}$ can be retrieved experimentally by performing a calibration experiment with the mode \mathbf{a} in the vacuum state, where $\langle (\mathbf{S}^\dagger)^n \mathbf{S}^m \rangle_{|0\rangle\langle 0|}$ comes from the raw data and the only remaining unknown is the gain G .

The gain G is calibrated by a control experiment. We send a well calibrated pulse (see [35]) on the waste port which reflects back and gets detected by the digitizer (Fig. 5.7f,g). Provided the waste is overcoupled to its transmission line (see table 5.1), the coherent state in the reflected mode-shape (Fig. 5.7h) is equal to the incoming one. Assuming the noise is unbiased, we have $\langle \mathbf{S} \rangle = \sqrt{G} \langle \mathbf{a} \rangle$ and hence measuring $\langle \mathbf{S} \rangle$ for 3 values of $\langle \mathbf{a} \rangle$ (Fig. 5.7i) we deduce G .

The relation (5.56) can then be inverted to obtain the moments of the field’s distribution $\langle (\mathbf{a}^\dagger)^n \mathbf{a}^m \rangle_{\rho_{\text{exp}}}$ (Fig. 5.7e,j). We perform this reconstruction up to 4th order ($n+m \leq 4$). We finally perform a maximum-likelihood estimation of the field’s density matrix ρ_{ml} by minimizing the distance between the measured and expected moments:

$$\mathcal{D}(\rho_{\text{exp}}, \rho_{\text{ml}}) = \sum_{\substack{m,n \\ m+n \leq 4}} \left| \langle (\mathbf{a}^\dagger)^n \mathbf{a}^m \rangle_{\rho_{\text{exp}}} - \langle (\mathbf{a}^\dagger)^n \mathbf{a}^m \rangle_{\rho_{\text{ml}}} \right|^2. \quad (5.57)$$

The Wigner-functions plotted in Figure 5.4 are calculated from the density matrix ρ_{ml} .

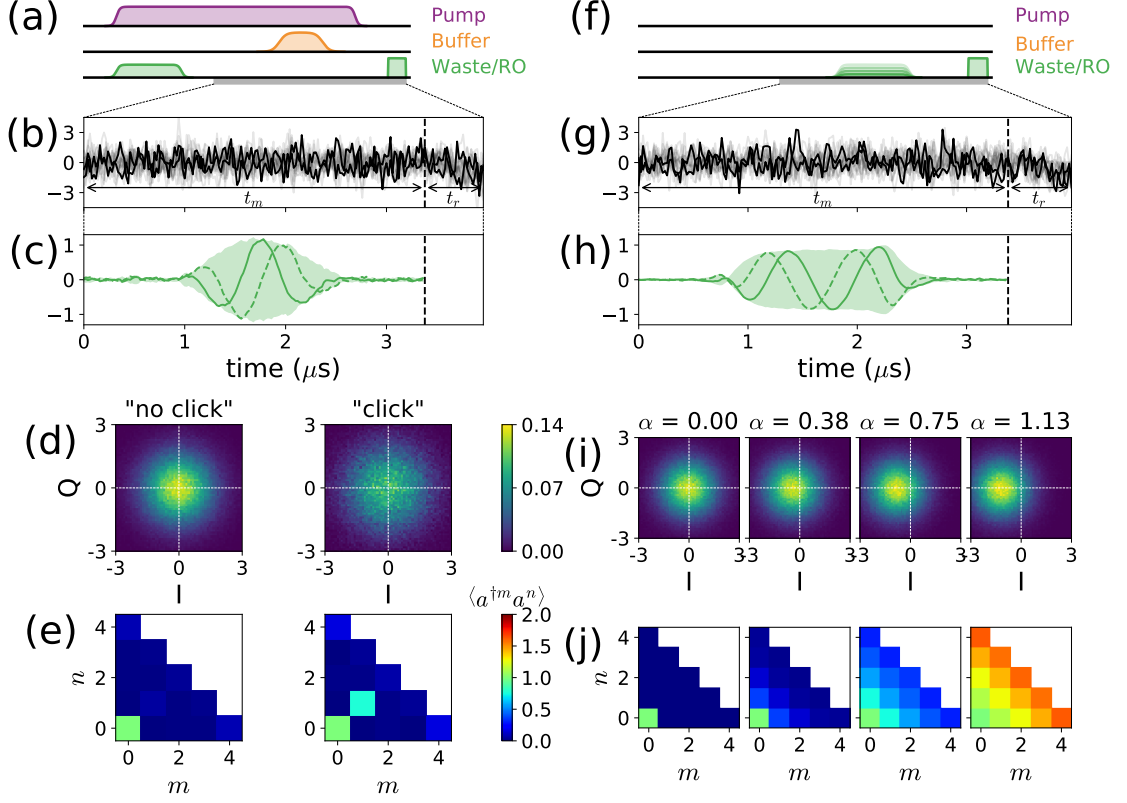


FIGURE 5.7: Tomography of the itinerant field states: measurement of the field emitted during a detection sequence (left) and calibration experiment (right). (a, e) Pulse sequences for the state-reconstruction experiment (a) and amplification calibration (e). The field emitted by the waste is monitored by a phase preserving amplifier (grey rectangle). (b, g) Experimental traces demodulated at $(\omega_w^g + \omega_w^e)/2$ (only one quadrature is represented): the first part of the trace (duration t_m) is used for the itinerant field-state reconstruction while the second part (duration t_r) is used for qubit state discrimination. (c-h) Mode-shape determined experimentally for the single-photon (c) and coherent fields (h) used for calibration. (d, i) Measured phase space distribution of the propagating field before amplification \mathbf{S}/\sqrt{G} , it corresponds to the Husimi-Q representation of the quantum state broadened by the equivalent input noise of the amplifier expressed in unit of square-root of photons. The distribution is conditioned on the detection of the qubit in $|g\rangle$ or $|e\rangle$ (d) and for the various coherent state amplitudes used for calibration (i). (e,j) Experimental reconstruction of the moments of the distribution $\langle (\mathbf{a}^\dagger)^n \mathbf{a}^m \rangle_\rho$ obtained by inverting eq. (5.56).

Conclusion and perspectives

The goal of error correction is to decrease the error rate of a logical qubit to a small enough value in order to execute a desired algorithm. In fact, simply decreasing this rate below the physical qubit error rate has been an long standing challenge, which has only been barely met recently [143]. The reason why "doing nothing" is almost always better than deploying the arsenal of QEC, is that the additional complexity of ancillary qubits, measurements and gates, introduce errors themselves. Remarkably, the quantum error correction threshold theorem states that even though all the constituent parts of a quantum processor are faulty, these can be arranged to prolong the QI lifetime for arbitrary long times, simply by increasing the encoding redundancy and provided the errors are below a threshold. In practice, one would expect that this increase will saturate at finite lifetimes [103] due to unforeseen error processes which are not corrected by the code architecture. Such processes could arise from highly correlated noise due for example to the impact of high energy particles on a chip, hardware failure or more subtle phenomena. Research on quantum error correction will most likely require identifying these error processes and designing new codes accordingly. Using quantum error correction as a tool to probe subtle physical processes which limit QI lifetimes would be a beautiful application of quantum information science.

In this thesis, we have revisited the strategy of QEC by encoding QI in a resonator and focussing on a single error channel, the bit-flip. The large Hilbert space of the resonator provides the redundancy and the non-locality in which quantum error correction is rooted. If one is willing to abandon the protection against phase-flips, the cat-qubit encoding presents two advantages among the bosonic codes. First, it offers a compact (single mode and small photon numbers) way of encoding information non-locally in the real field quadrature space. Second and more importantly, the basis states are stable steady-states of dissipative dynamics that do not induce phase-flips. Thus, the two-photon dissipation autonomously protects against bit-flips which makes this approach appealing for practical implementation. By carefully designing the two-photon non-linear coupling, we were able to cross the demanding threshold where the correction

is faster than the occurrence of all errors. We demonstrated that the bit-flips are suppressed exponentially in the cat-qubit photon number while the phase-flips only linearly increase, leading to a 300 fold improvement in the bit flip time.

In order to reach this milestone, we had to go back to the fundamentals of parametric pumping and question its past limitations. We found that circuits with bounded potential energy, such as transmon based architectures, were inherently unstable when subject to strong pumps and experimentally verified that they get propelled into high energy unconfined states losing their non-linear properties. This observation motivated shunted Josephson circuits as non-linear couplers compatible with parametric pumping.

The expertise developed during this thesis in dissipation engineering also led to an unforeseen application: a single microwave photon detector. The dissipative mechanism counterintuitively excites a qubit upon the arrival of a microwave photon. In fact, thanks to the pump, the detector converts the incoming photon into two: one excitation in the qubit and one photon that rapidly decays out, preventing the reverse process to happen. This proof-of-concept exhibited good performances: the detection is robust to the photon arrival time and its waveform, and a record low dark count rate for it is independent of the coherence properties of the circuit.

Future implementations of QEC with cat-qubits would benefit from simple design improvements which should extend the bit-flip time of a cat-qubit to macroscopic times (of order seconds). Still, the cat-qubit strategy would be flawed if it were not for the possibility to correct for the remaining error, phase-flips, without inducing bit-flips [108]. Crucially, the two dimensional field-quadrature space of cat-qubits can be accessed to perform simple gates while preserving the distance between the two basis states. This key feature points towards a linear chain of cat qubits forming a repetition code, as presented in the introduction, to correct for the single remaining error type. Provided, one reaches below-threshold error rates in measuring joint-parities of cat-qubits, the phase-flip rate should decrease exponentially with the length of the chain. This would dramatically reduce the overhead required for QEC, bringing it closer to the realm of experimental implementation.

Appendix A

Circuit quantization

A.1 LC-oscillator	108
A.1.1 Quantization	108
A.1.2 Coupling to the circuit	110
A.1.3 Dissipation	111
A.2 General Circuit quantization	113
A.2.1 Circuit description	113
A.2.2 Equations of motion	114
A.2.3 Circuit eigenmodes	117
A.2.4 Distributed elements	120

In this appendix, we detail the quantization procedure we summarized in chapter 2. This is meant to closely follow the notation of the Python program we developed.

A.1 LC-oscillator

Let us start with the most simple circuit that has a single degree of freedom, the LC-oscillator. In this section, we reproduce standard derivations to setup the notations for the rest of the chapter.

A.1.1 Quantization

At any point in time, the circuit is fully described by the voltage and current across each dipole $V(t)$ and $I(t)$ respectively. The underlying relevant variable is the flux threading each dipole defined as $\dot{\Phi}(t) = V(t)$ [39].

Canonical quantization The Lagrangian of the system is $\mathcal{L} = C\dot{\Phi}^2/2 - \Phi^2/2L$. The conjugate variable of Φ is the charge across the dipole $Q = \frac{d\mathcal{L}}{d\dot{\Phi}} = C\dot{\Phi}$ so the Hamiltonian writes $\mathcal{H} = \dot{\Phi}Q - \mathcal{L} = Q^2/2C + \Phi^2/2L$. From the Hamiltonian, we get the following equations of motion

$$\begin{bmatrix} \dot{\Phi} \\ \dot{Q} \end{bmatrix} = \begin{bmatrix} 0 & 1/C \\ -1/L & 0 \end{bmatrix} \begin{bmatrix} \Phi \\ Q \end{bmatrix}. \quad (\text{A.1})$$

It is useful to diagonalize them into

$$\begin{bmatrix} \dot{\alpha} \\ \dot{\alpha}^* \end{bmatrix} = \begin{bmatrix} -i\omega_0 & 0 \\ 0 & i\omega_0 \end{bmatrix} \begin{bmatrix} \alpha \\ \alpha^* \end{bmatrix} \quad (\text{A.2})$$

with $\omega_0 = 1/\sqrt{LC}$, $Z = \sqrt{L/C}$ and

$$\begin{bmatrix} \Phi \\ Q \end{bmatrix} = \lambda \begin{bmatrix} 1 & 1 \\ -i/Z & i/Z \end{bmatrix} \begin{bmatrix} \alpha \\ \alpha^* \end{bmatrix} \quad \text{or} \quad \begin{bmatrix} \alpha \\ \alpha^* \end{bmatrix} = \frac{1}{2\lambda} \begin{bmatrix} 1 & iZ \\ 1 & -iZ \end{bmatrix} \begin{bmatrix} \Phi \\ Q \end{bmatrix}. \quad (\text{A.3})$$

where λ is a free scalar to be determined. Quantizing this harmonic oscillator amounts to promoting Φ and Q to the quantum operators $\mathbf{\Phi}$ and \mathbf{Q} which have the following commutation relation $[\mathbf{\Phi}, \mathbf{Q}] = i\hbar$. The equations of motion A.2 reveal two independent degrees of freedom α and α^* which have an oscillatory behaviour at frequency ω_0 . We promote them to operators \mathbf{a} and \mathbf{a}^\dagger using relation A.3. One recognises the annihilation and creation operators if the free parameter is set so that $[\mathbf{a}, \mathbf{a}^\dagger] = 1$. This leads to $\lambda = \sqrt{\hbar Z/2} \equiv \Phi_{\text{zpf}}$ the zero-point fluctuations of the flux. In term of these ladder operators, the Hamiltonian writes.

$$\mathbf{H} = \hbar\omega_0(\mathbf{a}^\dagger\mathbf{a} + 1/2). \quad (\text{A.4})$$

Pragmatic method Foreseeing the addition of dissipative elements, we will adopt an alternative method to the canonical one described above. In the following paragraph, we base our analysis on the equations of motion of the circuit which leads to a systematic analysis.

To write the final Hamiltonian, the only required ingredients is the mode frequency ω_0 which we had access to as of the equations of motion. However, in the following, the Hamiltonian will include some non-linearity ^{V¹}

$$\mathcal{H} = Q^2/2C + \Phi^2/2L + V(\Phi) \quad (\text{A.5})$$

¹Here we assume that V can be expanded in a power series where the lowest degree is at least 3 in order not to perturb the quadratic term of the Hamiltonian and hence the mode frequency.

so that Φ_{zpf} is also required to write the quantized version

$$\mathbf{H} = \hbar\omega_0(\mathbf{a}^\dagger\mathbf{a} + 1/2) + V(\Phi_{\text{zpf}}(\mathbf{a} + \mathbf{a}^\dagger)). \quad (\text{A.6})$$

Then, a direct route to quantization is to find ω_0 and Φ_{zpf} . First, let us write the equation of motion (the Euler-Lagrange equation) from the Lagrangian

$$C\ddot{\Phi} + \Phi/L = 0 \quad \text{or} \quad \begin{bmatrix} \dot{\Phi} \\ \ddot{\Phi} \end{bmatrix} = \begin{bmatrix} 0 & 1 \\ -(LC)^{-1} & 0 \end{bmatrix} \begin{bmatrix} \Phi \\ \dot{\Phi} \end{bmatrix}. \quad (\text{A.7})$$

as a first order differential equation. This diagonalizes into

$$\begin{bmatrix} \dot{\alpha} \\ \dot{\alpha}^* \end{bmatrix} = \begin{bmatrix} -i\omega_0 & 0 \\ 0 & i\omega_0 \end{bmatrix} \begin{bmatrix} \alpha \\ \alpha^* \end{bmatrix} \quad \text{with} \quad \begin{bmatrix} \Phi \\ \dot{\Phi} \end{bmatrix} = \Phi_{\text{zpf}} \begin{bmatrix} 1 & 1 \\ -i\omega_0 & i\omega_0 \end{bmatrix} \begin{bmatrix} \alpha \\ \alpha^* \end{bmatrix}. \quad (\text{A.8})$$

which gives ω_0 . Then, to find Φ_{zpf} we use the fact that the magnetic part of the energy associated to the vacuum fluctuations accounts for half the total vacuum energy. In this case, this condition writes

$$\langle 0 | \frac{(\Phi_{\text{zpf}}(\mathbf{a} + \mathbf{a}^\dagger))^2}{2L} | 0 \rangle = \frac{\Phi_{\text{zpf}}^2}{2L} = \frac{1}{2} \frac{\hbar\omega_0}{2}. \quad (\text{A.9})$$

We recover $\Phi_{\text{zpf}} = \sqrt{\hbar\omega_0 L/2} = \sqrt{\hbar Z/2}$ like earlier. This approach, inspired by [47], will prove useful when more complicated circuits will be considered and that the total energy will be the easiest quantity to compute.

A.1.2 Coupling to the circuit

For now, we have described a simple LC oscillator but this oscillator proves to be useless until we are able to address it. One can couple to this oscillator in two different ways:

- each node has a finite capacitance to the outside world
- each loop shares a finite mutual inductance with the outside world.

Using this, we can either use a voltage source to induce a charge difference between two nodes of the circuit or a current source to induce a flux difference between to loops¹. These two ways to couple to a circuit are depicted in fig. A.1. The voltage and current sources are not ideal. The voltage source has a finite impedance represented by a resistor in series. The current source has a finite admittance represented by a resistor in parallel. These imperfections will lead to dissipation. In our case, we address the circuit via transmission lines that constitute $50\,\Omega$ environments.

¹Note that given a connected circuit, we consider the outside of the circuit as a last loop that can be flux biased.

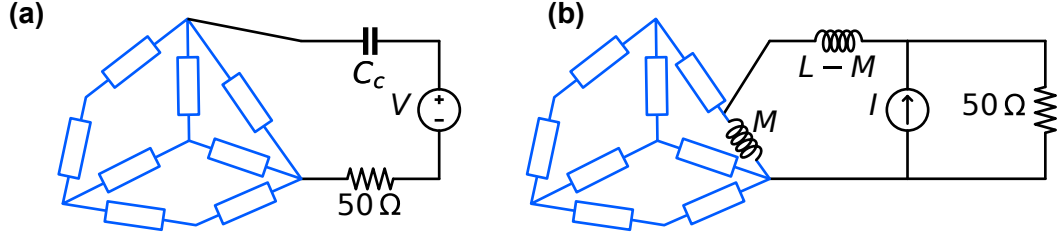


FIGURE A.1: **Coupling to the environment.** An arbitrary superconducting circuit is depicted in blue. (a) Each node has a finite capacitance to the environment. Hence, charge biasing the circuit with a voltage source is possible. (b) Each loop has a finite mutual inductance with the environment. Hence, flux biasing the circuit with a current source is possible. (a,b) This coupling comes with a finite dissipation that is represented by the $50\,\Omega$ resistor.

Let us forget about the induced dissipation for a moment and compute the coupling Hamiltonian.

Capacitive coupling When capacitively coupled, the Hamiltonian writes (see Appendix B.1)

$$\mathbf{H} = \hbar\omega_a \mathbf{a}^\dagger \mathbf{a} - i \frac{D}{C+D} Q_{\text{zpf}} (\mathbf{a} - \mathbf{a}^\dagger) V(t). \quad (\text{A.10})$$

with $\omega_a = 1/\sqrt{L(C+D)}$ and $Q_{\text{zpf}} = \sqrt{\hbar/Z/2}$ where $Z = \sqrt{L/(C+D)}$.

Inductive coupling When inductively coupled, the Hamiltonian writes (see Appendix B.3)

$$\mathbf{H} = \hbar\omega_a \mathbf{a}^\dagger \mathbf{a} - \frac{M}{L} \Phi_{\text{zpf}} (\mathbf{a} + \mathbf{a}^\dagger) I(t). \quad (\text{A.11})$$

with $\omega_a = 1/\sqrt{LC}$ and $\Phi_{\text{zpf}} = \sqrt{\hbar Z/2}$ where $Z = \sqrt{L/C}$.

A.1.3 Dissipation

Let us go back to the dissipation that is induced when coupling to the system. When quantizing the LC-oscillator, we put emphasis on the equations of motion because they remain valid when adding dissipation. Here, we seek both the Hamiltonian and the loss operators. To keep the derivation simple and contrary to the previous paragraph, we directly add a resistor in parallel with the circuit to account for dissipation.

Eigenvalue analysis The new equations of motion write

$$C\ddot{\Phi} + \dot{\Phi}/R + \Phi/L = 0 \quad \text{or} \quad \begin{bmatrix} \dot{\Phi} \\ \ddot{\Phi} \end{bmatrix} = \begin{bmatrix} 0 & 1 \\ -(LC)^{-1} & -(RC)^{-1} \end{bmatrix} \begin{bmatrix} \Phi \\ \dot{\Phi} \end{bmatrix}. \quad (\text{A.12})$$

It diagonalizes into

$$\begin{bmatrix} \dot{\alpha} \\ \dot{\alpha}^* \end{bmatrix} = \begin{bmatrix} -i\Omega & 0 \\ 0 & i\Omega^* \end{bmatrix} \begin{bmatrix} \alpha \\ \alpha^* \end{bmatrix} \quad (\text{A.13})$$

where $\Omega = \sqrt{\omega_0^2 - (\kappa/2)^2} - i\kappa/2 \equiv \omega_1 - i\kappa/2$ ¹, $\kappa = (RC)^{-1}$ and

$$\begin{bmatrix} \Phi \\ \dot{\Phi} \end{bmatrix} = \frac{\lambda}{\sqrt{2}} \begin{bmatrix} 1 & 1 \\ -i\Omega & i\Omega^* \end{bmatrix} \begin{bmatrix} \alpha \\ \alpha^* \end{bmatrix} \quad \text{or} \quad \begin{bmatrix} \alpha \\ \alpha^* \end{bmatrix} = \frac{1}{\lambda\sqrt{2}} \begin{bmatrix} 1 & i/\Omega^* \\ 1 & -i/\Omega \end{bmatrix} \begin{bmatrix} \Phi \\ \dot{\Phi} \end{bmatrix}. \quad (\text{A.14})$$

Now, the new degrees of freedom α and α^* have a damped oscillatory behaviour. It is tempting to conserve the form of these equation while quantizing

$$\dot{\mathbf{a}} = -i\omega_1 \mathbf{a} - \frac{\kappa}{2} \mathbf{a} \quad (\text{A.15})$$

$$\dot{\mathbf{a}}^\dagger = i\omega_1 \mathbf{a}^\dagger - \frac{\kappa}{2} \mathbf{a}^\dagger. \quad (\text{A.16})$$

However, these equation of motion do not preserve the commutation relation for \mathbf{a} and \mathbf{a}^\dagger . Indeed, adding dissipation is essentially coupling to a bath which has to induce fluctuations. The full treatment, the so-called input-output theory [41] leads to the following equation of motion for \mathbf{a}

$$\dot{\mathbf{a}} = -i\omega_1 \mathbf{a} - \frac{\kappa}{2} \mathbf{a} + \sqrt{\kappa} \mathbf{a}_{\text{in}} \quad (\text{A.17})$$

If the statistic of the noise process \mathbf{a}_{in} (typically vacuum or thermal fluctuations) allows it, the dynamics of the system can be put in the Lindblad form with the following Hamiltonian and loss operator

$$\mathbf{H} = \hbar\omega_1(\mathbf{a}^\dagger \mathbf{a} + 1/2) \quad (\text{A.18})$$

$$\mathbf{L} = \sqrt{\kappa} \mathbf{a}. \quad (\text{A.19})$$

In the limit of small dissipation, $\kappa/\omega_0 \ll 1$, the zero-point fluctuations of the phase do not differ much from the non-dissipative case and are computed in the same manner. One can refine this assumption by following [38, 41, 44]

¹Notice that $|\Omega| = \omega_0$.

Quantity	Capacitor	Resistor	Inductor	Josephson junction
Energy/ φ_0^2	$\frac{C}{2}\dot{\varphi}^2$	n/a	$\frac{1}{2L}\varphi^2$	$-\frac{1}{L_J}\cos(\varphi)$
Current/ φ_0	$C\ddot{\varphi}$	$\frac{1}{R}\dot{\varphi}$	$\frac{1}{L}\varphi$	$\frac{1}{L_J}\sin(\varphi)$

TABLE A.1: **Energy and current for each dipole type.** The reduced flux quantum is defined as $\varphi_0 = \Phi_0/2\pi = \hbar/2e$. The inductance of a Josephson junction is referred to as $L_J = \varphi_0/I_0 = \varphi_0^2/E_J$ where I_0 is the critical current of the junction and E_J its Josephson energy.

A.2 General Circuit quantization

We are mainly interested in weakly non-linear harmonic oscillators. Here we provided our recipe for quantizing such circuits. The strategy is to find the equations of motion of an arbitrary circuit containing capacitors, inductors, resistors and Josephson junctions, in the same spirit as in [40]. This circuit may be DC biased by offset fluxes. From there, we diagonalize the linear part of the equation of motion to find the normal modes, their frequencies and loss rates. These modes are then canonically quantized and we write a Lindblad master equation for the system. The non-linear part is added back which couples the modes. This gives an appropriate description of the system provided the loss rates are small with respect to the modes frequencies.

A.2.1 Circuit description

For now, we have treated the case of a one-mode circuit, the LC or RLC oscillator. In the following, we systematize this approach to more complex circuits. An effort was made to understand and compile the best of all the existing methods [38–40, 45, 144] to our specific quantization problem: weakly anharmonic circuits.

As we deal with superconducting circuits, we define the phase variable

$$\varphi(t) = 2\pi \frac{\Phi(t)}{\Phi_0}, \quad (\text{A.20})$$

where $\Phi_0 = h/2e = 2\pi\varphi_0$ is the superconducting flux quantum. In tab. A.1, we summarize the energy and current for each dipole type in terms of the phase variable.

Circuit topology Let's pick an arbitrary circuit with n nodes and d dipoles. Once each dipole is arbitrarily oriented, the circuit is fully represented by an oriented incidence

matrix \mathbf{A} . This matrix has n rows and d columns and each coefficient $A_{i,j}$ is such that

$$A_{i,j} = \begin{cases} 1 & \text{if dipole } j \text{ points towards node } i \\ -1 & \text{if dipole } j \text{ points away from node } i \\ 0 & \text{if dipole } j \text{ is not directly connected to node } i \end{cases}, \quad (\text{A.21})$$

hence each column of this matrix contains exactly one 1 and one -1 coefficient. If one picks a subset of oriented dipoles in the form of a column vector \mathbf{p} with length d where

$$p_j = \begin{cases} 1 & \text{if dipole } j \text{ is chosen with its normal orientation} \\ -1 & \text{if dipole } j \text{ is chosen with the opposite orientation} \\ 0 & \text{if dipole } j \text{ is not in the chosen subset of dipoles} \end{cases}, \quad (\text{A.22})$$

then $\mathbf{A}\mathbf{p} = \mathbf{0}$ means that the subset \mathbf{p} forms a closed loop in the circuit. This property proves useful when dealing with Kirchhoff's voltage law and external flux biases. Indeed, $\ker \mathbf{A}$ returns a set of independent loops. We denote $\boldsymbol{\varphi}$ the column vector containing the phase difference across each dipole.

Circuit parameters The circuit parameters are stored in four $d \times d$ matrices. These matrices are diagonal and the diagonal contains the dipole value. We define the capacitance matrix \mathbf{C}_d , the inverse resistance matrix \mathbf{R}_d^{-1} , the inverse inductance matrix \mathbf{L}_d^{-1} and the inverse Josephson inductance matrix \mathbf{J}_d^{-1} . We choose these quantities since they are directly related to the current flowing through each element (see tab. A.1). In the absence of resistor and junctions, the Lagrangian simply writes

$$\frac{1}{\varphi_0^2} \mathcal{L}(\boldsymbol{\varphi}) = \frac{1}{2} \dot{\boldsymbol{\varphi}}^\top \mathbf{C}_d \dot{\boldsymbol{\varphi}} - \frac{1}{2} \boldsymbol{\varphi}^\top \mathbf{L}_d^{-1} \boldsymbol{\varphi}. \quad (\text{A.23})$$

At this stage, no information on the circuit topology is used yet. In this Lagrangian, each dipole phase is considered as an independent degree of freedom. In the next section, we add the constraints derived from the incidence matrix \mathbf{A} to find the equations of motion.

A.2.2 Equations of motion

Voltage Kirchhoff's law Contrary to, chapter 2, here we allow for external magnetic bias. Both approaches are equivalent as illustrated in sec. B.2. In a superconducting circuit one can write the voltage Kirchhoff's law in a given loop as

$$\mathbf{p}^\top \cdot \boldsymbol{\varphi} = \varphi_{\text{ext}} \quad (\text{A.24})$$

where \mathbf{p} is a loop as defined earlier and $\varphi_{\text{ext}} = 2\pi\Phi_{\text{ext}}/\Phi_0$, Φ_{ext} being the magnetic flux threading the loop.

Denote by l the number of loops in the circuit. According to the voltage Kirchhoff's laws, for each loop in the system one variable can be written in terms of the others. In other words, each voltage Kirchhoff's law sets a constrain on the variables $\{\varphi_j\}$. Hence, the circuit is fully described by a column vector $\boldsymbol{\gamma}$ with size $d-l$ containing only a subset of $\{\varphi_j\}$ that one can choose. If one write $\ker \mathbf{A}$ as¹

$$\ker \mathbf{A} = \left\{ \begin{bmatrix} \cdots \\ \cdots \quad p_j \quad \cdots \\ \cdots \end{bmatrix} \right\}^l \quad (\text{A.25})$$

then the constraints are

$$(\ker \mathbf{A})\boldsymbol{\varphi} = \boldsymbol{\varphi}_{\text{ext}} \quad (\text{A.26})$$

where $\boldsymbol{\varphi}_{\text{ext}}$ is the column vector containing the fluxes threading each loop². To relate $\boldsymbol{\gamma}$ and $\boldsymbol{\varphi}$, we complete $\ker \mathbf{A}$ with $d-l$ 1 on the diagonal. These 1 represent the φ_j that are kept in $\boldsymbol{\gamma}$. To prevent cumbersome notations, we choose to keep the $d-l$ last φ_j . The constraint relation then writes

$$\begin{bmatrix} \cdots \\ \cdots \quad c_j \quad \cdots \\ \cdots \\ 1 & & 0 \\ & \ddots & \\ 0 & & 1 \end{bmatrix} \boldsymbol{\varphi} = \begin{bmatrix} \vdots \\ \varphi_{\text{ext},j} \\ \vdots \\ 0 \\ \vdots \end{bmatrix} + \begin{bmatrix} 0 \\ 1 & & 0 \\ & \ddots & \\ 0 & & 1 \end{bmatrix} \boldsymbol{\gamma}. \quad (\text{A.27})$$

By inverting³ the first matrix, one can write $\boldsymbol{\varphi}$ as a function of $\boldsymbol{\gamma}$

$$\boldsymbol{\varphi} = \mathbf{F}\boldsymbol{\gamma} + \mathbf{f} \quad (\text{A.28})$$

where \mathbf{F} is a $d \times (d-l)$ matrix.

Equations of motion At any time, the current Kirchhoff's law indicates that the sum over all the algebraic currents that flow towards a given node is 0. In the matrix

¹ $\ker \mathbf{A}$ should only contain 1, -1 and 0, indeed it describes oriented loops of the circuit. In practice, a simple Gaussian elimination gives $\ker \mathbf{A}$ in this form.

²There are many 0 in $\boldsymbol{\varphi}_{\text{ext}}$ since any two dipoles in parallel are regarded as loops at this stage.

³The choice of the φ_j that are being kept is not arbitrary. One need to ensure the resulting matrix is invertible. In [39], this choice is made with the spanning tree method.

representation of the network, this writes

$$\mathbf{A}\mathbf{i} = \mathbf{0} \quad (\text{A.29})$$

where \mathbf{i} is the column vector containing the currents flowing through each circuit dipole. Each row of this equation corresponds to the sum of all the current arriving to a given node. Using tab. A.1, we deduce

$$\mathbf{i} = \mathbf{C}_d \ddot{\boldsymbol{\varphi}} + \mathbf{R}_d^{-1} \dot{\boldsymbol{\varphi}} + \mathbf{L}_d^{-1} \boldsymbol{\varphi} + \mathbf{J}_d^{-1} \sin(\boldsymbol{\varphi}). \quad (\text{A.30})$$

Plugging in the voltage constraints from (A.28) and the current Kirchhoff's law (A.29), we write the n equations of motion as¹

$$\mathbf{A}\mathbf{C}_d \mathbf{F} \ddot{\boldsymbol{\gamma}} + \mathbf{A}\mathbf{R}_d^{-1} \mathbf{F} \dot{\boldsymbol{\gamma}} + \mathbf{A}\mathbf{L}_d^{-1} (\mathbf{F}\boldsymbol{\gamma} + \mathbf{f}) + \mathbf{A}\mathbf{J}_d^{-1} \sin(\mathbf{F}\boldsymbol{\gamma} + \mathbf{f}) = \mathbf{0}. \quad (\text{A.31})$$

This represents n equations of motion (one for each node). However $\boldsymbol{\gamma}$ is a $d-l$ column vector, which equals $n-1$ for such graphs. So, one of the equation defined in (A.31) is linearly dependent on the other. Indeed, if the net current flowing towards each node but one is 0, then the current flowing towards the last node is 0 too.

Equilibrium At equilibrium, due to the external fluxes, the system does not settle at $\boldsymbol{\varphi} = \{0\}$. To find an equilibrium position, one needs to solve

$$\mathbf{A}\mathbf{L}_d^{-1} (\mathbf{F}\boldsymbol{\gamma} + \mathbf{f}) + \mathbf{A}\mathbf{J}_d^{-1} \sin(\mathbf{F}\boldsymbol{\gamma} + \mathbf{f}) = \mathbf{0}. \quad (\text{A.32})$$

which gives a set of transcendental equations. These equations do not have a unique solution in general and the solutions are not analytical either. The system being at rest also correspond to minimizing the potential energy

$$U(\boldsymbol{\varphi}) = \frac{1}{2} \sum_j L_{dj}^{-1} \varphi_j^2 - \frac{1}{2} \sum_j J_{dj}^{-1} \cos(\varphi_j) \quad (\text{A.33})$$

under the following constraint $\boldsymbol{\varphi} = \mathbf{F}\boldsymbol{\gamma} + \mathbf{f}$. Computing the gradient of U with respect to $\boldsymbol{\gamma}$ gives

$$\nabla U(\boldsymbol{\gamma}) = \mathbf{F}^\top \mathbf{L}_d^{-1} (\mathbf{F}\boldsymbol{\gamma} + \mathbf{f}) + \mathbf{F}^\top \mathbf{J}_d^{-1} \sin(\mathbf{F}\boldsymbol{\gamma} + \mathbf{f}). \quad (\text{A.34})$$

Finding the minimum of the potential where $\nabla U = \mathbf{0}$ also satisfies (A.32). Indeed, one can show that, by construction, the rows of \mathbf{F}^\top are orthogonal to $\ker \mathbf{A}$. Thus solving

¹Assuming DC flux bias for simplicity. Otherwise, time derivatives of \mathbf{f} appear.

$\mathbf{A}\mathbf{Y} = \mathbf{0}$ and $\mathbf{F}^\top \mathbf{Y} = \mathbf{0}$ is the equivalent¹. In practice, we numerically minimize the potential to find an equilibrium position γ_{eq} (or φ_{eq}) for the system.

Linearised equations of motion Around this equilibrium position, we define a new variable $\delta\gamma = \gamma - \gamma_{\text{eq}}$ respectively $\delta\varphi = \mathbf{F}\delta\gamma$. In terms of this new variable, we can linearise (A.33) as follows

$$U(\varphi_{\text{eq}} + \delta\varphi) = \frac{1}{2} \sum_j L_{dj}^{-1} (\varphi_{\text{eq},j} + \delta\varphi_j)^2 - \sum_j J_{dj}^{-1} \cos(\varphi_{\text{eq},j} + \delta\varphi_j) \quad (\text{A.35})$$

$$\begin{aligned} &= U(\varphi_{\text{eq}}) + \sum_j L_{dj}^{-1} \varphi_{\text{eq},j} \delta\varphi_j + J_{dj}^{-1} \sin(\varphi_{\text{eq},j}) \sin(\delta\varphi_j) \\ &\quad + \sum_j \frac{1}{2} L_{dj}^{-1} \delta\varphi_j^2 + J_{dj}^{-1} \cos(\varphi_{\text{eq},j}) (1 - \cos(\delta\varphi_j)) . \end{aligned} \quad (\text{A.36})$$

The linear part of the second term vanishes since we are at a minimum of the constrained potential, see (A.34), hence

$$\begin{aligned} U(\varphi_{\text{eq}} + \delta\varphi) &= U(\varphi_{\text{eq}}) + \sum_j \frac{1}{2} \left(L_{dj}^{-1} + J_{dj}^{-1} \cos(\varphi_{\text{eq},j}) \right) \delta\varphi_j^2 \\ &\quad + \sum_j J_{dj}^{-1} \sin(\varphi_{\text{eq},j}) \sin_3(\delta\varphi_j) - \sum_j J_{dj}^{-1} \cos(\varphi_{\text{eq},j}) \cos_4(\delta\varphi_j) , \end{aligned} \quad (\text{A.37})$$

where $\sin_3(x)$ and $\cos_4(x)$ stand for $\sin(x) - x$ and $\cos(x) - (1 - x^2/2)$. This is the general form of the potential around the minimum, where we put the emphasis on the quadratic term. In the following, we drop the non-linear part to find the eigenmodes of the system. The linearized equation of motion then rewrite

$$\mathbf{C}\ddot{\delta\gamma} + \mathbf{R}^{-1}\dot{\delta\gamma} + \mathbf{L}^{-1}\delta\gamma = \mathbf{0} . \quad (\text{A.38})$$

with $\mathbf{C} = \mathbf{A}\mathbf{C}_d\mathbf{F}$, $\mathbf{R}^{-1} = \mathbf{A}\mathbf{R}_d^{-1}\mathbf{F}$ and $\mathbf{L}^{-1} = \mathbf{A} \left(\mathbf{L}_d^{-1} + \mathbf{J}_d^{-1} \cos(\varphi_{\text{eq}}) \right) \mathbf{F}$.

A.2.3 Circuit eigenmodes

The equation (A.38) has the same form as the differential equation for a damped harmonic oscillator (A.12). We expect to find two sets of complex eigenfrequencies, conjugate to one another $\{-i\boldsymbol{\Omega}, i\boldsymbol{\Omega}^*\}$ with $\boldsymbol{\Omega} = \{\omega_1 - i\kappa_1/2, \dots, \omega_{n-1} - i\kappa_{n-1}/2\}$ and their corresponding eigenmodes defined over the full circuit $\{\boldsymbol{\Lambda}, \boldsymbol{\Lambda}^*\}$ with $\boldsymbol{\Lambda} =$

¹The first set has one more equation than the second one, this equation being linearly dependent on the others as we saw earlier.

$\{\lambda_1, \dots, \lambda_{n-1}\}$ ¹. To solve the equation of motion, we rewrite it in a first order form

$$\left[\begin{array}{c|c} \mathbf{I}_d & 0 \\ \hline 0 & \mathbf{C} \end{array} \right] \delta \dot{\mathbf{\Gamma}} = \left[\begin{array}{c|c} 0 & \mathbf{I}_d \\ \hline -\mathbf{L}^{-1} & -\mathbf{R}^{-1} \end{array} \right] \delta \mathbf{\Gamma} \quad (\text{A.39})$$

where $\delta \mathbf{\Gamma}$ is the column vector

$$\delta \mathbf{\Gamma} = \begin{bmatrix} \delta \gamma \\ \delta \dot{\gamma} \end{bmatrix}. \quad (\text{A.40})$$

Provided \mathbf{C} is invertible (see next paragraph), we have

$$\delta \dot{\mathbf{\Gamma}} = \left[\begin{array}{c|c} 0 & \mathbf{I}_d \\ \hline -\mathbf{C}^{-1}\mathbf{L}^{-1} & -\mathbf{C}^{-1}\mathbf{R}^{-1} \end{array} \right] \delta \mathbf{\Gamma}. \quad (\text{A.41})$$

We find Ω in the set of eigenvalues of this matrix and, if we denote the eigenvectors by

$$\begin{bmatrix} \mathbf{v}_i \\ -i\Omega_i \mathbf{v}_i \end{bmatrix}, \quad (\text{A.42})$$

the eigenmodes are $\lambda_i = \mathbf{F} \mathbf{v}_i$.

Invertibility of \mathbf{C} If \mathbf{C} is not invertible, it must have at least one 0 eigenvalue. Let us diagonalize \mathbf{C} into $\mathbf{D} = \mathbf{P}^\top \mathbf{C} \mathbf{P}$ and rewrite the equations of motion

$$\mathbf{D} \ddot{\mathbf{h}} + \mathbf{S} \dot{\mathbf{h}} + \mathbf{M} \mathbf{h} = \mathbf{0} \quad (\text{A.43})$$

with $\mathbf{S} = \mathbf{P}^\top \mathbf{R}^{-1} \mathbf{P}$, $\mathbf{M} = \mathbf{P}^\top \mathbf{L}^{-1} \mathbf{P}$ and $\mathbf{h} = \mathbf{P}^\top \delta \gamma$. Let us say, that \mathbf{D} has only one 0 eigenvalue at the j th position for simplicity, the same reasoning holds if there are several 0. Then, the j th equation of motion writes

$$\mathbf{a} \cdot \dot{\delta \gamma} + \mathbf{b} \cdot \delta \gamma = 0 \quad (\text{A.44})$$

where \mathbf{a} and \mathbf{b} are the j th rows of $\mathbf{P}^\top \mathbf{R}^{-1}$ and $\mathbf{P}^\top \mathbf{L}^{-1}$ respectively. This is the equation of motion of a LR-type mode which is purely dissipative. To formally take it into account in the rest of the calculation, one can take the derivative of this equation with respect to time which boils down to plugging \mathbf{a} in the j -th row of \mathbf{D} and \mathbf{b} in the j -th row of \mathbf{S} . That is transforming the LR-type dissipative mode into a RC-type.

¹Note that one only needs Ω and \mathbf{A} to quantize the system. We omit the other conjugate solution from now on.

If $\mathbf{a} = \mathbf{0}^1$, the j th equation of motion is left with

$$\mathbf{b} \cdot \delta\boldsymbol{\gamma} = 0 \quad (\text{A.45})$$

which is a new constraint (A.24) on the set of variables. Even though, the treatment of the previous section should have let us with an independent set of variables $\delta\boldsymbol{\gamma}$, special circuit configurations can reduce the number of independent variables. A good example is the JPC [145] where the 4th mode is sent to infinity due to the absence of a capacitor connected to the centre of the JRM² reducing the number of independent variables to 3.

Taking into account this constraint leads to a new set of equations of motion with one less equation. For simplicity but without loss of generality, we assume that \mathbf{C} is invertible, in the following.

Alternative derivation In the previous paragraphs, we solved the second order differential equation completely. If one is only interested in oscillatory solutions, we can look for solutions of the form $\delta\boldsymbol{\gamma}(t) = \text{Re}(\delta\tilde{\boldsymbol{\gamma}}e^{-i\Omega t})$ where $\delta\tilde{\boldsymbol{\gamma}}$ and Ω are complex. Plugging this into (A.38) gives

$$\left(-\Omega^2\mathbf{C} - i\Omega\mathbf{R}^{-1} + \mathbf{L}^{-1}\right)\delta\tilde{\boldsymbol{\gamma}} \equiv \mathbf{M}(\Omega)\delta\tilde{\boldsymbol{\gamma}} = \mathbf{0}. \quad (\text{A.46})$$

This equation has non-trivial solutions when $\det(\mathbf{M}(\Omega)) = 0$. The set of zeros of this determinant in the right half of the complex plane is precisely $\boldsymbol{\Omega}$. Once a solution Ω_i is found, the corresponding eigenmode is $\boldsymbol{\lambda}_i = \mathbf{F}\mathbf{v}_i$ where \mathbf{v}_i lies in $\ker(\mathbf{M}(\Omega_i))$.

The function $\det(\mathbf{M}(\Omega))$ is simply polynomial in Ω and we can find the zeros numerically. These solutions are the same as the one given by the former eigenvalue problem that we solve with powerful algorithms. On the contrary, in this alternative approach it is more computationally involved to find all the roots. Still this will prove meaningful in the following when we introduce distributed elements.

Mode normalization As in the simple case (A.8), each eigenvector is defined up to a constant prefactor. Thus, each eigenmode is normalized so that the energy of the magnetic vacuum fluctuations account for half the vacuum energy. In other words, each

¹It is the case when the circuit is treated without dissipation for instance

²This is an artefact of the circuit representation. In a real circuit, there is a finite capacitance which brings the 4th mode back to a finite frequency.

λ_i is normalized such that

$$\lambda_i^\top \left(\mathbf{L}_d^{-1} + \mathbf{J}_d^{-1} \cos(\varphi_{\text{eq}}) \right) \lambda_i = \frac{1}{2} \frac{\hbar \Omega_i}{2\varphi_0^2}. \quad (\text{A.47})$$

Therefore, once normalized λ_i writes

$$\lambda_i = \begin{bmatrix} \vdots \\ \phi_{i,j} \\ \vdots \end{bmatrix}, \quad (\text{A.48})$$

where $\phi_{i,j}$ is the zero-point fluctuation of the phase of dipole j due to the eigenmode i . The quantized phase across a dipole j then writes $\phi_j = \sum_i \phi_{i,j} (\mathbf{a}_i + \mathbf{a}_i^\dagger)$.

To conclude, using (A.6) and (A.37), the Hamiltonian and loss operators of the system write

$$\mathbf{H} = \hbar \sum_i \omega_i \mathbf{a}_i^\dagger \mathbf{a}_i + \sum_j E_{J,j} \left(\sin(\varphi_{\text{eq},j}) \sin_3(\phi_j) - \cos(\varphi_{\text{eq},j}) \cos_4(\phi_j) \right) \quad (\text{A.49})$$

$$\mathbf{L}_i = \sqrt{\kappa_i} \mathbf{a}_i \quad (\text{A.50})$$

where the second sum only runs over the junctions and $\phi_j = \sum_i \phi_{i,j} (\mathbf{a}_i + \mathbf{a}_i^\dagger)$.

A.2.4 Distributed elements

The previous analysis is convenient for solving lumped element circuits. However, even though we could fabricate lumped element devices, we prefer to work with distributed modes which are less sensitive to interface losses [83]. The distributed modes arise from portions of CPW transmission lines that are fabricated on the chip. When both ends of the portion are open, the mode is called $\lambda/2$. If one end is shorted, it is called $\lambda/4$. These modes are well approximated by lumped-LC oscillators around the resonance. However when we couple two of these modes with significantly different frequencies, the lumped element approximation is not suited any more.

In practice, this lumped element approximation is good enough for circuit analysis because eventually we fine tune the parameters using a full 3D simulation of the circuit with a finite-element solver. However, full 3D simulations take time. Here we describe how we included transmission lines in our circuit analysis.

A typical use case is designing on-chip filtering. In this case, the resulting Q-factor of the circuit modes may be very sensitive on the chosen approximation depending on the frequency difference..

Lumped LC concatenation model One standard way [42, 45] to better take into account transmission lines is to consider several modes. For example, a transmission line portion of length l opened on both ends support several modes at frequencies $\omega_n = n\pi c/l$. Hence, the transmission line can be replaced by an infinite series of lumped LC-oscillator corresponding to the different modes of the transmission line.

This gives good predictions provided we take into account a large enough number of modes. These numerous LC-oscillators may prove difficult to handle when solving the eigenvalue problem. Moreover, most of the time we only care about the effect of theses additional modes on our modes of interest. In the following, we suggest to go back to the definition of the transmission line [46] to treat it without approximations.

Transmission line portion model Let us consider a portion of a lossless transmission line with length l , phase velocity c and impedance Z_0 . Over this portion of transmission line, let us look for sinusoidal steady state at frequency ω and define the wave parameter $\beta = \omega/c$. It is convenient to define the complex phase $\varphi(z, t)$ which decomposes into its right moving part $\varphi_+(z, t) = \varphi_+ e^{j\omega t - \beta z}$ and its left moving part $\varphi_-(z, t) = \varphi_- e^{j\omega t + \beta z}$ where φ_+ and φ_- are the complex phasors characterising the field. At any point in time and space, the actual phase is then simply $\text{Re}(\varphi(z, t))$. In particular, if one takes the origin for z in the middle of the transmission line portion, we have

$$\begin{bmatrix} \varphi_{-l/2} \\ \varphi_{l/2} \end{bmatrix} = \begin{bmatrix} e^{j\beta l/2} & e^{-j\beta l/2} \\ e^{-j\beta l/2} & e^{j\beta l/2} \end{bmatrix} \begin{bmatrix} \varphi_+ \\ \varphi_- \end{bmatrix}. \quad (\text{A.51})$$

These are the oscillating complex phase at the ends of the portion of transmission line that are connected to the rest of the circuit. The outgoing currents [46] at these points write

$$\begin{bmatrix} i_{-l/2} \\ i_{l/2} \end{bmatrix} = \frac{j\omega}{Z_0} \begin{bmatrix} -e^{j\beta l/2} & e^{-j\beta l/2} \\ e^{-j\beta l/2} & -e^{j\beta l/2} \end{bmatrix} \begin{bmatrix} \varphi_+ \\ \varphi_- \end{bmatrix}. \quad (\text{A.52})$$

So, to connect the transmission line to the rest of the circuit one simply needs to relate $(i_{-l/2}, i_{l/2})$ with $(\varphi_{-l/2}, \varphi_{l/2})$. By inverting (A.51), we find

$$\begin{bmatrix} i_{-l/2} \\ i_{l/2} \end{bmatrix} = \frac{\omega}{Z_0 \sin(\beta l)} \begin{bmatrix} \cos(\beta l) & -1 \\ -1 & \cos(\beta l) \end{bmatrix} \begin{bmatrix} \varphi_{-l/2} \\ \varphi_{l/2} \end{bmatrix}. \quad (\text{A.53})$$

The special case were (A.51) is not invertible are

$$\beta l = 0[2\pi] \Rightarrow \varphi_{-l/2} = \varphi_{l/2} \text{ and } i_{-l/2} = -i_{l/2} \quad (\text{A.54})$$

$$\beta l = \pi[2\pi] \Rightarrow \varphi_{-l/2} = -\varphi_{l/2} \text{ and } i_{-l/2} = i_{l/2} \quad (\text{A.55})$$

which are simple constraints. If t_d denotes the time delay due to the transmission line, $t_d = l/c$ the previous equation rewrites

$$\begin{bmatrix} i_{-l/2} \\ i_{l/2} \end{bmatrix} = \frac{\omega}{Z_0 \sin(\omega t_d)} \begin{bmatrix} \cos(\omega t_d) & -1 \\ -1 & \cos(\omega t_d) \end{bmatrix} \begin{bmatrix} \varphi_{-l/2} \\ \varphi_{l/2} \end{bmatrix} \equiv \mathbf{T}_d \begin{bmatrix} \varphi_{-l/2} \\ \varphi_{l/2} \end{bmatrix}. \quad (\text{A.56})$$

This \mathbf{T}_d matrix can readily be added to the current relation (A.30) to find the equation of motion with transmission lines. The specificity of this matrix with respect to \mathbf{C}_d , \mathbf{L}_d , etc. is that it is diagonal by block of 2×2 since it couples phases and current at both ends of the transmission line contrary to a simple dipole.

The determinant of $M(\Omega)$ (A.46), the matrix that represents the circuit equations of motion is no more well behaved. It is no more polynomial and has poles whenever $\sin(\Omega t_{d,i}) = 0$ where the index i runs over all the portions of transmission lines of the circuit. Empirically, we found the function $\det(\mathbf{M}(\Omega)) \times \prod_i \sin(\Omega t_{d,i})$ has no more poles. Hence, solving the eigenfrequency problem is numerically and graphically sound.

Stored energy To normalize the eigenmodes found with (A.46), one needs to compute the total magnetic energy of the circuit. The computation is straight forward for a lumped inductance or junction. In the following we perform the computation for a portion of transmission.

For now, we restrict to the case of a circuit with no dissipation. Then, the eigenfrequency is real. Knowing $\varphi_{-l/2}$ and $\varphi_{l/2}$ one recover φ_+ and φ_- by inverting¹ (A.51). One can show that in the absence of dissipation, the mode stored in the transmission line is steady so that φ_+ and are complex conjugate φ_- to one another.

The magnetic energy stored in the transmission at a time t is then [46]

$$E_{\text{mag}}(t) = \int_{-l/2}^{l/2} \frac{dz}{2L_t} \left(\frac{\partial}{\partial z} \text{Re}(\varphi_+ e^{-i\beta z} + \varphi_- e^{i\beta z}) e^{i\omega t} \right)^2 \quad (\text{A.57})$$

¹The special cases when the relation is non invertible are easy to treat separately

where $L_t = L/l$ is the inductance per unit length of the transmission line. We are interested in the average stored energy during a period

$$E_{\text{mag}} = \frac{l}{2L} \int_{-l/2}^{l/2} dz \left(\frac{\partial}{\partial z} \text{Re } \varphi_+ e^{-i\beta z} + \varphi_- e^{i\beta z} \right)^2 \quad (\text{A.58})$$

$$= \frac{2\beta^2 |\varphi_+|^2 l}{L} \int_{-l/2}^{l/2} dz \sin(\beta z - \theta_+)^2 \quad (\text{A.59})$$

where $\theta_+ = \arg(\varphi_+)$. Hence, we have

$$E_{\text{mag}} = \frac{2\beta^2 |\varphi_+|^2 l}{L} \left(\frac{l}{2} + \frac{1}{2\beta} \sin(2\theta_+) \cos(\beta l) \right) \quad (\text{A.60})$$

$$= \frac{|\varphi_+|^2 \omega t_d}{L} \left(\omega t_d + \sin(2\theta_+) \cos(\omega t_d) \right) \quad (\text{A.61})$$

where t_d is the time-delay in the transmission line.

Appendix B

Native couplings in superconducting circuits

B.1 Capacitively coupled resonators	124
B.2 Mutual inductances in superconducting loops	127
B.3 Inductively coupled resonators	128

B.1 Capacitively coupled resonators

We quickly reproduced the treatment one can find in [20] to find the Hamiltonian of the two capacitively coupled resonators of fig. B.1.

General case We first write the Lagrangian

$$\mathcal{L} = \frac{1}{2} \dot{\Phi}^\top C \dot{\Phi} - \frac{1}{2} \Phi^\top L^{-1} \Phi \quad (\text{B.1})$$

with

$$C = \begin{bmatrix} C_a + D & -D \\ -D & C_b + D \end{bmatrix} \quad \text{and} \quad L^{-1} = \begin{bmatrix} \frac{1}{L_a} & 0 \\ 0 & \frac{1}{L_b} \end{bmatrix}. \quad (\text{B.2})$$

The conjugate variables are $Q_i = \sum_j C_{ij} \dot{\Phi}_j$ so that the Hamiltonian writes

$$\mathcal{H} = \frac{1}{2} Q^\top C^{-1} Q + \frac{1}{2} \Phi^\top L^{-1} \Phi \quad (\text{B.3})$$

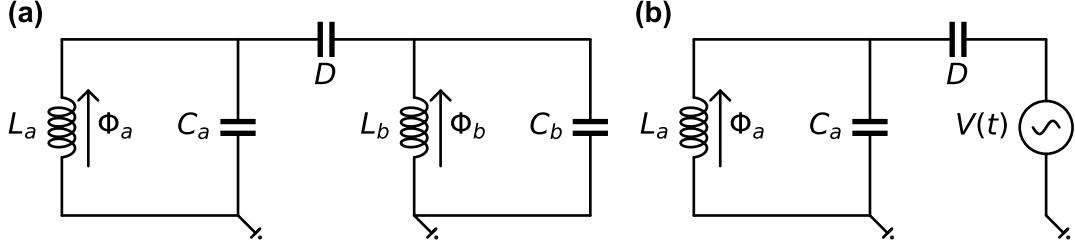


FIGURE B.1: **Capacitive coupling.** (a) Two capacitively coupled resonators. (b) Resonator coupled to a voltage source.

with

$$\mathbf{C}^{-1} = \begin{bmatrix} 1/C_{a\Sigma} & \beta_e/\sqrt{C_{a\Sigma}C_{b\Sigma}} \\ \beta_e/\sqrt{C_{a\Sigma}C_{b\Sigma}} & 1/C_{b\Sigma} \end{bmatrix} \quad (\text{B.4})$$

where $C_{a\Sigma} = C_a + C_b D/(C_b + D)$ and $C_{b\Sigma} = C_b + C_a D/(C_a + D)$ are the total capacitance to ground from node a and b respectively and $\beta_e = D/\sqrt{(C_a + D)(C_b + D)}$ is a dimensionless parameter characterising the coupling strength. Eventually using canonical quantization for Q and Φ we write the Hamiltonian as

$$\mathbf{H}/\hbar = \omega_a \mathbf{a}^\dagger \mathbf{a} + \omega_b \mathbf{b}^\dagger \mathbf{b} - \beta_e \sqrt{\omega_a \omega_b} (\mathbf{a} - \mathbf{a}^\dagger)(\mathbf{b} - \mathbf{b}^\dagger) \quad (\text{B.5})$$

with $\omega_a = 1/\sqrt{L_a C_{a\Sigma}}$ and $\omega_b = 1/\sqrt{L_b C_{b\Sigma}}$.

Voltage source From this derivation we deduce the Hamiltonian of a harmonic oscillator capacitively coupled to a perfect voltage source. An ideal DC voltage source with voltage V can be viewed as an infinitely charged infinite capacitor such that $Q_\infty/C_\infty = V$. One can adapt Hamiltonian (B.3) in such a way by taking the limit $C_b, Q_b, L_b \rightarrow \infty$ and $Q_b/C_b \rightarrow V$. One can also write the Lagrangian of the system as

$$\mathcal{L} = \frac{C_a}{2} \dot{\Phi}_a^2 + \frac{D}{2} (\dot{\Phi}_a - V(t))^2 - \frac{1}{2L_a} \Phi_a^2 \quad (\text{B.6})$$

so that the conjugate variable Q writes

$$Q = \frac{\partial \mathcal{L}}{\partial \dot{\Phi}_a} = C_a \dot{\Phi}_a + D (\dot{\Phi}_a - V(t)) \quad \Rightarrow \quad \dot{\Phi}_a = \frac{Q + DV(t)}{C_a + D} \quad (\text{B.7})$$

leading to

$$\mathcal{H} = \frac{1}{2(C_a + D)} Q_a^2 + \frac{1}{2L_a} \Phi_a + \frac{D}{C_a + D} Q_a V(t) \quad (\text{B.8})$$

if we drop the constant of motion terms in $V(t)^2$. Rearranging the terms, we rewrite the Hamiltonian as

$$\mathcal{H} = \frac{1}{2(C_a + D)} \left(Q_a + Q(t) \right)^2 + \frac{1}{2L_a} \Phi_a \quad (\text{B.9})$$

which emphasizes the offset charge $Q(t) = DV(t)$ induced by the voltage source on the oscillator. Performing canonical quantization, one gets

$$\mathbf{H} = \hbar\omega_a \mathbf{a}^\dagger \mathbf{a} - i \frac{D}{C_a + D} Q_a^{\text{zpf}} (\mathbf{a} - \mathbf{a}^\dagger) V(t). \quad (\text{B.10})$$

with $\omega_a = 1/\sqrt{L_a(C_a + D)}$ and $Q_a^{\text{zpf}} = \sqrt{\hbar/Z_a/2}$ where $Z_a = \sqrt{L_a/(C_a + D)}$.

Moving into displaced frame We start from Hamiltonian (B.10) that we recall here

$$\mathbf{H} = \hbar\omega_a \mathbf{a}^\dagger \mathbf{a} - i \frac{D}{C_a + D} Q_a^{\text{zpf}} (\mathbf{a} - \mathbf{a}^\dagger) V(t). \quad (\text{B.11})$$

and in the following we denote $\beta \equiv D/(C_a + D)$ and $V(t) = V_0 \cos(\omega t)$ is a microwave drive at frequency ω . The goal is to solve for the dynamics of \mathbf{a} to move in the displaced frame as one does usually to compute the effect of a pump. We discard dissipation here but the same reasoning hold if we take it into account.

The Heisenberg equation of motion for \mathbf{a} writes

$$\dot{\mathbf{a}} = -i\omega_a \mathbf{a} + \beta \frac{Q_a^{\text{zpf}}}{\hbar} V(t) \quad (\text{B.12})$$

which has, as a limit cycle,

$$\mathbf{a}(t) = \frac{i\beta Q_a^{\text{zpf}} V_0}{2\hbar(\omega^2 - \omega_a^2)} \left((\omega_a - \omega) e^{i\omega t} + (\omega_a + \omega) e^{-i\omega t} \right) \quad (\text{B.13})$$

Hence $\Phi(t)$ the induced flux across the inductance writes

$$\Phi_a(t) = \Phi_a^{\text{zpf}} (\mathbf{a} + \mathbf{a}^\dagger) = \Phi_a^{\text{zpf}} \frac{\beta Q_a^{\text{zpf}} \omega}{\hbar(\omega^2 - \omega_a^2)} 2V_0 \sin(\omega t) = \frac{\beta \omega^2}{(\omega^2 - \omega_a^2)} \int V(t) \quad (\text{B.14})$$

On the other hand, simply solving the classical equation of motion gives the same quantity. Let us call Z_a the impedance of the LC-oscillator and Z_c the impedance of the

coupling capacitance. We have

$$Z_a = \left(\frac{1}{jL\omega} + jC\omega \right)^{-1} \quad (\text{B.15})$$

$$Z_c = \frac{1}{jD\omega} . \quad (\text{B.16})$$

From the voltage divider formula we write the voltage across the resonator

$$V_a[\omega] = \frac{Z_a}{Z + Z_a} V[\omega] = \frac{\beta\omega^2}{(\omega^2 - \omega_a^2)} V[\omega] . \quad (\text{B.17})$$

As the flux is defined as the integral of the voltage, we recover (B.14).

B.2 Mutual inductances in superconducting loops

Let us consider the circuit of fig. B.2a. We have a large superconducting loop enclosing a magnetic flux Φ with self-inductance L_B and supercurrent $I_B = \Phi/L_B$. From infinity, we bring a smaller loop enclosing zero flux with self-inductance L_S and current $I_S = 0$. Due to Lenz's law, a current develops in the small loop to maintain the enclosed flux at $0 = \Phi_{\text{ext}} + L_S I_S$ with $\Phi_{\text{ext}} = -M I_B$. The mutual inductance M increases as the small loop gets closer to the big one. The current I_S that builds in the small loop has an effect back on the big loop and affects the supercurrent I_B . For a given mutual inductance, one needs to solve

$$\begin{bmatrix} 0 \\ \Phi \end{bmatrix} = \begin{bmatrix} L_S & -M \\ -M & L_B \end{bmatrix} \begin{bmatrix} I_S \\ I_B \end{bmatrix} \Rightarrow \begin{bmatrix} I_S \\ I_B \end{bmatrix} = \frac{1}{L_S L_B - M^2} \begin{bmatrix} L_B & M \\ M & L_S \end{bmatrix} \begin{bmatrix} 0 \\ \Phi \end{bmatrix} \quad (\text{B.18})$$

from which we recover $I_S = M I_B / L_S$ and $I_B = \Phi / L_B$ provided $M^2 \ll L_S L_B$. There exists an equivalent circuit to this problem depicted in fig. B.2b. If one works out the closed loop condition for the superconducting phase, one finds

$$0 = \Phi_S - \Phi_M = (L_S - M) I_S - M(I_B - I_S) = L_S I_S - M I_B \quad (\text{B.19})$$

$$\Phi = \Phi_B + \Phi_M = (L_B - M) I_B + M(I_B - I_S) = -M I_S + L_B I_B \quad (\text{B.20})$$

which is equivalent to (B.18). In typical superconducting circuit, one imposes the current I entering on the left of fig. B.2c which leads to the single equation

$$0 = L_S I_S - M I \Rightarrow \Phi_S = \Phi_{\text{ext}} \quad (\text{B.21})$$

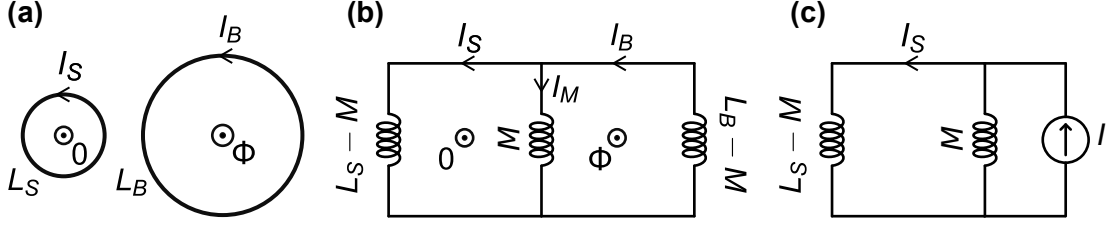


FIGURE B.2: **Superconducting loops and flux bias.** (a) Two superconducting rings with some mutual inductance. (b) Equivalent circuit. (c) In practice, one bias the superconducting loop with a current source that shares a small mutual inductance M .

with $\Phi_{\text{ext}} \equiv MI$. This describes on-chip flux loop as well as magnetic coils in the limit $M \rightarrow 0$ and $I \rightarrow \infty$. This alternate picture is useful because it enables to keep in mind the sources of the external flux and the coupling to the outside world it implies.

B.3 Inductively coupled resonators

Let us find the Hamiltonian of the circuit of fig. B.3.

General case Writing the current Kirchhoff's law at the central node we get

$$\frac{\Phi_m}{M} - \frac{\Phi_a - \Phi_m}{L_a - M} - \frac{\Phi_b - \Phi_m}{L_b - M} = 0 \quad (\text{B.22})$$

where Φ_m is the flux threading the mutual inductance M . From this, we get Φ_m as a linear combination of the degrees of freedom Φ_a and Φ_b

$$\Phi_m = L \left(\frac{\Phi_a}{L_a - M} + \frac{\Phi_b}{L_b - M} \right) \quad (\text{B.23})$$

where $1/L = 1/M + 1/(L_a - M) + 1/(L_b - M)$. Therefore, the potential energy of the system writes

$$\mathcal{U} = \frac{1}{2(L_a - M)}(\Phi_a - \Phi_m)^2 + \frac{1}{2(L_b - M)}(\Phi_b - \Phi_m)^2 + \frac{1}{2M}\Phi_m^2 \quad (\text{B.24})$$

and the Lagrangian

$$\mathcal{L} = \frac{1}{2}\dot{\Phi}^\top \mathbf{C} \dot{\Phi} - \frac{1}{2}\Phi^\top \mathbf{L}^{-1} \Phi \quad (\text{B.25})$$

with

$$\mathbf{C} = \begin{bmatrix} C_a & 0 \\ 0 & C_b \end{bmatrix} \quad \text{and} \quad \mathbf{L}^{-1} = \frac{1}{L_a L_b - M^2} \begin{bmatrix} L_b & -M \\ -M & L_a \end{bmatrix}. \quad (\text{B.26})$$

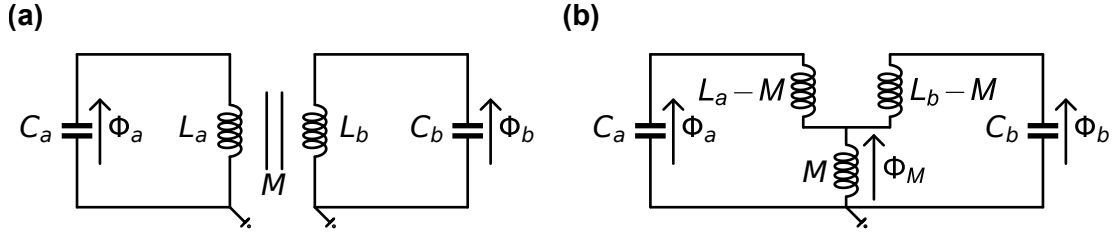


FIGURE B.3: **Inductive coupling.** (a) Two inductively coupled resonators with mutual inductance M . (b) Equivalent circuit

The conjugate variables are $Q_a = C_a \dot{\Phi}_a$ and $Q_b = C_b \dot{\Phi}_b$, so that the Hamiltonian writes

$$\mathcal{H} = \frac{1}{2} Q^\top C^{-1} Q + \frac{1}{2} \Phi^\top L^{-1} \Phi \quad (\text{B.27})$$

If we rewrite L^{-1} as

$$L^{-1} = \begin{bmatrix} 1/L_{a\Sigma} & -\beta_m/\sqrt{L_{a\Sigma}L_{b\Sigma}} \\ -\beta_m/\sqrt{L_{a\Sigma}L_{b\Sigma}} & 1/L_{b\Sigma} \end{bmatrix} \quad (\text{B.28})$$

where $\beta_m = M/\sqrt{L_a L_b}$ is a dimensionless parameter characterising the coupling strength, the Hamiltonian writes

$$\mathbf{H}/\hbar = \omega_a \mathbf{a}^\dagger \mathbf{a} + \omega_b \mathbf{b}^\dagger \mathbf{b} - \beta_m \sqrt{\omega_a \omega_b} (\mathbf{a} + \mathbf{a}^\dagger)(\mathbf{b} + \mathbf{b}^\dagger) \quad (\text{B.29})$$

with $\omega_a = 1/\sqrt{L_{a\Sigma} C_a}$ and $\omega_b = 1/\sqrt{L_{b\Sigma} C_b}$. We wrote the Hamiltonian before diagonalization to emphasize the coupling term.

Current source From this derivation we deduce the Hamiltonian of a harmonic oscillator inductively coupled to a perfect current source. An ideal DC current source with current I can be viewed as an infinitely charged infinite inductor such that $\Phi_\infty/L_\infty = I$. One can adapt Lagrangian (B.25) in such a way by taking the limit $L_b, \Phi_b \rightarrow \infty$ with $\Phi_b/L_b \rightarrow I$ and $C_b \rightarrow 0$ so that

$$\mathcal{L} = \frac{C}{2} \dot{\Phi}_a^2 - \frac{1}{2L_a} \Phi_a^2 + \frac{M}{L_a} \Phi_a I. \quad (\text{B.30})$$

Canonical quantization and generalizing for time-dependent currents¹ lead to

$$\mathbf{H} = \hbar \omega_a \mathbf{a}^\dagger \mathbf{a} - \frac{M}{L} \Phi_a^{\text{zpf}} (\mathbf{a} + \mathbf{a}^\dagger) I(t). \quad (\text{B.31})$$

¹One can check that the classical equations of motion that derive from the Lagrangian/Hamiltonian are valid even for a time dependant current.

with $\omega_a = 1/\sqrt{L_a C_a}$ and $\Phi_a^{\text{zpf}} = \sqrt{\hbar Z_a/2}$ where $Z_a = \sqrt{L_a/C_a}$.

Appendix C

Useful Formulae

C.1	Miscellaneous	131
C.2	Standard changes of frame	133
C.2.1	Rotating frame	133
C.2.2	Displaced frame	134

C.1 Miscellaneous

Evolution of a closed system

The time evolution of the state $|\psi\rangle$ of a closed quantum system with a Hamiltonian $\mathbf{H}(t)$ is governed by the Schrödinger equation

$$\frac{d}{dt} |\psi(t)\rangle = -\frac{i}{\hbar} \mathbf{H}(t) |\psi(t)\rangle . \quad (\text{C.1})$$

Evolution of an open system

If a quantum system is coupled to a bath in the so-called Markov approximation then the time evolution of its density matrix ρ is given by the Lindblad master equation

$$\dot{\rho} = -\frac{i}{\hbar} [\mathbf{H}, \rho] + \sum_k \mathcal{D}[\mathbf{L}_k] \rho . \quad (\text{C.2})$$

where \mathbf{H} is the Hamiltonian of the system and $\{\mathbf{L}_k\}$ the set of Lindblad operators describing the irreversible part of the evolution.

Dissipation super-operator

The dissipation super-operator \mathcal{D} is define as follows

$$\mathcal{D}[A]\rho = A\rho A^\dagger - \frac{1}{2}A^\dagger A\rho - \frac{1}{2}\rho A^\dagger A. \quad (\text{C.3})$$

where A and ρ are operators.

Baker-Hausdorff Lemma

A and B being two operators, we have

$$e^B A e^{-B} = A + [B, A] + \frac{1}{2!}[B, [B, A]] + \cdots. \quad (\text{C.4})$$

Unitary transformation with analytic functions

Let f be an analytic function, U a unitary operator such that $U^\dagger U = I$ and A an operator, then

$$U f(A) U^\dagger = f(U A U^\dagger). \quad (\text{C.5})$$

This relation arises by inserting the identity into the power series expansion of $f(A)$.

Displacement operator

The displacement operator D with amplitude β writes

$$D(\beta) = e^{\beta a^\dagger - \beta^* a} \quad \text{and} \quad D(\beta) |\alpha\rangle = |\alpha + \beta\rangle. \quad (\text{C.6})$$

Rotation operator

The rotation operator R with angle θ writes

$$R(\theta) = e^{i\theta a^\dagger a} \quad \text{and} \quad R(\theta) |\alpha\rangle = |\alpha e^{i\theta}\rangle. \quad (\text{C.7})$$

Commutator computation

Let a and a^\dagger be annihilation and creation operators respectively and f an analytical function. Then the following holds

$$[a, f(a, a^\dagger)] = \frac{\partial}{\partial a^\dagger} f(a, a^\dagger) \quad (\text{C.8})$$

$$[a^\dagger, f(a, a^\dagger)] = -\frac{\partial}{\partial a} f(a, a^\dagger) \quad (\text{C.9})$$

Commutator computation (bis) If θ and N verify $[\theta, N] = i$ then for any analytic function f [39, (4.12)]

$$[\theta, f(N)] = i \frac{\partial f}{\partial N}(N) \quad (\text{C.10})$$

C.2 Standard changes of frame

Consider the following general Hamiltonian for an oscillator

$$\mathbf{H}/\hbar = f(\mathbf{a}, \mathbf{a}^\dagger, t) \quad (\text{C.11})$$

where \mathbf{a} and \mathbf{a}^\dagger are the annihilation and creation operators over the oscillator Hilbert space. Consider an arbitrary set of loss operators $\{\mathbf{L}_k\}$

$$\mathbf{L}_k = f_k(\mathbf{a}, \mathbf{a}^\dagger, t). \quad (\text{C.12})$$

The functions f and $\{f_k\}$ are analytic functions.

C.2.1 Rotating frame

If ρ is a solution for the time evolution

$$\dot{\rho} = -\frac{i}{\hbar}[\mathbf{H}, \rho] + \sum_k \mathcal{D}[\mathbf{L}_k]\rho \quad (\text{C.13})$$

then $\tilde{\rho} = \mathbf{U}\rho\mathbf{U}^\dagger$ with $\mathbf{U}(t) = e^{i\omega t \mathbf{a}^\dagger \mathbf{a}}$, is a solution of

$$\dot{\tilde{\rho}} = -i[\tilde{\mathbf{H}}, \tilde{\rho}] + \sum_k \mathcal{D}[\tilde{\mathbf{L}}_k]\tilde{\rho} \quad (\text{C.14})$$

with

$$\tilde{\mathbf{H}} = f(\mathbf{a}e^{-i\omega t}, \mathbf{a}^\dagger e^{i\omega t}, t) - \omega \mathbf{a}^\dagger \mathbf{a} \quad (\text{C.15})$$

$$\tilde{\mathbf{L}}_k = \mathbf{L}_k. \quad (\text{C.16})$$

The unitary \mathbf{U} is a rotation (C.7) with an ever increasing angle ωt , so $\tilde{\rho}$ is the rotated version of ρ . That is why doing this transformation is called going into the rotating frame at frequency ω .

Proof Taking the time derivative of $\tilde{\rho}$ one gets

$$\dot{\tilde{\rho}} = -i[-\omega \mathbf{a}^\dagger \mathbf{a}, \tilde{\rho}] + \mathbf{U}\dot{\rho}\mathbf{U}^\dagger. \quad (\text{C.17})$$

Using eq. (C.5) and the fact that

$$UaU^\dagger = ae^{-i\omega t} \quad (\text{C.18})$$

$$Ua^\dagger U^\dagger = a^\dagger e^{i\omega t} \quad (\text{C.19})$$

which arises from eq. (C.4), one arrives at the time evolution in the rotating frame. Note that the dissipative part of the equation does not change. Indeed, the factors $e^{i\omega t}$ and $e^{-i\omega t}$ compensate for themselves in the expansion of the dissipation super-operator \mathcal{D} .

C.2.2 Displaced frame

If ρ is a solution for the time evolution

$$\dot{\rho} = -\frac{i}{\hbar}[H, \rho] + \sum_k \mathcal{D}[L_k]\rho \quad (\text{C.20})$$

then $\tilde{\rho} = U\rho U^\dagger$ with $U(t) = e^{\alpha(t)a^\dagger - \alpha(t)^*a}$, is a solution of

$$\dot{\tilde{\rho}} = -i[\tilde{H}, \tilde{\rho}] + \sum_k \mathcal{D}[\tilde{L}_k]\tilde{\rho} \quad (\text{C.21})$$

with

$$\tilde{H} = f(a - \alpha I, a^\dagger - \alpha^* I, t) + i(\dot{\alpha}a^\dagger - \dot{\alpha}^*a) \quad (\text{C.22})$$

$$\tilde{L}_k = f_k(a - \alpha I, a^\dagger - \alpha^* I, t). \quad (\text{C.23})$$

The unitary U is a displacement (C.6) with amplitude $\alpha(t)$, so $\tilde{\rho}$ is the displaced version of ρ . That is why doing this transformation is called going into the displaced frame.

Proof Taking the time derivative of $\tilde{\rho}$ one gets

$$\dot{\tilde{\rho}} = -i[i(\dot{\alpha}a^\dagger - \dot{\alpha}^*a), \tilde{\rho}] + U\dot{\rho}U^\dagger. \quad (\text{C.24})$$

Using eq. (C.5) and the fact that

$$UaU^\dagger = a - \alpha I \quad (\text{C.25})$$

$$Ua^\dagger U^\dagger = a^\dagger - \alpha^* I \quad (\text{C.26})$$

which arises from eq. (C.4), one arrives at the time evolution in the displaced frame.

Appendix D

Classical mechanical analogy to the stabilisation of cat-qubits

Let us consider the mechanical system of fig. D.1 which has two degrees of freedom ℓ and φ (we consider that the spring mass is constrained to move on the vertical axis only). Let us denote m_1 and m_2 , the masses of the anchoring point and of the pendulum respectively, k the spring constant, ℓ_0 its free length, L the pendulum length and g the gravitational acceleration. The speeds of the two masses along the two coordinates x and z write

$$v_1 = \begin{bmatrix} 0 \\ -\dot{\ell} \end{bmatrix}, \quad v_2 = \begin{bmatrix} L\dot{\varphi} \cos(\varphi) \\ -\dot{\ell} + L\dot{\varphi} \sin(\varphi) \end{bmatrix}. \quad (\text{D.1})$$

From this we write the kinetic and potential energy

$$T = \frac{1}{2}m_1\dot{\ell}^2 + \frac{1}{2}m_2 \left(L^2\dot{\varphi}^2 + \dot{\ell}^2 + 2L\dot{\ell}\dot{\varphi} \sin(\varphi) \right) \quad (\text{D.2})$$

$$U = \frac{1}{2}(\ell - \ell_0)^2 - m_1 g \ell - m_2 g (\ell + L \cos(\varphi)). \quad (\text{D.3})$$

Using the Euler-Lagrange equations, we deduce the equations of motion

$$\begin{aligned} (m_1 + m_2)\ddot{\ell} - m_2 L \ddot{\varphi} \sin(\varphi) - m_2 L \dot{\varphi}^2 \cos(\varphi) + \\ k(\ell - \ell_0) - (m_1 + m_2)g = 0 \\ m_2 L \ddot{\varphi} - m_2 \ddot{\ell} \sin(\varphi) + m_2 g \sin(\varphi) = 0. \end{aligned} \quad (\text{D.4})$$

On top of this, we should add a friction force acting on the spring degree of freedom due to the presence of a dashpot with friction coefficient η and a drive $a(t)$ that displaces

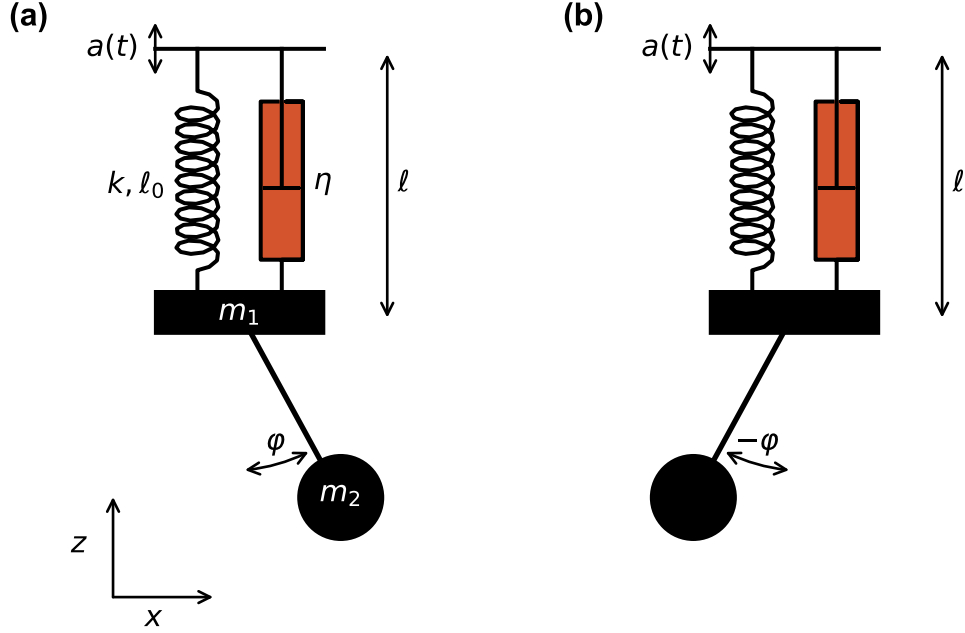


FIGURE D.1: **Classical analogous system.** (a) A pendulum is connected to a lossy spring. By driving the anchoring point of the spring we can excite the pendulum degree of freedom. Numerical integration shows that the driven system converges to a fixed amplitude oscillatory motion of the pendulum. (b) Same system with an opposite response for the pendulum degree of freedom. This motion is also solution of the equations of motion (D.6).

the top of the spring. The equations of motion write

$$(m_1 + m_2)\ddot{\ell} - m_2 L \ddot{\varphi} \sin(\varphi) - m_2 L \dot{\varphi}^2 \cos(\varphi) + k(\ell + a(t) - \ell_0) - (m_1 + m_2)g + \eta(\dot{\ell} + \dot{a}(t)) = 0 \quad (\text{D.5})$$

$$L \ddot{\varphi} + (g - \ddot{\ell}) \sin(\varphi) = 0,$$

which rewrite for a better identification of all the terms

$$\left(m_1 + m_2(1 - \sin(\varphi)^2)\right)\ddot{\ell} - m_2 L \dot{\varphi}^2 \cos(\varphi) + k(\ell + a(t) - \ell_0) - \left(m_1 + m_2(1 - \sin(\varphi)^2)\right)g + \eta(\dot{\ell} + \dot{a}(t)) = 0 \quad (\text{D.6})$$

$$L \ddot{\varphi} + (g - \ddot{\ell}) \sin(\varphi) = 0.$$

It is clear that if $\{\ell(t), \varphi(t)\}$ is a solution of these equations then $\{\ell(t), -\varphi(t)\}$ is. Also, it can be checked by numerical integration that whatever the starting position, $\varphi(t)$ converges to either $\varphi_\infty(t)$ or $-\varphi_\infty(t)$ which are two oscillatory motions with constant amplitude and opposite phase. These are equivalent to the two coherent states of the cat-qubit. We expect this by construction. Indeed, to build this system we started with a simple parametric oscillator, the vertically driven oscillator to which we added a dissipative degree of freedom, the lossy spring. The parametric oscillator has diverging

solutions which are tamed by the losses of the additional degree of freedom. Crucially, this new degree of freedom only couples to the system via the variable squared. In other words, we engineered a channel for the energy to come out of the system (evacuate the entropy coming from perturbations) without any leak of information (that would lead to decoherence). This is a necessary condition for stabilizing quantum information.

Appendix E

Fabrication Recipes

E.1	Wafer preparation	138
E.2	Circuit patterning	139
E.3	Junction fabrication	140
E.3.1	Electron-beam Lithography	140
E.3.2	Angle Evaporation	141
E.3.3	Junction characterisation	142

In the following appendix, we describe the different fabrication steps required to go from the electromagnetic simulation sketch to the actual chip. The main features of the design are fabricated out of niobium on top of a silicon chip. The junctions are made in a later step out of aluminium.

E.1 Wafer preparation

We start with a 280 μm , 2 inch intrinsic silicon wafer to reduce losses. However, its surface oxidizes spontaneously with atmospheric oxygen. This SiO_2 layer is known to alter the electromagnetic modes quality factor. Diluted HF is used to remove the oxide layer just before (< 5 min) sputtering the wafer with niobium. To protect the niobium while dicing it into several chips, the wafer is spin-coated with S1813. The width of the dicing saw track is typically 40 μm . Before using a chip, one needs to remove the protecting resist. It is crucial to rinse very well within this step otherwise silicon dust sticks to the niobium and becomes impossible to remove. One may start with pre-heated acetone ($< 50^\circ\text{C}$) and stir the chip for best results. Also, one should not sonicate two chips in the same beaker, the chips rub against each other and make scratches on the niobium.

Recipe:

- Sonicate wafer in acetone then IPA (10 + 10 min)
- Clean with HF in water (1:7) for 1 min, rinse with distilled water
- Sputter 120 nm of niobium
- Spin-coat PMMA (3000 rpm, 90 s) and bake (185 °C, 3 min)
- Dice (normal dicing saw)
- Clean individual chips in acetone (50 °C) then IPA (5 + 5 min)

E.2 Circuit patterning

The main features of the chip are etched in the niobium after a laser lithography process. We first spin-coat the chip with optical resist (S1805). The amount of resist (1 drop) deposited before spin-coating is critical: a bulge tends to form along the edges of the chip and distort the pattern since the dose is not enough to go through the thicker layer. The exposure has been increased to mitigate this phenomenon at the cost of overdeveloping patterns at the centre of the chip. This overdevelopment was calibrated (0.5 μm at each boundary) and is taken into account in the lithography drawing. Once in the laser lithography, the chip will be scanned according to the stage orientation which cannot be rotated. Hence, one needs to carefully align the chip with the stage to prevent aberrations at the stitching level. Then a three-point focus should be done: assuming the chip is flat the objective will adapt its height during the process so that it is focussed at any time. Sometimes, due to resist residues at the back of the chip, the vacuum that maintains the chip also deforms it. In this case, it is better to turn off the vacuum. To save time, one can draw the bigger features with a larger objective, we do not usually do so to prevent possible alignment errors. A full chip lithography typically takes one hour. After, the chip is developed in MF319 and rinsed with distilled water. The etching of the niobium is done using RIE with SF_6 . Eventually, we remove the remaining resist in pre-heated acetone. The optical resist is fairly touch at the end of the RIE since it reacted with the plasma. One should stir the chip vigorously while dissolving the resist in the warm acetone.

Recipe:

- Sonicate chip in acetone then IPA (5 + 5 min)
- Spread 1 drop of S1805 evenly on the chip
- Spin-coat (3000 rpm, 90 s) and bake (115 °C, 1 min)
- Align in Laser Lithography (vacuum ON, lens 3 to check alignment)
- Turn off vacuum and proceed to frame initialisation and 3 points focus
- Launch lithography with the following settings:
 - Lens 5

- Filter 30%
- Gain 11 (200 mJ cm^{-2})
- Pos 1 (1 mm s^{-1})
- D-step 1
- Focus 3-point
- Alignment AB centre+direction
- Sweep bidirectional
- Develop in MF319 (60 s, room T) \triangle This solvent oxidises with atmospheric oxygen
- Rinse in distilled water (60 s, room T), dry
- Load in RIE, wait for vacuum ($< 8 \text{ mTorr}$) and purge lines, open SF_6 line
- Launch niobium recipe: Nb. Etching should last approximately 60 s + 20 s over-etching¹
- Remove the remaining resist by stirring the chip vigorously in preheated acetone, rinse with IPA

E.3 Junction fabrication

E.3.1 Electron-beam Lithography

The smallest Dolan bridges required to pattern the JJs are typically several hundreds of nm wide and long. We fabricate these features by using electron-beam lithography in an SEM². To create the bridge we spin-coat a MMA layer (non-polymerized PMMA, hence brittle) below a PMMA layer. During the development, the MMA will dissolve rapidly revealing a bridge.

Recipe:

- Sonicate chip in acetone then IPA (5 + 5 min)
- Bake (185°C , 1 min) to desorb solvents.
- Spin-coat MMA (3000 rpm, 90 s) and bake (185°C , 3 min)
- Let the chip cool down $\sim 30 \text{ s}$
- Spin-coat PMMA (3000 rpm, 90 s) and bake (185°C , 3 min)
- Load in SEM, focus, calibrate current, initialize frame with alignment marks, align writefield.
- Launch lithography with the following settings³:
 - Beam current 25 pA (26 nA), Voltage 25 kV

¹Overetching longer may increase the quality factors by pulling the surfaces away from the conductors

²The junctions may be much bigger e.g. in amplifiers. In this case, we can use a transposed technique with laser lithography

³When bigger features are also to be written, we change the lithography settings with the one in parenthesis to save time

- Working distance 10 mm
- Magnification $\times 600$ ($\times 100$), writefield 100 μm (800 μm)
- Step size 16 nm (180 nm)
- Dose 283 $\mu\text{C cm}^{-2}$
- Develop in IPA in water (3:1) (90 s, 6 $^{\circ}\text{C}$)
- Rinse in IPA (10 s, room T), dry

E.3.2 Angle Evaporation

The chip is then placed in a Plassys evaporator to perform the two angle evaporations that make the junctions. The chip is secured on the evaporator stage using Kapton tape on each edge to prevent aluminium to deposit on the edges of the chip making the lift-off harder. We use a high oxygen pressure (200 mbar) for 10 min to have a large oxide barrier between the superconducting leads. This was intended to make larger surface junctions for a given inductance to increase the reproducibility of the junctions. The downside is that the oxide volume for a given junction inductance increases hence the probability of having a TLS trapped in the junction oxide is greater. Indeed, when we sweep the frequency of our tunable resonators, unexpected avoided crossings appear that we believe are due to TLSs. A TLS in the transmon junction at the transmon frequency decreases its coherence time. When this happen, one can warm-up to ~ 50 K to change the atomic configuration of the oxide¹ hopping no TLS will be close to the transmon as we cool back down. On top of this, its surface is not what eventually limits the junction reproducibility, more likely it is the uniformity of the oxide layer. During this thesis we kept the following recipe

Recipe:

- Tape chip on the evaporator stage and load Δ The orientation of the stage with respect to the rotation axis of the stage is crucial for the angle evaporation.
- Let pump overnight
- Clean substrate with ion beam
- Evaporate 35 nm of Al at a 1 nm s^{-1} rate with a $+35^{\circ}$ angle
- Oxidize at 200 mbar for 10 min
- Evaporate 70 nm of Al at a 1 nm s^{-1} rate with a -35° angle
- Oxidize at 300 mbar for 3 min for a clean overall protecting layer
- Lift-off in preheated ($< 50^{\circ}\text{C}$) acetone for 5 min, stir vigorously at the beginning
- Rinse in IPA, (sonicate 5 s to remove last bits of Aluminium)

¹The oxide configuration is essentially frozen at 20 mK but still drifts. Being cold for weeks, we can "see" a TLS slowly approaching the transmon frequency through the degradation of its coherence time. The warm-up is intended to speed-up the crossing.

E.3.3 Junction characterisation

The size of this bridge governs the size of the JJ which is directly related to its inductance L_J once cold. Using the Ambegaokar-Baratov formula [146], we find

$$L_J = \alpha_{\text{adj}} \frac{\hbar R_J}{\pi \Delta} \quad (\text{E.1})$$

where Δ is the superconducting gap of the leads (for a 30 nm film of aluminium, $\Delta = 2.08 \times 10^{-4}$ eV [147]) and α_{adj} is a proportionality constant that we learn and adjust experimentally (in our case $\alpha_{\text{adj}} = 1.35$), from which we can predict L_J by measuring the room temperature resistance R_J . To calibrate the electron beam dose together with the shape of the bridge, we fabricate arrays of JJs along which these parameters are swept and measure their resistance. The tuning parameter α_{adj} is tuned by measuring a transmon. Indeed, this superconducting qubit has only two parameters E_J and E_C respectively the Josephson and the charging energy and we can measure two quantities, its frequency ω_{ge} and its anharmonicity $\alpha = \omega_{ef} - \omega_{ge}$ where ω_{mn} is the transition frequency between states m and n and states $|g\rangle, |e\rangle$ and $|f\rangle$ refer to the three first states of the transmon. The measured quantities relate to E_J and E_C in the following way, $\hbar\omega_{ge} = \sqrt{8E_J E_C} - E_C$ and $\hbar\alpha = -E_C$ [69]. Hence we have

$$L_J = \frac{8\varphi_0^2 |\alpha|}{\hbar(\omega_{ge} + |\alpha|)^2} \quad (\text{E.2})$$

where $\varphi_0 = \hbar/2e$ is the reduced flux quantum.

Bibliography

- [1] Serge Haroche and Jean-Michel Raimond. *Exploring the Quantum*. Oxford University Press, August 2006. doi:[10.1093/acprof:oso/9780198509141.001.0001](https://doi.org/10.1093/acprof:oso/9780198509141.001.0001).
- [2] Michael A. Nielsen and Isaac L. Chuang. *Quantum Computation and Quantum Information*. Cambridge University Press, 2009. doi:[10.1017/cbo9780511976667](https://doi.org/10.1017/cbo9780511976667).
- [3] Peter W. Shor. Polynomial-time algorithms for prime factorization and discrete logarithms on a quantum computer. *SIAM Journal on Computing*, 26(5):1484–1509, October 1997. doi:[10.1137/s0097539795293172](https://doi.org/10.1137/s0097539795293172).
- [4] Peter W. Shor. Scheme for reducing decoherence in quantum computer memory. *Physical Review A*, 52(4):R2493–R2496, October 1995. doi:[10.1103/physreva.52.r2493](https://doi.org/10.1103/physreva.52.r2493).
- [5] A. M. Steane. Error correcting codes in quantum theory. *Physical Review Letters*, 77(5):793–797, July 1996. doi:[10.1103/physrevlett.77.793](https://doi.org/10.1103/physrevlett.77.793).
- [6] S. B. Bravyi and A. Yu. Kitaev. Quantum codes on a lattice with boundary, 1998.
- [7] R. Barends, J. Kelly, A. Megrant, A. Veitia, D. Sank, E. Jeffrey, T. C. White, J. Mutus, A. G. Fowler, B. Campbell, Y. Chen, Z. Chen, B. Chiaro, A. Dunsworth, C. Neill, P. O’Malley, P. Roushan, A. Vainsencher, J. Wenner, A. N. Korotkov, A. N. Cleland, and John M. Martinis. Superconducting quantum circuits at the surface code threshold for fault tolerance. *Nature*, 508(7497):500–503, April 2014. doi:[10.1038/nature13171](https://doi.org/10.1038/nature13171).
- [8] Austin G. Fowler, Matteo Mariantoni, John M. Martinis, and Andrew N. Cleland. Surface codes: Towards practical large-scale quantum computation. *Physical Review A*, 86(3), September 2012. doi:[10.1103/physreva.86.032324](https://doi.org/10.1103/physreva.86.032324).
- [9] Frank Arute, Kunal Arya, Ryan Babbush, Dave Bacon, Joseph C. Bardin, Rami Barends, Rupak Biswas, Sergio Boixo, Fernando G. S. L. Brandao, David A. Buell, Brian Burkett, Yu Chen, Zijun Chen, Ben Chiaro, Roberto Collins, William Courtney, Andrew Dunsworth, Edward Farhi, Brooks Foxen, Austin Fowler, Craig Gidney, Marissa Giustina, Rob Graff, Keith Guerin, Steve Habegger, Matthew P. Harrigan, Michael J. Hartmann, Alan Ho, Markus Hoffmann, Trent Huang, Travis S. Humble, Sergei V. Isakov, Evan Jeffrey, Zhang Jiang, Dvir Kafri, Kostyantyn Kechedzhi, Julian Kelly, Paul V. Klimov, Sergey Knysh, Alexander Korotkov, Fedor Kostritsa, David Landhuis, Mike Lindmark, Erik Lucero, Dmitry Lyakh, Salvatore Mandrà, Jarrod R. McClean, Matthew McEwen, Anthony Megrant, Xiao

- Mi, Kristel Michielsen, Masoud Mohseni, Josh Mutus, Ofer Naaman, Matthew Neeley, Charles Neill, Murphy Yuezhen Niu, Eric Ostby, Andre Petukhov, John C. Platt, Chris Quintana, Eleanor G. Rieffel, Pedram Roushan, Nicholas C. Rubin, Daniel Sank, Kevin J. Satzinger, Vadim Smelyanskiy, Kevin J. Sung, Matthew D. Trevithick, Amit Vainsencher, Benjamin Villalonga, Theodore White, Z. Jamie Yao, Ping Yeh, Adam Zalcman, Hartmut Neven, and John M. Martinis. Quantum supremacy using a programmable superconducting processor. *Nature*, 574(7779): 505–510, October 2019. doi:[10.1038/s41586-019-1666-5](https://doi.org/10.1038/s41586-019-1666-5).
- [10] Shruti Puri, Samuel Boutin, and Alexandre Blais. Engineering the quantum states of light in a kerr-nonlinear resonator by two-photon driving. *npj Quantum Information*, 3(1), April 2017. doi:[10.1038/s41534-017-0019-1](https://doi.org/10.1038/s41534-017-0019-1).
- [11] Mazyar Mirrahimi, Zaki Leghtas, Victor V Albert, Steven Touzard, Robert J Schoelkopf, Liang Jiang, and Michel H Devoret. Dynamically protected cat-qubits: a new paradigm for universal quantum computation. *New Journal of Physics*, 16(4):045014, April 2014. doi:[10.1088/1367-2630/16/4/045014](https://doi.org/10.1088/1367-2630/16/4/045014).
- [12] T. Yamamoto, K. Inomata, M. Watanabe, K. Matsuba, T. Miyazaki, W. D. Oliver, Y. Nakamura, and J. S. Tsai. Flux-driven josephson parametric amplifier. *Applied Physics Letters*, 93(4):042510, July 2008. doi:[10.1063/1.2964182](https://doi.org/10.1063/1.2964182).
- [13] David P. DiVincenzo. The physical implementation of quantum computation. *Fortschritte der Physik*, 48(9-11):771–783, 2000. doi:[10.1002/1521-3978\(200009\)48:9/11<771::AID-PROP771>3.0.CO;2-E](https://doi.org/10.1002/1521-3978(200009)48:9/11<771::AID-PROP771>3.0.CO;2-E).
- [14] D. D. Awschalom, L. C. Bassett, A. S. Dzurak, E. L. Hu, and J. R. Petta. Quantum spintronics: Engineering and manipulating atom-like spins in semiconductors. *Science*, 339(6124):1174–1179, March 2013. doi:[10.1126/science.1231364](https://doi.org/10.1126/science.1231364).
- [15] M Saffman. Quantum computing with atomic qubits and rydberg interactions: progress and challenges. *Journal of Physics B: Atomic, Molecular and Optical Physics*, 49(20):202001, October 2016. doi:[10.1088/0953-4075/49/20/202001](https://doi.org/10.1088/0953-4075/49/20/202001).
- [16] C. Monroe and J. Kim. Scaling the ion trap quantum processor. *Science*, 339(6124):1164–1169, March 2013. doi:[10.1126/science.1231298](https://doi.org/10.1126/science.1231298).
- [17] Pieter Kok, W. J. Munro, Kae Nemoto, T. C. Ralph, Jonathan P. Dowling, and G. J. Milburn. Linear optical quantum computing with photonic qubits. *Reviews of Modern Physics*, 79(1):135–174, January 2007. doi:[10.1103/revmodphys.79.135](https://doi.org/10.1103/revmodphys.79.135).
- [18] A. Stern and N. H. Lindner. Topological quantum computation—from basic concepts to first experiments. *Science*, 339(6124):1179–1184, March 2013. doi:[10.1126/science.1231473](https://doi.org/10.1126/science.1231473).
- [19] M. H. Devoret and R. J. Schoelkopf. Superconducting circuits for quantum information: An outlook. *Science*, 339(6124):1169–1174, March 2013. doi:[10.1126/science.1231930](https://doi.org/10.1126/science.1231930).

- [20] S. M. Girvin. Circuit QED: superconducting qubits coupled to microwave photons. *Les Houches Session XCVI, Quantum Machines*, pages 113–256, June 2014. doi:[10.1093/acprof:oso/9780199681181.003.0003](https://doi.org/10.1093/acprof:oso/9780199681181.003.0003).
- [21] John M. Martinis, Michel H. Devoret, and John Clarke. Energy-level quantization in the zero-voltage state of a current-biased josephson junction. *Physical Review Letters*, 55(15):1543–1546, October 1985. doi:[10.1103/physrevlett.55.1543](https://doi.org/10.1103/physrevlett.55.1543).
- [22] Michael Tinkham. *Introduction to Superconductivity*. Dover, 06 2004. ISBN 9780486435039.
- [23] Ananda Roy and Michel Devoret. Introduction to parametric amplification of quantum signals with josephson circuits. *Comptes Rendus Physique*, 17(7):740–755, August 2016. doi:[10.1016/j.crhy.2016.07.012](https://doi.org/10.1016/j.crhy.2016.07.012).
- [24] Y.-F. Chen, D. Hover, S. Sendelbach, L. Maurer, S. T. Merkel, E. J. Pritchett, F. K. Wilhelm, and R. McDermott. Microwave photon counter based on josephson junctions. *Physical Review Letters*, 107(21), November 2011. doi:[10.1103/physrevlett.107.217401](https://doi.org/10.1103/physrevlett.107.217401).
- [25] A. Narla, S. Shankar, M. Hatridge, Z. Leghtas, K. M. Sliwa, E. Zalusky-Geller, S. O. Mundhada, W. Pfaff, L. Frunzio, R. J. Schoelkopf, and M. H. Devoret. Robust concurrent remote entanglement between two superconducting qubits. *Phys. Rev. X*, 6:031036, Sep 2016. doi:[10.1103/PhysRevX.6.031036](https://doi.org/10.1103/PhysRevX.6.031036).
- [26] A. Opremcak, I. V. Pechenezhskiy, C. Howington, B. G. Christensen, M. A. Beck, E. Leonard, J. Suttle, C. Wilen, K. N. Nesterov, G. J. Ribeill, T. Thorbeck, F. Schlenker, M. G. Vavilov, B. L. T. Plourde, and R. McDermott. Measurement of a superconducting qubit with a microwave photon counter. *Science*, 361(6408): 1239–1242, 2018. ISSN 0036-8075. doi:[10.1126/science.aat4625](https://doi.org/10.1126/science.aat4625).
- [27] S Kono, K Koshino, Y Tabuchi, A Noguchi, and Y Nakamura. Quantum non-demolition detection of an itinerant microwave photon. *Nature Physics*, 14(6): 546–549, 2018. ISSN 1745-2481. doi:[10.1038/s41567-018-0066-3](https://doi.org/10.1038/s41567-018-0066-3).
- [28] Jean-Claude Besse, Simone Gasparinetti, Michele C. Collodo, Theo Walter, Philipp Kurpiers, Marek Pechal, Christopher Eichler, and Andreas Wallraff. Single-shot quantum nondemolition detection of individual itinerant microwave photons. *Phys. Rev. X*, 8:021003, Apr 2018. doi:[10.1103/PhysRevX.8.021003](https://doi.org/10.1103/PhysRevX.8.021003).
- [29] Audrey Cottet, Matthieu C Dartiailh, Matthieu M Desjardins, Tino Cubaynes, Lauriane C Contamin, Matthieu Delbecq, Jérémie J Viennot, Laure E Bruhat, Benoit Douçot, and Takis Kontos. Cavity QED with hybrid nanocircuits: from atomic-like physics to condensed matter phenomena. *Journal of Physics: Condensed Matter*, 29(43):433002, September 2017. doi:[10.1088/1361-648x/aa7b4d](https://doi.org/10.1088/1361-648x/aa7b4d).
- [30] J.J. Viennot, X. Ma, and K.W. Lehnert. Phonon-number-sensitive electromechanics. *Physical Review Letters*, 121(18), October 2018. doi:[10.1103/physrevlett.121.183601](https://doi.org/10.1103/physrevlett.121.183601).

- [31] Marta Pita-Vidal, Arno Bargerbos, Chung-Kai Yang, David J. van Woerkom, Wolfgang Pfaff, Nadia Haider, Peter Krogstrup, Leo P. Kouwenhoven, Gijs de Lange, and Angela Kou. A gate-tunable, field-compatible fluxonium, 2019. <https://arxiv.org/pdf/1910.07978.pdf>.
- [32] Z. Leghtas, S. Touzard, I. M. Pop, A. Kou, B. Vlastakis, A. Petrenko, K. M. Sliwa, A. Narla, S. Shankar, M. J. Hatridge, M. Reagor, L. Frunzio, R. J. Schoelkopf, M. Mirrahimi, and M. H. Devoret. Confining the state of light to a quantum manifold by engineered two-photon loss. *Science*, 347(6224):853–857, 2015. ISSN 0036-8075. doi:[10.1126/science.aaa2085](https://doi.org/10.1126/science.aaa2085).
- [33] S. Touzard, A. Grimm, Z. Leghtas, S. O. Mundhada, P. Reinhold, C. Axline, M. Reagor, K. Chou, J. Blumoff, K. M. Sliwa, S. Shankar, L. Frunzio, R. J. Schoelkopf, M. Mirrahimi, and M. H. Devoret. Coherent oscillations inside a quantum manifold stabilized by dissipation. *Phys. Rev. X*, 8:021005, Apr 2018. doi:[10.1103/PhysRevX.8.021005](https://doi.org/10.1103/PhysRevX.8.021005).
- [34] Lucas Verney, Raphaël Lescanne, Michel H. Devoret, Zaki Leghtas, and Maz-
yar Mirrahimi. Structural instability of driven josephson circuits prevented
by an inductive shunt. *Physical Review Applied*, 11(2), February 2019.
doi:[10.1103/physrevapplied.11.024003](https://doi.org/10.1103/physrevapplied.11.024003).
- [35] Raphaël Lescanne, Lucas Verney, Quentin Ficheux, Michel H. Devoret, Benjamin
Huard, Mazyar Mirrahimi, and Zaki Leghtas. Escape of a driven quantum joseph-
son circuit into unconfined states. *Physical Review Applied*, 11(1), January 2019.
doi:[10.1103/physrevapplied.11.014030](https://doi.org/10.1103/physrevapplied.11.014030).
- [36] Raphaël Lescanne, Marius Villiers, Théau Peronnin, Alain Sarlette, Matthieu Del-
becq, Benjamin Huard, Takis Kontos, Mazyar Mirrahimi, and Zaki Leghtas. Expo-
nential suppression of bit-flips in a qubit encoded in an oscillator. *Nature Physics*,
March 2020. doi:[10.1038/s41567-020-0824-x](https://doi.org/10.1038/s41567-020-0824-x).
- [37] Raphaël Lescanne, Samuel Deléglise, Emanuele Albertinale, Ulysse Réglade,
Thibault Capelle, Edouard Ivanov, Thibaut Jacqmin, Zaki Leghtas, and Em-
manuel Flurin. Detecting itinerant microwave photons with engineered non-linear
dissipation. *arXiv:1902.05102*, 2019. <https://arxiv.org/abs/1902.05102>.
- [38] Bernard Yurke and John S. Denker. Quantum network theory. *Physical Review*
A, 29(3):1419–1437, March 1984. doi:[10.1103/physreva.29.1419](https://doi.org/10.1103/physreva.29.1419).
- [39] M. H. Devoret. Quantum fluctuations in electrical circuits. *Les Houches Session*
LXIII, Quantum Fluctuations, pages 351–386, 1995. [https://qulab.eng.yale.
edu/documents/reprints/Houches_fluctuations.pdf](https://qulab.eng.yale.edu/documents/reprints/Houches_fluctuations.pdf).
- [40] Guido Burkard, Roger H. Koch, and David P. DiVincenzo. Multilevel quantum
description of decoherence in superconducting qubits. *Physical Review B*, 69(6),
February 2004. doi:[10.1103/physrevb.69.064503](https://doi.org/10.1103/physrevb.69.064503).
- [41] A. A. Clerk, M. H. Devoret, S. M. Girvin, Florian Marquardt, and R. J. Schoelkopf.
introduction to quantum noise, measurement, and amplification. *Reviews of Mod-
ern Physics*, 82(2):1155–1208, April 2010. doi:[10.1103/revmodphys.82.1155](https://doi.org/10.1103/revmodphys.82.1155).

- [42] Simon E. Nigg, Hanhee Paik, Brian Vlastakis, Gerhard Kirchmair, S. Shankar, Luigi Frunzio, M. H. Devoret, R. J. Schoelkopf, and S. M. Girvin. Black-box superconducting circuit quantization. *Physical Review Letters*, 108(24), June 2012. doi:[10.1103/physrevlett.108.240502](https://doi.org/10.1103/physrevlett.108.240502).
- [43] Firat Solgun, David W. Abraham, and David P. DiVincenzo. Blackbox quantization of superconducting circuits using exact impedance synthesis. *Physical Review B*, 90(13), October 2014. doi:[10.1103/physrevb.90.134504](https://doi.org/10.1103/physrevb.90.134504).
- [44] Uri Vool and Michel Devoret. introduction to quantum electromagnetic circuits. *International Journal of Circuit Theory and Applications*, 45(7):897–934, June 2017. doi:[10.1002/cta.2359](https://doi.org/10.1002/cta.2359).
- [45] Mario F. Gely and Gary A. Steele. Qucat: Quantum circuit analyzer tool in python, 2019.
- [46] David Pozar. *Microwave engineering*. Wiley, Hoboken, NJ, 2012. ISBN 978-0470631553.
- [47] Zlatko K. Minev. Catching and reversing a quantum jump mid-flight. *arXiv:1902.10355*, 2019. <https://arxiv.org/abs/1902.10355>.
- [48] Eliot Kapit. The upside of noise: engineered dissipation as a resource in superconducting circuits. *Quantum Science and Technology*, 2(3):033002, aug 2017. doi:[10.1088/2058-9565/aa7e5d](https://doi.org/10.1088/2058-9565/aa7e5d).
- [49] J. D. Teufel, T. Donner, Dale Li, J. W. Harlow, M. S. Allman, K. Cicak, A. J. Sirois, J. D. Whittaker, K. W. Lehnert, and R. W. Simmonds. Sideband cooling of micromechanical motion to the quantum ground state. *Nature*, 475(7356):359–363, July 2011. doi:[10.1038/nature10261](https://doi.org/10.1038/nature10261).
- [50] K. W. Murch, U. Vool, D. Zhou, S. J. Weber, S. M. Girvin, and I. Siddiqi. Cavity-assisted quantum bath engineering. *Physical Review Letters*, 109(18), October 2012. doi:[10.1103/physrevlett.109.183602](https://doi.org/10.1103/physrevlett.109.183602).
- [51] S. Shankar, M. Hatridge, Z. Leghtas, K. M. Sliwa, A. Narla, U. Vool, S. M. Girvin, L. Frunzio, M. Mirrahimi, and M. H. Devoret. Autonomously stabilized entanglement between two superconducting quantum bits. *Nature*, 504(7480):419–422, November 2013. doi:[10.1038/nature12802](https://doi.org/10.1038/nature12802).
- [52] K. M. Sliwa, M. Hatridge, A. Narla, S. Shankar, L. Frunzio, R. J. Schoelkopf, and M. H. Devoret. Reconfigurable josephson circulator/directional amplifier. *Phys. Rev. X*, 5:041020, Nov 2015. doi:[10.1103/PhysRevX.5.041020](https://doi.org/10.1103/PhysRevX.5.041020).
- [53] A. Metelmann and A. A. Clerk. Nonreciprocal photon transmission and amplification via reservoir engineering. *Phys. Rev. X*, 5:021025, Jun 2015. doi:[10.1103/PhysRevX.5.021025](https://doi.org/10.1103/PhysRevX.5.021025).
- [54] A. Metelmann and A. A. Clerk. Nonreciprocal quantum interactions and devices via autonomous feedforward. *Physical Review A*, 95(1), January 2017. doi:[10.1103/physreva.95.013837](https://doi.org/10.1103/physreva.95.013837).

- [55] Hoi-Kwan Lau and Aashish A. Clerk. Fundamental limits and non-reciprocal approaches in non-hermitian quantum sensing. *Nature Communications*, 9(1), October 2018. doi:[10.1038/s41467-018-06477-7](https://doi.org/10.1038/s41467-018-06477-7).
- [56] Rémi Azouit, Alain Sarlette, and Pierre Rouchon. Adiabatic elimination for open quantum systems with effective lindblad master equations. *5th Conference on Decision and Control (CDC 2016)*, December 2016. <https://hal.archives-ouvertes.fr/hal-01398460>.
- [57] R Azouit, F Chittaro, A Sarlette, and P Rouchon. Towards generic adiabatic elimination for bipartite open quantum systems. *Quantum Science and Technology*, 2(4):044011, sep 2017. doi:[10.1088/2058-9565/aa7f3f](https://doi.org/10.1088/2058-9565/aa7f3f).
- [58] M. A. Castellanos-Beltran, K. D. Irwin, G. C. Hilton, L. R. Vale, and K. W. Lehnert. Amplification and squeezing of quantum noise with a tunable josephson meta-material. *Nature Physics*, 4(12):929–931, October 2008. doi:[10.1038/nphys1090](https://doi.org/10.1038/nphys1090).
- [59] N. Bergeal, F. Schackert, M. Metcalfe, R. Vijay, V. E. Manucharyan, L. Frunzio, D. E. Prober, R. J. Schoelkopf, S. M. Girvin, and M. H. Devoret. Phase-preserving amplification near the quantum limit with a josephson ring modulator. *Nature*, 465(7294):64–68, May 2010. doi:[10.1038/nature09035](https://doi.org/10.1038/nature09035).
- [60] C. Macklin, K. O’Brien, D. Hover, M. E. Schwartz, V. Bolkhovskiy, X. Zhang, W. D. Oliver, and I. Siddiqi. A near-quantum-limited josephson traveling-wave parametric amplifier. *Science*, 350(6258):307–310, 2015. ISSN 0036-8075. doi:[10.1126/science.aaa8525](https://doi.org/10.1126/science.aaa8525).
- [61] M. Pechal, L. Huthmacher, C. Eichler, S. Zeytinoglu, A.A. Abdumalikov, S. Berger, A. Wallraff, and S. Filipp. Microwave-controlled generation of shaped single photons in circuit quantum electrodynamics. *Physical Review X*, 4(4), October 2014. doi:[10.1103/physrevx.4.041010](https://doi.org/10.1103/physrevx.4.041010).
- [62] E. Flurin, N. Roch, F. Mallet, M. H. Devoret, and B. Huard. Generating entangled microwave radiation over two transmission lines. *Physical Review Letters*, 109(18), October 2012. doi:[10.1103/physrevlett.109.183901](https://doi.org/10.1103/physrevlett.109.183901).
- [63] Wolfgang Pfaff, Christopher J. Axline, Luke D. Burkhardt, Uri Vool, Philip Reinhold, Luigi Frunzio, Liang Jiang, Michel H. Devoret, and Robert J. Schoelkopf. Controlled release of multiphoton quantum states from a microwave cavity memory. *Nature Physics*, 13(9):882–887, June 2017. doi:[10.1038/nphys4143](https://doi.org/10.1038/nphys4143).
- [64] Théau Peronnin, Danijela Marković, Quentin Ficheux, and Benjamin Huard. Sequential measurement of a superconducting qubit, 2019. <https://arxiv.org/pdf/1904.04635.pdf>.
- [65] Shruti Puri, Christian Kraglund Andersen, Arne L. Grimsmo, and Alexandre Blais. Quantum annealing with all-to-all connected nonlinear oscillators. *Nature Communications*, 8(1), June 2017. doi:[10.1038/ncomms15785](https://doi.org/10.1038/ncomms15785).

- [66] M. D. Reed, L. DiCarlo, B. R. Johnson, L. Sun, D. I. Schuster, L. Frunzio, and R. J. Schoelkopf. High-fidelity readout in circuit quantum electrodynamics using the jaynes-cummings nonlinearity. *Physical Review Letters*, 105(17), October 2010. doi:[10.1103/physrevlett.105.173601](https://doi.org/10.1103/physrevlett.105.173601).
- [67] Yvonne Y. Gao, Brian J. Lester, Yaxing Zhang, Chen Wang, Serge Rosenblum, Luigi Frunzio, Liang Jiang, S. M. Girvin, and Robert J. Schoelkopf. Programmable interference between two microwave quantum memories. *Physical Review X*, 8(2), June 2018. doi:[10.1103/physrevx.8.021073](https://doi.org/10.1103/physrevx.8.021073).
- [68] S. Touzard, A. Kou, N. E. Frattini, V. V. Sivak, S. Puri, A. Grimm, L. Frunzio, S. Shankar, and M. H. Devoret. Gated conditional displacement readout of superconducting qubits. *Phys. Rev. Lett.*, 122:080502, Feb 2019. doi:[10.1103/PhysRevLett.122.080502](https://doi.org/10.1103/PhysRevLett.122.080502).
- [69] Jens Koch, Terri M. Yu, Jay Gambetta, A. A. Houck, D. I. Schuster, J. Majer, Alexandre Blais, M. H. Devoret, S. M. Girvin, and R. J. Schoelkopf. Charge-insensitive qubit design derived from the cooper pair box. *Physical Review A*, 76(4), October 2007. doi:[10.1103/physreva.76.042319](https://doi.org/10.1103/physreva.76.042319).
- [70] Audrey Cottet. *Implémentation d'un bit quantique dans un circuit supraconducteur / Implementation of a quantum bit in a superconducting circuit*. Theses, Université Pierre et Marie Curie - Paris VI, September 2002. <https://tel.archives-ouvertes.fr/tel-00003511>.
- [71] E. Ginossar, Lev S. Bishop, D. I. Schuster, and S. M. Girvin. Protocol for high-fidelity readout in the photon-blockade regime of circuit QED. *Physical Review A*, 82(2), August 2010. doi:[10.1103/physreva.82.022335](https://doi.org/10.1103/physreva.82.022335).
- [72] Lev S. Bishop, Eran Ginossar, and S. M. Girvin. Response of the strongly driven jaynes-cummings oscillator. *Physical Review Letters*, 105(10), September 2010. doi:[10.1103/physrevlett.105.100505](https://doi.org/10.1103/physrevlett.105.100505).
- [73] Maxime Boissonneault, J. M. Gambetta, and Alexandre Blais. Improved superconducting qubit readout by qubit-induced nonlinearities. *Physical Review Letters*, 105(10), September 2010. doi:[10.1103/physrevlett.105.100504](https://doi.org/10.1103/physrevlett.105.100504).
- [74] Th. K. Mavrogordatos, G. Tancredi, M. Elliott, M. J. Peterer, A. Patterson, J. Rahamim, P. J. Leek, E. Ginossar, and M. H. Szymańska. Simultaneous bistability of a qubit and resonator in circuit quantum electrodynamics. *Physical Review Letters*, 118(4), January 2017. doi:[10.1103/physrevlett.118.040402](https://doi.org/10.1103/physrevlett.118.040402).
- [75] Daniel Sank, Zijun Chen, Mostafa Khezri, J. Kelly, R. Barends, B. Campbell, Y. Chen, B. Chiaro, A. Dunsworth, A. Fowler, E. Jeffrey, E. Lucero, A. Megrant, J. Mutus, M. Neeley, C. Neill, P. J. J. O'Malley, C. Quintana, P. Roushan, A. Vainsencher, T. White, J. Wenner, Alexander N. Korotkov, and John M. Martinis. Measurement-induced state transitions in a superconducting qubit: Beyond the rotating wave approximation. *Physical Review Letters*, 117(19), November 2016. doi:[10.1103/physrevlett.117.190503](https://doi.org/10.1103/physrevlett.117.190503).

- [76] J. M. Fink, A. Dombi, A. Vukics, A. Wallraff, and P. Domokos. Observation of the photon-blockade breakdown phase transition. *Physical Review X*, 7(1), January 2017. doi:[10.1103/physrevx.7.011012](https://doi.org/10.1103/physrevx.7.011012).
- [77] Hanhee Paik, D. I. Schuster, Lev S. Bishop, G. Kirchmair, G. Catelani, a. P. Sears, B. R. Johnson, M. J. Reagor, L. Frunzio, L. I. Glazman, S. M. Girvin, M. H. Devoret, and R. J. Schoelkopf. Observation of High Coherence in Josephson Junction Qubits Measured in a Three-Dimensional Circuit QED Architecture. *Physical Review Letters*, 107(24):240501, dec 2011. ISSN 0031-9007. doi:[10.1103/PhysRevLett.107.240501](https://doi.org/10.1103/PhysRevLett.107.240501).
- [78] A Wallraff, D I Schuster, A Blais, L Frunzio, R-S Huang, J Majer, S Kumar, S M Girvin, and R J Schoelkopf. Strong coupling of a single photon to a superconducting qubit using circuit quantum electrodynamics. *Nature*, 431(7005):162–167, 2004. ISSN 0028-0836. doi:[10.1038/nature02851](https://doi.org/10.1038/nature02851).
- [79] Milena Grifoni and Peter Hänggi. Driven quantum tunneling. *Physics Reports*, 304(5-6):229–354, October 1998. doi:[10.1016/s0370-1573\(98\)00022-2](https://doi.org/10.1016/s0370-1573(98)00022-2).
- [80] J.R. Johansson, P.D. Nation, and Franco Nori. QuTiP 2: A python framework for the dynamics of open quantum systems. *Computer Physics Communications*, 184(4):1234–1240, April 2013. doi:[10.1016/j.cpc.2012.11.019](https://doi.org/10.1016/j.cpc.2012.11.019).
- [81] I. Pietikäinen, S. Danilin, K. S. Kumar, A. Vepsäläinen, D. S. Golubev, J. Tuorila, and G. S. Paraoanu. Observation of the bloch-siegert shift in a driven quantum-to-classical transition. *Physical Review B*, 96(2), July 2017. doi:[10.1103/physrevb.96.020501](https://doi.org/10.1103/physrevb.96.020501).
- [82] I. Pietikäinen, S. Danilin, K. S. Kumar, J. Tuorila, and G. S. Paraoanu. Multilevel effects in a driven generalized rabi model. *Journal of Low Temperature Physics*, 191(5-6):354–364, January 2018. doi:[10.1007/s10909-018-1857-8](https://doi.org/10.1007/s10909-018-1857-8).
- [83] C. Wang, Y. Y. Gao, I. M. Pop, U. Vool, C. Axline, T. Brecht, R. W. Heeres, L. Frunzio, M. H. Devoret, G. Catelani, L. I. Glazman, and R. J. Schoelkopf. Measurement and control of quasiparticle dynamics in a superconducting qubit. *Nature Communications*, 5(1), December 2014. doi:[10.1038/ncomms6836](https://doi.org/10.1038/ncomms6836).
- [84] U. Vool, I. M. Pop, K. Sliwa, B. Abdo, C. Wang, T. Brecht, Y. Y. Gao, S. Shankar, M. Hatridge, G. Catelani, M. Mirrahimi, L. Frunzio, R. J. Schoelkopf, L. I. Glazman, and M. H. Devoret. Non-poissonian quantum jumps of a fluxonium qubit due to quasiparticle excitations. *Physical Review Letters*, 113(24), December 2014. doi:[10.1103/physrevlett.113.247001](https://doi.org/10.1103/physrevlett.113.247001).
- [85] Jens Koch, V. Manucharyan, M. H. Devoret, and L. I. Glazman. Charging effects in the inductively shunted josephson junction. *Physical Review Letters*, 103(21), November 2009. doi:[10.1103/physrevlett.103.217004](https://doi.org/10.1103/physrevlett.103.217004).
- [86] Q. Ficheux, S. Jezouin, Z. Leghtas, and B. Huard. Dynamics of a qubit while simultaneously monitoring its relaxation and dephasing. *Nature Communications*, 9(1), May 2018. doi:[10.1038/s41467-018-04372-9](https://doi.org/10.1038/s41467-018-04372-9).

- [87] Jay Gambetta, Alexandre Blais, D. I. Schuster, A. Wallraff, L. Frunzio, J. Majer, M. H. Devoret, S. M. Girvin, and R. J. Schoelkopf. Qubit-photon interactions in a cavity: Measurement-induced dephasing and number splitting. *Physical Review A*, 74(4), October 2006. doi:[10.1103/physreva.74.042318](https://doi.org/10.1103/physreva.74.042318).
- [88] D. Ristè, C. C. Bultink, M. J. Tiggelman, R. N. Schouten, K. W. Lehnert, and L. DiCarlo. Millisecond charge-parity fluctuations and induced decoherence in a superconducting transmon qubit. *Nature Communications*, 4(1), May 2013. doi:[10.1038/ncomms2936](https://doi.org/10.1038/ncomms2936).
- [89] Wojciech H. Zurek. Decoherence and the transition from quantum to classical. *Physics Today*, 44(10):36–44, October 1991. doi:[10.1063/1.881293](https://doi.org/10.1063/1.881293).
- [90] M. Brune, E. Hagley, J. Dreyer, X. Maître, A. Maali, C. Wunderlich, J. M. Raimond, and S. Haroche. Observing the progressive decoherence of the “meter” in a quantum measurement. *Physical Review Letters*, 77(24):4887–4890, December 1996. doi:[10.1103/physrevlett.77.4887](https://doi.org/10.1103/physrevlett.77.4887).
- [91] Christopher C Gerry and Edwin E Hach. Generation of even and odd coherent states in a competitive two-photon process. *Physics Letters A*, 174(3):185–189, March 1993. doi:[10.1016/0375-9601\(93\)90756-p](https://doi.org/10.1016/0375-9601(93)90756-p).
- [92] B. M. Garraway and P. L. Knight. Evolution of quantum superpositions in open environments: Quantum trajectories, jumps, and localization in phase space. *Physical Review A*, 50(3):2548–2563, September 1994. doi:[10.1103/physreva.50.2548](https://doi.org/10.1103/physreva.50.2548).
- [93] J. F. Poyatos, J. I. Cirac, and P. Zoller. Quantum reservoir engineering with laser cooled trapped ions. *Physical Review Letters*, 77(23):4728–4731, December 1996. doi:[10.1103/physrevlett.77.4728](https://doi.org/10.1103/physrevlett.77.4728).
- [94] John Preskill. Sufficient condition on noise correlations for scalable quantum computing. *Quantum Information and Computation*, 13(3-4):0181–0194, jul 2012. ISSN 15337146. <http://arxiv.org/abs/1207.6131>.
- [95] Daniel Gottesman, Alexei Kitaev, and John Preskill. Encoding a qubit in an oscillator. *Physical Review A*, 64(1), June 2001. doi:[10.1103/physreva.64.012310](https://doi.org/10.1103/physreva.64.012310).
- [96] Marios H. Michael, Matti Silveri, R. T. Brierley, Victor V. Albert, Juha Salmilehto, Liang Jiang, and S. M. Girvin. New class of quantum error-correcting codes for a bosonic mode. *Physical Review X*, 6(3), July 2016. doi:[10.1103/physrevx.6.031006](https://doi.org/10.1103/physrevx.6.031006).
- [97] Charles H. Bennett, David P. DiVincenzo, John A. Smolin, and William K. Wootters. Mixed-state entanglement and quantum error correction. *Physical Review A*, 54(5):3824–3851, November 1996. doi:[10.1103/physreva.54.3824](https://doi.org/10.1103/physreva.54.3824).
- [98] Emanuel Knill and Raymond Laflamme. Theory of quantum error-correcting codes. *Physical Review A*, 55(2):900–911, February 1997. doi:[10.1103/physreva.55.900](https://doi.org/10.1103/physreva.55.900).
- [99] S. M. Girvin. Introduction to quantum error correction and fault tolerance. *Les Houches Session CXIII, Quantum Machines*, July 2019. doi:[In press](#).

- [100] Debbie W. Leung, M. A. Nielsen, Isaac L. Chuang, and Yoshihisa Yamamoto. Approximate quantum error correction can lead to better codes. *Physical Review A*, 56(4):2567–2573, October 1997. doi:[10.1103/physreva.56.2567](https://doi.org/10.1103/physreva.56.2567).
- [101] Shruti Puri, Alexander Grimm, Philippe Campagne-Ibarcq, Alec Eickbusch, Kyungjoo Noh, Gabrielle Roberts, Liang Jiang, Mazyar Mirrahimi, Michel H. Devoret, and S.M. Girvin. Stabilized cat in a driven nonlinear cavity: A fault-tolerant error syndrome detector. *Physical Review X*, 9(4), October 2019. doi:[10.1103/physrevx.9.041009](https://doi.org/10.1103/physrevx.9.041009).
- [102] Daniel Gottesman. Theory of fault-tolerant quantum computation. *Physical Review A*, 57(1):127–137, January 1998. doi:[10.1103/physreva.57.127](https://doi.org/10.1103/physreva.57.127).
- [103] Xavier Waintal. What determines the ultimate precision of a quantum computer. *Physical Review A*, 99(4), April 2019. doi:[10.1103/physreva.99.042318](https://doi.org/10.1103/physreva.99.042318).
- [104] Matthew Reagor, Hanhee Paik, Gianluigi Catelani, Luyan Sun, Christopher Axline, Eric Holland, Ioan M. Pop, Nicholas A. Masluk, Teresa Brecht, Luigi Frunzio, Michel H. Devoret, Leonid Glazman, and Robert J. Schoelkopf. Reaching 10 ms single photon lifetimes for superconducting aluminum cavities. *Applied Physics Letters*, 102(19):192604, May 2013. doi:[10.1063/1.4807015](https://doi.org/10.1063/1.4807015).
- [105] Matthew Reagor, Wolfgang Pfaff, Christopher Axline, Reinier W. Heeres, Nissim Ofek, Katrina Sliwa, Eric Holland, Chen Wang, Jacob Blumoff, Kevin Chou, Michael J. Hatridge, Luigi Frunzio, Michel H. Devoret, Liang Jiang, and Robert J. Schoelkopf. Quantum memory with millisecond coherence in circuit qed. *Phys. Rev. B*, 94:014506, Jul 2016. doi:[10.1103/PhysRevB.94.014506](https://doi.org/10.1103/PhysRevB.94.014506).
- [106] S. Rosenblum, P. Reinhold, M. Mirrahimi, Liang Jiang, L. Frunzio, and R. J. Schoelkopf. Fault-tolerant detection of a quantum error. *Science*, 361(6399):266–270, July 2018. doi:[10.1126/science.aat3996](https://doi.org/10.1126/science.aat3996).
- [107] B. M. Terhal and D. Weigand. Encoding a qubit into a cavity mode in circuit QED using phase estimation. *Physical Review A*, 93(1), January 2016. doi:[10.1103/physreva.93.012315](https://doi.org/10.1103/physreva.93.012315).
- [108] Jérémie Guillaud and Mazyar Mirrahimi. Repetition cat qubits for fault-tolerant quantum computation. *Physical Review X*, 9(4), December 2019. doi:[10.1103/physrevx.9.041053](https://doi.org/10.1103/physrevx.9.041053).
- [109] L. Hu, Y. Ma, W. Cai, X. Mu, Y. Xu, W. Wang, Y. Wu, H. Wang, Y. P. Song, C.-L. Zou, S. M. Girvin, L.-M. Duan, and L. Sun. Quantum error correction and universal gate set operation on a binomial bosonic logical qubit. *Nature Physics*, 15(5):503–508, February 2019. doi:[10.1038/s41567-018-0414-3](https://doi.org/10.1038/s41567-018-0414-3).
- [110] C. Flühmann, T. L. Nguyen, M. Marinelli, V. Negnevitsky, K. Mehta, and J. P. Home. Encoding a qubit in a trapped-ion mechanical oscillator. *Nature*, 566(7745):513–517, February 2019. doi:[10.1038/s41586-019-0960-6](https://doi.org/10.1038/s41586-019-0960-6).

- [111] P. Campagne-Ibarcq, A. Eickbusch, S. Touzard, E. Zalys-Geller, N. E. Frattini, V. V. Sivak, P. Reinhold, S. Puri, S. Shankar, R. J. Schoelkopf, L. Frunzio, M. Mirrahimi, and M. H. Devoret. A stabilized logical quantum bit encoded in grid states of a superconducting cavity. *arXiv:1907.12487*, 2019. <https://arxiv.org/abs/1907.12487>.
- [112] Peter Brooks, Alexei Kitaev, and John Preskill. Protected gates for superconducting qubits. *Physical Review A*, 87(5), May 2013. doi:[10.1103/physreva.87.052306](https://doi.org/10.1103/physreva.87.052306).
- [113] Joshua M. Dempster, Bo Fu, David G. Ferguson, D. I. Schuster, and Jens Koch. Understanding degenerate ground states of a protected quantum circuit in the presence of disorder. *Physical Review B*, 90(9), September 2014. doi:[10.1103/physrevb.90.094518](https://doi.org/10.1103/physrevb.90.094518).
- [114] Peter Groszkowski, A Di Paolo, A L Grimsmo, A Blais, D I Schuster, A A Houck, and Jens Koch. Coherence properties of the $0-\pi$ qubit. *New Journal of Physics*, 20(4):043053, April 2018. doi:[10.1088/1367-2630/aab7cd](https://doi.org/10.1088/1367-2630/aab7cd).
- [115] Benoit Douçot and Julien Vidal. Pairing of cooper pairs in a fully frustrated josephson-junction chain. *Physical Review Letters*, 88(22), May 2002. doi:[10.1103/physrevlett.88.227005](https://doi.org/10.1103/physrevlett.88.227005).
- [116] W. C. Smith, A. Kou, X. Xiao, U. Vool, and M. H. Devoret. Superconducting circuit protected by two-cooper-pair tunneling. *arXiv:1905.01206*, 2019. <https://arxiv.org/abs/1905.01206>.
- [117] Alexander Grimm, Nicholas E. Frattini, Shruti Puri, Shantanu O. Mundhada, Steven Touzard, Mazyar Mirrahimi, Steven M. Girvin, Shyam Shankar, and Michel H. Devoret. The kerr-cat qubit: Stabilization, readout, and gates. *arXiv:1907.12131*, 2019. <https://arxiv.org/abs/1907.12131>.
- [118] Shruti Puri, Lucas St-Jean, Jonathan A. Gross, Alexander Grimm, N. E. Frattini, Pavithran S. Iyer, Anirudh Krishna, Steven Touzard, Liang Jiang, Alexandre Blais, Steven T. Flammia, and S. M. Girvin. Bias-preserving gates with stabilized cat qubits. *arXiv:1905.00450*, 2019. <https://arxiv.org/abs/1905.00450>.
- [119] Zaki Leghtas, Gerhard Kirchmair, Brian Vlastakis, Robert J. Schoelkopf, Michel H. Devoret, and Mazyar Mirrahimi. Hardware-efficient autonomous quantum memory protection. *Physical Review Letters*, 111(12), September 2013. doi:[10.1103/physrevlett.111.120501](https://doi.org/10.1103/physrevlett.111.120501).
- [120] L. Gilles, B. M. Garraway, and P. L. Knight. Generation of nonclassical light by dissipative two-photon processes. *Phys. Rev. A*, 49:2785–2799, Apr 1994. doi:[10.1103/PhysRevA.49.2785](https://doi.org/10.1103/PhysRevA.49.2785).
- [121] Howard J. Carmichael. *Statistical Methods in Quantum Optics 2*. Springer Berlin Heidelberg, 2008. doi:[10.1007/978-3-540-71320-3](https://doi.org/10.1007/978-3-540-71320-3).

- [122] N. E. Frattini, V. V. Sivak, A. Lingenfelter, S. Shankar, and M. H. Devoret. Optimizing the nonlinearity and dissipation of a snail parametric amplifier for dynamic range. *Phys. Rev. Applied*, 10:054020, Nov 2018. doi:[10.1103/PhysRevApplied.10.054020](https://doi.org/10.1103/PhysRevApplied.10.054020).
- [123] Andrei Vrajitoarea, Ziwen Huang, Peter Groszkowski, Jens Koch, and Andrew A. Houck. Quantum control of an oscillator using stimulated nonlinearity. *arXiv:1810.10025*, 2018. <https://arxiv.org/abs/1810.10025>.
- [124] JM Raimond and S Haroche. Exploring the Quantum. *Oxford University Press*, 82(1):86, 2006. ISSN 00029505. doi:[10.1119/1.4827830](https://doi.org/10.1119/1.4827830).
- [125] Joachim Cohen. *Autonomous quantum error correction with superconducting qubits*. Theses, PSL Research University, February 2017. <https://tel.archives-ouvertes.fr/tel-01545186>.
- [126] P. Haikka, Y. Kubo, A. Bienfait, P. Bertet, and K. Mølmer. Proposal for detecting a single electron spin in a microwave resonator. *Physical Review A*, 95(2), February 2017. doi:[10.1103/physreva.95.022306](https://doi.org/10.1103/physreva.95.022306).
- [127] John J.L. Morton and Patrice Bertet. Storing quantum information in spins and high-sensitivity ESR. *Journal of Magnetic Resonance*, 287:128–139, February 2018. doi:[10.1016/j.jmr.2017.11.015](https://doi.org/10.1016/j.jmr.2017.11.015).
- [128] Christophe Galland, Nicolas Sangouard, Nicolas Piro, Nicolas Gisin, and Tobias J. Kippenberg. Heralded single-phonon preparation, storage, and read-out in cavity optomechanics. *Physical Review Letters*, 112(14), April 2014. doi:[10.1103/physrevlett.112.143602](https://doi.org/10.1103/physrevlett.112.143602).
- [129] Robert H. Hadfield. Single-photon detectors for optical quantum information applications. *Nature Photonics*, 3:696 EP –, Dec 2009. <https://doi.org/10.1038/nphoton.2009.230>. Review Article.
- [130] Alexei Ourjoumtsev, Rosa Tualle-Brouri, Julien Laurat, and Philippe Grangier. Generating optical schrödinger kittens for quantum information processing. *Science*, 312(5770):83–86, 2006. ISSN 0036-8075. doi:[10.1126/science.1122858](https://doi.org/10.1126/science.1122858).
- [131] Peter C. Humphreys, Norbert Kalb, Jaco P. J. Morits, Raymond N. Schouten, Raymond F. L. Vermeulen, Daniel J. Twitchen, Matthew Markham, and Ronald Hanson. Deterministic delivery of remote entanglement on a quantum network. *Nature*, 558(7709):268–273, June 2018. doi:[10.1038/s41586-018-0200-5](https://doi.org/10.1038/s41586-018-0200-5).
- [132] Sheng-Kai Liao, Wen-Qi Cai, Johannes Handsteiner, Bo Liu, Juan Yin, Liang Zhang, Dominik Rauch, Matthias Fink, Ji-Gang Ren, Wei-Yue Liu, Yang Li, Qi Shen, Yuan Cao, Feng-Zhi Li, Jian-Feng Wang, Yong-Mei Huang, Lei Deng, Tao Xi, Lu Ma, Tai Hu, Li Li, Nai-Le Liu, Franz Koidl, Peiyuan Wang, Yu-Ao Chen, Xiang-Bin Wang, Michael Steindorfer, Georg Kirchner, Chao-Yang Lu, Rong Shu, Rupert Ursin, Thomas Scheidl, Cheng-Zhi Peng, Jian-Yu Wang, Anton Zeilinger, and Jian-Wei Pan. Satellite-relayed intercontinental quantum network. *Phys. Rev. Lett.*, 120:030501, Jan 2018. doi:[10.1103/PhysRevLett.120.030501](https://doi.org/10.1103/PhysRevLett.120.030501).

- [133] Robert Raussendorf and Hans J. Briegel. A one-way quantum computer. *Physical Review Letters*, 86(22):5188–5191, May 2001. doi:[10.1103/physrevlett.86.5188](https://doi.org/10.1103/physrevlett.86.5188).
- [134] G. Nogues, A. Rauschenbeutel, S. Osnaghi, M. Brune, J. M. Raimond, and S. Haroche. Seeing a single photon without destroying it. *Nature*, 400(6741):239–242, July 1999. doi:[10.1038/22275](https://doi.org/10.1038/22275).
- [135] Sébastien Gleyzes, Stefan Kuhr, Christine Guerlin, Julien Bernu, Samuel Deléglise, Ulrich Busk Hoff, Michel Brune, Jean-Michel Raimond, and Serge Haroche. Quantum jumps of light recording the birth and death of a photon in a cavity. *Nature*, 446(7133):297–300, mar 2007. ISSN 1476-4687. doi:[10.1038/nature05589](https://doi.org/10.1038/nature05589).
- [136] D. I. Schuster, A. A. Houck, J. A. Schreier, A. Wallraff, J. M. Gambetta, A. Blais, L. Frunzio, J. Majer, B. Johnson, M. H. Devoret, S. M. Girvin, and R. J. Schoelkopf. Resolving photon number states in a superconducting circuit. *Nature*, 445(7127):515–518, February 2007. doi:[10.1038/nature05461](https://doi.org/10.1038/nature05461).
- [137] Kunihiro Inomata, Zhirong Lin, Kazuki Koshino, William D. Oliver, Jaw-Shen Tsai, Tsuyoshi Yamamoto, and Yasunobu Nakamura. Single microwave-photon detector using an artificial l-type three-level system. *Nature Communications*, 7:12303 EP –, Jul 2016. <https://doi.org/10.1038/ncomms12303>. Article.
- [138] Gerhard Kirchmair, Brian Vlastakis, Zaki Leghtas, Simon E. Nigg, Hanhee Paik, Eran Ginossar, Mazyar Mirrahimi, Luigi Frunzio, S. M. Girvin, and R. J. Schoelkopf. Observation of quantum state collapse and revival due to the single-photon kerr effect. *Nature*, 495(7440):205–209, March 2013. doi:[10.1038/nature11902](https://doi.org/10.1038/nature11902).
- [139] Philip Krantz, Andreas Bengtsson, Michaël Simoen, Simon Gustavsson, Vitaly Shumeiko, W D Oliver, C M Wilson, Per Delsing, and Jonas Bylander. Single-shot read-out of a superconducting qubit using a Josephson parametric oscillator. *Nature Communications*, 7:11417, may 2016. <http://dx.doi.org/10.1038/ncomms11417><http://10.0.4.14/ncomms11417https://www.nature.com/articles/ncomms11417{#}supplementary-information>.
- [140] Olivier Morin, Claude Fabre, and Julien Laurat. Experimentally accessing the optimal temporal mode of traveling quantum light states. *Phys. Rev. Lett.*, 111:213602, Nov 2013. doi:[10.1103/PhysRevLett.111.213602](https://doi.org/10.1103/PhysRevLett.111.213602).
- [141] C. Eichler, D. Bozyigit, C. Lang, L. Steffen, J. Fink, and A. Wallraff. Experimental state tomography of itinerant single microwave photons. *Phys. Rev. Lett.*, 106:220503, Jun 2011. doi:[10.1103/PhysRevLett.106.220503](https://doi.org/10.1103/PhysRevLett.106.220503).
- [142] Eyob A. Sete, John M. Martinis, and Alexander N. Korotkov. Quantum theory of a bandpass purcell filter for qubit readout. *Physical Review A*, 92(1), July 2015. doi:[10.1103/physreva.92.012325](https://doi.org/10.1103/physreva.92.012325).
- [143] Nissim Ofek, Andrei Petrenko, Reinier Heeres, Philip Reinhold, Zaki Leghtas, Brian Vlastakis, Yehan Liu, Luigi Frunzio, S. M. Girvin, L. Jiang, Mazyar Mirrahimi, M. H. Devoret, and R. J. Schoelkopf. Extending the lifetime of a quantum

- bit with error correction in superconducting circuits. *Nature*, 536(7617):441–445, July 2016. doi:[10.1038/nature18949](https://doi.org/10.1038/nature18949).
- [144] Xinyuan You, J. A. Sauls, and Jens Koch. Circuit quantization in the presence of time-dependent external flux. *Physical Review B*, 99(17), May 2019. doi:[10.1103/physrevb.99.174512](https://doi.org/10.1103/physrevb.99.174512).
- [145] Emmanuel Flurin. *The Josephson mixer : a swiss army knife for microwave quantum optics*. Theses, Ecole normale supérieure - ENS PARIS, December 2014. <https://tel.archives-ouvertes.fr/tel-01241123>.
- [146] Vinay Ambegaokar and Alexis Baratoff. Tunneling between superconductors. *Physical Review Letters*, 10(11):486–489, June 1963. doi:[10.1103/physrevlett.10.486](https://doi.org/10.1103/physrevlett.10.486).
- [147] N A Court, A J Ferguson, and R G Clark. Energy gap measurement of nanostructured aluminium thin films for single cooper-pair devices. *Superconductor Science and Technology*, 21(1):015013, November 2007. doi:[10.1088/0953-2048/21/01/015013](https://doi.org/10.1088/0953-2048/21/01/015013).

RÉSUMÉ

Les états quantiques peuvent occuper des états particuliers tels que les états de superposition ou intriqués. Ces états sont fragiles et finissent toujours par être détruits par d'inévitables interactions avec l'environnement. La protection d'états quantiques contre la décohérence est un problème fondamental en physique mais aussi un point crucial pour l'avenir de l'informatique quantique. Dans cette thèse, nous discutons d'expériences conduites sur des circuits supraconducteurs qui cherchent à mettre en évidence un nouveau qubit : le qubit de chat de Schrödinger. Ce qubit appartient à la classe des codes bosoniques qui encodent l'information quantique dans l'espace de Hilbert de dimension infinie d'un résonateur microonde.

En modelant avec soin la dissipation de ce résonateur, nous parvenons à stabiliser les états de base du qubit de chat sans affecter leurs superpositions. En terme d'erreurs, cela se traduit en un taux de bit-flip réduit sans augmenter le taux de phase-flip initial. Cette approche vient défier l'intuition selon laquelle un qubit doit être isolé de son environnement. Au lieu de cela, cette dissipation bien choisie agit comme une boucle de rétroaction qui corrige les erreurs de manière continue et autonome. Cette dissipation décisive est connue sous le nom de dissipation à deux photons et est générée grâce à la méthode du pompage paramétrique. Dans notre cas, il est utilisé pour intensifier sélectivement une interaction d'échange de photons deux-pour-un entre le résonateur du qubit de chat et un autre résonateur dissipatif.

Pour démontrer la correction d'erreur avec les qubits de chats, des efforts expérimentaux ont été fournis pendant cette thèse pour franchir le seuil au delà duquel la correction est plus rapide que l'apparition de nouvelles erreurs, notamment celles induites par le mécanisme de correction lui-même. Ceci nous a conduit à questionner les limites actuelles du pompage paramétrique afin de mieux concevoir nos circuits supraconducteurs. Maîtriser ces dissipations exotiques nous a aussi amené à d'autres applications telles que la détection de photon microondes itinérants pour laquelle une preuve de principe expérimentale a été réalisée au cours de cette thèse.

MOTS CLÉS

Circuits supraconducteurs, Correction d'erreur quantique, Ingénierie de dissipation, Jonction Josephson.

ABSTRACT

Quantum systems can occupy peculiar states, such as superposition or entangled states. These states are intrinsically fragile and eventually get wiped out by inevitable interactions with the environment. Protecting quantum states against decoherence is a fundamental problem in physics and is pivotal for the future of quantum computing. In this thesis, we discuss experiments on superconducting circuits that investigate a new kind of qubit: the Schrödinger cat qubit. It belongs to the class of bosonic codes that store quantum information in the infinite dimensional Hilbert space of a microwave resonator.

By carefully tailoring the dissipation of the resonator, we are able to stabilize the two basis states of the cat-qubit without affecting their superposition. In terms of errors, this translates into a reduced bit-flip rate while keeping a native phase-flip rate. This approach challenges the intuition that a qubit must be isolated from its environment. Instead, the dissipation acts as a feedback loop which continuously and autonomously corrects against errors. This enabling dissipation is known as two-photon dissipation and was engineered by the general method of parametric pumping. In our case, it is used to selectively intensify a two-to-one photon exchange interaction between the cat-qubit resonator and a dissipative resonator.

To demonstrate error correction with cat-qubits, experimental efforts have been made during this thesis to cross the demanding threshold where the correction is faster than the occurrence of all errors, including those induced by the correcting mechanism itself. This has led us to question the current limitations of parametric pumping to better design our superconducting circuits. Mastering the dissipation engineering toolbox also brought us to other applications such as itinerant microwave photon detection for which an experimental proof of principle was realised during this thesis.

KEYWORDS

Superconducting circuits, Quantum Error Correction, Dissipation engineering, Josephson junctions.